Dissertation

submitted to the

Combined Faculty of Mathematics, Engineering and Natural Sciences

of Heidelberg University, Germany

for the degree of

Doctor of Natural Sciences

Put forward by

Jan Victor Arneth

born in: Coburg, Germany

Oral examination: 23.10.2025

Experimental Studies on the Ligand Field Effects and Magnetic Interactions in $3d$, $4f$ and $5d$ Mono- and Heterometallic Molecular Compounds

Referees: Prof. Dr. Rüdiger Klingeler

Prof. Dr. Maurits Haverkort

Experimental Studies on the Ligand Field Effects and Magnetic Interactions in 3*d*, 4*f* and 5*d* Mono- and Heterometallic Molecular Compounds

This thesis presents detailed magnetic investigations on metal-organic compounds hosting $4f$ lanthanide ions, as well as $3d$ and $5d$ transition metal ions. Using combined magnetic susceptibility and tunable high-frequency/high-field electron paramagnetic resonance spectroscopy studies, the microscopic spin Hamiltonian parameters are determined with a high degree of precision. The triply-capped, slightly distorted trigonal-prismatic ligand field of a muffin-shaped, mononuclear Er^{III} complex is found to stabilise the $m_J = \pm 9/2$ Kramers doublet (KD) as the magnetic ground state. Furthermore, significant transverse components of the effective g-tensor account for the observed fast quantum tunnelling of the magnetisation (QTM) in zero magnetic field and indicate that slow relaxation at $B = 0.1$ T occurs through a thermally-activated process including the first excited KD at $\Delta = 37.4(2)$ K. The experimental findings are in close agreement with the results of *ab-initio* CASOCI calculations. In a series of pentagonal-bipyramidal, mononuclear Er^{III} complexes with similar equatorial but differing apical ligands, thermally-assisted QTM governs the different in-field relaxation dynamics. While all complexes exhibit QTM in the predominantly $m_J = \pm 11/2$ ground state KD, due to non-axial effective g-tensors, the incorporation of two charged axial ligands results in considerably low-lying excited energy states, thereby increasing the relaxation rate. The spectroscopic data are used to assess the validity of numerical crystal field analysis and *ab-initio* CASSCF calculations. For anionic complexes, the latter are demonstrated to overestimate the energy splittings. An interplay of the single-ion anisotropy and the antiferromagnetic $3d$-$4f$ exchange coupling is revealed in a family of $V_2^{III}Ln_2^{III}$ complexes with butterfly architecture. The observed correlation indicates that $3d \rightarrow 4f$ charge transfer is the dominant exchange process and strongly depends on the anisotropic electron distribution of the lanthanide $4f$ orbitals. The importance of the $4f$ anisotropy shape also manifests in the magnetic relaxation dynamics. Antiferromagnetic intermolecular interactions in a Re^{IV}-based molecular complex are found to lead to the formation of spin chains. Analysis of the magnetic data shows that an isotropic Heisenberg-chain model with local single-ion anisotropy fails to describe the observed magnetic behaviour. Instead, the diffuse nature of the involved $5d$ orbitals gives rise to a more complex exchange mechanism.

Experimentelle Untersuchungen der Ligandenfeldeffekte und magnetischen Kopplungen in 3*d*-, 4*f*- und 5*d*-mono- und heterometallischen molekularen Verbindungen

Die vorliegende Arbeit befasst sich mit detaillierten magnetischen Untersuchungen metall-organischer Verbindungen, die 4*f*-Lanthanoid- sowie 3*d*- und 5*d*-Übergangsmetallionen enthalten. Mittels Messungen der magnetischen Suszeptibilität und hochfrequenter Hochfeld-Elektronenspinresonanz-Spektroskopie werden die mikroskopischen Parameter des Spin-Hamiltonians mit hoher Präzision bestimmt. Das dreifach überkappte, leicht verzerrt trigonal-prismatische Ligandenfeld eines muffinförmigen, mononuklearen Er^{III}-Komplexes stabilisiert das Kramers-Dublett (KD) mit $m_J = \pm 9/2$ als magnetischen Grundzustand. Signifikante transversale Komponenten des effektiven *g*-Tensors erklären das beobachtete schnelle Quantentunneln der Magnetisierung (QTM) im Nullfeld und legen nahe, dass die langsame magnetische Relaxation bei $B = 0{,}1$ T, thermisch aktiviert, über das erste angeregte KD bei $\Delta = 37{,}4(2)$ K erfolgt. Die experimentellen Ergebnisse stimmen mit den Vorhersagen numerischer *ab-initio* CASOCI-Rechnungen überein. In einer Serie pentagonal-bipyramidaler, mononuklearer Er^{III}-Komplexe mit ähnlichen äquatorialen, aber verschiedenen apikalen Liganden, bestimmt überwiegend das thermisch aktivierte QTM die unterschiedlichen Relaxationsdynamiken. In allen Komplexen tritt aufgrund eines nichtaxialen effektiven *g*-Tensors QTM im Grundzustands-KD mit überwiegend $m_J = \pm 11/2$ auf. Das Vorliegen zweier geladener axialer Liganden führt zu niedrigeren angeregten Energiezuständen und dadurch zu einer höheren Relaxationsrate. Ein Vergleich der spektroskopischen Daten mit numerischen Vorhersagen zeigt, dass *ab-initio* CASSCF-Rechnungen die Energieaufspaltungen für anionische Komplexe überschätzen. In $V_2^{III}Ln_2^{III}$-Komplexen mit Schmetterlingsgeometrie wird eine Korrelation der Einzelionenanisotropie (EIA) und der antiferromagnetischen 3*d*-4*f*-Austauschwechselwirkung beobachtet, welche darauf hinweist, dass 3*d*→4*f*-Ladungstransfer der dominierende Austauschprozess ist und stark von der anisotropen Elektronenverteilung in den 4*f*-Orbitalen der Lanthanoide abhängt. Die 4*f*-Orbitalanisotropie ist auch maßgeblich für die magnetische Relaxationsdynamik. Antiferromagnetische intermolekulare Wechselwirkungen in einem Re^{IV}-basierten Molekülkomplex führen zur Ausbildung von Spinketten. Die Analyse der magnetischen Daten zeigt, dass ein isotropes Heisenberg-Kettenmodell mit lokaler EIA das beobachtete magnetische Verhalten nicht adäquat beschreibt, sondern dass die diffuse räumliche Ausdehnung der beteiligten 5*d*-Orbitale zu einem komplizierteren Austauschmechanismus führt.

List of Partial Publications

Publications that are presented in the main part of the thesis at hand:

- **J. Arneth**, X. Li, J. Braun, S. Paul, M. Schulze, C. E. Anson, W. Wernsdorfer, A. K. Powell and R. Klingeler, "The Interplay of Single Ion Anisotropy and Magnetic 3d-4f Interactions in $V_2^{III}Ln_2^{III}$ Butterfly Complexes", *ChemistryEurope* 3, e202500011 (2025)
  DOI: 10.1002/ceur.202500011

- **J. Arneth**, L. Spillecke, C. Koo, T. A. Bazhenova, E. B. Yagubskii and R. Klingeler, "The Relevance of Non-Axiality and Low-Lying Excited States for Slow Magnetic Relaxation in Pentagonal-Bipyramidal Erbium(III) Complexes Probed by High-frequency EPR", *Chem. Eur. J.* 33, e202500369 (2025)
  DOI: 10.1002/chem.202500369

- **J. Arneth**, C. Pachl, G. Greif, B. Beier, P. W. Roesky, K. Fink and R. Klingeler, "Towards Understanding Prolate $4f$ Monomers: Numerical Predictions and Experimental Validation of Electronic Properties and Slow Relaxation in a Muffin-shaped Er^{III} Complex", arXiv/2507.15547 (2025) (submitted to *Inorg. Chem.*)
  DOI: 10.48550/arXiv.2507.15547

Publications that are presented in the appendix of the thesis at hand:

- **J. Arneth**, K.-Y. Choi, R. Kalaivanan, R. Sankar and R. Klingeler, "Signatures of a quantum critical endpoint in the Kitaev candidate $Na_2Co_2TeO_6$" *Phys. Rev. B* 110, L140402 (2025)
  DOI: 10.1103/PhysRevB.110.L140402

- **J. Arneth**, K.-Y. Choi, R. Kalaivanan, R. Sankar and R. Klingeler, "Competing Interactions and the Effects of Uniaxial Out-of-plane Perturbations in the Honeycomb Antiferromagnet $Na_2Co_2TeO_6$", arXiv:2506.06189 (2025) (submitted to *Phys. Rev. Mat.*)
  DOI: 10.48550/arXiv.2506.06189

Further publications:

- **J. Arneth**, M. Jonak, S. Spachmann, M. Abdel-Hafiez and R. Klingeler, "Uniaxial pressure effects in the two-dimensional van der Waals ferromagnet CrI_3", *Phys. Rev. B* 105, L060404 (2022)
  DOI: 10.1103/PhysRevB.105.L060404

- M. Jonak, E. Walendy, **J. Arneth**, M. Abdel-Hafiez and R. Klingeler, "Low-energy magnon excitations and emerging anisotropic nature of short-range order in CrI_3", *Phys. Rev. B* 106, 214412 (2022)
  DOI: 10.1103/PhysRevB.106.214412

- N. Yuan, A. Elghandour, **J. Arneth**, K. Dey and R. Klingeler, "High-pressure crystal growth and investigation of the metal-to-metal transition of Ruddlesden–Popper trilayer nickelates $La_4Ni_3O_{10}$", *J. Cryst. Growth* 621, 127511 (2024)
  DOI: 10.1016/j.jcrysgro.2023.127511

- A. Elghandour, **J. Arneth**, A. Yadav, S. Luther, P. Kunthia and R. Klingeler, "Magnetic and thermodynamic studies on the distorted kagome magnet Pr_3BWO_{10}", *Phys. Rev. B* 112, 024418 (2025)
  DOI: 10.1103/43bm-x8cj

- L. Bischof, **J. Arneth**, R. Kalaivanan, R. Sankar, K.-Y. Choi and R. Klingeler, "Spin waves in $Na_2Co_2TeO_6$ studied by high-frequency/high-field ESR: Successes and failures of the triple-**q** model", arXiv:2506.03789 (2025) (submitted to *Phys. Rev. B*)
  DOI: 10.48550/arXiv.2506.03789

- B. Beier, E. Walendy, **J. Arneth**, E. Brüchner, R. K. Kremer and R. Klingeler, "Elucidating the origin of long-range ferromagnetic order in Fe_3GeTe_2 by low-energy magnon excitation studies", arXiv:2507.15366 (2025) (submitted to *Phys. Rev. B*)
  DOI: 10.48550/arXiv.2507.15366

Contents

1 Introduction **1**

2 Theoretical Background **5**

2.1 The Free Ion 5

2.2 Ions in a Magnetic Field 7

2.3 Spin-Orbit Coupling 8

2.4 Ligand Field Effects and Magnetic Anisotropy 10

2.5 Energy Scales in Lanthanide and Transition Metal Ions 12

2.6 (Effective) Spin Hamiltonians 15

2.7 Spin-Spin Interaction 16

2.7.1 Dipolar Coupling 16

2.7.2 Exchange Coupling 17

2.8 Electron Paramagnetic Resonance 18

2.9 Magnetic Relaxation 19

2.9.1 Dynamic Magnetic Susceptibility 19

2.9.2 Magnetic Relaxation Processes 21

3 Experimental Methods **25**

3.1 Magnetometry 25

3.1.1 Experimental Setup 25

3.1.2 Sample Preparation 27

3.1.3 Data Processing 28

3.2 High-frequency/High-field Electron Paramagnetic Resonance Spectroscopy 28

3.2.1 Experimental Setup 28

3.2.2 Sample Preparation 31

3.2.3 Data Processing 32

4 Towards Understanding Prolate 4*f* Monomers: Numerical Predictions and Experimental Validation of Electronic Properties and Slow Relaxation in a Muffin-shaped Er^{III} Complex 33

5 The Relevance of Non-Axiality and Low-Lying Excited States for Slow Magnetic Relaxation in Pentagonal-Bipyramidal Erbium(III) Complexes Probed by High-frequency EPR 47

6 The Interplay of Single Ion Anisotropy and Magnetic 3d-4f Interactions in $V_2^{III}Ln_2^{III}$ Butterfly Complexes 63

7 Anisotropic Spin Chains in a Re^{IV}-based Metal-organic Compound 89

7.1 Molecular Structure 90

7.2 Direct Current Magnetisation 92

7.3 Conclusion 98

8 Summary and Conclusion 99

A Measurements on Toroidal Cu_6Ln_3 Complexes 103

B Magnetisation Studies on Dimeric Ln_2 Complexes 111

C Construction of a V-band Cavity for the HF-EPR Setup 121

D Studies Beyond the Scope of this Thesis 129

D.1 Signatures of a Quantum Critical Endpoint in the Kitaev Candidate $Na_2Co_2TeO_6$ 129

D.2 Competing Interactions and the Effects of Uniaxial Out-of-plane Perturbations in the Honeycomb Antiferromagnet $Na_2Co_2TeO_6$ 145

Bibliography 159

Chapter 1

Introduction

Although Otto Stern received the physics Nobel prize (with a total of 82 nominations!) "for his contribution to the development of the molecular ray method and his discovery of the magnetic moment of the proton" [1], most physics graduates connect his name to the seminal Stern-Gerlach experiment [2]. Also owing to Stern smoking cheap, sulfur-containing cigars in the laboratory, this pivotal experiment became the first to demonstrate the quantisation of angular momentum and to provide evidence for the intrinsic angular momentum of the electron, called spin. Both of these fundamental phenomena lay the foundation of magnetism in solid state systems - an effect that is now widely studied across many distinct research fields [3–5].

In the decades following the elucidation of the quantum mechanical origin of magnetism at the beginning of the twentieth century, most studied magnetic materials were structurally based on inorganic metals and oxides. As a result, many technological applications, including electric motors, data storage, and magnetic resonance imaging, emerged from developments in the field of solid state magnetism. It was only in the early 1990s that metal-**organic** magnetic compounds, also termed *molecular magnets*, began to attract greater interest in the scientific community. The spark for this newly emerging research field at the interface of chemistry and physics was ignited by the discovery of magnetic bistability, i.e., magnetic hysteresis, at liquid helium temperatures in the dodecanuclear Mn_{12}ac complex by R. Sessoli and D. Gatteschi [6]. Unlike in conventional ferromagnets, the magnetic hysteresis in Mn_{12}ac does not originate from the irreversibility of many-body domain wall formation effects, but from the slow relaxation of the magnetic moment within a single molecule. The ability of an individual molecule to retain a remnant magnetisation over long timescales generated significant excitement, as it potentially allows information to be stored in a single molecular unit with a diameter of almost only 1 nm [7]. Moreover, such compounds promised to provide an ideal testbed for the coexistence of classical and quantum effects in magnets [8], eventually leading to the experimental observation of quantum tunnelling of the magnetisation [9–11] and oscillation of the tunnel splitting [12]. Not long after this ground-breaking experimental finding, more molecular complexes hosting slowly relaxing magnetic moments were discovered [13–16]. It became clear that magnetic ground states with large spins and strong uniaxial anisotropy are responsible

for the required high effective energy barriers [17,18]. Throughout the years, the term *single-molecule magnets* (SMM) has established itself for this class of materials.

The pursuit of SMM with enhanced performance metrics, such as higher blocking temperatures and longer relaxation times, historically began with the study of high-symmetry polynuclear coordination clusters consisting of $3d$ transition metal ions. This approach aimed to increase the total spin by introducing a large number of ferromagnetically coupled ions [19–21]. However, it was found that the total anisotropy of the cluster decreases with the number of included metal centres, which naturally limits the realised energy barriers in purely $3d$-based molecular magnets [22,23]. About ten years after the discovery of the first SMM, the observation of slow magnetic relaxation in the mononuclear $[TbPc_2]^-$ double-decker complex marked the birth of a promising new class of molecular compounds with only a single magnetic centre: the *single-ion magnets* (SIM) [24]. Most known SIM are based on $4f$ lanthanide ions, in which strong spin-orbit coupling and large unquenched orbital momentum intrinsically favour energy schemes with large effective barriers [25]. The dominant factor determining the SIM performance is the electrostatic ligand field acting on the $4f$ moment [26], which is investigated in the present work for Er^{III}-based complexes with muffin-shaped and pentagonal-bipyramidal coordination. Due to the complex coordination chemistry of rare earth elements, the ligand fields typically exhibit low symmetry. As a result, fast through-barrier relaxation processes often occur and strongly limit the SIM performance [18].

A promising strategy to eliminate these unwanted relaxation paths is the introduction of effective internal magnetic fields through magnetic interactions with other ions. Since the localised nature of the $4f$ orbitals hinders strong magnetic coupling between lanthanide moments, the idea of combining transition metal and lanthanide ions in $3d$-$4f$ complexes emerged quickly [27–29]. This thesis presents a detailed magnetic investigation on a family of isostructural $V_2^{III}Ln_2^{III}$ complexes with a butterfly-shaped core structure - one of the most prominent and thoroughly studied architectures in the literature [30]. Nonetheless, only a few reported examples exist in which the magnetic relaxation is slowed down by magnetic $3d$-$4f$ interactions [31–33]. A relatively recent approach in SMM-design involves the incorporation of $5d$ transition metal ions [34–37]. Despite their atomic similarities to the lighter $3d$ elements, the diffuse nature and strong spin-orbit coupling of the $5d$ orbitals lead to pronounced anisotropic exchange interactions and large single-ion anisotropies [38]. These effects are investigated in the present thesis through the magnetic analysis of a metal-organic compound, in which Re^{IV} ions form a $S = 3/2$ spin chain with local single-ion anisotropy.

While the rise of molecular magnetism was initially dominated by the search for slowly relaxing single-molecule magnets, the years of intense research have revealed many additional possible nanomagnet-based technological applications, such as quantum computing [39,40], magnetic refrigeration [41] and a plethora of molecular spintronic devices [42–44]. The advantage of molecular magnets, hereby, lies in the ability to effectively tune their electronic properties through chemical engineering [45,46]. Depending on the targeted application, the required magnetic behaviour of a molecular

complex may vary significantly. Thus, understanding the microscopic mechanisms that govern the macroscopic magnetic properties is paramount for interpreting the various observed characteristic phenomena and advancing towards functional materials. Alongside static and dynamic magnetic susceptibility measurements, tunable high-frequency/high-field electron paramagnetic resonance spectroscopy (HF-EPR) has established itself as a powerful tool to obtain quantitative information on magnetic molecular compounds [47–49]. Originally developed to investigate the magnetic anisotropy in strongly gapped, non-Kramers systems, HF-EPR was demonstrated to also elucidate the nature of inter- and intramolecular magnetic interactions in coupled polynuclear coordination clusters [50–52].

The thesis at hand provides a detailed study on the magnetic properties of several metal-organic molecular complexes hosting $3d$, $4f$ and $5d$ ions. In particular, the microscopic spin Hamiltonian parameters are quantitatively determined using mainly combined HF-EPR and magnetic susceptibility measurements. Subsequent to this introductory chapter, Chapter 2 provides the basic theoretical concepts of ions in solid state materials necessary for analysing the results of magnetisation and electron paramagnetic resonance spectroscopy studies. The working principle and utilised instrumentation of these two experimental methods are described in Chapter 3. The fourth and fifth chapters present detailed spectroscopic investigations of crystal field effects in mononuclear Er^{III} molecular complexes. Chapter 6 discusses the interplay of single-ion anisotropy and magnetic $3d$-$4f$ exchange interaction in a family of butterfly-shaped $V_2^{III}Ln_2^{III}$ clusters. After Chapter 7 covers a magnetic susceptibility study on a Re^{IV}-containing molecular compound featuring $5d$ spin-chains, Chapter 8 finally summarises the experimental findings and gives a synoptic conclusion of the topics discussed throughout the thesis.

Chapter 2

Theoretical Background

This chapter provides a concise step-by-step introduction to the physical properties of ions in solid state materials that are needed to discuss the results of magnetic susceptibility and electron paramagnetic resonance spectroscopy studies. The presented theoretical framework is mainly based on Refs. [3, 53–57]; a more detailed treatment can be found there.

2.1 The Free Ion

In the Born-Oppenheimer approximation [58], i.e. under the assumption that the nuclear mass M_p is much greater than the electron mass m_e,[1] the Hamiltonian of a free ion with N electrons expressed in its center-of-mass reference frame is given by

$$\hat{\mathcal{H}}_{\text{free}} = \sum_{\text{i}}^{N} \left(\frac{\hat{\boldsymbol{p}}_{\text{i}}^2}{2m_e} - \frac{Ze^2}{|\hat{\boldsymbol{r}}_{\text{i}}|} \right) + \sum_{i \neq j} \left(\frac{e^2}{|\hat{\boldsymbol{r}}_{\text{i}} - \hat{\boldsymbol{r}}_{\text{j}}|} \right). \tag{2.1}$$

Here, Z denotes the atomic number of the nucleus, e is the elementary charge, and $\hat{\boldsymbol{p}}_{\text{i}}$ and $\hat{\boldsymbol{r}}_{\text{i}}$ are the momentum and position operator of the i^{th} electron, respectively.[2] The first sum describes the kinetic and potential energy of all electrons moving in the central potential of the positively charged nucleus individually and contains only terms that act on single-particle states. In contrast, the second term in eq. (2.1) expresses the repulsive Coulomb interaction between the negative charges of the electrons as a pairwise sum over the respective electric potentials. This electron-electron coupling renders an analytic solution of the Hamiltonian for more than one electron impossible. Therefore, iterative and/or approximate methods are required to obtain the eigenfunctions and eigenvalues of $\hat{\mathcal{H}}_{\text{free}}$. One commonly used approach is given by the Hartree-Fock approximation, also called self-consistent field (SCF) method, in which the sum of electronic Coulomb interactions is replaced by an effective mean-field potential $V_{\text{i}}(|\hat{\boldsymbol{r}}_{\text{i}}|)$ generated by all electrons [59–62]. In this approximation, eq. (2.1)

[1] More precisely, the Born-Oppenheimer approximation assumes $M_p \to \infty$.

[2] The notation of the inverse position operator $1/\hat{\boldsymbol{r}}$ is mathematically correctly defined as the Taylor series expanded in orders of $\hat{\boldsymbol{r}}$.

simplifies to

$$\hat{\mathcal{H}}_{\text{free}} = \sum_{\text{i}}^{N} \left(\frac{\hat{\boldsymbol{p}}_{\text{i}}^2}{2m_e} - \frac{Ze^2}{|\hat{\boldsymbol{r}}_{\text{i}}|} + V_{\text{i}}(|\hat{\boldsymbol{r}}_{\text{i}}|) \right), \tag{2.2}$$

where every term acts only on a single electron. The single-particle solutions of eq. (2.2) are given by individual configuration state functions with well-defined quantum numbers. Since the effective mean-field potential $V_{\text{i}}(|\hat{\boldsymbol{r}}_{\text{i}}|)$ is spherically symmetric by construction, the eigenfunctions can be separated into their radial, angular and spin contributions, and, thus, read [63, 64]

$$\psi_{\text{i}}(\boldsymbol{r}) = R_{nl}(r) Y_l^{m_l}(\phi, \theta) \chi(m_s). \tag{2.3}$$

Here, the radial part R_{nl} depends only on the distance between the electron and the nucleus and is characterised by the principal quantum number n and the orbital quantum number l ($0 \leq l \leq n-1$). The angular part is given by the spherical harmonics $Y_l^{m_l}(\phi, \theta)$ of degree l and order m_l ($-l \leq m_l \leq l$), where m_l is the magnetic quantum number corresponding to the z-component of the orbital angular momentum. As electrons exhibit an intrinsic spin degree of freedom, the wave function contains a distinct spin component $\chi(m_s)$ distinguishing the two $m_s = \pm 1/2$ states. The eigenfunctions in eq. (2.3) are often written in a more compact form using the Bra-Ket-notation

$$|\psi_{\text{i}}\rangle = |n, l, m_l, s, m_s\rangle \,. \tag{2.4}$$

To ensure the antisymmetry of the many-electron wavefunction, as required by the Pauli principle for fermionic systems [65], the eigenfunctions of eq. (2.2) can be constructed by setting up the $N \times N$ Slater determinant of single-particle states $|\psi_{\text{i}}\rangle$.

Unlike in single-electron systems, i.e., hydrogen-like ions, where electronic states with the same n but different l are energetically degenerate, the deviation of the effective potential $V_{\text{i}}(|\hat{\boldsymbol{r}}_{\text{i}}|)$ from a Coulomb-like $1/r$-dependence in multi-electron ions leads to a shift of the energy levels depending on their orbital angular momentum. Electronic states with smaller l exhibit a higher probability density close to the origin, whereas electrons in states with larger orbital momenta are, on average, located farther from the nucleus. Thus, they "feel" a nuclear charge that is shielded by the inner-shell electrons. This leads to an energy level scheme, where strongly separated level-bunches, characterised by different n, consist of $2n^2$ states with varying l that are further split into groups of $2(2l+1)$ degenerate m_l and m_s levels. In the Hartree-Fock approximation, the total electronic wavefunction is then given by "filling up" these single-particle states beginning with the lowest energy levels. The order in which the energetically degenerate m_l and m_s states are populated is governed by the first two semi-empirical Hund's rules [66]. Those state that first the total spin $S = \sum_{\text{i}}^{N} s_{\text{i}}$ and then the total orbital angular momentum $L = \sum_{\text{i}}^{N} l_{\text{i}}$ of the ion should be maximised under consideration of the Pauli principle.

2.2 Ions in a Magnetic Field

The remaining degeneracy of the m_l and m_s states can be lifted when the ion is placed in an external magnetic field $\boldsymbol{B}$, also known as the *Zeeman effect* [67]. This effect can be separated into two parts: The influence of the magnetic field on the total spin S of an atom is described by the interaction between the magnetic moment $\boldsymbol{\mu}$ and the field

$$\hat{\mathcal{H}}_S = -\boldsymbol{B} \cdot \hat{\boldsymbol{\mu}} = g_e \mu_\mathrm{B} \boldsymbol{B} \cdot \hat{\boldsymbol{S}}, \tag{2.5}$$

where $g_e \approx 2$ denotes the electron g-factor and μ_B is the Bohr magneton. As quantum mechanics only allows for discrete spin projections along a given axis (here, the field is chosen to be applied along z), states with different m_s exhibit an energy splitting that depends linearly on the magnetic field

$$E(m_s) = g_e \mu_\mathrm{B} B m_s. \tag{2.6}$$

To derive the effect of magnetic fields on the orbital angular momentum L, the magnetic vector potential

$$\hat{\boldsymbol{A}}(\hat{\boldsymbol{r}}) = \frac{\boldsymbol{B} \times \hat{\boldsymbol{r}}}{2} \tag{2.7}$$

has to be included in eq. (2.2).[3] With this, the Hamiltonian becomes

$$\hat{\mathcal{H}} = \sum_\mathrm{i}^N \left(\frac{(\hat{\boldsymbol{p}}_\mathrm{i} + e\hat{\boldsymbol{A}}(\hat{\boldsymbol{r}}_\mathrm{i}))^2}{2m_e} - \frac{Ze^2}{|\hat{\boldsymbol{r}}_\mathrm{i}|} + V_\mathrm{i}(|\hat{\boldsymbol{r}}_\mathrm{i}|) \right) + g_e \mu_\mathrm{B} \boldsymbol{B} \cdot \hat{\boldsymbol{S}}, \tag{2.8}$$

where the Spin-Zeeman interaction from eq. (2.5) has already been included. Assuming a uniform magnetic field and expanding the kinetic term, using $\hat{\boldsymbol{l}} = \hat{\boldsymbol{r}} \times \hat{\boldsymbol{p}}$, yields the total Hamiltonian

$$\hat{\mathcal{H}} = \hat{\mathcal{H}}_\mathrm{free} + \mu_\mathrm{B} \boldsymbol{B} \left(\hat{\boldsymbol{L}} + g_e \hat{\boldsymbol{S}} \right) + \frac{e^2}{8m_e} \sum_\mathrm{i}^N \left(\boldsymbol{B} \times \hat{\boldsymbol{r}}_\mathrm{i} \right)^2. \tag{2.9}$$

The second term in eq. (2.9) represents the Zeeman interaction, which describes the paramagnetic response of an ion with partially filled electron shells to an external magnetic field, due to the finite magnetic moment arising from both orbital and spin angular momentum. This interaction causes the energy levels with different m_l and m_s to split, forming the basis of electron paramagnetic resonance (EPR) spectroscopy experiments. In contrast, the third term does not lead to any energy splitting but accounts for the field-induced diamagnetic contribution of the ion. Although all the

[3] The magnetic field and a corresponding vector potential are related by $\boldsymbol{B} = \boldsymbol{\nabla} \times \boldsymbol{A}$. Hence, the vector potential for a given field is not uniquely defined, but the gradient of any scalar potential may be added without altering the physical magnetic field. This freedom is referred to as the choice of gauge.

electrons, including those in closed shells, contribute to diamagnetism, this term is typically much weaker than the Zeeman interaction at moderate field strengths and is, therefore, often neglected.

2.3 Spin-Orbit Coupling

Up to now, the discussion of the free ion has been conducted in the rest frame of its nucleus, as this provides an intuitive point of view on the studied atomic systems. From this perspective, the total magnetic field acting on the electron is given solely by the applied external field, if present at all. In contrast, in the rest frame of the electron, the electron also "feels" an additional magnetic field stemming from the orbiting positive charge of the nucleus.[4] Although this reference frame is technically non-inertial, approximating it as such allows for the calculation of the effective internal magnetic field as

$$\hat{\boldsymbol{B}}_{\mathrm{SOC}} = \frac{\hat{\boldsymbol{E}} \times \hat{\boldsymbol{p}}}{m_e c^2} = \frac{1}{m_e c^2 r} \frac{dU(r)}{dr} \hat{\boldsymbol{r}} \times \hat{\boldsymbol{p}}, \tag{2.10}$$

where c is the speed of light[5] and $\hat{\boldsymbol{E}}$ and U denote the electric field and corresponding electrostatic potential originating from the charged nucleus, respectively. Here, U was assumed to be spherically symmetric, which corresponds to the Hartree-Fock approximation discussed in section 2.1. This approximation is exact only for hydrogen-like ions. Coupling of the electron spin to $\hat{\boldsymbol{B}}_{\mathrm{SOC}}$ is then given by

$$\hat{\mathcal{H}}_{\mathrm{SOC}} = -\frac{1}{2} \hat{\boldsymbol{\mu}} \cdot \hat{\boldsymbol{B}}_{\mathrm{SOC}} = \frac{g_e \mu_{\mathrm{B}}}{2\hbar m_e c^2 r} \frac{\partial U(r)}{\partial r} \hat{\boldsymbol{s}} \cdot \hat{\boldsymbol{l}} = \lambda \hat{\boldsymbol{s}} \cdot \hat{\boldsymbol{l}}, \tag{2.11}$$

where $\hbar$ is the reduced Planck constant and λ is the spin-orbit coupling parameter. The factor $1/2$ arises from the relativistic correction to the spin of elementary particles, known as *Thomas precession* [68]. $\hat{\mathcal{H}}_{\mathrm{SOC}}$ couples the spin and the orbital momentum of the electron with the coupling strength λ. Since approximately $\lambda \sim U \sim Z$, spin-orbit interaction is more pronounced in heavier elements. In multi-electron systems, the structure of eq. (2.11) will be similar for all electrons. However, screening effects due to electrons in inner shells reduce the effective electrostatic potential $U(r)$ seen by outer electrons. This leads to weaker spin-orbit coupling in outer orbits. As can be calculated, $\hat{\mathcal{H}}_{\mathrm{SOC}}$ does not commute with l_z or s_z. Hence, when spin-orbit coupling is included in the full Hamiltonian (2.9), the individual z-components of spin and orbital angular momentum are no longer conserved, and m_l and m_s cease to be good quantum numbers. However, by introducing the total angular momentum $\hat{\boldsymbol{j}} = \hat{\boldsymbol{l}} + \hat{\boldsymbol{s}}$ one finds that $\hat{\boldsymbol{j}}^2$ and $\hat{j}_z$ commute with both $\hat{\boldsymbol{l}}^2$ and $\hat{\boldsymbol{s}}^2$, such that a new set of eigenstates can be written as

[4] As spin-orbit coupling arises from the interaction of the electron spin with the velocity-dependent, relativistic correction of the nucleus' magnetic field, it is often described as a relativistic effect.

[5] In a more precise fashion, c is the speed of causality at which all particles with zero mass travel in the vacuum.

$$|\psi_\mathrm{i}\rangle = |n, l, s, j, m_j\rangle \,. \tag{2.12}$$

For multi-electron systems, the coupling of the individual angular momenta depends on the relative strengths of spin-orbit and electrostatic interaction. Two different coupling schemes arise: As discussed earlier, spin-orbit coupling is the dominant energy scale in heavy elements (high Z) and in the inner electron orbitals of intermediate heavy elements. In this case, the total angular momentum $\hat{\boldsymbol{j}}_\mathrm{i} = \hat{\boldsymbol{l}}_\mathrm{i} + \hat{\boldsymbol{s}}_\mathrm{i}$ of each individual electron is, to a good approximation, conserved. The electron-electron interaction then couples the different $\hat{\boldsymbol{j}}$ to form the total angular momentum

$$\hat{\boldsymbol{J}} = \sum_\mathrm{i}^N \hat{\boldsymbol{j}}_\mathrm{i}. \tag{2.13}$$

This scheme is known as jj-coupling.

In contrast, spin-orbit interaction is only a small perturbation in lighter ions. Thus, $\hat{\boldsymbol{l}}^2$ and $\hat{\boldsymbol{s}}^2$ approximately commute with the full Hamiltonian and l and s remain conserved quantities. The total spin $\hat{\boldsymbol{S}}$ and the total angular momentum $\hat{\boldsymbol{L}}$ are then given by

$$\hat{\boldsymbol{S}} = \sum_\mathrm{i}^N \hat{\boldsymbol{s}}_\mathrm{i} \quad \text{and} \quad \hat{\boldsymbol{L}} = \sum_\mathrm{i}^N \hat{\boldsymbol{l}}_\mathrm{i}, \tag{2.14}$$

and the total angular momentum is $\hat{\boldsymbol{J}} = \hat{\boldsymbol{L}} + \hat{\boldsymbol{S}}$. This is known as LS-coupling or *Russell-Saunders coupling*. Typically, the transition metal and lanthanide ions studied in the presented thesis follow this coupling scheme. Hence, unless stated otherwise, LS-coupling is assumed throughout this work. The total angular momentum J of an ion's ground state is usually predicted using the third semi-empirical Hund's rule [66]: If the electronic shell is less than half-filled, then $J = |L - S|$ and if the shell is more than half-filled, then $J = |L + S|$.

To incorporate spin-orbit coupling into the magnetic response of the ion, eq. (2.11) has to be included in eq. (2.9). Since $\hat{L}_z$ and $\hat{S}_z$ no longer commute with the full Hamiltonian, it is convenient to reformulate the Zeeman interaction in the total angular momentum basis. It can be shown that [3]

$$\hat{\mathcal{H}}_\mathrm{Z} = -\mu_\mathrm{B} \boldsymbol{B} \left(\hat{\boldsymbol{L}} + g_e \hat{\boldsymbol{S}} \right) = -\mu_\mathrm{B} g_J \boldsymbol{B} \cdot \hat{\boldsymbol{J}}, \tag{2.15}$$

with the so-called *Landé-factor*

$$g_J = 1 + \frac{j(j+1) - l(l+1) + s(s+1)}{2j(j+1)}. \tag{2.16}$$

Eq. (2.15) reveals that each J-level is $(2j+1)$-fold degenerate in the absence of an external magnetic field and that the Zeeman splitting remains linear in B even in the presence of spin-orbit interaction.

2.4 Ligand Field Effects and Magnetic Anisotropy

In solid state systems, the magnetic ion is by no means free, but embedded in a well-defined crystallographic structure. With a few exceptions, such as covalent bonding in heavy actinides, metal ions typically form ionic bonds with the surrounding negatively charged ligands. Those ligands give rise to an electrostatic field, the so-called *ligand field*, that acts on the unpaired electrons of the magnetic ion. A general approach to express the electrostatic potential arising from the ligand field in a spin Hamiltonian is given by the series expansion of an effective potential which operates on the total angular momentum basis functions. In the literature, a handful of equivalent notations are known, but the most commonly used one in the field of molecular magnetism is the Stevens formalism [69]:

$$\hat{\mathcal{H}}_{\mathrm{LF}} = \sum_{\mathrm{k}=0}^{\mathrm{k_{max}=2J}} \sum_{\mathrm{q}=-\mathrm{k}}^{\mathrm{k}} B_{\mathrm{k}}^{\mathrm{q}} \hat{O}_{\mathrm{k}}^{\mathrm{q}} \left(\hat{\boldsymbol{J}} \right). \tag{2.17}$$

Here, $B_{\mathrm{k}}^{\mathrm{q}}$ are the real-valued Stevens parameters and $\hat{O}_{\mathrm{k}}^{\mathrm{q}}$ denote the extended Steven operators, which are functions of the total angular momentum operators $\hat{J}_z$, $\hat{J}_+$, $\hat{J}_-$ and their higher orders [70]. Since Stevens operators with odd k do not influence the magnetism of the spin system but only the intensity of the induced electric dipole transitions, only $\hat{O}_{\mathrm{k}}^{\mathrm{q}}$ with even k are usually considered when describing the results of magnetic and EPR experiments [71]. As one can see from eq. (2.17), the electrostatic ligand field lifts the degeneracy of the m_J-levels even in zero external magnetic field. The effect of $\hat{\mathcal{H}}_{\mathrm{LF}}$ is, therefore, often referred to as *zero field splitting*. More specifically, the axial Stevens operators $\hat{O}_{\mathrm{k}}^{0}$ consist exclusively of powers of $\hat{J}_{\mathrm{z}}$, such that m_J is still conserved and states with the same absolute value $|m_J|$ remain degenerate. In contrast, the off-diagonal operators $\hat{O}_{\mathrm{k}}^{\mathrm{q}\neq 0}$ contain also ladder operators of power q, i.e., $\hat{J}_{+}^{\mathrm{q}}$ and $\hat{J}_{-}^{\mathrm{q}}$, which leads to a mixing of states with m_J and $m_J \pm \mathrm{q}$. The specific values and signs of the coefficients $B_{\mathrm{k}}^{\mathrm{q}}$ depend on the symmetry and strength of the surrounding ligand field.[6] In particular, since symmetry operations are not allowed to change the energy of the ion, the Hamiltonian has to transform as the totally symmetric representation of the point group of the ligand field. This symmetry constraint causes distinct $B_{\mathrm{k}}^{\mathrm{q}}$ to vanish depending on the local crystal symmetry. For high-symmetry environments, such as cubic ligand fields, this drastically reduces the complexity of eq. (2.17). In low-symmetry ligand fields, however, up to 27 free parameters can remain. As an illustrative example, in the case of a weak rhombic ligand field, it is often sufficient to consider only the quadratic terms in $\hat{\boldsymbol{J}}$. The ligand field Hamiltonian then reduces to

$$\hat{\mathcal{H}}_{\mathrm{LF}} = \hat{\boldsymbol{J}} \overleftrightarrow{D} \hat{\boldsymbol{J}}, \tag{2.18}$$

where $\overleftrightarrow{D}$ is a traceless, real and symmetric tensor. Due to these properties, it is always

[6] The Stevens parameters $B_{\mathrm{k}}^{\mathrm{q}}$ with $\mathrm{q} \neq 0$ are not invariant under rotation. Thus, their sign and magnitude depend on the choice of the coordinate system.

possible to rotate the coordinate frame such that $\overleftrightarrow{D} = \mathrm{diag}(D_\mathrm{x}, D_\mathrm{y}, D_\mathrm{z})$ is diagonal with the z-axis pointing along the principal anisotropy direction.[7] By defining the parameters

$$D = D_\mathrm{z} - \frac{D_\mathrm{x} + D_\mathrm{y}}{2} \quad \text{and} \quad E = \frac{D_\mathrm{x} - D_\mathrm{y}}{2}, \tag{2.19}$$

eq. (2.18) can be rewritten as

$$\begin{aligned} \hat{\mathcal{H}}_\mathrm{LF} &= D_\mathrm{x}\hat{J}_\mathrm{x}^2 + D_\mathrm{y}\hat{J}_\mathrm{y}^2 + D_\mathrm{z}\hat{J}_\mathrm{z}^2 - \frac{J(J+1)}{3} \\ &= D\left(\hat{J}_\mathrm{z}^2 - \frac{J(J+1)}{3}\right) + E\left(\hat{J}_\mathrm{x}^2 - \hat{J}_\mathrm{y}^2\right). \end{aligned} \tag{2.20}$$

Here, the constant term $DJ(J+1)/3$ has been subtracted to retain $\mathrm{tr}(\hat{\mathcal{H}}_\mathrm{LF}) = 0$ without changing the system's physical properties, as it merely causes a uniform energy shift. It is convenient to restrict the ratio of D and E to

$$-1/3 \leq D/E \leq 1/3, \tag{2.21}$$

since values outside these limits are physically identical to a rotation of the coordinate frame. By explicitly writing out the $\hat{O}_\mathrm{k}^\mathrm{q}$ and comparing to eq. (2.17), the parameters D and E are related to the second-order Stevens parameters by

$$D = 3B_2^0 \quad \text{and} \quad E = B_2^2. \tag{2.22}$$

Thus, D describes an axial magnetic anisotropy with z being the easy axis for $D < 0$ or the hard axis for $D > 0$. A finite E produces an additional transverse anisotropy, favouring alignment of the magnetic moment along the x- or y-direction. The influence of eq. (2.20) on the level scheme of a system with $J = 1$ is sketched in Fig. 2.1. In an octahedral ligand field, symmetry enforces $D = E = 0$ such that the m_J-levels are degenerate in zero magnetic field. Elongation of the surrounding octahedron along one axis (here chosen to be z) allows for a non-zero D. Since the first term in eq. (2.20) contains only the $\hat{J}_z^2$ operator, m_J remains conserved and the $m_J = 0$ state splits from the still two-fold degenerate $m_J = \pm 1$ manifold. If an additional rhombic distortion of the ligand field is introduced, E also becomes non-zero. The last term in eq. (2.20) then lifts the remaining degeneracy by mixing states with $\Delta m_J \pm 2$, such that the eigenstates become linear combinations of these states. For $J = 1$ those eigenstates take the form $a\,|{+1}\rangle \pm b\,|{-1}\rangle$.

[7] Choosing the principal axis of the magnetic anisotropy to point along z is referred to as the standardisation of the ligand field parameters [72].

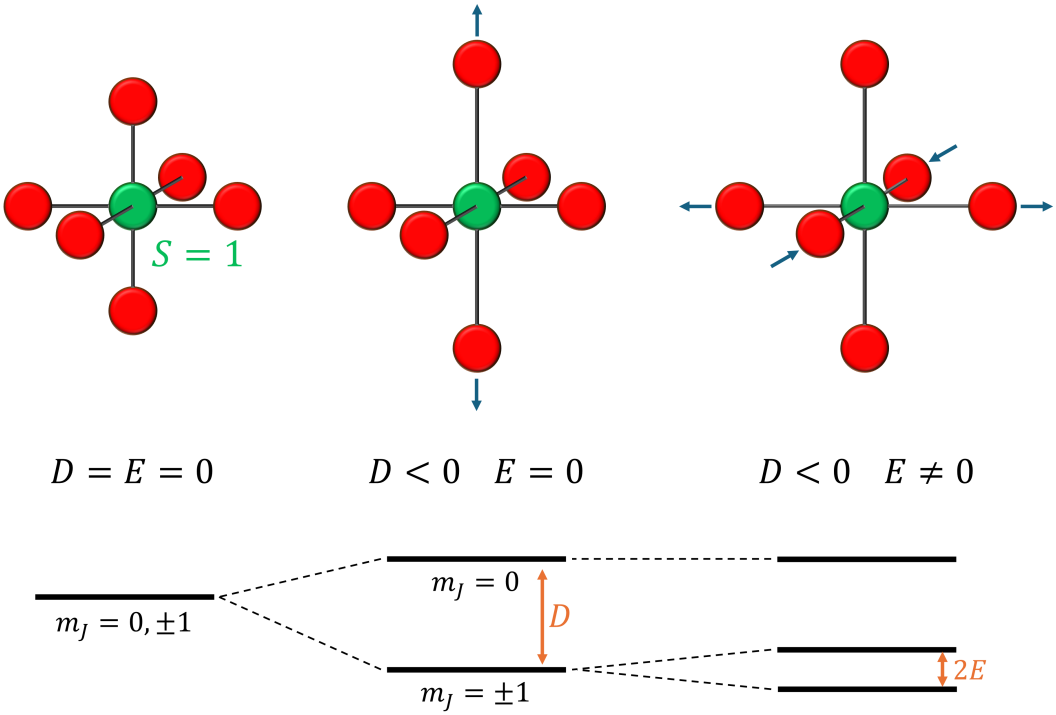


Figure 2.1. Splitting of the m_J-levels in an ion with $J = 1$ due to axial (D) and rhombic (E) anisotropy. Green and red spheres depict the magnetic ion and the ligands, respectively.

2.5 Energy Scales in Lanthanide and Transition Metal Ions

By combining the effects discussed up to here, the full Hamiltonian for a single dressed ion in an external magnetic field reads

$$\hat{\mathcal{H}} = \hat{\mathcal{H}}_{\text{free}} + \hat{\mathcal{H}}_{\text{Z}} + \hat{\mathcal{H}}_{\text{SOC}} + \hat{\mathcal{H}}_{\text{LF}}. \tag{2.23}$$

The resulting energy level scheme, and hence the magnetic ground state, is governed by the competition between these contributions. Their relative strengths strongly depend on the electronic configuration of the ion. For lanthanide ions with the general electron configuration [Xe]$4f^n$, the partially filled $4f$ orbitals exhibit high angular momentum and are well-shielded from the ligand environment by the outer $5s$ and $5p$ electrons. This leads to intrinsically strong spin-orbit coupling and comparatively weak ligand field effects, such that typically $\hat{\mathcal{H}}_{\text{SOC}} \gg \hat{\mathcal{H}}_{\text{LF}}$ holds [57]. As discussed previously, the orbital momentum coupling scheme in lanthanides is not far from perfect LS-coupling, and the magnetic ground state with total angular momentum J is usually determined by Hund's rules. The ligand field then lifts the degeneracy of the m_J levels, although the resulting energy splittings are typically two orders of magnitude smaller than the spin-orbit excitation gap [53, 56, 57]. Fig. 2.2 schematically depicts the energy level scheme for a trivalent holmium ion with $4f^{10}$ electronic configuration in a low-symmetry ligand field.

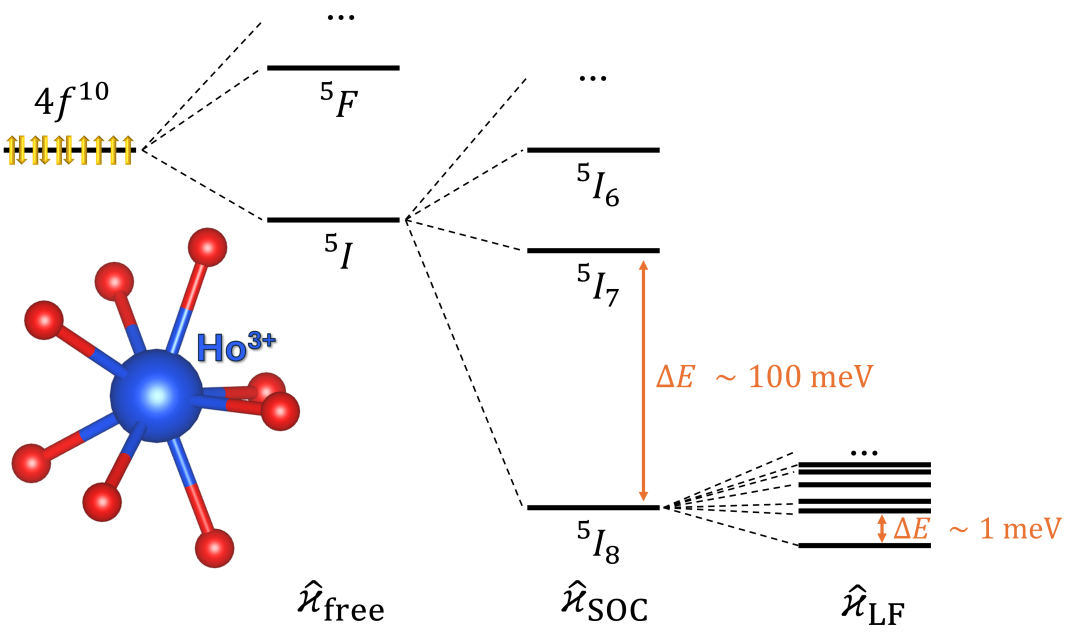


Figure 2.2. Energy level scheme of a Ho^{3+} ion with $4f^{10}$ electronic configuration in a low-symmetry ligand field. From left to right, the free ion, spin-orbit coupling, and ligand field effects are depicted.

In contrast, the partially occupied $3d$ orbitals in $3d$ transition metal ions with the electronic configuration $[Ar]3d^n$ strongly overlap with the ligand orbitals. This usually results in dominant ligand field effects over spin-orbit coupling $\hat{\mathcal{H}}_{\text{LF}} \gg \hat{\mathcal{H}}_{\text{SOC}}$ [3, 57]. Since spin-orbit coupling is negligible to first order and the ligand field only acts on the orbital angular momentum, the degeneracy of the $3d$ orbitals is lifted in a way that strongly depends on the symmetry of the ligand field. Several examples of this are depicted in Fig. 2.3. As a consequence of the ligand field splitting, the orbital states are often left non-degenerate. In a time-reversal symmetric system, the wavefunction of such a non-degenerate state must be real-valued. On the other hand, the orbital momentum operator is purely imaginary, such that

$$\langle\psi|\,\hat{L}_z\,|\psi\rangle = \langle\psi| - i\hbar\frac{\partial}{\partial\phi}\,|\psi\rangle = 0 \tag{2.24}$$

must hold to retain real eigenvalues.[8] In other words, the ligand field quenches the orbital momentum to $L = 0$. Thus, the magnetism of transition metal ions can often be described by assuming a total angular momentum that consists only of the spin component $J \approx S$ instead of the ground state predicted by Hund's rules [3]. For degenerate states, the orbital momentum may be only partially quenched, and a fictitious pseudo-orbital-moment $\tilde{L}$ is retained. The most prominent example of this are the t_{2g} levels in an octahedral ligand field, which can be described by $\tilde{L} = 1$ with the three possible values $m_{\tilde{l}} = 0, \pm 1$ [54].

[8] The same argument holds also for the other two components of the angular momentum vector operator, $\hat{L}_x$ and $\hat{L}_y$.

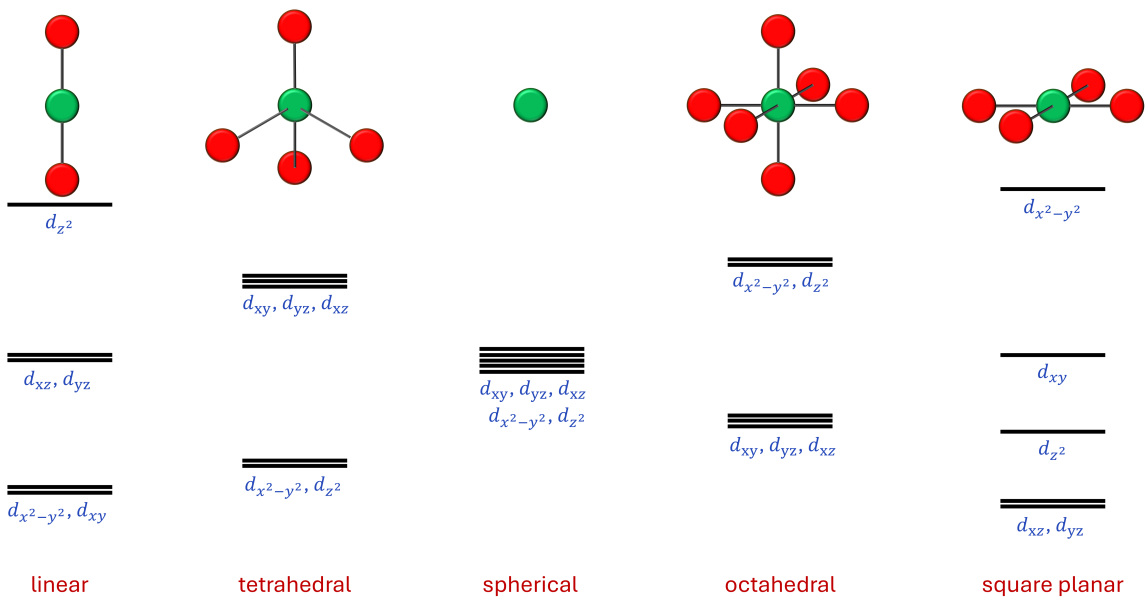


Figure 2.3. Splitting of the five electronic d-levels in linear, tetrahedral, spherical, octahedral, and square planar ligand field symmetries. Green and red spheres depict the magnetic ion and the ligands, respectively. The energy scales in different symmetries are not to scale with each other.

Although strong ligand fields often lead to orbital quenching in $3d$ ions, the weak spin-orbit coupling causes the spin to drag some orbital angular momentum along with it. While $\hat{\mathcal{H}}_{\mathrm{SOC}}$ is usually small compared to the ligand field, it partially restores the orbital angular momentum in a way that it leads to macroscopically measurable effects, especially in EPR experiments [53]. By assuming that spin-orbit coupling in eq. (2.23) is small compared to all other contributions, second-order perturbation theory yields an effective Zeeman term

$$\hat{\mathcal{H}}_{\mathrm{Z}} = \mu_{\mathrm{B}} \boldsymbol{B} \overleftrightarrow{g} \hat{\boldsymbol{S}}. \tag{2.25}$$

Here, $\overleftrightarrow{g}$ is an anisotropic tensor with the components

$$g_{\mathrm{ij}} = 2\delta_{\mathrm{ij}} - 2\lambda \sum_{k \neq 0} \frac{\langle 0| \hat{L}_{\mathrm{i}} |k\rangle \langle k| \hat{L}_{\mathrm{j}} |0\rangle}{|E_k - E_0|}, \tag{2.26}$$

where δ_{ij} is the Kronecker delta. This reduces to

$$g_{\mathrm{i}} = 2 - 2\lambda \sum_{k \neq 0} \frac{|\langle 0| \hat{L}_{\mathrm{i}} |k\rangle|^2}{|E_k - E_0|} \tag{2.27}$$

in its diagonal form. The sum runs over all excited states $k \neq 0$ with the corresponding energies E_k. In eq. (2.25), the orbital angular momentum operator $\hat{L}$ is effectively absorbed by the remaining terms and its effects due to spin-orbit coupling are transmitted through the anisotropic g-tensor.

2.6 (Effective) Spin Hamiltonians

As discussed earlier, spin-orbit coupling leads to a splitting of the energy levels in zero magnetic field based on their total angular momentum J. With a few exceptions, these splittings are typically on the order of a few thousand Kelvin [25, 53, 57], requiring X-ray or UV/Vis spectroscopy to probe transitions between them. In contrast, EPR experiments operate at energies in the GHz range ($\simeq$ 50 K), and measurements on metal-organic complexes are usually performed only up to room temperature. Therefore, in most cases, it is sufficient to consider only the ground state J manifold, while neglecting excited states. This allows for the description of experimental observations by setting up a spin Hamiltonian that does not require knowledge of each electron's state but acts only on the total angular momentum space.

Due to ligand field effects, as introduced in a previous section, the $(2j + 1)$ energetically degenerate levels within the ground state J manifold can split even in the absence of an external magnetic field. Depending on the symmetry of the ligand field, this leads to groups of m_J-levels with reduced degeneracy. For example, a cubic ligand field yields multiplets with up to four-fold degeneracy, whereas in low-symmetry environments, single or double degenerate states are more commonly found. Hereby, Kramer's theorem imposes a fundamental constraint: Any system with an odd number of electrons (or more precisely, with half-integer total spin) must retain at least two-fold degeneracy in zero magnetic field [73].[9] Such pairs of states are called Kramers doublets (KD) and are time conjugate, i.e., obtained from each other by applying the time-reversal operator $\hat{\tau}$.

If the energy gap between such groups of degenerate levels exceeds all relevant experimental energy scales, such as thermal, magnetic, and spectroscopic excitation energies, the measured physical properties of such a group can be described by an effective spin $\hat{\boldsymbol{S}}_{\text{eff}}$ with an associated effective g-tensor $\overleftrightarrow{g}_{\text{eff}}$. This allows to formulate an effective spin Hamiltonian with reduced complexity, where $\hat{\boldsymbol{S}}_{\text{eff}}$ is a fictitious angular momentum, chosen such that $(2S_{\text{eff}} + 1)$ matches the degeneracy of the considered group, and $\overleftrightarrow{g}_{\text{eff}}$ encodes the anisotropy of the underlying system. For a well-isolated Kramers doublet arising from the ground state J-manifold, the effective spin is $S_{\text{eff}} = 1/2$ and the spin Hamiltonian takes the form

$$\mathcal{H} = \hat{\boldsymbol{S}}_{\text{eff}} \overleftrightarrow{g}_{\text{eff}} \boldsymbol{B}. \tag{2.28}$$

In its diagonal frame, the effective g-tensor is then given by the Abragam-Bleaney tensor [53]

$$g_{\text{eff,i}} = g_J \sqrt{2 \sum_{v=\pm} \sum_{w=\pm} \langle v| \hat{J}_{\text{i}} |w\rangle \langle w| \hat{J}_{\text{i}} |v\rangle}, \tag{2.29}$$

[9] Actually, Kramer's theorem demands at least pairwise degeneracy for time-reversal systems with half-integer total spin. Unlike electric fields, magnetic fields break time reversal symmetry, which eventually allows for a splitting of the Kramers doublets.

where $|-\rangle$ and $|+\rangle$ are the two time-conjugate doublet states. The linear dependence on magnetic field in eq. (2.28) relies on the assumption that the Zeeman energy is small compared to the energy splitting between the groups of degenerate levels. In this limit, $|-\rangle$ and $|+\rangle$ remain approximate eigenstates of the full Hamiltonian even in finite magnetic fields. However, at higher fields, when the Zeeman energy becomes comparable to the splitting between the groups, this approximation breaks down, and higher-order Zeeman terms must be included in the effective spin Hamiltonian.

2.7 Spin-Spin Interaction

Up to here, the physical properties of a single, isolated or dressed ion were discussed. However, in compounds containing multiple magnetic centres, the full Hamiltonian typically comprises not only the sum of individual single-ion terms, but also explicit interactions between the ions. The most prominent types of such spin-spin interactions are discussed in the following.

2.7.1 Dipolar Coupling

The most intuitive spin-spin interaction is magnetic dipolar coupling, which describes the magnetic energy of a magnetic moment $\boldsymbol{\mu}_1$ in the magnetic field created by another moment $\boldsymbol{\mu}_2$. The total dipolar coupling energy of the magnetic moments $\hat{\boldsymbol{\mu}}_\mathrm{i} = g_\mathrm{i}\mu_\mathrm{B}\hat{\boldsymbol{S}}_\mathrm{i}$ of two spins separated by $\boldsymbol{r}$ is given by [3]

$$\hat{\mathcal{H}}_\mathrm{dip} = -\frac{\mu_0\mu_\mathrm{B}^2 g_1 g_2}{4\pi|\boldsymbol{r}|^3}\left(3\left(\hat{\boldsymbol{S}}_1\cdot\boldsymbol{e}_r\right)\left(\hat{\boldsymbol{S}}_2\cdot\boldsymbol{e}_r\right) - \hat{\boldsymbol{S}}_1\hat{\boldsymbol{S}}_2\right), \tag{2.30}$$

where μ_0 is the vacuum permeability and $\boldsymbol{e}_r$ is the unit vector along $\boldsymbol{r}$. As indicated by the r^{-3} dependence, dipolar coupling is particularly effective at short distances but decays rapidly with increasing separation. In typical solid state systems with atomic distances of a few Å, the corresponding coupling energy is on the order of 1 K and, therefore, often subordinate to other magnetic interactions. Nonetheless, dipolar interactions can still significantly affect the magnetic properties of a system, such as the magnetic relaxation dynamics [74–76] or magnetic long-range ordering at low temperatures [77–80]. In a more classical description, where the spin operators are treated as classical vectors, eq. (2.30) can be reformulated as

$$\mathcal{H}_\mathrm{dip} = -\frac{\mu_0\mu_\mathrm{B}^2}{4\pi|\boldsymbol{r}|^3}(g_1S_1)(g_2S_2)\left(3\cos(\theta_1)\cos(\theta_2) - \cos(\phi)\right), \tag{2.31}$$

where θ_1 and θ_2 are the angles between $\boldsymbol{r}$ and $\boldsymbol{S}_1$ and $\boldsymbol{S}_2$, respectively, and ϕ is the angle between $\boldsymbol{S}_1$ and $\boldsymbol{S}_2$. This geometry is illustrated schematically in Fig. 2.4. It follows from eq. (2.31) that the energetically most favourable configuration due to dipolar coupling corresponds to a ferromagnetic alignment of both spins along the distance vector $\boldsymbol{r}$. The next favourable configuration is an antiferromagnetic arrange-

ment, where the spins lie perpendicular to $\boldsymbol{r}$. Since dipolar coupling is not mediated by a physical medium, it is also often referred to as the *through-space interaction*.

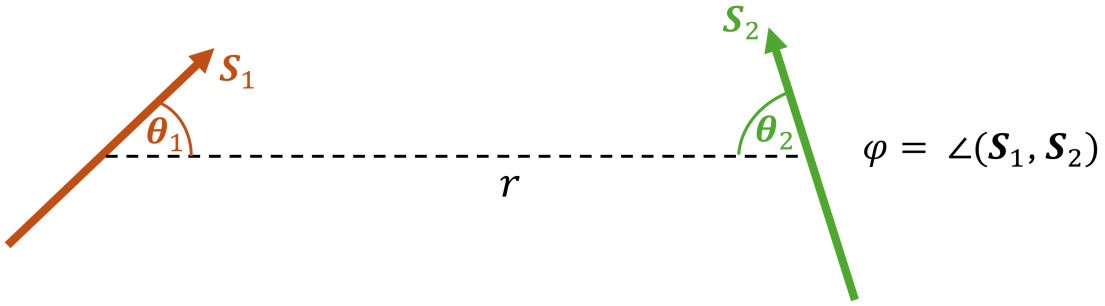


Figure 2.4. Two-dimensional schematic visualisation of the geometry used to calculate the magnetic dipolar interaction of two spins as described in the text.

2.7.2 Exchange Coupling

In most magnetic systems, the dominant spin-spin interaction arises from exchange coupling - a quantum mechanical effect stemming from the fermionic nature of electrons. For two neighbouring magnetic ions with unpaired electrons, the system can lower its kinetic energy through delocalisation of the electrons from their atomic bound states. Due to the combined effects of Pauli blocking and Coulomb repulsion, parallel (ferromagnetic) and antiparallel (antiferromagnetic) spin configurations then acquire different energies.[10] This energy difference defines a coupling constant J as

$$\Delta E = E_{\uparrow\uparrow} - E_{\uparrow\downarrow} = -JS_1S_2. \tag{2.32}$$

The corresponding effective spin Hamiltonian is given by the bilinear term

$$\hat{\mathcal{H}}_{\text{ex}} = -J\hat{\boldsymbol{S}}_1\hat{\boldsymbol{S}}_2. \tag{2.33}$$

The sign and magnitude of J strongly depend on the bonding geometry and the involved ionic orbitals. In the case of *direct exchange*, the electrons delocalise over the overlapping orbitals of the two ions, thus forming molecular bonds. However, direct orbital overlap is usually weak in solid state materials, since typical atomic distances exceed the spatial extension of electronic orbitals. Consequently, the dominant contribution to exchange coupling is often given by indirect exchange, also called *superexchange*, mediated by one or more non-magnetic proxy ions. Here, the electrons delocalise (in their excited state) from their ionic position by virtually hopping onto a non-magnetic bridging ion. The calculation of superexchange couplings in general

[10] The complexities of this subject will not be explored in this work, but detailed treatment of the microscopic nature of exchange coupling can be found, for example, in Ref. [54].

systems is rather complex, since large numbers of possible orbital occupations and exchange paths have to be evaluated. For compounds based on $3d$ transition metals, the semi-empirical Goodenough-Kanamori-Anderson rules offer predictive guidelines for the sign and relative magnitudes of the resulting superexchange interaction [81–83]. These rules were extended and specialised over the years to also take into account more complex exchange coupling scenarios [54], such as, for example, $3d$-$4f$ superexchange [84, 85].

Due to spin-orbit coupling, the excited orbital states of an electron are admixed to its ground state. As such, the spin is sensitive to the local ligand environment, and the exchange coupling becomes anisotropic. The exchange Hamiltonian in eq. (2.33) generalises to

$$\hat{\mathcal{H}}_{\mathrm{ex}} = \hat{\boldsymbol{S}}_1 \overleftrightarrow{J} \hat{\boldsymbol{S}}_2, \tag{2.34}$$

with an anisotropic interaction tensor $\overleftrightarrow{J}$. By decomposing $\overleftrightarrow{J}$ in its isotropic and anisotropic parts, eq. (2.34) can be written as

$$\hat{\mathcal{H}}_{\mathrm{ex}} = -J\hat{\boldsymbol{S}}_1 \cdot \hat{\boldsymbol{S}}_2 + \boldsymbol{d}\left(\hat{\boldsymbol{S}}_1 \times \hat{\boldsymbol{S}}_2\right) + \hat{\boldsymbol{S}}_1 \overleftrightarrow{A} \hat{\boldsymbol{S}}_2. \tag{2.35}$$

Here, the first term corresponds to the isotropic *Heisenberg interaction*, which is usually the dominant contribution to the magnetic coupling. The second term is the anisotropic and antisymmetric *Dzyaloshinskii-Moria interaction* (DMI) defined by the corresponding vector $\boldsymbol{d}$.[11] Due to the underlying symmetry, DMI only occurs for non-centrosymmetric exchange paths and eventually leads to non-collinear spin configurations. Finally, the last part is characterised by an anisotropic symmetric matrix $\overleftrightarrow{A}$. Owing to its mathematical form, it is often called *pseudo-dipolar coupling*.

2.8 Electron Paramagnetic Resonance

As will be discussed in the next chapter, electron paramagnetic resonance spectroscopy (EPR) utilises the absorption of microwave radiation to study the low-energy excitations of a spin system. The full Hamiltonian for a system of magnetic ions in a solid yields an energy level scheme consisting of eigenstates $|\psi_{\mathrm{k}}\rangle$ with energies E_{k}. An incoming microwave photon can now be absorbed by inducing a transition from an occupied initial state $|\psi_{\mathrm{i}}\rangle$ to an empty final state $|\psi_{\mathrm{f}}\rangle$. Due to energy conservation, the energy difference between the two involved levels has to match the microwave frequency ω_{mw} such that the resonance condition

$$\Delta E = E_{\mathrm{f}} - E_{\mathrm{i}} = \hbar\omega_{\mathrm{mw}}. \tag{2.36}$$

is fulfilled. Typically, only energy splittings between the magnetic m_J-levels lie within

[11] As it arises from spin-orbit coupling, the Dzyaloshinskii-Moria interaction is a fully relativistic effect.

the microwave frequency range. Hence, the electromagnetic radiation must drive a magnetic dipole transition, and only its magnetic field component

$$\boldsymbol{B} = \boldsymbol{B}_0 \cos(\omega_{\mathrm{mw}} t) \tag{2.37}$$

needs to be considered. Without the loss of generality, it can be assumed that the microwave magnetic field points along the x-axis.[12] The interaction with the magnetic moment is governed by the interaction Hamiltonian

$$\hat{\mathcal{H}}_{\mathrm{int}} = g_J \mu_{\mathrm{B}} B_0 \hat{J}_{\mathrm{x}} \cos(\omega_{\mathrm{mw}} t). \tag{2.38}$$

According to Fermi's golden rule, the transition probability and, thus, its intensity is proportional to the perturbation matrix element

$$I \sim |\langle \psi_{\mathrm{f}} | \hat{\mathcal{H}}_{\mathrm{int}} | \psi_{\mathrm{i}} \rangle|^2 \sim |\langle \psi_{\mathrm{f}} | \hat{S}_{\mathrm{x}} | \psi_{\mathrm{i}} \rangle|^2 = |\langle \psi_{\mathrm{f}} | \hat{S}_+ + i\hat{S}_- | \psi_{\mathrm{i}} \rangle|^2. \tag{2.39}$$

The spin ladder operators raise or lower the magnetic quantum number m_J of a state $|\psi_{\mathrm{k}}\rangle$ by ± 1, so that eq. (2.39) is non-zero only if

$$\Delta m_J = \pm 1 \quad \text{and} \quad \Delta S = 0 \tag{2.40}$$

holds. These conditions are known as the *dipole selection rules*.

So-called *forbidden* transitions with $\Delta m > 1$ are strongly suppressed, as they arise from weaker higher-order perturbation terms, such as magnetic quadrupole coupling, not included in eq. (2.38). As discussed earlier, the presence of transverse single-ion anisotropy or the application of an external magnetic field perpendicular to the principal anisotropy axis can lead to a mixing of the magnetic m_J-levels in a spin system. In this case, the eigenstates $|\psi_{\mathrm{k}}\rangle$ become linear combinations of the m_J-states, such that transitions between two energy levels can also be partially allowed. Thus, those partially allowed transitions can sometimes be observed in EPR experiments, although they are typically still labelled as *forbidden* due to their unusual field dependence.

2.9 Magnetic Relaxation

2.9.1 Dynamic Magnetic Susceptibility

Since the establishment of thermodynamic equilibrium requires a finite time, the macroscopic magnetisation of a spin system can not follow the variations of an external magnetic field instantaneously, but always lags at least slightly behind. In a static external magnetic field B_0, the spin system exhibits a magnetisation determined by its static magnetic susceptibility χ as $M_0 = \chi B_0$. When the external field is removed

[12] The same selection rules are obtained if $\boldsymbol{B}$ is chosen to point along the y-axis. The z-component of the magnetic field does not contribute to the transition probability, since the orthogonality of the eigenstates $|\psi_{\mathrm{k}}\rangle$ leads to vanishing matrix elements.

instantaneously at $t = 0$, and assuming only a single dominant relaxation time τ, the magnetisation decays exponentially as

$$M(t) = M_0 e^{-t/\tau}. \tag{2.41}$$

If the spin system is subjected to a sinusoidal ac magnetic field $B_{\mathrm{ac}} e^{i\omega t}$, its dynamic magnetisation response depends strongly on the driving frequency ω. For frequencies significantly lower than the system's relaxation rate $\omega\tau \ll 1$, the magnetic moment follows the external field without a phase lag, corresponding to the isothermal susceptibility χ_{T}. In contrast, for $\omega\tau \gg 1$, the system can not react to the rapid oscillations and no energy is exchanged with the external magnetic field. Thus, one recovers the adiabatic susceptibility χ_{S}. For a system of weakly interacting magnetic moments, i. e., $\chi_{\mathrm{T}} - \chi_{\mathrm{S}} < 1$, the dynamic magnetic susceptibility can be calculated to read [86, 87]

$$\chi(\omega) = \chi_{\mathrm{S}} + \frac{\chi_{\mathrm{T}} - \chi_{\mathrm{S}}}{1 + i\omega\tau}, \tag{2.42}$$

which is commonly referred to as the *Debye equation*. Since χ_{T} and χ_{S} are typically real-valued [56], eq. (2.42) can be decomposed into its real (in-phase) $\chi'(\omega)$ and imaginary (out-of-phase) $\chi''(\omega)$ components:

$$\chi'(\omega) = \chi_{\mathrm{S}} + \frac{\chi_{\mathrm{T}} - \chi_{\mathrm{S}}}{1 + \omega^2\tau^2} \quad \text{and} \quad \chi''(\omega) = \frac{(\chi_{\mathrm{T}} - \chi_{\mathrm{S}})\omega\tau}{1 + \omega^2\tau^2}. \tag{2.43}$$

Fig. 2.5(a) displays the frequency dependence of the in-phase and out-of-phase component of the dynamic magnetic susceptibility on a semi-logarithmic scale. At very low and very high frequencies, $\chi''(\omega)$ vanishes, indicating that no energy is dissipated by the system. Correspondingly, $\chi'(\omega)$ tends towards χ_{T} at $\omega = 0$ and χ_{S} as $\omega \to \infty$. The condition $\omega\tau = 1$ marks a characteristic point: $\chi'(\omega)$ exhibits a distinct step-like drop, while $\chi''(\omega)$ reaches a clear maximum. These features are often used to extract the relaxation time τ from the results of ac susceptibility measurements. Another way of visualising the magnetic relaxation dynamics is given by the *Cole-Cole plot*, which traces the parametric relation of $\chi'(\omega)$ and $\chi''(\omega)$ at different frequencies (see Fig. 2.5(b)). As such, eq. (2.43) describes a semicircle centred around the χ'-axis. The top of the semicircle corresponds to the condition $\omega\tau = 1$, allowing a straightforward extraction of the relaxation time τ.

In solid state systems, the magnetic relaxation is rarely governed by a single time constant, but structural disorder or local variations often lead to a distribution of different relaxation times. To account for this, eq. (2.42) can be extended to

$$\chi(\omega) = \chi_{\mathrm{S}} + \frac{\chi_{\mathrm{T}} - \chi_{\mathrm{S}}}{1 + (i\omega\tau)^{1-\alpha}}, \tag{2.44}$$

where $0 < \alpha < 1$ is a phenomenological parameter characterising the width of the relaxation time distribution [88]. For $\alpha = 0$, eq. (2.44) recovers the Debye equation. A finite distribution of relaxation times ($\alpha > 1$) leads to a shift of the semicircle's

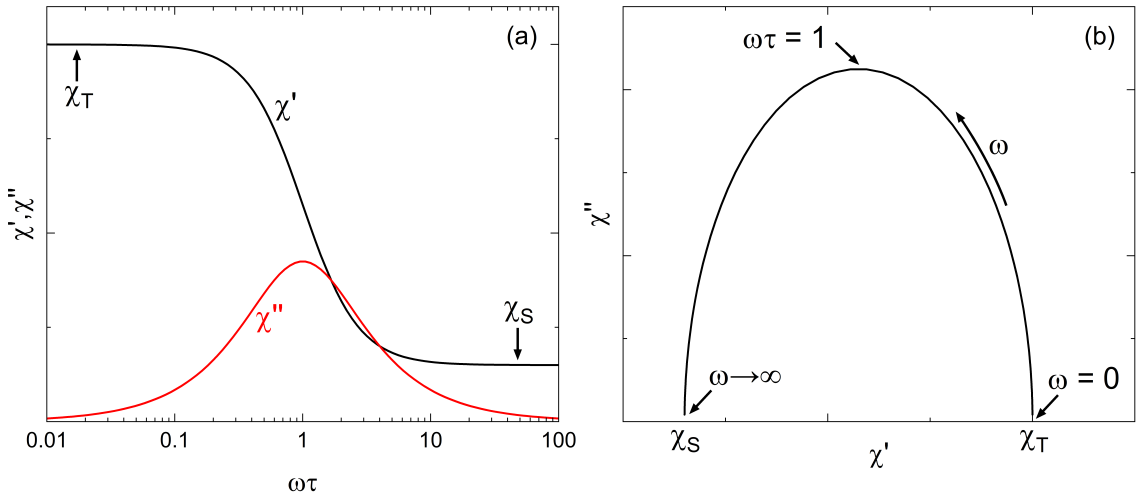


Figure 2.5. (a) Frequency dependence of the in-phase (χ') and out-of-phase (χ'') component of the dynamic magnetic susceptibility and (b) Cole-Cole plot for a weakly interacting spin system with only one relaxation time. χ_T and χ_S denote the isothermal and adiabatic susceptibility, respectively.

center in the Cole-Cole plot and to a broadening of the features in $\chi'(\omega)$ and $\chi''(\omega)$, while retaining the symmetry about $\omega\tau = 1$. Asymmetric behaviour arises when different relaxation times originate from distinct relaxation pathways [89, 90].

2.9.2 Magnetic Relaxation Processes

As discussed in the previous section, the relaxation time τ determines how fast a spin system returns to its magnetic ground state after being excited into a higher-lying energy state at ΔE. In general, several relaxation processes can contribute to the magnetic relaxation along a certain pathway. The most relevant relaxation processes for metal-organic molecular compounds, as studied in the present thesis, are schematically displayed in Fig. 2.6 and listed in the following:

- **Direct Relaxation:** The spin system can make a direct transition to its magnetic ground state by emitting a long-wavelength acoustic phonon into the lattice. Since the density of phonon states at typical energies ($\simeq 1$ K) is rather low, this process is usually slow compared to two-phonon processes at most accessible temperatures. The relaxation rate of the direct process can be calculated as

$$\tau_{\text{direct}}^{-1} = AB^nT, \tag{2.45}$$

  with the system-specific parameter A [53]. The field dependence of $\tau_{\text{direct}}^{-1}$ is governed by the exponent n, which assumes $n = 2$ for non-Kramers systems and $n = 4$ for Kramers systems.

- **Raman Relaxation:** Magnetic relaxation may also occur through a two-phonon process involving a virtual intermediate phonon state. The spin system

relaxes by virtually absorbing a phonon with energy ω_1 and emitting another with energy $\omega_1 + \Delta E$. The corresponding relaxation rate is given by

$$\tau_{\text{Raman}}^{-1} = CT^m, \tag{2.46}$$

where C is a system-specific parameter and m is an exponent that depends strongly on the electronic structure and temperature [53]. While eq. (2.46) assumes that all phonon modes contribute, two recent independent, theoretical studies suggest that Raman relaxation in molecular magnets predominantly involves optical phonons [91–93]. In this case, the relaxation rate becomes

$$\tau_{\text{Raman}}^{-1} = \tau_{\text{R}}^{-1} \frac{e^{-W/k_{\text{B}}T}}{\left(e^{-W/k_{\text{B}}T} - 1\right)^2}, \tag{2.47}$$

where τ_{R}^{-1} is the high-temperature relaxation rate and W is the energy gap of the lowest-lying optical phonon modes at the Γ-point.

- **Orbach Relaxation:** This process occurs when a low-lying excited state of the spin system is thermally accessible. The spin system absorbs a phonon to reach this excited state and then emits another phonon to return to the ground state. Because each step conserves energy, the process can be considered as two sequential one-phonon transitions.[13] The energy needed to excite the spin-system defines an effective energy barrier U_{eff}, such that the Orbach relaxation rate reads

$$\tau_{\text{Orbach}}^{-1} = \tau_0^{-1} e^{-U_{\text{eff}}/k_{\text{B}}T} \tag{2.48}$$

with τ_0^{-1} being the high-temperature relaxation rate.

- **Quantum Tunnelling of the Magnetisation (QTM):** As discussed earlier, the presence of transverse interactions leads to energy eigenstates that are given by superpositions of different m_J-states. As such, the spin system can tunnel from one magnetic state to the other and magnetic relaxation can occur without coupling to the lattice. Since no phonons are involved in this relaxation process, the corresponding relaxation time is independent of temperature. However, the energy splitting of the magnetic levels strongly depends on the external static magnetic field. For magnetic fields close to an (avoided) level crossing at B_0, the relaxation rate of QTM can be calculated as

$$\tau_{\text{QTM}}^{-1} = \frac{k_1}{1 + k_2(B - B_0)^2}, \tag{2.49}$$

where k_1 and k_2 are system-specific parameters. Eq. (2.49) shows that QTM can be effectively suppressed by applying a static external magnetic field.

[13] The Orbach process can also be viewed as a concerted two-phonon resonant Raman process.

The total magnetic relaxation rate τ^{-1} is given by the contributions of the individual relaxation processes

$$\tau^{-1} = \tau_{\text{direct}}^{-1} + \tau_{\text{Raman}}^{-1} + \tau_{\text{Orbach}}^{-1} + \tau_{\text{QTM}}^{-1}, \tag{2.50}$$

which all exhibit distinct temperature dependencies. At the lowest temperatures, only a few phononic states are excited, and QTM gives an upper limit for the relaxation time for $T \to 0$. In contrast, its exponential temperature dependence renders Orbach relaxation the dominant process for $T \to \infty$, such that U_{eff} can be determined from the magnetic relaxation behaviour at high temperatures.

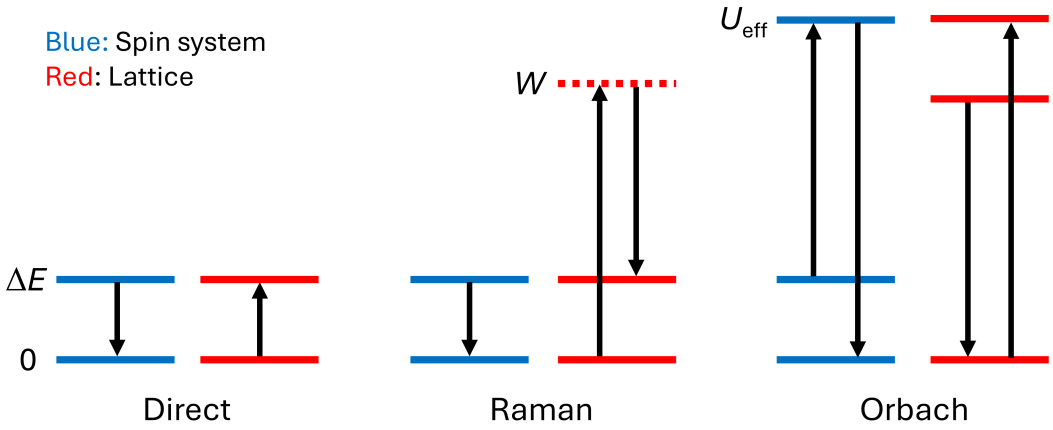


Figure 2.6. Schematic visualisation of the most relevant spin-phonon relaxation processes in molecular magnets. Blue and red lines depict the energy levels of the spin system and of the lattice vibrations, respectively. Black arrows mark transitions between the energy levels.

Chapter 3

Experimental Methods

3.1 Magnetometry

3.1.1 Experimental Setup

The magnetic moment and susceptibility of the investigated samples were measured by means of a *Magnetic Properties Measurement System* (MPMS3) and a *Physical Properties Measurement System* (PPMS-14) equipped with the *Vibrating Sample Magnetometer* (VSM) option. Both devices are products from *Quantum Design* and a detailed description of their working principle can be found in the respective manuals [94, 95]. The MPMS allows for magnetic measurements at temperatures from 1.8 K to 400 K and in magnetic fields up to 7 T. This temperature range can be further extended down to 0.4 K by equipping the MPMS with an *iQuantum-*^{3}*He* option, which exploits the base cryostat as a precooling stage [96]. The magneto-cryogenic system of the PPMS can provide magnetic fields up to 14 T in a temperature range from 1.8 K to 350 K.

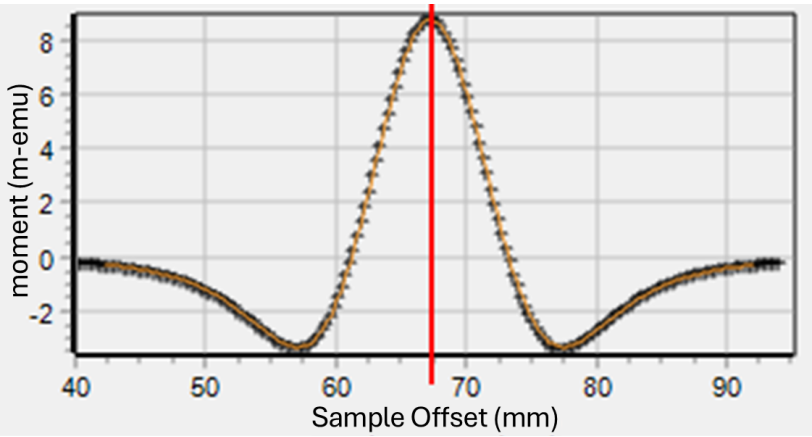


Figure 3.1. Measured (black points) and fitted (yellow line) dipole moment as a function of position for a paramagnetic sample moving through the coil set of the MPMS. The vertical red line marks the central position of the sample as extracted from the fit.

Direct current (dc) magnetisation measurements are based on two different detection techniques, depending on the device used. In the MPMS, the sample is gradually moved through a set of pick-up coils arranged in a second-order gradiometer configuration. As such, the sample's magnetic dipole moment induces a voltage in the coils, which is transferred to and read out by a *superconducting quantum interference device* (SQUID) [97, 98]. This procedure yields a specific voltage-position curve shown in Fig. 3.1. By fitting the expected magnetic dipole model (yellow line) to this curve, the magnetic moment of the sample can be extracted with high precision. The conversion factor from voltage to magnetic moment is device-specific and determined by measuring a reference sample made from high-purity palladium.

The PPMS employs the so-called vibrating sample magnetometer method, where the sample oscillates around the centre of a pick-up coil with the frequency f [99]. The magnetic flux Φ generated by the sample will then induce an oscillating voltage in the coil according to

$$V = \frac{d\Phi}{dt} = \frac{d\Phi}{dz}\frac{dz}{dt} = 2\pi f C M A \sin(2\pi f t). \tag{3.1}$$

Here, z is the vertical position of the sample with respect to the centre of the coil, t is the time, C is a coupling constant, M is the magnetic moment of the sample, and A is the amplitude of the oscillation. Therefore, the magnetic moment can be calculated by measuring the coefficient of the sinusoidal voltage response from the detection coil. Similar to the MPMS, the coupling constant C is specific for each device and is determined by measuring a high-purity palladium reference sample.

Alternating current (ac) susceptibility measurements are performed by applying a small oscillating magnetic field $B_{\mathrm{ac}}e^{i\omega t}$ on the background of a static field B_{dc}.[1] This induces a time-dependent magnetic moment of the form $M(\omega)e^{i(\omega t-\delta(\omega))}$ in the sample, where $\delta(\omega)$ is a frequency-dependent phase shift. Similar to the dc magnetisation detection, the MPMS determines the time-dependent moment from the induced voltage in the pick-up coils as read out by a SQUID [100]. From the measured moment, the complex magnetic susceptibility

$$\chi(\omega) = \frac{M(\omega)}{B_{\mathrm{ac}}}\cos(\delta(\omega)) + i\frac{M(\omega)}{B_{\mathrm{ac}}}\sin(\delta(\omega)) = \chi'(\omega) + i\chi''(\omega) \tag{3.2}$$

is calculated. Here $\chi'(\omega)$ is the in-phase component and $\chi''(\omega)$ is the out-of-phase component of the dynamic magnetic susceptibility. The MPMS provides excitation frequencies in the range from 1 Hz to 1000 Hz in its standard operation mode down to 1.8 K. For enhanced sensitivity, it is possible to measure the time-dependent magnetic moment at different positions in the coil setup. As a compromise between time consumption and experimental precision, all ac susceptibility data shown in this work were acquired using a three-point measurement. The voltage-to-moment conversion factor for the ac measurements is determined by measuring a high-purity Dy_2O_3 reference sample.

[1] The static magnetic field is not necessarily non-zero, but can be chosen to assume $B_{\mathrm{dc}} = 0$.

3.1.2 Sample Preparation

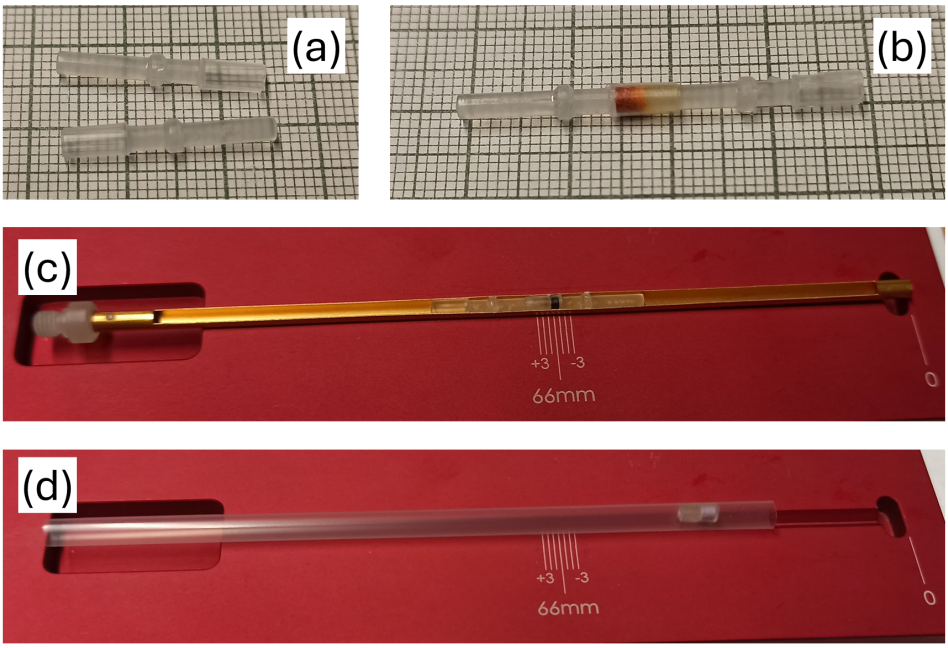


Figure 3.2. Powder sample preparation for magnetic moment and susceptibility measurements. (a) Empty polypropylene capsules; (b) filled and sealed powder sample holder; (c) powder sample holder clicked into a brass holder; (d) cut powder sample holder glued into a straw.

Unless stated otherwise, magnetic studies were performed on polycrystalline powder samples. The powder sample holder consists of two polypropylene capsules provided by *Quantum Design* as shown in Fig. 3.2(a). For that, the upper side of one of the capsules serves as a container in which the powder sample is filled. The lower part of the other capsule is then used as a stamp to press the sample into the container and seal the sample space (Fig. 3.2(b)). When measuring strongly anisotropic compounds, the powder samples were mixed with eicosane ($C_{20}H_{42}$, CAS-Nr. 112-95-8) and subsequently heated to 50 °C. As such, the eicosane powder melts and flows through the powder sample. After removing the heat source, the liquid eicosane solidifies again and fixes the crystallites in their initial random orientation. For samples exhibiting only a small magnetic anisotropy, the compression via the stamp is sufficient to prevent reorientation of the crystallites in the applied magnetic fields. Therefore, no additional fixation by means of eicosane is needed, which reduces the diamagnetic background signal as described in the next section. When measuring in standard operation mode down to 1.8 K, the prepared powder sample holder was clicked into a semi-hollow cylinder brass holder from *Quantum Design* as depicted in Fig. 3.2(c). Since the brass holder would act as an unwanted heat-bridge in the iQ-^{3}He option, the powder sample holder was cut and glued into a straw by means of *Apiezon vacuum N-grease* for measurements down to 0.4 K (Fig. 3.2(d)).

3.1.3 Data Processing

The used polypropylene capsules, eicosane, straws and brass holders all yield a diamagnetic contribution to the measured magnetic moment. To extract the contribution of the sample, the background signal for each preparation technique was acquired by performing the same measurement routines on empty powder sample holders. The so-obtained background was then subtracted from the measured data. Due to the close proximity of the thermometer and sample in the iQ-^{3}He option, such a correction was not possible for data points below 1.8 K. To account for putative background effects, the low-temperature data were scaled to the results of the MPMS standard operation measurements in an overlapping temperature range. As pointed out by eq. (2.9), the magnetic moment of the sample consists of the paramagnetic contribution of the unpaired electrons and the diamagnetic contribution of all electrons in the compound. The latter was estimated by means of *Pascal's constants* [101] and subtracted from the measured data. Due to the finite hysteresis of the built-in magnets, the magnetic field is corrected by the corresponding magnet's remanence field. Therefore, the remanence field is determined from the first zero point of the measured $M(B)$ loops.

3.2 High-frequency/High-field Electron Paramagnetic Resonance Spectroscopy

3.2.1 Experimental Setup

The tunable high-frequency/high-field EPR (HF-EPR) instrumentation utilised in this work has been set up in the frame of Ref. [102]; a more detailed description can be found there. The heart piece of the HF-EPR experiment is a *Millimeter Vector Network Analyser Model-8-350* (MVNA) from *AB Millimetre*, which is used as a phase-sensitive microwave spectrometer. Fig. 3.3 schematically depicts the working principle of the MVNA. Two Gunn oscillators (GO1/2) generate microwaves with the tunable base frequency f in the range from 8 to 18 GHz. To avoid large signal fluctuations, the frequency of the Gunn oscillators is stabilised by an external *EIP 575B source locking frequency counter* from *Phase Matrix*. Via coaxial cables, the microwaves generated by GO1 are transmitted to a harmonic generator (HG), where the frequency is multiplied by the corresponding harmonic number N. After being guided through the sample, the transmitted microwaves are mixed with the reference microwave signal generated by GO2 in a harmonic mixer (HM). Depending on the desired harmonic number, the HG and HM are based on a series of one or more Schottky diodes, attenuators, amplifiers and filters produced by *AB Millimetre*. The reference signal from GO2 is slightly detuned by $\Delta f \simeq 34$ MHz with respect to the base frequency f, such that mixing yields a signal of the form

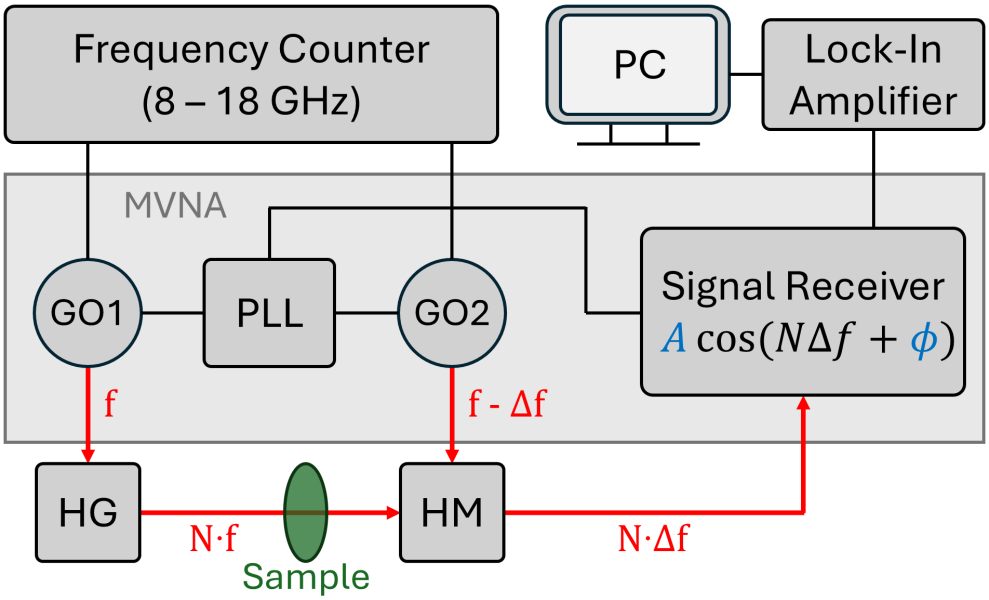


Figure 3.3. Schematic working principle of the microwave vector network analyser (MVNA). Red arrows depict the microwave radiation. All abbreviations are described in the text.

$$A\cos(Nft+\phi)\cdot\cos(N(f-\Delta f)t) = \frac{A}{2}\left(\cos(N(2f+\Delta f)t+\phi)+\cos(N\Delta ft+\phi)\right). \tag{3.3}$$

To reduce the phase noise, a phase-lock loop (PLL) regulates the phase difference between the two Gunn diodes. The first term in eq. (3.3) oscillates at a frequency $N(2f + \Delta f)$, which is in the GHz- or even THz-range. This part is filtered out by an internal low-pass filter. A signal receiver then reads out the amplitude and phase of the second, slowly oscillating part and, as such, acquires information about the transmission and dispersion of the microwaves in the sample. To enhance the sensitivity, the received signal is modulated with a frequency of $f_{\mathrm{mod}} = 10.448$ kHz and detected by a *SR 830 DSP Lock-In Amplifier* from *Stanford Research Systems*. The digitised amplitude and phase information is subsequently read out by a home-written *NI LabView* program.

Precise control of the thermodynamic external parameters is ensured by performing the measurements inside an evaporation cryostat equipped with a superconducting magnet as commercially available from *Oxford Instruments*. Its physical working principle shall not be discussed here, but a detailed explanation can be found, for example, in Ref. [103]. The full experimental setup is schematically shown in Fig. 3.4. Unpolarized microwaves (red arrows) coming from the HG are introduced into oversized circular brass waveguides, i.e., pipes with diameters much larger than the radiation wavelength, by means of feed horns (not shown). Four gold-plated mirrors then guide the microwaves first into the cryostat and subsequently back out to the HM. The prepared sample is placed inside the microwave path such that only the transmitted

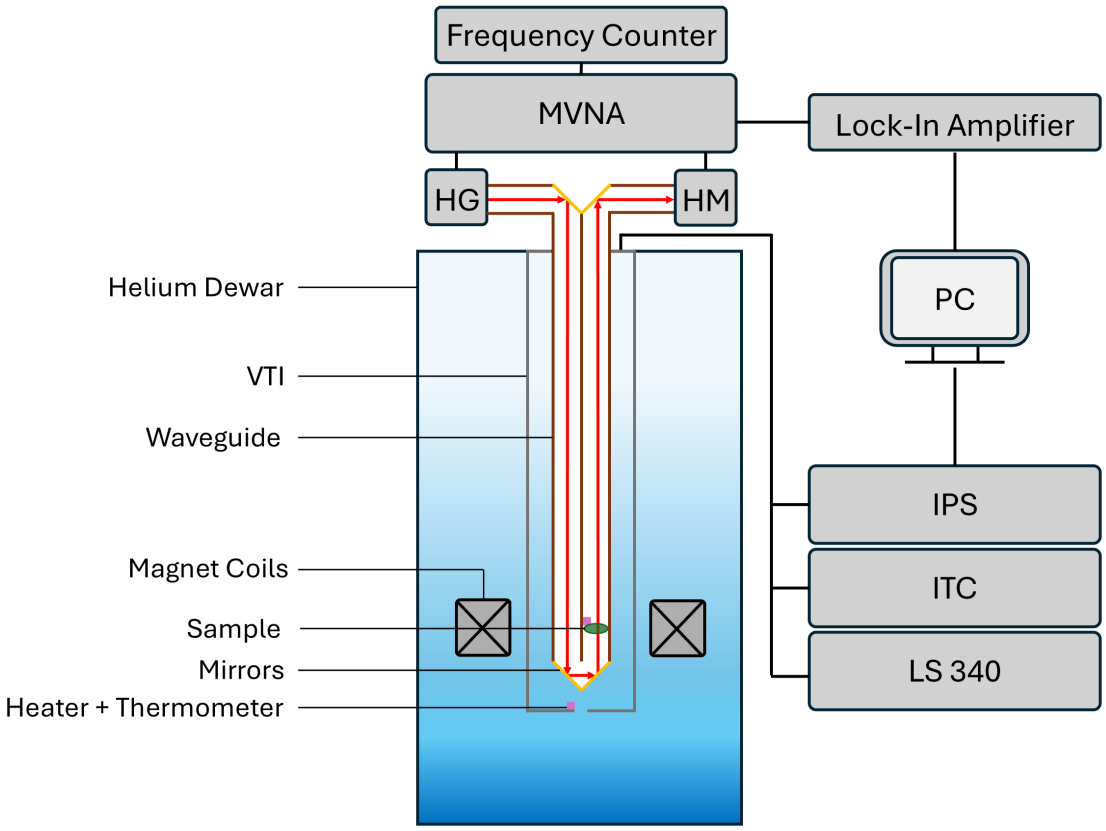


Figure 3.4. Schematic visualisation of the utilised high-frequency/high-field electron paramagnetic resonance spectroscopy setup. Red arrows depict the microwave radiation. All abbreviations are described in the text.

signal is detected. With this setup, a (quasi-)continuous frequency range from 30 GHz to 1000 GHz can be accessed. While the upper limit arises from the rapidly decreasing dynamic range at high frequencies, the lower limit is determined by the cut-off frequency of the centimetre-sized waveguides [104].

The waveguides, including the prepared sample, are placed inside a variable temperature insert (VTI) controlled by a *Mercury Intelligent Temperature Controller* (ITC) from *Oxford Instruments*, which allows for stable cryostat temperatures between 1.7 K and 300 K. To avoid errors due to temperature gradients in the sample space, an additional *LS 340 Temperature Controller* from *LakeShore* regulates the temperature directly at the sample position by means of a *CX-1040 Cernox thermometer* and a separate heater. External magnetic fields are provided by a Nb_3Sn superconducting coil located in the liquid helium reservoir of the cryostat. The electric current through the coil is controlled by a *Mercury Intelligent Power Supply* (IPS) from *Oxford Instruments*, which can generate magnetic fields up to ±16 T in standard operation mode. At the sample position, the magnetic field is parallel to the propagation vector of the microwaves ($\boldsymbol{B} \parallel \boldsymbol{k}_{\mathrm{mw}}$), such that all measurements are performed in Faraday geometry. The LS 340, ITC and IPS are all controlled by a computer running a home-written *NI LabView* program.

EPR experiments can either be conducted by sweeping the magnetic field at a constant microwave radiation frequency or by sweeping the microwave frequency while keeping the magnetic field constant. Since the generated microwave power of the MVNA is strongly dependent on the frequency, it is technically very challenging to perform meaningful frequency-swept spectra. Hence, throughout this work, all spectra were obtained in a field-swept fashion.

3.2.2 Sample Preparation

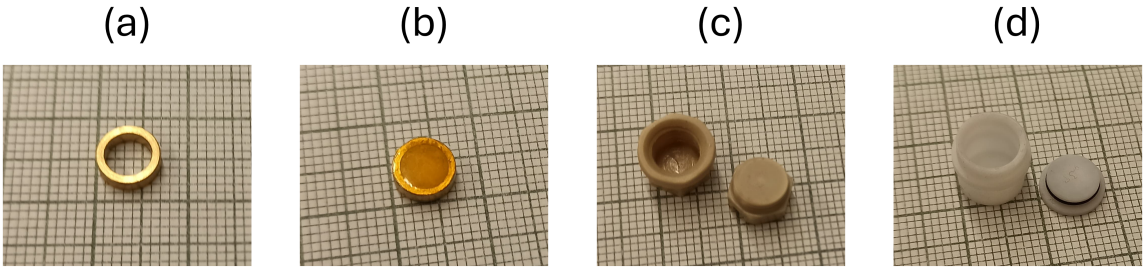


Figure 3.5. Sample holders used in HF-EPR measurements. (a) Empty brass ring; (b) filled brass ring sealed with kapton tape on both sides; (c) empty screw container made from PEEK used for air-sensitive samples; (d) empty liquid sample holder made from teflon.

Unless stated otherwise, all samples measured in the HF-EPR setup were present as polycrystalline powder. Non-air-sensitive samples were prepared in home-built brass rings (Fig. 3.5(a)), which were sealed from both sides by microwave-transmittive *Kapton* tape (Fig. 3.5(b)). To avoid sticking of the crystallites to the tape, the inner sites of the "Kapton windows" were isolated by another inverse layer of Kapton, such that the two sticking sides face each other. Compounds for which air contact should be avoided were placed in a home-built PEEK (polyetheretherketone) container and sealed with a screw cap (Fig. 3.5(c)). To ensure good isolation, the screw thread was additionally covered by *Teflon* tape (not shown) before closing the container. All preparation steps for air-sensitive samples were conducted under an argon atmosphere inside a glovebox. Liquid samples were filled in a home-built Teflon container, which was sealed tightly by means of a rubber O-ring and *parafilm* (Fig. 3.5(d)).

Polycrystalline powder samples were measured in two distinct ways. In a *loose powder* measurement, no further preparation step beyond filling and sealing of the respective sample holder is conducted. As such, the crystallites are free to move within the sample space and will align their magnetic easy anisotropy axis along the applied magnetic field. This technique yields pseudo-single-crystal spectra with reduced complexity, as only one sample orientation has to be considered. Alignment of the crystallites during the measurements is ensured by the observation of clear reorientation jumps in the transmitted microwave power at low fields and subsequently restricting the applied magnetic field to $B \gtrsim 0.1$ T. For *fixed powder* measurements, the sample was mixed with eicosane and subsequently heated to 50 °C, such that the eicosane powder melts.

After cooling back to room temperature, the melt solidifies again and, thereby, fixes the sample crystallites in their initial random orientation. With this method, a powder average over all sample orientations is obtained. All powder samples were thoroughly ground before performing the experiments.

The waveguides, including the prepared sample, are slid into a sample rod, which is fabricated from stainless steel at the top and from copper at the bottom, where the sample is located. This minimises the heat input to the sample space from external sources, while still allowing for good thermal conductivity to the cooling stage. After three consecutive cycles of vacuum-pumping and helium-purging, the sample rod is filled up to 250 mbar with helium as thermal exchange gas and finally lowered into the cryostat.

3.2.3 Data Processing

Due to the magnetoresistive effect of the thermometer and/or thermal fluctuations in the cryostat, the experimental temperature may not be perfectly stable throughout a measurement. Considering that all integrated parts in the experiment are subject to thermal expansion, the transmitted microwave power is also not necessarily constant even when the magnetic field is not varied. Since temperature usually exhibits a simple drift or oscillations over long timescales, the spectra are corrected by subtracting a phenomenological polynomial background obtained by fitting the data, while excluding the observed resonance features. As such, a constant baseline is generated, which enables the analysis of the spectra.

When performing EPR experiments, the finite penetration depth of microwaves can yield a phase shift in the spectrometer [104]. This phase shift eventually leads to a mixing of the amplitude $A(B)$ and phase $D(B)$ signal, such that the actually measured quantities $A_{\mathrm{meas}}(B)$ and $D_{\mathrm{meas}}(B)$ are given by superpositions of the pure components. The so-called *phase mixing*, thereby, alters the shape of an observed resonance feature, which complicates the determination of the corresponding resonance field. To recover the true amplitude signal from the experimental data, a linear combination of the form

$$A(B) = \pm(1-\epsilon^2)^{-1/2}\left(A_{\mathrm{meas}}(B) + \epsilon D_{\mathrm{meas}}(B)\right) \tag{3.4}$$

can be calculated [105, 106]. Here, $|\epsilon| \leq 1$ is a phenomenological parameter, which represents the fractional admixture of one signal component to the other. The prefactor in eq. (3.4) ensures conservation of the signal intensities normalised by the Kramers-Kronig relation [104, 107].

Chapter 4

Towards Understanding Prolate $4f$ Monomers: Numerical Predictions and Experimental Validation of Electronic Properties and Slow Relaxation in a Muffin-shaped Er^{III} Complex

The results of this chapter were submitted as a research article to *Inorganic Chemistry*. A preprint of the manuscript has been uploaded to *arXiv* under the arXiv number: 2507.15547 and is available via the DOI: https://doi.org/10.48550/arXiv.2507.15547 [108]. Specific contributions of each co-author, especially the contribution of J. Arneth, who serves as the corresponding and first author, are given in the following list:

- J. Arneth carried out the HF-EPR measurements, analysed the HF-EPR and magnetisation data, constructed the plotted figures, and wrote the presented manuscript draft except the "Crystal Structure" and "Quantum Chemical Calculations" sections.
- C. Pachl and K. Fink performed the quantum chemical calculations and wrote the "Quantum Chemical Calculations" section of the manuscript draft.
- B. Beier carried out the magnetisation measurements under the supervision of J. Arneth.
- G. Greif and P. Roesky synthesised the sample, conducted the structural analysis and wrote the "Structural Analysis" section of the manuscript draft.
- R. Klingeler led the project and supported the data analysis and manuscript writing.
- All authors proofread the manuscript.

arXiv:2507.15547v1 [cond-mat.str-el] 21 Jul 2025

Towards Understanding Prolate $4f$ Monomers: Numerical Predictions and Experimental Validation of Electronic Properties and Slow Relaxation in a Muffin-shaped Er^{III} Complex

J. Arneth[+],[1,*] C. Pachl[+],[2,3] G. Greif,[3] B. Beier,[1] P. W. Roesky,[3,2,†] K. Fink,[2,‡] and R. Klingeler[1,§]

[1] *Kirchhoff Institute for Physics, Heidelberg University, INF 227, D-69120 Heidelberg, Germany*

[2] *Institute of Nanotechnology, Karlsruhe Institute of Technology (KIT), Kaiserstr. 12, 76131 Karlsruhe, Germany*

[3] *Institute of Inorganic Chemistry, Karlsruhe Institute of Technology, Kaiserstr. 12, 76131 Karlsruhe, Germany*

We report the synthesis, crystal structure and magnetic properties of the triply-capped, slightly distorted trigonal-prismatic complex $[Er(PPTMP)_2(H_2O)][OTf]_3$ (PPTMP = (4-(6-(1,10-phenanthrolin-2-yl)pyridin-2-yl)-1H-1,2,3-triazol-1-yl)methyl pivalate) (**1**). Complex **1** is shown to exhibit field-induced slow relaxation of the magnetisation at $B = 0.1$ T via two distinct relaxation paths. Using tunable high-frequency/high-field electron paramagnetic resonance spectroscopy, we experimentally determine the effective g-factors and zero field splittings of the two energetically lowest Kramers doublets (KD). Our data reveal that the triply-capped, slightly distorted trigonal-prismatic ligand field favours an $m \simeq \pm 9/2$ magnetic ground state, while the main contribution to the first excited KD at $\Delta_{1\to 2} = 780(5)$ GHz is suggested to be $m \simeq \pm 5/2$. The ground state g-tensor has generally axial form but hosts significant transversal components, which we conclude to be the source of SMM-silent behaviour in zero field. Our findings are backed up by *ab-initio* spin-orbit configuration interaction calculations showing excellent agreement with the experimental data.

I. INTRODUCTION

The seminal paper by Sessoli *et al.* on the magnetic bistability in the famous dodecanuclear Mn_{12}ac-molecule [1] marked the birth of the ever-increasing research field centred around so-called single molecule magnets (SMM) [2–4]. In SMM the combination of large spins and strong magnetic anisotropy leads to high effective energy barriers (U_{eff}), due to which the magnetic moment relaxes only slowly and a remanent magnetisation can be retained over long timescales below the blocking temperature T_B [5]. Therefore, such complexes have potential applications in quantum computing [6], high-density information storage [7] and novel molecular spintronic devices [8, 9].

On the route to high-performance SMM $3d$ transition metal and $4f$ lanthanide ions have established themselves as the most promising building-blocks to realise high U_{eff} and T_B [4, 10]. While the large spin and magnetic anisotropy of polynuclear $3d$ coordination clusters typically arise from strong ferromagnetic interactions between the distinct magnetic centres, $4f$ moments exhibit good magnetic relaxation properties due to intrinsically strong spin-orbit coupling and large unquenched orbital momentum [3, 11, 12]. Hence, almost 10 years after the discovery of Mn_{12}ac, Ishikawa *et al.* reported the first single ion magnet (SIM) $[TbPc_2]^-$, in which slow magnetic relaxation occurs for a single terbium(III) in a double-decker coordination [13]. From there on, a vast amount of studies have been performed on $4f$-based SIM and record barriers of $U_{\text{eff}} > 1800$ K [14] and magnetic hysteresis above liquid nitrogen temperatures $T_B = 100$ K [15] were achieved in this class of materials. However, despite huge zero field energy splittings, magnetic relaxation in SIM is often limited by under-barrier processes due to deviations from a perfectly axial crystal field. The resulting transversal magnetic anisotropy leads to a mixing of the m_J-levels, which enables quantum tunnelling of the magnetisation (QTM) between energetically degenerate states [16]. Therefore, the choice of a suitable coordination environment for the central $4f$ ion is a key step in the effective design of SIM.

In the literature, most of the reported SIM are based on the oblate $4f$ ions (Tb^{III}, Dy^{III}, Ho^{III}), while those with predominantly prolate electron distribution (Er^{III}, Tm^{III}, Yb^{III}) rather scarcely exhibit slow relaxation of the magnetisation [17–24]. This mainly results from the need for equatorial ligand fields to minimize the Coulomb interaction with the paramagnetic ion and, hence, to enhance the single ion anisotropy, while still retaining a sufficient axiality [25]. However, this oblate versus prolate ion theory was demonstrated to be too simplified for the complex electronic structure of Er^{III}, which renders trivalent erbium-based molecular complexes as interesting systems to investigate magnetic anisotropy in more detail [17, 26]. Nonetheless, although a wide variety of Er^{III} complexes with different relaxation properties, i.e. SMM, field-induced SMM and completely SMM-silent, are known, quantitative analysis of the single ion anisotropy is only rarely performed.

Here, we report the synthesis and magnetic characterisation of the triply-capped, slightly distorted trigonal-prismatic complex $[Er(PPTMP)_2(H_2O)][OTf]_3$ (PPTMP

* jan.arneth@kip.uni-heidelberg.de
† roesky@kit.edu
‡ karin.fink@kit.edu
§ klingeler@kip.uni-heidelberg.de
+ These authors contributed equally to this work.

= (4-(6-(1,10-phenanthrolin-2-yl)pyridin-2-yl)-1H-1,2,3-triazol-1-yl)methyl pivalate) (**1**). Our ac susceptibility data show that **1** exhibits field-induced slow relaxation of the magnetisation via two distinct relaxation pathways. We employ tunable high-frequency and high-field electron paramagnetic resonance (HF-EPR) spectroscopy which has been proven as a valuable method to study the magnetic anisotropy in Er^{III}-based molecular complexes by direct experimental determination of the effective g-factors and zero field splittings of the low-energy Kramers doublets (KD) [27, 28]. The spectroscopic data indicate that SMM-silent behaviour in zero field arises from pronounced transverse components of the effective ground state g-tensor, while slow relaxation at finite fields occurs via an excited Kramers doublet at $\Delta_{1\to2} = 780$ GHz. A direct comparison of our experimental findings with the numerical results of spin-orbit configuration interaction calculations using the CASOCI program [29] allows us to validate and assess *ab-initio* predictions as recently done by us for various other mononuclear lanthanide complexes [27, 28, 30, 31].

II. EXPERIMENTAL RESULTS

A. Structural Analysis

Reaction of PPTMP with erbium(III)-trifluoromethanesulfonate in THF led, after workup, to **1**. Single crystals suitable for X-ray diffraction were grown from hot methanol (Scheme 1). Compound **1** crystallises in the triclinic space group $P\bar{1}$ and contains two PPTMP-ligands coordinating the Er^{III} metal center. Fig. 2 shows the molecular structure of the erbium complex in the solid-state. The lanthanoid atom has a coordination number of nine, resulting from the coordination of eight nitrogen atoms from the two PPTMP ligands and one oxygen atom from a coordinated water molecule. This leads to a coordination geometry resembling a triply-capped, slightly distorted trigonal prism. In contrast, the three remaining triflate anions in the unit cell do not coordinate the lanthanide ion.

In addition, the unit cell contains one non-coordinating methanol molecule, which interacts with the Er-coordinated water molecule via a hydrogen bond. Furthermore, two of the three triflate anions also exhibit hydrogen bonds: one hydrogen bond towards the coordinated water molecule, the other towards the methanol molecule. The water molecule originates from the non-dry solvents and the crystallisation was not carried out in the absence of moisture and oxygen. The bond distances between the erbium atom and the coordinating nitrogen atoms are in the range of 2.473(2) to 2.510(2) Å. As already observed in similar and phenanthroline-pyridine ligand systems [32–34], the nitrogen atoms N2 and N8 of the phenanthroline unit exhibit the shortest bond distances to the metal center with 2.473(2) Å each. The N–C bond lengths within the coordinated ligands also range from 1.327(3) Å to 1.373(3) Å, which is comparable with similar systems [32–34].

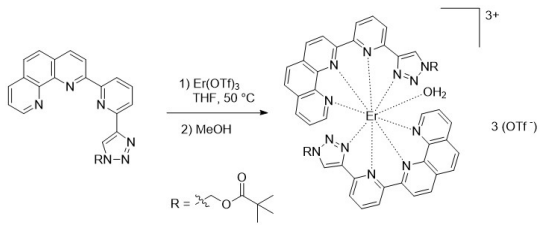


FIG. 1. Synthesis scheme of complex **1**.

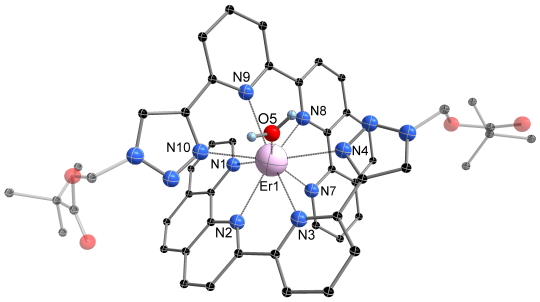


FIG. 2. Molecular structure of $[Er(PPTMP)_2(H_2O)][OTf]_3$ in the solid state. C-H-bound hydrogen atoms are omitted for clarity.

B. Magnetometry

The static magnetic susceptibility $\chi = M/B$ of **1** in an external magnetic field of $B = 0.1$ T shown in Fig. 3 by its $\chi T(T)$-profile is typical of mononuclear Er^{III} complexes [19, 35, 36]. At 300 K, the measured value of $\chi T = 10.71\,\mathrm{ergK/G^2mol}$ is close to $\chi T_{\mathrm{free}} = 11.48\,\mathrm{ergK/G^2mol}$ expected for a free Er^{III} ion. Since a sizeable depletion due to crystal field effects is ruled out by the numerical calculations, as described later, the remaining discrepancy likely arises from solvent molecules cocrystallising in the packing structure. Upon cooling, χT gradually decreases and then rapidly drops below 30 K, which is attributed to the depopulation of the Stark levels. The isothermal magnetisation at $T = 1.8$ K (inset of Fig. 3) is characterised by a steep increase at low fields followed by a plateau-like behaviour above 1 T. Up to the highest accessible field of 14 T the magnetisation gradually increases to $M(14\,\mathrm{T}, 1.8\,\mathrm{K}) = 5.5\,\mu_B$/f.u. (formula unit), i.e., does not reach the full saturation value ($M_{\mathrm{sat}} = 9\,\mu_B$/f.u.), thereby confirming the presence of considerable magnetic anisotropy.

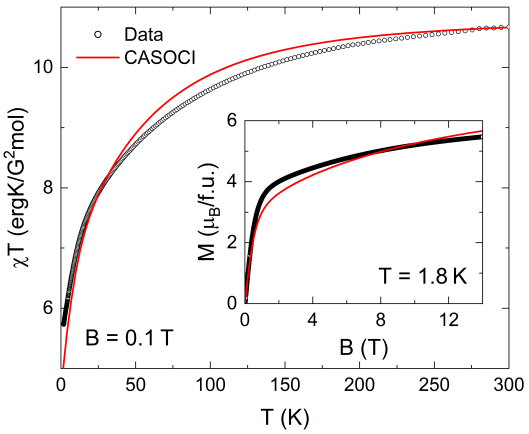


FIG. 3. Temperature dependence of the χT-product at $B = 0.1$ T and isothermal magnetisation at $T = 1.8$ K (inset) of **1**. Red lines depict the numerical results of *ab-initio* CASOCI calculations as described in the text.

While complex **1** does not exhibit slow magnetic relaxation (up to 1 kHz) at $B = 0$ T, a clear out-of-phase ac susceptibility signal is found at low temperatures when a small static external field of $B_{\mathrm{dc}} = 0.1$ T is applied (Fig. 4). From the frequency dependence of χ'' (a), two maxima can be clearly discerned as confirmed by the appearance of two distinct lobes in the Cole-Cole plot (b). Hence, the magnetisation in **1** relaxes via two separate pathways with differing relaxation rates. To corroborate our assignment, the ac susceptibility data were fitted by the sum of two generalised Debye-functions:

$$\chi_{\mathrm{ac}}(f) = \sum_{n=1}^{2} \left(\chi_{\mathrm{S,n}} + \frac{\chi_{\mathrm{T,n}} - \chi_{\mathrm{S,n}}}{1 + (if\tau_n)^{1-\alpha_n}} \right), \qquad (1)$$

where χ_{S} and χ_{T} denote the adiabatic and isothermal susceptibilities, τ is the relaxation time, and $0 \leq \alpha \leq 1$ qualitatively represents the distribution of relaxation times within the powder sample. As visible in Fig. 4, the data are well described by the used model. Although the limited frequency range does not allow for a quantitative analysis, both relaxation processes are qualitatively found to become faster upon increasing the temperature. The absence of SMM-behaviour in zero field straightforwardly implies a considerable transversal magnetic anisotropy acting on the Er^{III} moment. Such off-diagonal elements in the single ion anisotropy tensor lead to a mixing of the m_J-states and, thus, give rise to fast QTM, which can be effectively quenched by an external magnetic field [16].

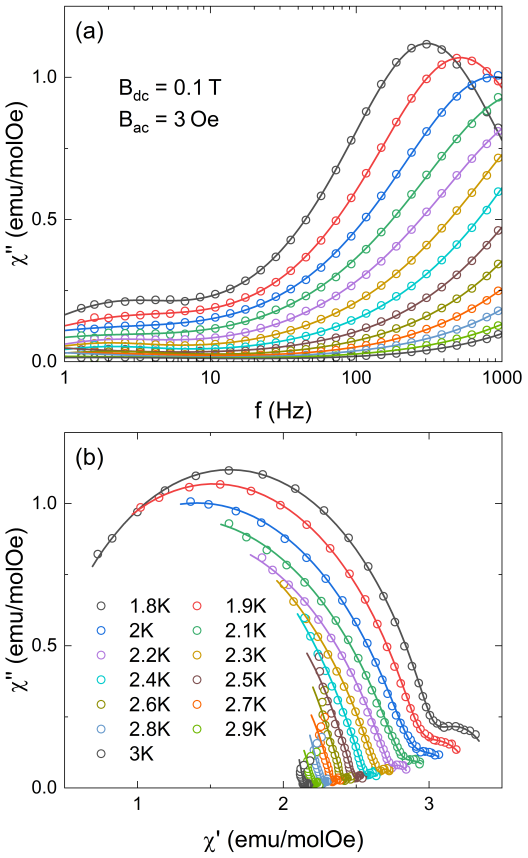


FIG. 4. Out-of-phase ac susceptibility (a) and Cole-Cole plot (b) of **1** at selected temperatures and external static magnetic field $B_{\mathrm{dc}} = 0.1$ T. Solid lines depict fits to the data using eq. 1 as described in the text.

C. High-field EPR studies

To experimentally probe the low-energy magnetic excitations in **1** and, in particular, to quantitatively determine the magnetic anisotropy, we performed multifrequency HF-EPR studies both on loose and fixed powders of freshly ground samples. The oriented loose-powder HF-EPR spectra obtained at $T = 2$ K (Fig. 5) display a pronounced Lorentzian-shaped absorption feature in the entire accessible frequency range up to 900 GHz. For frequencies higher than ca. 800 GHz, an additional weak broad resonance feature appears at smaller magnetic fields. The extracted resonance field positions at different frequencies are shown in Fig. 5, too. As visualised by the solid black lines, the pronounced main feature forms a gapless resonance branch, here labelled as α, which exhibits linear field dependence at small mag-

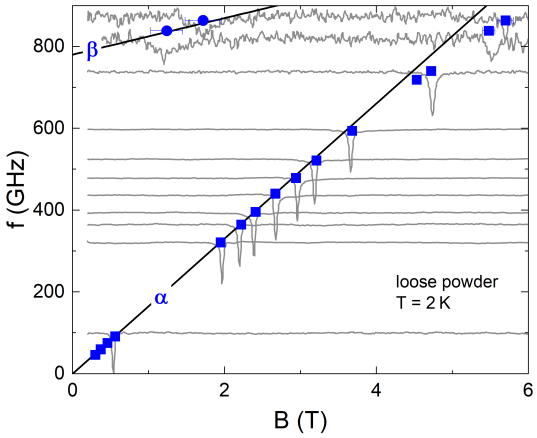


FIG. 5. Resonance frequency versus magnetic field diagram for a loose powder sample of **1** obtained at $T = 2$ K. Blue squares mark the resonance positions as read off the measured HF-EPR spectra displayed in the background. Solid black lines depict simulations of the ground state resonance branches using a $S = 1/2$ pseudospin model for each KD as described in the text.

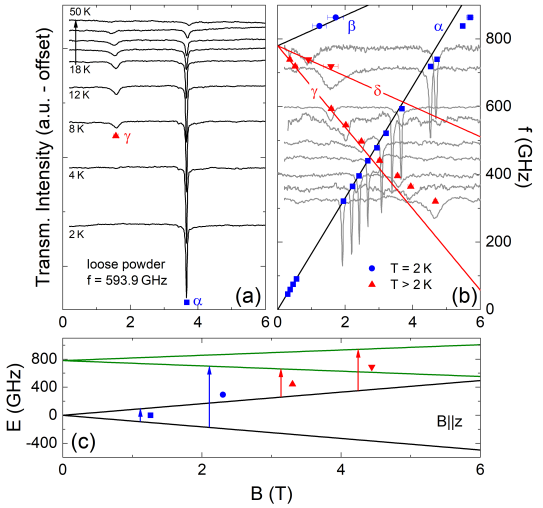


FIG. 6. Loose powder HF-EPR spectra (shifted along the ordinate) of **1** at selected temperatures and at fixed frequency $f = 593.9$ GHz (a), the corresponding frequency-field diagram (b) and simulated energy levels of the two energetically-lowest KDs (c). Solid black/red lines in (b) depict simulated ground/excited state transitions corresponding to the arrows in (c) which follow the same color scheme. Grey lines in the background of (b) display HF-EPR spectra measured at $T = 18$ K.

netic fields but begins to deviate from its initial linear behaviour for $B \gtrsim 4$ T. In agreement with the findings of the ac susceptibility studies and as further discussed below, the high-field bending of resonance branch α is associated with an avoided level crossing and, hence, indicates the mixing of different m_J-levels. Linear extrapolation of the two data points marking the weak low-field feature yields a tentative resonance branch β with a zero field splitting (ZFS) of $\Delta \simeq 780$ GHz. From the slopes of the observed resonance branches, we read off the effective g-factors $g_{\text{eff}} \simeq 11.8$ and 3.2 for α and β, respectively.

The effect of temperature on the HF-EPR spectra is shown in Fig. 6(a) at an exemplary frequency of $f = 593.9$ GHz. Upon heating, the spectral weight of the pronounced main feature corresponding to the resonance branch α gradually decreases until it becomes almost indiscernible around 50 K. Further, starting from $T \simeq 8$ K, an additional absorption peak (γ) appears in the spectra, which first increases in intensity with rising temperature and then vanishes again for $T \geq 50$ K. To investigate the field dependence of γ, HF-EPR spectra at different frequencies were acquired at $T = 18$ K, i.e., where the resonance feature is most pronounced. As visible in the spectra and the corresponding frequency-field diagram in Fig. 6(b), two additional resonance branches (γ and δ) are observed at elevated temperatures. Similar to the behaviour of α, γ follows a linear field dependence at small fields and exhibits significant bending at $B \gtrsim 4$ T. As will be discussed in detail below, this non-linear field dependence further confirms the occurrence of state mixing in **1**. The zero field gaps of γ and δ, obtained by extrapolating the branches to $B = 0$ T, coincide with that of β within the error bars of our experiment.

Due to the absence of a zero field excitation gap and its Curie-like temperature dependence, it is straightforward to attribute α to a transition within the energetically lowest Kramers doublet (KD1). In contrast, the observed finite ZFS of branches β-δ render them likely to be associated with transitions between two distinct KDs. While the occurrence of β at $T = 2$ K implies the magnetic ground state (GS) to be its initial state, the temperature dependencies of γ and δ show that the corresponding transitions arise from thermally excited states (ES) a few K above the GS.

The observed resonance branches can be rationalised by assuming an $S = 1/2$ pseudospin model for the two energetically lowest KDs. The best simulations (solid lines in Fig. 6(b)) are obtained using a zero field splitting of $\Delta_{1\to2} = 780(5)$ GHz and effective g-factors of $g_{\text{eff},1} = 11.8(2)$ and $g_{\text{eff},2} = 5.4(3)$ for KD1 and KD2, respectively. As can be seen from the corresponding simulated Zeeman diagram in Fig. 6(c), the upwards branch of KD1 and the downwards branch of KD2 cross at $B \simeq 6$ T. While transverse components of the magnetic anisotropy tensor are effectively neglected in the $S = 1/2$ pseudospin model, their presence in the actual complex is clearly suggested by an avoided-level-crossing behaviour which qualitatively explains the observed bending of branches α and γ.

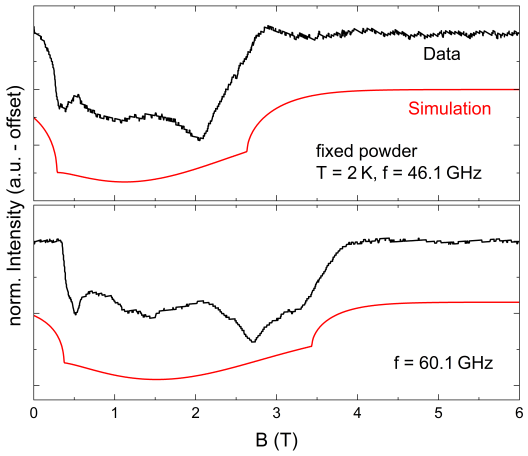


FIG. 7. Measured (black) and simulated (red) fixed powder HF-EPR spectra of **1** at $T = 2$ K for $f = 46.1$ GHz (top) and $f = 60.1$ GHz (bottom).

Due to the alignment of the sample with the external magnetic field, the loose powder studies provide quantitative information only on the easy anisotropy direction of the studied complex. To determine also the transverse components of the effective g-tensor, we performed HF-EPR measurements on a fixed powder of **1**. Fig. 7 displays the corresponding spectra obtained at $T = 2$ K for two exemplary frequencies in the V-band range. The general shape of the low-temperature fixed powder HF-EPR spectra is given by a broad absorption minimum superimposed by several sharper (but in comparison to the loose powder spectra very weak) resonance features. While the former is a typical characteristic of the measured powder average, the latter likely arise from clusters of crystallites that remained partially ordered after the loose powder measurements. The wide distribution of spectral weight straightforwardly indicates considerable transversal components of g_{eff} for KD1, i.e., a mixing of states due to off-diagonal crystal field parameters, which elucidates the absence of SMM behaviour in **1** at $B = 0$ T. The components of g_{eff} can be quantified by fitting the overall shape of the spectra using a $S = 1/2$ pseudospin model with a strongly anisotropic g-tensor. The best agreement with the experimental data is achieved by $g_{\text{eff,x}} = 1.2(3)$, $g_{\text{eff,y}} = 2.6(4)$ and $g_{\text{eff,z}} = 11.8(3)$ and the simulated spectra are shown as red lines in Fig. 7.

D. Quantum Chemical Calculations

Using the workflow described in the methods section, the influence of the counterions on the magnetic properties is investigated. Therefore, five model clusters are simulated: The first is the bare molecule with a charge of +3.

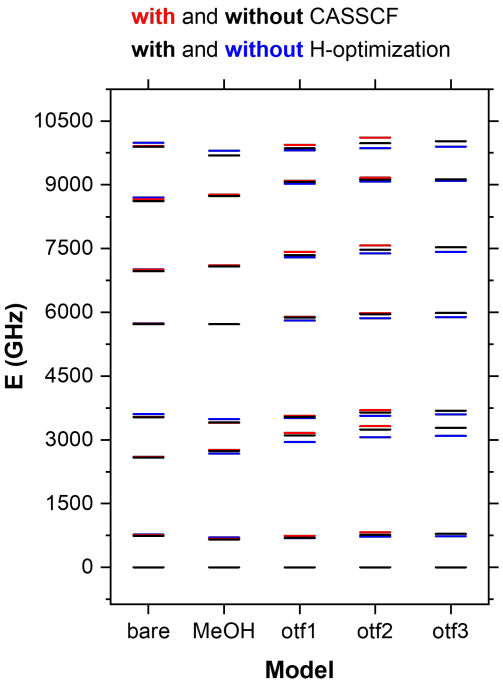


FIG. 8. Calculated Energies of the 8 lowest Kramers Doublets of the $^4I_{15/2}$-ground state of complex **1**. **Black**: Energies with H-optimization and without intermediate CASSCF step. **Blue**: Energies without H-optimisation and without intermediate CASSCF step. **Red**: Energies with H-optimisation and intermediate CASSCF step.

Secondly, the MeOH hydrogen bound to the coordinating water is included, which remains in the charge state +3. Next, the three counterions are added sequentially. The model complexes, therefore, exhibit a charge of +2, +1 and 0, respectively. Pictures of the different model complexes can be found in the SI, figure S10. Furthermore, calculations are carried out with and without a preliminary optimisation of hydrogen positions. Lastly, an intermediate CASSCF-step is tested for H-optimised models. This calculation has not been performed for the largest model, due to an internal basis set limit. The resulting splitting of the $^4I_{15/2}$-ground state is visualised in Fig. 8. The exact values, diagonal elements of the g-tensors for each KD, extended Stevens operator equivalents, and m_J-compositions for all calculations are summarised in the Supplemental Material, tables II-XXXIII. As can be seen, neither the optimisation of the hydrogen positions nor the inclusion of an intermediate CASSCF-step significantly influence the calculated energy splittings. The observed differences between the respective

models are smaller than 120 GHz for the first excited KD. Therefore, the optimised calculations without an intermediate CASSCF-step are used as the reference. The influence of including the counterions is only marginally larger, as the lowest value of $\Delta_{1\rightarrow2} \simeq 650$ GHz is calculated for the model that includes MeOH and 790 GHz is found for the full model. The small differences in energy translate to weak discrepancies in the calculated g_z-values of the ground state KD, which are between 11.8 and 12.8 for all calculated models. A similar difference in absolute values can be reported for the transversal components of the g-tensor, with values ranging from 0.10 to 1.63 for g_x and from 0.89 to 2.71 for g_y. Thus, the H-optimisation is shown to notably influence the transversal components of the g-tensor. Not optimising hydrogen positions and calculating the bare cluster would significantly overestimate the axiality of the underlying model by minimising the transversal components. Considering the optimised H positions and including also the counterions yields transversal g-tensor components of $g_x = 1.10$ and $g_y = 1.95$, which are in very good agreement with the experimental results.

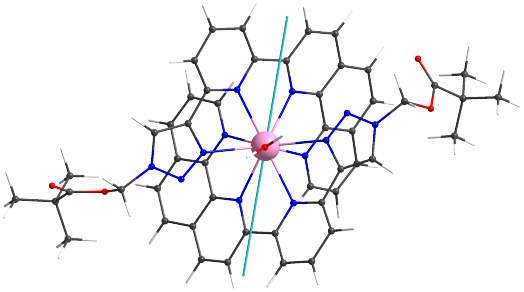


FIG. 9. Orientation of the magnetic easy anisotropy axis, as indicated by the light blue axis. Counterions and methanol are not shown for simplicity, but included in the calculation.

The molecular magnetic easy anisotropy axis calculated for the full model is shown in figure 9. It is orthogonal to the Er-O bond and is oriented through the two PPTMP ligands. It approximately penetrates the carbon-carbon bonds between the pyridine and phenanthroline moieties. Considering the prolate $4f$ electron distribution of Er^{III}, the main anisotropy axis points in the direction of the minimal electrostatic field [25]. In **1**, the water molecule exerts the largest electrostatic field. Therefore, the main axis must be orthogonal to the Er-O bond. In this plane, the magnetic main axis will go along the minimal crystal field. This is corroborated by the molecular symmetry being close to C_2, which allows only for anisotropy axes parallel and perpendicular to the Er-O bond which acts as the rotational axis. The resulting χT-product and isothermal magnetisation are depicted in Fig. 3. The anisotropy axes of models neglecting additional counterions and MeOH are perpendicular to the Er-O bond,

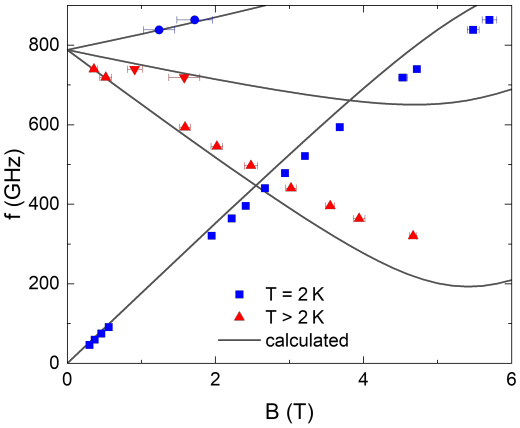


FIG. 10. Measured (points) and calculated (lines) transition energies of a loose powder sample of **1** within the lowest two Kramers doublets for the model including all counterions and optimised hydrogen positions.

too. However, their axes are oriented almost in parallel to the position of the water ligand's hydrogen positions, as depicted in the Supplementary Material.

For the first excited KD of the full model, a g_z-value of 9.2 is calculated. This value is not directly comparable to the $g_{\mathrm{eff,z}}$ obtained from the loose powder HF-EPR data, since in the experiment, the crystallites are oriented along the main magnetic anisotropy axis of the ground state. The calculated effective $g_{\mathrm{eff,z}}$, therefore, is given by the projection of the real g_z-value onto the magnetic field direction. This leads to $g_{\mathrm{eff,z}} = 7.0$ for KD2. In comparison, the calculated and projected g_z-values for the bare molecules with and without optimising the hydrogen positions are 1.8 and 2.7, respectively, which are far off the experimentally determined values. However, the calculated and projected g_z-value for the full model, without optimising hydrogen positions, is 5.8, which is very close to the experimental value. A summary of the orientations of the main anisotropy axes for the ground state KD of selected models can be found in the Supplementary Material.

By applying a magnetic field in the direction of the ground state magnetic easy anisotropy axis for the model with optimised hydrogen positions and all counterions, we are able to simulate the underlying Zeeman diagrams for the loose powder experiment as shown in the Supplementary Material. The transition energies between the four lowest states are shown in Fig. 10. We predict an avoided level crossing close to a field of 6 T with first deviations of the linear behaviour starting at around 4 T. This is in excellent agreement compared to the experimental measurements. The simulated versus experimentally observed Zeeman-splitting for the unoptimised model containing all counterions is shown in the Sup-

plementary Material. Considering that the agreement is worse compared to Fig. 10, we will rule out the unoptimised model.

The mixing of m_J-states is calculated for the eight Kramers Doublets. The ground state is mainly a mixture of the $m_J = \pm 15/2\,(\approx 31\ \%)$ and $m_J = \pm 9/2\,(\approx 51\ \%)$ states. In contrast, the first excited state dominantly consists of the $m_J = \pm 7/2\,(\approx 56\ \%)$ and $m_J = \pm 5/2\,(\approx 22\ \%)$ states. These values are in good agreement with the experiment but depend on the used model to a certain extent. For example, using the bare molecule and no optimisation of H-positions will lead to a ground state that is a mixture of $m_J = 15/2$, $9/2$ and $5/2$ with 26 %, 33 %, and 20 %, respectively, while the first excited state is an equal mixture of the $m_J = 7/2$, $3/2$ and $1/2$ states with contributions between 24 % and 28 %. In summary, the comparison of the different models shows that the methanol as well as the three counterions should be considered to obtain the correct magnetic axes and g-values, while the energy differences are already well described by the bare molecule.

III. DISCUSSION AND CONCLUSION

A summary of the effective g-tensors and crystal field splittings as obtained by HF-EPR measurements and *ab-initio* calculations is given in Tab. I. Our experimental and theoretical results clearly evidence a pronounced uniaxial behaviour, i.e., $g_{\mathrm{eff,z}} \gg g_{\mathrm{eff,x}}$, $g_{\mathrm{eff,y}}$, of the energetically lowest Kramers doublet in **1** and, hence, imply an Ising-like character of the Er^{III} moment in the magnetic ground state. According to the calculations, the water ligand is responsible for the largest contribution to the ligand field. Therefore, the direction of the Ising-axis is perpendicular to it. However, the observation of sizeable $g_{\mathrm{eff,x/y}}$ components in the effective g-tensor directly reveals a significant deviation from a perfect Ising scenario due to the presence of a considerable transversal crystal field. As described above, such off-diagonal elements in the single-ion anisotropy tensor lead to a mixing of the m_J states and, thereby, give rise to avoided level crossings and fast magnetic relaxation via QTM in zero field. As demonstrated by the ac susceptibility data, the QTM in **1** can be effectively quenched by shifting the energy levels of the initial and final state using a small magnetic field. In this in-field configuration, magnetic relaxation is dominated by temperature-activated processes, such as Orbach, Raman or thermally-assisted QTM. While KD3 is strongly gapped $\Delta_{2\to3} \gg 1$ THz, the first excited Kramers doublet KD2 lies approximately 37 K (780 GHz) above the ground state and can easily contribute to the observed slow magnetic relaxation.

The effective g-factors obtained from the pseudo-single-crystal loose powder spectra can be used to determine the effective magnetic quantum numbers $m_{\mathrm{eff}} = g_{\mathrm{eff,z}}/2g_{\mathrm{L}}$ for the experimentally accessible Kramers doublets [27, 28].

TABLE I. Experimentally and theoretically obtained effective g-tensors and zero field splittings of the two lowest KDs in **1**.

		HF-EPR	CASOCI
KD1	$g_{\mathrm{eff,x}}$	1.2(3)	1.1
	$g_{\mathrm{eff,y}}$	2.6(4)	2.0
	$g_{\mathrm{eff,z}}$	11.8(2)	12.6
$\Delta_{1\to2}$ (GHz)		780(5)	788
KD2	$g_{\mathrm{eff,z}}$	5.4(3)	7.0
$\Delta_{2\to3}$ (GHz)		$\gg 1000$	2495

Assuming that the free ion Landé factor $g_{\mathrm{L}} = 1.2$ is still a good approximation for Er^{III} moments in the present coordination geometry, our analysis yields $m_{\mathrm{eff},1} = 4.9(1)$ and $m_{\mathrm{eff},2} = 2.3(1)$ for KD1 and KD2, respectively. The almost integer value of $m_{\mathrm{eff},1}$ for KD1 confirms the occurrence of pronounced state mixing, as also evidenced by the observation of avoided level crossing in the frequency-field diagram. Furthermore, $m_{\mathrm{eff},1}$ is close to 4.5, which indicates that the low-symmetry crystal field in **1** stabilises the $m_J = \pm 9/2$ state as the magnetic ground state. As for KD2, the main contribution to the spin wavefunction is suggested to be $m_J = 5/2$.

As already evident from the good agreement of the measured and calculated dc magnetisation, the experimentally determined g-tensor for KD1 is well reproduced by CASOCI. While CASOCI also gives an accurate prediction of the zero-field gap to the first excited Kramers doublet, the effective g_z-value for KD2 is slightly overestimated by this approach. In agreement with the absence of corresponding transitions in the HF-EPR experiments, the calculation finds KD3 to be strongly gapped with $\Delta_{2\to3} \simeq 2.5$ THz, i.e., well beyond the experimentally accessible range.

To sum up, we successfully synthesised and magnetically characterised a triply-capped, slightly distorted trigonal-prismatic Er^{III} complex **1** using combined dc and ac magnetic, HF-EPR and numerical studies. Complex **1** is SMM-silent due to QTM in zero field, but exhibits field-induced slow relaxation of the magnetisation at $B = 0.1$ T. The dominance of under-barrier relaxation is rationalised by the presence of sizeable transversal components in the overall uniaxial effective g-tensor of the ground state KD1. When QTM is quenched, slow magnetic relaxation happens via thermally activated processes involving the first excited KD2 at 780 GHz above the ground state. KD3 is shown to be strongly gapped and, thus, does not contribute to the relaxation dynamics at low temperatures. In particular, our detailed spectroscopic investigations allow for a direct experimental determination of the effective g-tensors and zero-field splittings of the two energetically lowest Kramers doublets. The excellent agreement between the measured data and the results of the CASOCI calculations for g-tensors and zero-field splitting support the reliability of both approaches.

IV. EXPERIMENTAL DETAILS AND METHODS

Polycrystalline powder samples of **1** have been synthesised as described in the Supplemental Information.

For crystal structure determination a suitable crystal of **1** was covered in mineral oil (Aldrich) and mounted on a glass fibre. The crystal was transferred directly to the cold stream of a STOE IPDS 2 (150 K) or STOE StadiVari (100 or 110 K) diffractometer. All structures were solved by using the program SHELXS/T [37, 38] and Olex [39]. The remaining non-hydrogen atoms were located from successive difference Fourier map calculations. The refinements were carried out by using full-matrix least-squares techniques on F^2 by using the program SHELXL [37, 38]. The H-atoms were introduced into the geometrically calculated positions (SHELXL procedures) unless otherwise stated and refined riding on the corresponding parent atoms. In each case, the locations of the largest peaks in the final difference Fourier map calculations, as well as the magnitude of the residual electron densities, were of no chemical significance. Summary of the crystal data, data collection and refinement for compounds are given in the supplement. Crystallographic data for the structures reported in this paper halve been deposited with the Cambridge Crystallographic Data Centre as a supplementary publication no. CCDC 2472872. Copies of the data can be obtained free of charge on application to CCDC, 12 Union Road, Cambridge CB21EZ, UK (fax: (+(44)1223-336-033; email: deposit@ccdc.cam.ac.uk).

The direct current (dc) and alternating current (ac) magnetisation was studied in the temperature range $T = 1.8 - 300$ K by means of a Magnetic Properties Measurement System (MPMS3, Quantum Design) and a Physical Properties Measurement System (PPMS, Quantum Design) in magnetic fields up to 7 T and 14 T, respectively. For all measurements powder samples were pelletised in polycarbonate capsules to avoid reorientation in external magnetic fields. The experimental data were corrected for the contribution of the sample holder and of the diamagnetic ligand field calculated by means of Pascal's constants [40]. Simulations of the magnetic data were performed using the PHI software package [41].

Multifrequency high-field electron paramagnetic resonance studies were performed using a phase-sensitive millimeter vector network analyser (MVNA) by ABmm as a simultaneous microwave source and detector [30]. Temperature control from 2 K to 300 K was ensured by placing the sample space in the Variable Temperature Insert (VTI) of an Oxford magnet system equipped with a 16 T superconducting coil [42]. Polycrystalline powder samples were prepared in a brass ring sealed with kapton tape either as loose powder or fixed by mixing with eicosane. The former setup allows alignment of the crystallites with the external magnetic field, hence providing simplified pseudo-single-crystal spectra (see Refs. [27, 28, 43–46]). Alignment is ensured by sweeping up the magnetic field to 16 T prior to each measurement and confirmed by observation of corresponding orientation effects in the transmitted microwave intensity signal. Spectral simulations of the HFEPR data were performed using the EasySpin sofware package [47].

Ab-initio Complete Active Space Spin-orbit Configuration Interaction (CASOCI) calculations [29] are carried out in the following steps: First, the hydrogen positions of the experimentally determined structure are optimized on a B3-LYP-d4/def2-TZVP [48–50] level of theory in TURBOMOLE [51, 52], by replacing Er to Y. For each model complex investigated, Y is replaced to Gd and an unrestricted Kohn Sham calculation is performed using the B3-LYP functional, the all-electron basis x2c-TZVPall for Gd, the def2-TZVP basis for the remaining atoms and an energy convergence criterium of 10^{-7} E_h. Scalar relativistic effects are accounted for using X2C [53]. The half filled natural orbitals of this calculation are used as a starting point for a Restricted Open Shell Hartree Fock (ROHF) calculation on the same compound, now using the second order Douglass Kroll Hess approach to treat scalar relativstic effects [54, 55]. This ensures a reliable starting guess for pure f orbitals in the active space. In a next step, Gd is replaced to Er and the orbitals of the previous calculation are used as a starting guess. The Roothaan parameters used are $a = 119/121$ and $b = 126/121$ mimicking an average over all quartet states with eleven electrons in the seven $4f$ orbitals for the orbital optimization. In a last step DKH2 is changed to DKH4 and a density convergence criterium of 10^{-7} is introduced keeping the energy convergence criterium of 10^{-7} E_h for a tight convergence of the calculation. We have tested the influence of a subsequent state averaged CASSCF calculation for optimizing the orbitals explicitly for the ^4F-ground term. Afterwards the CASOCI calculations were carried out explicitly introducing spin-orbit coupling. This is done by diagonalizing the spin-orbit coupled Full CI matrix in an active space of eleven electrons in the seven $4f$ orbitals (11,7) active space using a Davidson algorithm to extract the lowest 100 eigenstates [29].

Supporting Information: The Supporting Information contains additional details about the synthesis; structure figures and X-ray crystallographic data; NMR, IR, mass spectroscopy data; it also includes Ref. [56]. Further information about the numerical results (file: ErIII-SI.pdf). In addition, it includes xyz-files on all model structures used in this manuscript. The difference between optimized and unoptimized is that in optimized structures, hydrogen positions were optimized on a DFT level as described in the text. This was done considering all counterions and lattice solvent, so on the "full" structure. Afterwards, the model was truncated to generate the other structures (file: ErIII-SI-xyz.zip).

ACKNOWLEDGMENTS

We thank Florian Bruder and Florian Weigend for valuable discussions and scientific input. David Frick is acknowledged for solving the single crystal X-ray structure of compound **1**. Support by Deutsche Forschungsgemeinschaft (DFG) under Germany's Excellence Strategy EXC2181/1-390900948 (the Heidelberg STRUCTURES Excellence Cluster) is gratefully acknowledged. J. A. acknowledges support by the International Max-Planck Research School for Quantum Dynamics (IMPRS-QD) Heidelberg. Financial support for this research was provided by the German Federal Ministry of Education and Research through the f-Char project under grant numbers 02NUK059A. C. P. acknowledges the state of Baden-Württemberg via the Landesgraduiertenförderung and the DFG via the CRC 1573 "4f for future" for funding.

[1] R. Sessoli, D. Gatteschi, A. Caneschi, and M. A. Novak, Magnetic bistability in a metal-ion cluster, Nature **365**, 141 (1993).

[2] G. Christou, D. Gatteschi, D. N. Hendrickson, and R. Sessoli, Single-molecule magnets, MRS Bull. **25**, 66–71 (2000).

[3] R. Sessoli and A. K. Powell, Strategies towards single molecule magnets based on lanthanide ions, Coord. Chem. Reviews **253**, 2328–2341 (2009).

[4] D. Shao and X. Wang, Development of single-molecule magnets, Chin. J. Chem. **38**, 1005–1018 (2020).

[5] R. Winpenny, ed., *Single-Molecule Magnets and Related Phenomena* (Springer Berlin Heidelberg, 2006).

[6] M. Shiddiq, D. Komijani, Y. Duan, A. Gaita-Ariño, E. Coronado, and S. Hill, Enhancing coherence in molecular spin qubits via atomic clock transitions, Nature **531**, 348–351 (2016).

[7] E. Coronado, Molecular magnetism: from chemical design to spin control in molecules, materials and devices, Nat. Rev. Mat. **5**, 87 (2019).

[8] S. Sanvito, The rise of spinterface science, Nat. Phys. **6**, 562–564 (2010).

[9] S. Sanvito, Molecular spintronics, Chem. Soc. Rev. **40**, 3336 (2011).

[10] V. Vieru, S. Gómez-Coca, E. Ruiz, and L. F. Chibotaru, Increasing the magnetic blocking temperature of single-molecule magnets, Angew. Chem. Int. Ed. **136**, 10.1002/ange.202303146 (2023).

[11] L. Sorace, C. Benelli, and D. Gatteschi, Lanthanides in molecular magnetism: old tools in a new field, Chem. Soc. Rev. **40**, 3092 (2011).

[12] S. T. Liddle and J. van Slageren, Improving f-element single molecule magnets, Chem. Soc. Rev. **44**, 6655–6669 (2015).

[13] N. Ishikawa, M. Sugita, T. Ishikawa, S. Koshihara, and Y. Kaizu, Lanthanide double-decker complexes functioning as magnets at the single-molecular level, J. Am. Chem. Soc. **125**, 8694 (2003).

[14] Z. Zhu, C. Zhao, T. Feng, X. Liu, X. Ying, X.-L. Li, Y.-Q. Zhang, and J. Tang, Air-stable chiral single-molecule magnets with record anisotropy barrier exceeding 1800 k, J. Am. Chem. Soc. **143**, 10077–10082 (2021).

[15] J. Emerson-King, G. K. Gransbury, B. E. Atkinson, W. J. A. Blackmore, G. F. S. Whitehead, N. F. Chilton, and D. P. Mills, Soft magnetic hysteresis in a dysprosium amide–alkene complex up to 100 kelvin, Nature **643**, 125–129 (2025).

[16] L. Thomas, F. Lionti, R. Ballou, D. Gatteschi, R. Sessoli, and B. Barbara, Macroscopic quantum tunnelling of magnetization in a single crystal of nanomagnets, Nature **383**, 145–147 (1996).

[17] A. J. Brown, D. Pinkowicz, M. R. Saber, and K. R. Dunbar, A trigonal-pyramidal erbium(iii) single-molecule magnet, Angew. Chem. Int. Ed. **127**, 5962–5966 (2015).

[18] A. Gorczyński, M. Kubicki, D. Pinkowicz, R. Pełka, V. Patroniak, and R. Podgajny, The first example of erbium triple-stranded helicates displaying smm behaviour, Dalt. Trans. **44**, 16833–16839 (2015).

[19] H. Zhang, R. Nakanishi, K. Katoh, B. K. Breedlove, Y. Kitagawa, and M. Yamashita, Low coordinated mononuclear erbium(iii) single-molecule magnets with c_{3v} symmetry: a method for altering single-molecule magnet properties by incorporating hard and soft donors, Dalt. Trans. **47**, 302–305 (2018).

[20] E. Castellanos, F. Benner, and S. Demir, Linear, electron-rich erbium single-molecule magnet with dibenzocyclooctatetraene ligands, Inorg. Chem. **63**, 9888–9898 (2024).

[21] A. V. Gavrikov, N. N. Efimov, A. B. Ilyukhin, Z. V. Dobrokhotova, and V. M. Novotortsev, Yb^{3+} can be much better than dy^{3+}: Smm properties and controllable self-assembly of novel lanthanide 3,5-dinitrobenzoate-acetylacetonate complexes, Dalt. Trans. **47**, 6199–6209 (2018).

[22] F. Guégan, J. Jung, B. Le Guennic, F. Riobé, O. Maury, B. Gillon, J.-F. Jacquot, Y. Guyot, C. Morell, and D. Luneau, Evidencing under-barrier phenomena in a yb(iii) smm: a joint luminescence/neutron diffraction/squid study, Inorg. Chem. Front. **6**, 3152–3157 (2019).

[23] N. Jain, F. Houard, R. Marchal, M. Cordier, B. Le Guennic, Y. Suffren, Y. Sarazin, and K. Bernot, Luminescence and single-molecule magnet properties in ideal symmetry compounds: Example of a near-planar tricoordinate ytterbium(iii) amide, ChemistryEurope **2**, 10.1002/ceur.202400062 (2024).

[24] N. Schwarz, F. Bruder, V. Bayer, E. Moreno-Pineda, S. Gillhuber, X. Sun, J. van Slageren, F. Weigend, and P. W. Roesky, Rare earth stibolyl and bismolyl sandwich complexes, Nat. Commun. **16**, 10.1038/s41467-024-55474-6 (2025).

[25] J. D. Rinehart and J. R. Long, Exploiting single-ion anisotropy in the design of f-element single-molecule magnets, Chem. Sci. **2**, 2078 (2011).

[26] E. Lucaccini, L. Sorace, M. Perfetti, J.-P. Costes, and R. Sessoli, Beyond the anisotropy barrier: slow relaxation of the magnetization in both easy-axis and easy-plane ln(trensal) complexes, Chem. Commun. **50**, 1648–1651 (2014).

[27] L. Spillecke, C. Koo, O. Maximova, V. S. Mironov,

V. A. Kopotkov, D. V. Korchagin, A. N. Vasiliev, E. B. Yagubskii, and R. Klingeler, Magnetic behavior of the novel pentagonal-bipyramidal erbium(iii) complex $(et_3nh)[er(h_2daps)cl_2]$: high-frequency EPR study and crystal-field analysis, Dalton Trans. **50**, 18143 (2021).

[28] J. Arneth, L. Spillecke, C. Koo, T. A. Bazhenova, E. B. Yagubskii, and R. Klingeler, The relevance of non-axiality and low-lying excited states for slow magnetic relaxation in pentagonal-bipyramidal erbium(iii) complexes probed by high-frequency epr, Chem. Eur. J. 10.1002/chem.202500369 (2025).

[29] T. Bodenstein, A. Heimermann, K. Fink, and C. van Wüllen, Development and Application of a Complete Active Space Spin-Orbit Configuration Interaction Program Designed for Single Molecule Magnets, Chem. Phys. Chem. **23**, 202100648 (2022).

[30] P. Comba, M. Großhauser, R. Klingeler, C. Koo, Y. Lan, D. Müller, J. Park, A. Powell, M. J. Riley, and H. Wadepohl, Magnetic interactions in a series of homodinuclear lanthanide complexes, Inorg. Chem. **54**, 11247 (2015).

[31] P. Comba, L. J. Daumann, R. Klingeler, C. Koo, M. J. Riley, A. E. Roberts, H. Wadepohl, and J. Werner, Correlation of structural and magnetic properties in a set of mononuclear lanthanide complexes, Chem. Eur. J. **24**, 5319 (2018).

[32] L. Schnaubelt, H. Petzold, J. M. Speck, E. Dmitrieva, M. Rosenkranz, and M. Korb, Redox properties and electron transfer in a triarylamine-substituted hs-co^{2+}/ls-co^{3+} redox couple, Dalt. Trans. **46**, 2690–2698 (2017).

[33] H. Petzold, P. Djomgoue, G. Hörner, S. Heider, C. Lochenie, B. Weber, T. Rüffer, and D. Schaarschmidt, Spin state variability in fe^{2+} complexes of substituted (2-(pyridin-2-yl)-1,10-phenanthroline) ligands as versatile terpyridine analogues, Dalt. Trans. **46**, 6218–6229 (2017).

[34] H. Petzold, P. Djomgoue, G. Hörner, C. Lochenie, B. Weber, and T. Rüffer, Bis-meridional fe^{2+} spin-crossover complexes of phenyl and pyridyl substituted 2-(pyridin-2-yl)-1,10-phenanthrolines, Dalt. Trans. **47**, 491–506 (2018).

[35] Y. Rechkemmer, J. E. Fischer, R. Marx, M. Dörfel, P. Neugebauer, S. Horvath, M. Gysler, T. Brock-Nannestad, W. Frey, M. F. Reid, and J. van Slageren, Comprehensive spectroscopic determination of the crystal field splitting in an erbium single-ion magnet, J. Am. Chem. Soc. **137**, 13114–13120 (2015).

[36] T. A. Bazhenova, V. A. Kopotkov, D. V. Korchagin, Y. V. Manakin, L. V. Zorina, S. V. Simonov, I. A. Yakushev, V. S. Mironov, A. N. Vasiliev, O. V. Maximova, and E. B. Yagubskii, A series of novel pentagonal-bipyramidal erbium(III) complexes with acyclic chelating n_3o_2 schiff-base ligands: Synthesis, structure, and magnetism, Molecules **26**, 6908 (2021).

[37] G. M. Sheldrick, A short history ofshelx, Acta Crystallogr. A **64**, 112–122 (2007).

[38] G. M. Sheldrick, Crystal structure refinement with shelxl, Acta Crystallogr. C **71**, 3–8 (2015).

[39] O. V. Dolomanov, L. J. Bourhis, R. J. Gildea, J. A. K. Howard, and H. Puschmann, Olex2: a complete structure solution, refinement and analysis program, J. Appl. Crystallogr. **42**, 339–341 (2009).

[40] G. A. Bain and J. F. Berry, Diamagnetic Corrections and Pascal's Constants, J. Chem. Educ. **85**, 532 (2008).

[41] N. F. Chilton, R. P. Anderson, L. D. Turner, A. Soncini, and K. S. Murray, PHI: A powerful new program for the analysis of anisotropic monomeric and exchange-coupled polynuclear *d*- and *f*-block complexes, J. Comp. Chem. **34**, 1164 (2013).

[42] J. Werner, W. Hergett, M. Gertig, J. Park, C. Koo, and R. Klingeler, Anisotropy-governed competition of magnetic phases in the honeycomb quantum magnet $Na_3Ni_2SbO_6$ studied by dilatometry and high-frequency ESR, Phys. Rev. B **95**, 214414 (2017).

[43] D. P. Goldberg, J. Telser, J. Krzystek, A. G. Montalban, L.-C. Brunel, A. G. M. Barrett, and B. M. Hoffman, EPR spectra from "EPR-silent" species: high-field EPR spectroscopy of manganese(III) porphyrins, J. Am. Chem. Soc. **119**, 8722 (1997).

[44] A.-L. Barra, P. Debrunner, D. Gatteschi, C. E. Schulz, and R. Sessoli, Superparamagnetic-like behavior in an octanuclear iron cluster, Europhys. Lett. **35**, 133 (1996).

[45] N. Ahmed, T. Sharma, L. Spillecke, C. Koo, K. U. Ansari, S. Tripathi, A. Caneschi, R. Klingeler, G. Rajaraman, and M. Shanmugam, Probing the origin of ferro-/antiferromagnetic exchange interactions in cu(ii)–4f complexes, Inorg. Chem. **61**, 5572 (2022).

[46] J. Arneth, X. Li, J. Braun, S. Paul, M. Schulze, C. E. Anson, W. Wernsdorfer, A. K. Powell, and R. Klingeler, The interplay of single ion anisotropy and magnetic 3d-4f interactions in $v_2^{III}ln_2^{III}$ butterfly complexes, ChemistryEurope **3**, 10.1002/ceur.202500011 (2025).

[47] S. Stoll and A. Schweiger, EasySpin, a comprehensive software package for spectral simulation and analysis in EPR, J. Mag. Reson. **178**, 42 (2006).

[48] A. D. Becke, A new mixing of Hartree–Fock and local density-functional theories, J. Chem. Phys. **98**, 1372 (1993).

[49] E. Caldeweyher, C. Bannwarth, and S. Grimme, Extension of the D3 dispersion coefficient model, J. Chem. Phys. **147**, 034112 (2017).

[50] E. Caldeweyher, S. Ehlert, A. Hansen, H. Neugebauer, S. Spicher, C. Bannwarth, and S. Grimme, A generally applicable atomic-charge dependent London dispersion correction, J. Chem. Phys. **150**, 154122 (2019).

[51] S. G. Balasubramani, G. P. Chen, S. Coriani, M. Diedenhofen, M. S. Frank, Y. J. Franzke, F. Furche, R. Grotjahn, M. E. Harding, C. Hättig, A. Hellweg, B. Helmich-Paris, C. Holzer, U. Huniar, M. Kaupp, A. Marefat Khah, S. Karbalaei Khani, T. Müller, F. Mack, B. D. Nguyen, S. M. Parker, E. Perlt, D. Rappoport, K. Reiter, S. Roy, M. Rückert, G. Schmitz, M. Sierka, E. Tapavicza, D. P. Tew, C. van Wüllen, V. K. Voora, F. Weigend, A. Wody\'nski, and J. M. Yu, TURBOMOLE: Modular program suite for ab initio quantum-chemical and condensed-matter simulations, J. Chem. Phys. **152**, 184107 (2020).

[52] *TURBOMOLE V7.7 2022: A Development of University of Karlsruhe and Forschungszentrum Karlsruhe GmbH* (since 2007).

[53] D. Peng, N. Middendorf, F. Weigend, and M. Reiher, An efficient implementation of two-component relativistic exact-decoupling methods for large molecules, J. Chem. Phys. **138**, 184105 (2013).

[54] C. van Wüllen, Relation between different variants of the generalized Douglas-Kroll transformation through sixth order, J. Chem. Phys. **120**, 7307 (2004).

[55] C. van Wüllen and C. Michauk, Accurate and efficient treatment of two-electron contributions in quasirelativistic high-order Douglas-Kroll density-functional calcula-

tions, J. Chem. Phys. **123**, 204113 (2005).

[56] R. Zong, D. Wang, R. Hammitt, and R. P. Thummel, Synthetic approaches to polypyridyl bridging ligands with proximal multidentate binding sites, J. Org. Chem. **71**, 167–175 (2005).

Supplemental Information

The Supporting Information (SI) contains additional details about the synthesis, structure figures and X-ray crystallographic data as well as NMR, IR, mass spectroscopy data. Due to the extended length of the SI, the interested reader is referred to https://doi.org/10.48550/arXiv.2507.15547.

Chapter 5

The Relevance of Non-Axiality and Low-Lying Excited States for Slow Magnetic Relaxation in Pentagonal-Bipyramidal Erbium(III) Complexes Probed by High-frequency EPR

The results of this chapter were published as a research article in *Chemistry - A European Journal* Volume 31, Issue 33 in June 2025 [109]. The corresponding manuscript is also available under the DOI: https://doi.org/10.1002/chem.202500369. Specific contributions of each co-author, especially the contribution of J. Arneth, who serves as the corresponding and first author, are given in the following list:

- J. Arneth performed the HF-EPR measurements on complex **(1)**, analysed the HF-EPR data for complexes **(1)** and **(2)**, constructed the plotted figures, and wrote the presented manuscript draft.
- L. Spillecke performed the HF-EPR measurements on complexes **(2)** and **(3)** and analysed the HF-EPR data for complex **(3)** as reported in Ref. [110]
- T. A. Bazhenova and E. B. Yagubskii synthesised the samples, conducted the structural analysis and performed the magnetic susceptibility measurements as reported in Ref. [111].
- C. Koo supervised the project and supported the data analysis and manuscript writing.
- R. Klingeler led the project and supported the data analysis and manuscript writing.
- All authors proofread the manuscript.

Check for updates

Chemistry–A European Journal

Research Article
doi.org/10.1002/chem.202500369

Chemistry Europe
European Chemical Societies Publishing

www.chemeurj.org

VIP *Very Important Paper*

The Relevance of Non-Axiality and Low-Lying Excited States for Slow Magnetic Relaxation in Pentagonal-Bipyramidal Erbium(III) Complexes Probed by High-frequency EPR

Jan Arneth,*[a] Lena Spillecke,[a] Changyun Koo,[a, b] Tamara A. Bazhenova,[c] Eduard B. Yagubskii,[c] and Rüdiger Klingeler*[a]

High-frequency/high-field electron paramagnetic resonance studies on a series of seven-coordinate pentagonal-bipyramidal (PBP) erbium(III) complexes Er(DAPMBH/H_2DAPS)X (H_2DAPMBH = 2,6-diacetylpyridine bis-4-methoxy benzoylhydrazone, H_4DAPS = 2,6-diacetylpyridine bis-(salicylhydrazone)) demonstrate the effects of different apical ligands (X = $(H_2O)Cl$ **(1)**, $(CH_3OH)N_3$ **(2)**, Cl_2 **(3)**) on the local magnetic anisotropy of the central Er^{III} ions. In particular, we report direct experimental determination of the effective *g*-values and zero field splittings of the energetically low-lying Kramers doublets. Our quantitative determination of the magnetic anisotropy highlights the relevance of an axial *g*-tensor for SMM behavior and suggests that fast magnetic relaxation is mainly driven by a thermally assisted quantum tunnelling process via low-lying excited states.

1. Introduction

The discovery of magnetic bistability, that is, the ability to retain magnetization for long times in the absence of an external magnetic field, at liquid helium temperatures in the famous dodecanuclear Mn_{12}ac-molecule[1] was followed by an intense search for further single molecular magnets (SMM) with ever higher blocking temperatures (T_B).[2–5] Due to their molecular nature, SMMs exhibit unique advantages over bulk magnetic materials, and a wide variety of possible applications in high-density data storage and processing and in quantum computing have been put forward.[6–8] In the early years of molecular magnetism, research was mainly focused on designing polynuclear 3d coordination clusters with high total spins and large anisotropy barriers.[9–11] Quickly, also the idea of implementing lanthanide ions for synthesizing SMMs emerged since intrinsically strong spin-orbit coupling and large unquenched orbital momentum of 4f moments lead to considerably enhanced single-ion anisotropy and, hence, large effective energy barriers (U_{eff}).[12,13] Furthermore, using rare-earth ions opens the possibility of constructing SMMs with only a single magnetic center, termed single ion magnets (SIM). However, it was not until about almost 10 years after the discovery of the first SMM that slow magnetic relaxation was demonstrated in the double-decker $[LnPc_2]^-$ (Ln = Tb, Dy) compounds.[14] From there on, an increasing amount of effort has been put into the design of lanthanide-based SIMs, and record values for effective energy barriers of U_{eff} = 1815 K and blocking temperatures as high as T_B = 80 K have been reached in mononuclear dysprosium complexes.[15,16]

In particular, it has become clear that engineering magnetic anisotropy is one of the most promising ways to design high-performance lanthanide-based SMMs.[17,18] Placing the magnetic center in a suitable coordination environment, that is, controlling the coordination geometry and the local symmetry around the 4f moment, results in strong uniaxial magnetic anisotropy and yields quenching of the quantum tunnelling of magnetization (QTM). In this context, mononuclear Dy^{III} complexes have been shown to exhibit substantial SMM characteristics when the magnetic ion is coordinated in a pentagonal-bipyramidal (PBP) crystal field.[15,19,20] The pseudo-D_{5h} symmetry yields a large crystal field splitting of the lowest $^6H_{15/2}$ multiplet and an almost strict axiality of the crystal field potential, rendering the m_J = 15/2 Kramers doublet (KD) with an Ising-like effective *g*-tensor ($g_{xx} = g_{yy} \approx 0$, $g_{zz} \approx 20$) the magnetic ground state.[15,21–24]

Despite the quite active and successful work on PBP Dy^{III} complexes, research on equally seven-coordinated Er^{III}-containing compounds, which also exhibit a high total angular momentum of *J* = 15/2 in the ground state, is hardly reported in the literature.[25–27] Generally, only a few Er^{III}-based SMMs are known, which arise from the need for equatorial ligand fields to effectively enhance the magnetic single ion anisotropy (SIA) of the predominantly prolate electron distribution, and quantitative

[a] J. Arneth, Dr. L. Spillecke, Dr. C. Koo, Prof. Dr. R. Klingeler
Kirchhoff Institute for Physics, Heidelberg University, INF 227 D-69120, Heidelberg, Germany
E-mail: jan.arneth@kip.uni-heidelberg.de
ruediger.klingeler@kip.uni-heidelberg.de

[b] Dr. C. Koo
Department of Physics, Sungkyunkwan University, Suwon 16419, Republic of Korea

[c] Dr. T. A. Bazhenova, Prof. Dr. E. B. Yagubskii
Federal Research Center of Problems of Chemical Physics and Medicinal Chemistry, Russian Academy of Sciences, Ac. Semenov Avenue 1, Chernogolovka, Moscow Region 142432, Russian Federation

Supporting information for this article is available on the WWW under https://doi.org/10.1002/chem.202500369

© 2025 The Author(s). Chemistry – A European Journal published by Wiley-VCH GmbH. This is an open access article under the terms of the Creative Commons Attribution License, which permits use, distribution and reproduction in any medium, provided the original work is properly cited.

© 2025 The Author(s). Chemistry – A European Journal published by Wiley-VCH GmbH

Chemistry–A European Journal
Research Article
doi.org/10.1002/chem.202500369
Chemistry Europe
European Chemical Societies Publishing

15213765, 2025, 33, Downloaded from https://chemistry-europe.onlinelibrary.wiley.com/doi/10.1002/chem.202500369, Wiley Online Library on [22/06/2025]. See the Terms and Conditions (https://onlinelibrary.wiley.com/terms-and-conditions) on Wiley Online Library for rules of use; OA articles are governed by the applicable Creative Commons License

analysis of the SIA is rarely performed.[28–30] Recently, Bazhenova et al. synthesized and studied a series of pentagonal-bipyramidal erbium complexes with acyclic chelating N_3O_2 Schiff base ligands in the equatorial plane and varying apical ligands.[31] Within this series, field-induced SMM behavior ($U_{eff} \approx 25$ K) is observed when the central Er^{III} ion is coordinated by one neutral and one charged axial ligand, while the complex $(Et_3NH)[Er(H_2DAPS)Cl_2]$ (H_4DAPS = 2,6-diacetylpyridine bis-(salicylhydrazone)) **(3)** with two negatively charged apical chlorine ligands exhibits fast magnetic relaxation. Numerical crystal field analysis of the dc magnetization and ab initio calculations suggest that slow relaxation of the magnetization occurs due to the strong axiality of the crystal field, as demonstrated by the dominance of a positive B_{40} crystal field parameter. For complex **(3)**, the different theoretical approaches yield significantly contrary results regarding the axiality of the ground state *g*-tensor and the size of the zero field splittings to the excited KDs.

To shed light on these discrepancies, we performed high-frequency/high-field electron paramagnetic resonance (HF-EPR) spectroscopy measurements on **(3)** in an earlier study.[32] Our experimental data validate the findings of numerical crystal field analysis, that is, the presence of energetically low-lying KDs ($\Delta_{1\to2}$ = 13.9 K and $\Delta_{1\to3}$ = 22.1 K) and considerable non-axiality of g_{eff} ($g_{eff,x}$ = 2.6, $g_{eff,y}$ = 3.2 and $g_{eff,z}$ = 12.5). In the present work we extend this study by reporting HF-EPR spectroscopy data on the equally pentagonal-bipyramidal coordinated erbium complexes Er(DAPMBH)X ($H_2DAPMBH$ = 2,6-diacetylpyridine bis-4-methoxy benzoylhydrazone and X = $(H_2O)Cl$ **(1)**, $(CH_3OH)N_3$ **(2)**) from the same series, which allows us to elucidate in detail the effect of variation of the apical ligands on the low-lying electronic states and, hence, on the electronic and magnetic properties in this series. In addition, a direct comparison of our experimental HF-EPR results with numerical studies allows us to validate numerical calculations and to critically assess the correctness of ab initio predictions as done recently by us for various lanthanide complexes.[33–35]

2. Experimental Results

The complexes investigated in this work were synthesized and characterized as reported in Ref. [31], and their molecular structures are displayed in Figure 1. Analogously to the previously reported complex **(3)**[32] [Figure 1c], the Er^{III} ions in both of the here studied compounds **(1)** and **(2)** are surrounded by a pentadentate ligand plane consisting of two oxygen and three nitrogen ions in the first coordination sphere. The key difference between the distinct molecules is, hence, given by the axial ligands: While the apical coordination sites in **(1)** and **(2)** are occupied by one charged group (Cl^-, N^-_3) and one neutral molecule (H_2O, CH_3OH), **(3)** hosts a charged chloride ion at both positions leading to a net negative charge of the complex.

To investigate the magnetic properties and decipher the origin of different relaxation dynamics, HF-EPR measurements were performed on Er^{III} complexes **(1)** and **(2)**. The absorption spectra obtained from oriented loose powder samples of both com-

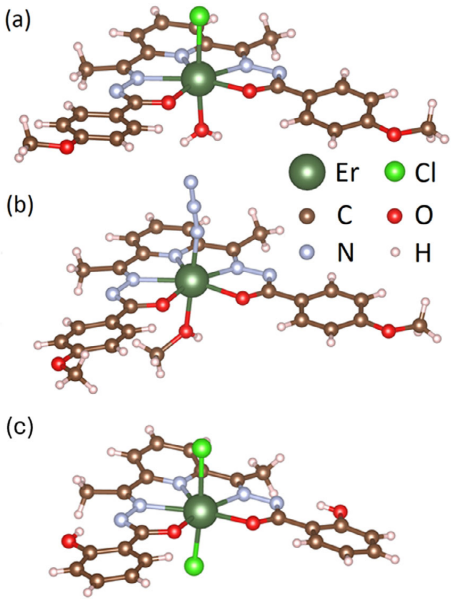


Figure 1. Molecular structure of the investigated pentagonal-bipyramidal Er^{III}-complexes (1) (a), (2) (b), and (3) (c). Figures were generated by VESTA[36] using the crystallographic information from Ref. [31].

plexes at T = 2 K are shown in the background of Figure 2a,b. For comparison, Figure 2c depicts the low-temperature loose powder HF-EPR spectra of the charged complex **(3)** with similar equatorial ligands but two chloride ions in the apical positions as reported in Ref. [32]. As can be seen, all spectra exhibit distinct Lorentzian-shaped resonance features in the whole measured frequency range of 0–900 GHz. The observed homogenous line broadening arises from the pseudo-single-crystal nature of the loose powder spectra, in which only a single molecular direction is probed. While the main absorption peak constitutes the only feature visible in complex **(1)** at the lowest temperature, complexes **(2)** and **(3)** exhibit two additional resonance features above 800 GHz and 300 GHz, respectively. The extracted resonance field positions at several fixed frequencies are summarized in Figure 2. As pointed out by the solid black lines, the resonance features form clear branches, which are labelled as (i) for **(1)**, α to γ for **(2)**, and R1 to R3 for **(3)**. All observed branches show a linear field dependence, except for the field region around 5 T in **(2)** and the crossing regime of R1 and R2 in **(3)**. The latter indicates avoided crossing behavior, that is, mixing of different energy states. While the branches (i), α and R1 are gapless within the resolution of our HF-EPR experiment, extrapolation of the resonance branches appearing at higher frequencies in **(2)** and **(3)** yields zero-field splittings (ZFS) of 760 GHz and 290 GHz, respectively. The effect of increasing temperature on the HF-EPR spectra of **(1)** at an exemplary fixed frequency of f = 593.9 GHz is shown in Figure 3a. As the temperature rises, the pronounced absorption peak (black square) gradually decreases in intensity until it is almost indiscernible at T = 60 K. Hence, the resonance branch (i) is associated with a ground state

© 2025 The Author(s). Chemistry – A European Journal published by Wiley-VCH GmbH

Chemistry–A European Journal
Research Article
doi.org/10.1002/chem.202500369
Chemistry Europe
European Chemical Societies Publishing

15213765, 2025, 33, Downloaded from https://chemistry-europe.onlinelibrary.wiley.com/doi/10.1002/chem.202500369, Wiley Online Library on [22/06/2025]. See the Terms and Conditions (https://onlinelibrary.wiley.com/terms-and-conditions) on Wiley Online Library for rules of use; OA articles are governed by the applicable Creative Commons License

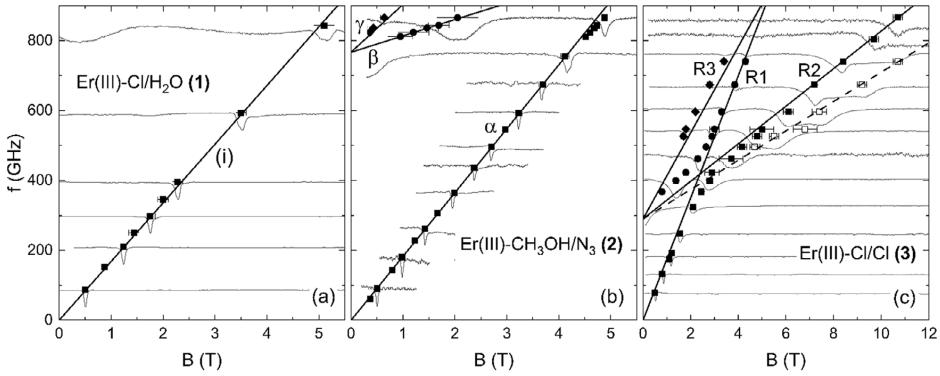


Figure 2. Resonance frequency versus magnetic field diagram for a loose powder sample of complex (**1**) (a), (**2**) (b), and (3)[32] (c) obtained at $T = 2$ K. Solid black lines depict simulated ground state transitions using a $S = 1/2$ pseudo-spin approximation for each KD (see text). Grey lines show the measured HF-EPR spectra, which are shifted along the ordinate for better comparison with the corresponding resonance feature.

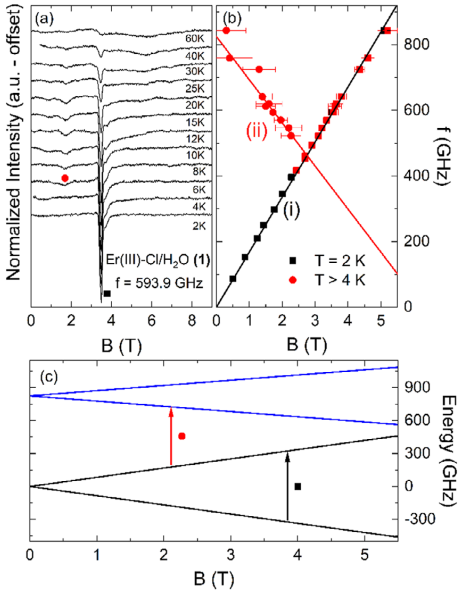


Figure 3. Loose powder HF-EPR spectra of complex (**1**) measured at selected fixed temperatures at $f = 593.9$ GHz (a), the corresponding frequency-field-diagram (b), and simulated energy levels of the two energetically lowest KDs (c). Solid lines in (b) and (c) depict simulations using a $S = 1/2$ pseudospin approximation (see the text). The arrows mark transitions between the energy levels corresponding to the observed resonance branches. For the HF-EPR spectra at elevated temperatures obtained at various frequencies, see Supporting Information (SI).

transition. Additionally, our data reveal another resonance feature (red circle) evolving at elevated temperatures around T ≈ 8 K, thereby implying the presence of energetically higher-lying spin states that are thermally populated. Similar to the ground-state transition, the resonance frequency of the excited-state feature also follows a linear branch, labeled as (ii) in the resonance frequency versus magnetic field diagram (Figure 3b), but exhibits a ZFS of 825 GHz. The resonance branches obtained on a loose powder sample of **(1)** at various temperatures and displayed in Figure 3b provide direct information on the low-lying excited energy levels. As mentioned above, the Curie-like temperature dependence and the absence of ZFS in (i) clearly imply that it is associated with a transition within the lowest Kramers doublet (KD1). In contrast, a finite resonance frequency in zero magnetic field, along with its appearance at higher temperatures, renders (ii) a transition between two KDs starting from an excited energy state. From the slope of the branches at small magnetic fields, we read off effective g-values g_{eff} of 12.0(3) and 9.4(5) for branches (i) and (ii), respectively. Applying a phenomenological $S = 1/2$ pseudospin approximation for each individual KD of the $^4I_{15/2}$ ground state multiplet (cf. Ref. [32]) yields the energy level diagram shown in Figure 3c. Since the experimentally accessible energy range does not allow probing higher-lying KDs, only the two energetically lowest KDs are shown in Figure 3c, while further energy states are omitted. Note here that the construction of this energy level diagram is solely based on the effective g-values and ZFS observed for the branches (i) and (ii). Our analysis yields effective g-values of 12.0(3) and 6.8(4) for KD1 and KD2, respectively.

Due to the alignment of the loose powder sample with the external magnetic field, the obtained spectra correspond to a measurement along the easy-anisotropy axis, and thus, only the corresponding component of the g-tensor can be quantified from these measurements. In order to obtain the complete g-tensor, and hence to further elucidate magnetic anisotropy, fixed powder HF-EPR measurements on complex **(1)** have been performed. Exemplary fixed powder spectra obtained at $f = 252.3$ GHz and $f = 168.4$ GHz are displayed in Figure 4. Two resonance features can be identified in the spectra. By comparing the fixed powder spectra to the loose powder spectra in Figure 2a, the feature at lower magnetic fields can be assigned to the easy axis orientation, here denoted as the z-direction, with $g_{eff,z} = 12.0(1)$ (see Figure S3 for a direct comparison of fixed and loose powder spectra). The g-values corresponding to the other crystallographic directions ($g_{eff,x}$ and $g_{eff,y}$) are implied to be considerably smaller. In particular, the almost equal intensity of the resonance features indicates that only two directions contribute

© 2025 The Author(s). Chemistry – A European Journal published by Wiley-VCH GmbH

Chemistry–A European Journal | Research Article
doi.org/10.1002/chem.202500369
Chemistry Europe
European Chemical Societies Publishing

15213765, 2025, 33, Downloaded from https://chemistry-europe.onlinelibrary.wiley.com/doi/10.1002/chem.202500369, Wiley Online Library on [22/06/2025]. See the Terms and Conditions (https://onlinelibrary.wiley.com/terms-and-conditions) on Wiley Online Library for rules of use; OA articles are governed by the applicable Creative Commons License

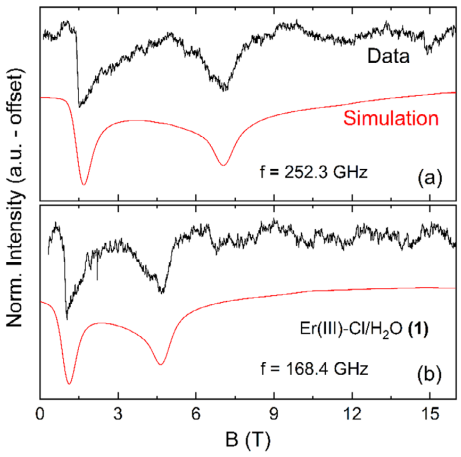


Figure 4. HF-EPR spectra (black lines) of a fixed powder sample of complex (**1**) measured at $f = 252.3$ GHz (a) and $f = 168.4$ GHz (b) at $T = 2$ K. Red lines depict simulated spectra using a $S = 1/2$ pseudo-spin approximation with a strongly anisotropic g-tensor as described in the text.

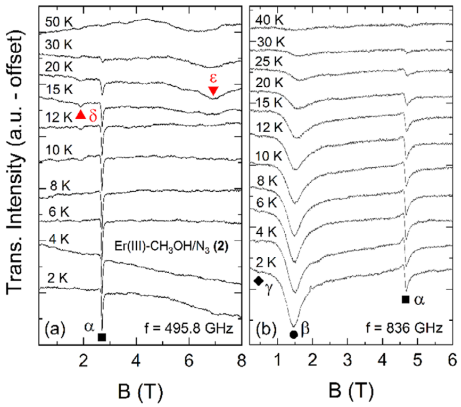


Figure 5. Temperature dependence of the loose powder HF-EPR spectra of complex (**2**) measured at fixed frequencies of $f = 495.8$ GHz (a) and $f = 863$ GHz (b). The symbols mark resonance features appearing at T = 2 K (black) and at higher temperatures (red).

to the measured spectra while the third g-value component is most likely too small to yield a corresponding feature in the accessible field range, that is, $g_{eff,z} > g_{eff,y} \gg g_{eff,x}$. To quantify the g-tensor components, the obtained HF-EPR fixed powder spectra were fit assuming an $S = 1/2$ pseudospin approximation with a strongly anisotropic g-tensor (solid red lines in Figure 4). The best agreement with the experimental data was achieved by using $g_{eff,z} = 12.0(1)$, $g_{eff,y} = 2.6(5)$, and $g_{eff,x} < 0.5(5)$, where $g_{eff,x}$ is fixed to the highest possible value that still reasonably reproduces the measured spectra while the other two components are varied.

Continuing the investigation of complex **(2)**, Figure 5 displays the temperature dependence of the loose powder spectra measured at frequencies of $f = 495.8$ GHz (a) and $f = 836.0$ GHz (b). Similar to the observation in **(1)**, the spectral weight of all resonances that can be identified at $T = 2$ K, that is, α, β, and γ, decreases with rising temperature, which suggests that they are associated with transitions from the magnetic ground state. Further, the appearance of two additional resonance features upon heating (red triangles), here labeled as δ and ε, implies transitions from excited energy states that are thermally populated.

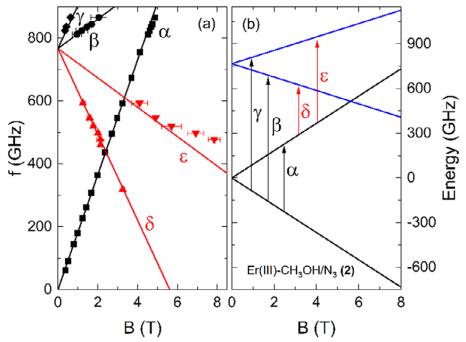


Figure 6. Frequency versus magnetic field diagram of complex (**2**) obtained from loose powder HF-EPR measurements at different temperatures (a) and simulated energy levels including the two energetically lowest KDs (b). Solid lines depict simulations using a $S = 1/2$ pseudospin approximation for each KD as described in the text. The arrows mark transitions between the energy levels corresponding to the observed resonance branches. For the HF-EPR spectra at elevated temperatures obtained at various frequencies, see Supporting Information (SI).

A summary of all resonance positions observed at different temperatures in a loose powder sample of **(2)** is given in Figure 6a. In total, we observe five resonance branches, all of which follow a linear field dependence up to a magnetic field of approximately 5 T. Above this field, an avoided crossing behavior of branch ε confirms the mixing of energy states, as already implied by the weak right-bending of branch α. The absence of a finite excitation gap at zero magnetic field allows for the assignment of resonance branch α to a transition within the energetically lowest Kramers doublet (KD1). In contrast, branches β – ε are gapped with a ZFS of $\Delta = 767$ GHz and, hence, associated with transitions from the lowest to the first excited KD (KD2). As depicted in Figure 6b, the observed resonance positions can be rationalized again in a phenomenological pseudospin $S = 1/2$ approximation for the two lowest-lying KDs, where the arrows assign the resonance branches to the transitions from the ground state (black) or the first excited state (red). By fitting the ground state branches α–γ, effective g-factors of $g_{eff} = 13.1(1)$ and 6.2(3) can be calculated for KD1 and KD2, respectively. The consistency of the used model is demonstrated by a very good agreement with the observed transitions δ and ε as indicated by the simulated branches (solid lines) in Figure 6a.

The anisotropic nature of complex **(2)** can almost directly be seen from the fixed powder HF-EPR spectra, one of which is exemplarily shown in Figure 7a. Similar to the findings in complex **(3)**, the fixed powder spectra of **(2)** exhibit the typical shape for an XXZ-type g-tensor anisotropy in the case of a randomly oriented powder sample, and two distinct resonance features can be identified.[32,37] The resonance positions of both observed features at different measurement frequencies form two clear

© 2025 The Author(s). Chemistry – A European Journal published by Wiley-VCH GmbH

Chemistry–A European Journal | Research Article
doi.org/10.1002/chem.202500369
Chemistry Europe
European Chemical Societies Publishing

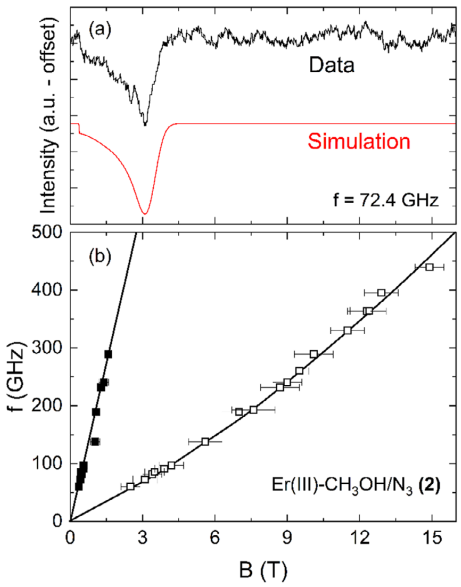


Figure 7. (a) Fixed powder HF-EPR spectrum (black) of complex (**2**) measured at $f = 72.4$ GHz and $T = 2$ K and simulation assuming a $S = 1/2$ pseudospin approximation (red) as described in the text. (b) Frequency versus magnetic field diagram obtained at $T = 2$ K including the loose (closed) and fixed (open) powder resonance features. All lines in (b) are a guide to the eye. For the HF-EPR spectra at higher frequencies, see Supporting Information.

resonance branches, as displayed in Figure 7b. By comparison to Figure 6a, the linear branch appearing at lower magnetic fields (solid squares) can be straightforwardly assigned to the resonances arising from the easy axis direction as observed in the loose powder measurement (see Figure S6 for a direct comparison of fixed and loose powder spectra), while the stronger resonance feature at higher fields (open squares) corresponds to another crystallographic direction within the molecular complex. Since the external magnetic field rotates the Er^{III} moments out of their zero-field easy-axis orientation, the branch associated with the transversal molecular direction exhibits slight left-bending to higher magnetic fields, which complicates the determination of an effective g-value. In order to at least estimate $g_{eff,x/y}$, the HF-EPR spectra obtained at small frequencies, that is, in a regime where the corresponding branch is in good approximation linear, were simulated analogous to the procedure used for **(1)** and illustrated in Figure 4a. The best fit to the data is depicted as a red solid line in Figure 7a. From the intensity distribution and the positions of the resonance features, an XXZ-type g-tensor with principal values of $g_{eff,z} = 13.1(2)$, $g_{eff,y} = 1.5(1)$, and $g_{eff,x} = 1.5(3)$ can be derived.

3. Discussion

Table 1 summarizes the anisotropic g-values and crystal field splittings of complexes **(1)–(3)** as experimentally determined by

Table 1. Effective g-values and zero field splittings of the up to three energetically lowest Kramers doublets in the complexes (1)–(3) as obtained from our analysis of the HF-EPR measurements. For comparison, the corresponding values determined by means of numerical studies based on crystal field analysis (CF) of the dc magnetization and ab initio calculations from Ref. [31] are shown.

	Er^{III}-Cl/H_2O (1) Slow Relaxation (U_{eff} = 23 K)[31]			Er^{III}-CH_3OH/N_3 (2) Slow Relaxation (U_{eff} = 28 K)[31]			Er^{III}-Cl/Cl (3) SMM-Silent[31]			
	$g_{eff,x}$	$g_{eff,y}$	$g_{eff,z}$	$g_{eff,x}$	$g_{eff,y}$	$g_{eff,z}$	$g_{eff,x}$	$g_{eff,y}$	$g_{eff,z}$	
KD1	12.0(3)13.44/10.9	2.5(3)2.10/5.17	<0.5(5)0.53/0.03	13.1(2)14.20/11.51	1.5(1)2.0/4.7	1.5(3)0.1/0.46	12.5(4)12.37/15.04	3.2(3)4.88/0.55	2.6(2)2.07/0.44	This workCF/ab initio[31]
KD2	6.8(5)9.68/6.16	−5.09/2.64	−1.96/0.35	6.2(3)8.92/5.05	−5.24/1.80	−2.75/0.39	4.9(2)7.75/4.14	−6.34/6.73	−2.70/7.31	This workCF/ab initio[31]
KD3	–	–	–	–	–	–	3.2(2)	–	–	This work
$\Delta_{1\to2}$	825(13) GHz873/992 GHz			767(8) GHz655/786 GHz			290(11) GHz270/785 GHz			This workCF/ab initio[31]
$\Delta_{1\to3}$	≫1 THz1486/1633 GHz			≫1 THz1510/1333 GHz			460(10) GHz658/1799 GHz			This workCF/ab initio[31]

© 2025 The Author(s). Chemistry – A European Journal published by Wiley-VCH GmbH

15213765, 2025, 33, Downloaded from https://chemistry-europe.onlinelibrary.wiley.com/doi/10.1002/chem.202500369, Wiley Online Library on [22/06/2025]. See the Terms and Conditions (https://onlinelibrary.wiley.com/terms-and-conditions) on Wiley Online Library for rules of use; OA articles are governed by the applicable Creative Commons License

Chemistry–A European Journal | Research Article doi.org/10.1002/chem.202500369 | Chemistry Europe European Chemical Societies Publishing

15213765, 2025, 33, Downloaded from https://chemistry-europe.onlinelibrary.wiley.com/doi/10.1002/chem.202500369, Wiley Online Library on [22/06/2025]. See the Terms and Conditions (https://onlinelibrary.wiley.com/terms-and-conditions) on Wiley Online Library for rules of use; OA articles are governed by the applicable Creative Commons License

Table 2. Effective magnetic quantum numbers m_{eff} for the lowest KDs as obtained from the HF-EPR data assuming $g_L = 1.2$ (see text).

	Complex (1)	Complex (2)	Complex (3)
KD1	5.0(1)	5.5(1)	5.2(2)
KD2	2.8(2)	2.6(1)	2.0(1)
KD3	–	–	1.3(1)

simulating the HF-EPR spectra in an effective $S = 1/2$ pseudospin model for each KD. In addition, we cite the results of numerical studies based on crystal field (CF) analysis of magnetic data and ab initio calculations, respectively, from Ref. [31]. For all three complexes under study, the ground-state *g*-tensor shows a pronounced uniaxial behavior ($g_{eff,z} \gg g_{eff,x}$, $g_{eff,y}$) which suggests an Ising-like character in the low-temperature magnetic behavior of the Er^{III} ions. However, the presence of finite $g_{eff,x}$ and $g_{eff,y}$ values directly implies considerable contributions from non-axial crystal field parameters as predicted by numerical studies.[31] For **(2)**, the Ising character is most pronounced and $g_{eff,x} \approx g_{eff,y}$ is found within the resolution of the experiment. Concomitantly, **(2)** features the largest anisotropy barrier of $U_{eff} = 28$ K among the studied complexes.[31] In contrast, the *g*-tensors of **(1)** and **(3)** exhibit larger transversal components with $g_{eff,x} \neq g_{eff,y}$, which probably mainly arises from the distorted equatorial N_3O_2 pentagon (Figure 1).[31,32] The presence of non-axial crystal-field parameters leads to a mixing of the $\pm m$ states and, hence, favors a fast QTM in the ground state KD.[38]

In order to gain further insights into the crystal field effects on the spin manifold, we turn back to the pseudo-single-crystalline loose powder spectra: The large effective *g*-values observed in particular for the ground state KDs in all studied compounds imply that the observed resonance features arise from strongly forbidden transitions with $\Delta m > 1$. By assuming that the theoretical free-ion Landé-factor $g_L = 1.2$ for Er^{III} is in good approximation still valid in the presence of the pentagonal-bipyramidal ligand coordination, the effective magnetic quantum number of the corresponding KDs can be determined via $m_{eff} = \Delta m/2 = g_{eff,z}/2g_L$. The so-calculated m_{eff} are summarized in Table 2. The half-integer m_{eff} values found for KD1 and KD2 in complex **(2)** directly indicate an almost pure $m = 11/2$ and $m = 5/2$ composition of the magnetic ground state and the first excited state, respectively. While the ground state m_{eff} in **(3)** is also close to a half-integer value within its error bars, our analysis implies a clear mixing of states in complex **(1)**. The observed trend is in qualitative agreement with the finding of **(2)** exhibiting the smallest transversal anisotropy (Table 1), which is directly responsible for the occurrence of state mixing. Further, it becomes evident that $m = 11/2$ is the main contribution to the spin wavefunction in the magnetic ground state of all studied compounds, which confirms the dominance of a positive B_{40} crystal field parameter as suggested by crystal field analysis.[31]

In addition to the important role of the transverse components of the anisotropic *g*-tensor for the magnetic relaxation mechanisms, one main difference in the electronic structure of the studied complexes is the presence of particularly low-lying excited KDs. While **(1)** and **(3)** exhibit comparable non-axiality of g_{eff}, the energy gap between the ground state and the first excited KD ($\Delta_{1\to2}$) is almost three times larger in **(1)**. Considering the predominantly prolate electron distribution of Er^{III}, this observation implies that the additional charge on the apical ligand effectively reduces the equatorial nature of the crystal field acting on the magnetic center. The absence of field-induced slow magnetic relaxation in **(3)** but not in **(1)**, hence, indicates that the dominant relaxation process is thermally activated and involves excited energy levels. Considering the effective energy barriers measured for **(1)** and **(2)**, it seems plausible to attribute fast magnetic relaxation to thermally assisted QTM (TA-QTM), which we conclude to be the main driver of the SMM-silent behavior in **(3)**. In this respect, we also note that the energy gap between KD1 and KD2 in **(2)** is slightly smaller than in **(1)**, and the non-axiality of g_{eff} is more pronounced in **(1)**. In both complexes, KD3 is strongly gapped $\Delta_{1\to3} \gg 1$ THz and likely does not contribute to TA-QTM. While a comparison of $\Delta_{1\to2}$ implies stronger effects of thermally assisted QTM in **(2)** than in **(1)**, the observed smaller U_{eff} in **(1)** highlights the relevance of non-axiality.[31]

For KD1, our experimental results of both the *g*-tensor and the energy gap $\Delta_{1\to2}$ are in reasonably good quantitative agreement with the findings of CF analysis of the dc magnetization,[31] which indicates the validity of the numerical approach for the ground state KD (see Table 1). Reported ab initio results for KD1 fairly agree with the actual *g*-values and only yield a rather qualitative prognosis on the magnetic anisotropy in the complexes under study. In particular, the considerable differences between the predictions of ab initio calculations and experimentally obtained parameters for the anionic complex **(3)** highlight the difficulty of including the effects of the total molecular charge on the crystal packing in the quantum chemical calculations of pseudo-isolated complexes.[26,31] In contrast to the observations for KD1, the parameters of the excited states seem to be better reproduced by ab initio results, while the results of CF analysis, except for a reasonable agreement of the energy differences between the KDs, are quite off from the actually observed values. The observation of CF analysis performing worse for higher-lying KDs is not unsurprising since the contribution of the excited states to the dc magnetization decreases with their energy difference to the magnetic ground state.

4. Conclusion

In summary, we have experimentally investigated the influence of the apical ligand in mononuclear pentagonal-bipyramidal coordinated erbium complexes using HF-EPR. Our spectroscopic data enable us to precisely determine effective *g*-tensors and crystal field splittings of the two energetically lowest Kramers doublets and, hence, allow us to assess the validity of recently reported crystal field analysis and ab initio studies. For all studied compounds, the anisotropic *g*-tensor of the ground state KD was shown to possess high axiality. Yet, substituting the apical ligands from CH_3OH/N_3 to Cl/H_2O and Cl/Cl and leaving the equatorial N_3O_2 Schiff base ligand unchanged introduces

© 2025 The Author(s). Chemistry – A European Journal published by Wiley-VCH GmbH

Chemistry–A European Journal | Research Article
doi.org/10.1002/chem.202500369
Chemistry Europe
European Chemical Societies Publishing

15213765, 2025, 33, Downloaded from https://chemistry-europe.onlinelibrary.wiley.com/doi/10.1002/chem.202500369, Wiley Online Library on [22/06/2025]. See the Terms and Conditions (https://onlinelibrary.wiley.com/terms-and-conditions) on Wiley Online Library for rules of use; OA articles are governed by the applicable Creative Commons License

transversal anisotropy, thereby leading to a mixing of the *m*-levels. Furthermore, direct observation of the crystal field splittings reveals significantly larger energy separation of the first excited Kramers doublet to the magnetic ground state in the two neutral complexes ($\Delta^{(1)}_{1\to2} = 825$ GHz and $\Delta^{(2)}_{1\to2} = 767$ GHz) as compared to the charged complex ($\Delta^{(3)}_{1\to2} = 270$ GHz). The experimentally found *g*-values suggest clear mixing of states in KD1 and KD2 of complex **(1)**, while half-integer m_{eff} values found for KD1 and KD2 in complex **(2)** indicate almost pure $m = 11/2$ and $m = 5/2$ compositions of the magnetic ground state and first excited state, respectively. Combining our findings, the absence of field-induced SMM behavior in complex **(3)**, but not in **(1)** and **(2)**, as found in ac susceptibility measurements,[31] can likely be explained by a comparably small energy barrier along with pronounced transversal anisotropy giving rise to relatively fast relaxation pathways via QTM and/or thermally assisted QTM.

5. Experimental Methods

Continuous wave high-frequency/high-field electron paramagnetic resonance (HF-EPR) measurements were performed using a millimeter vector network analyzer (MVNA) from *ABmm* as a phase-sensitive microwave source and detector.[35] Thoroughly ground powder samples were prepared inside a brass ring sealed with Kapton tape and placed into the microwave path of cylindrical brass waveguides. The data were obtained by simultaneously measuring the transmitted microwave amplitude and phase at frequencies ranging from 80 to 850 GHz in magnetic fields up to 16 T. All spectra were corrected for phase mixing and background effects, such as temperature drifts and contributions from the experimental setup.[39] Temperature control down to 2 K was achieved in a variable temperature insert (VTI) of an Oxford magnet system. Powder samples were firstly prepared inside a brass ring without glue or grease, that is, a loose powder experiment was performed to allow for the alignment of the crystallites along their effective anisotropy axis in the external magnetic field. This technique has proven to strongly reduce the complexity of the so-obtained pseudo-single-crystal spectra, especially for 3*d* metal-containing compounds.[40–45] Alignment was ensured by applying a magnetic field of 16 T prior to the measurements and restricting the field range to 0.2–16 T. To investigate the magnetic anisotropy in all directions of the molecules, further HF-EPR experiments were carried out on powder samples, which were fixed in their initial randomly distributed orientation using n-eicosane ($C_{20}H_{42}$, CAS-Nr. 112–95–8). Spectral simulations were performed using the MATLAB software package EasySpin.[46]

Acknowledgements

Measurements were performed before February 2022 supported by Deutsche Forschungsgemeinschaft (DFG) under Germany's Excellence Strategy EXC2181/1–390900948 (the Heidelberg STRUCTURES Excellence Cluster). Jan Arneth acknowledges support by the International Max-Planck Research School for Quantum Dynamics (IMPRS-QD) Heidelberg. Eduard B. Yagubskii and Tamara A. Bazhenova thank the Ministry of Science and Higher Education of the Russian Federation for financial support (Government Assignment No. 124013100858–3 and 124020200104–8).

Open access funding enabled and organized by Projekt DEAL.

Conflict of Interests

The authors declare no conflict of interest.

Data Availability Statement

The data that support the findings of this study are available from the corresponding author upon reasonable request.

Keywords: HF-EPR · lanthanides · magnetic anisotropy · magnetic properties · relaxation mechanisms

[1] R. Sessoli, D. Gatteschi, A. Caneschi, M. A. Novak, *Nature* **1993**, *365*, 141–143.
[2] M. J. Giansiracusa, A. K. Kostopoulos, D. Collison, R. E. P. Winpenny, N. F. Chilton, *Chem. Commun. (Camb)* **2019**, *55*, 7025–7028.
[3] S. K. Langley, D. P. Wielechowski, V. Vieru, N. F. Chilton, B. Moubaraki, B. F. Abrahams, L. F. Chibotaru, K. S. Murray, *Angew. Chem. Int. Ed. Engl.* **2013**, *52*, 12014–12019.
[4] K. S. Pedersen, M. Schau-Magnussen, J. Bendix, H. Weihe, A. V. Palii, S. I. Klokishner, S. Ostrovsky, O. S. Reu, H. Mutka, P. L. Tregenna-Piggott, *Chemistry* **2010**, *16*, 13458–13464.
[5] C. J. Milios, A. Vinslava, W. Wernsdorfer, S. Moggach, S. Parsons, S. P. Perlepes, G. Christou, E. K. Brechin, *J. Am. Chem. Soc.* **2007**, *129*, 2754–2755.
[6] E. Coronado, *Nat. Rev. Mater.* **2019**, *5*, 87–104.
[7] L. Bogani, W. Wernsdorfer, *Nat. Mater.* **2008**, *7*, 179–186.
[8] M. N. Leuenberger, D. Loss, *Nature* **2001**, *410*, 789–793.
[9] A. L. Barra, P. Debrunner, D. Gatteschi, C. E. Schulz, R. Sessoli, *Europhy. Lett.* **1996**, *35*, 133–138.
[10] C. Cadiou, M. Murrie, C. Paulsen, V. Villar, W. Wernsdorfer, R. E. P. Winpenny, *Chem. Commun.* **2001**, *37*, 2666–2667.
[11] Y. Z. Zhang, W. Wernsdorfer, F. Pan, Z. M. Wang, S. Gao, *Chem. Commun. (Camb)* **2006**, *42*, 3302–3304.
[12] A. Dey, P. Kalita, V. Chandrasekhar, *ACS Omega* **2018**, *3*, 9462–9475.
[13] D. N. Woodruff, R. E. Winpenny, R. A. Layfield, *Chem. Rev.* **2013**, *113*, 5110–5148.
[14] N. Ishikawa, M. Sugita, T. Ishikawa, S. Y. Koshihara, Y. Kaizu, *J. Am. Chem. Soc.* **2003**, *125*, 8694–8695.
[15] Y. S. Ding, N. F. Chilton, R. E. Winpenny, Y. Z. Zheng, *Angew. Chem. Int. Ed. Engl.* **2016**, *55*, 16071–16074.
[16] F. S. Guo, B. M. Day, Y. C. Chen, M. L. Tong, A. Mansikkamaki, R. A. Layfield, *Science* **2018**, *362*, 1400–1403.
[17] F. Neese, D. A. Pantazis, *Faraday Discuss.* **2011**, *148*, 229–238, discussion 299–314.
[18] O. Waldmann, *Inorg. Chem.* **2007**, *46*, 10035–10037.
[19] J. Long, A. O. Tolpygin, D. M. Lyubov, N. Y. Rad'kova, A. V. Cherkasov, Y. V. Nelyubina, Y. Guari, J. Larionova, A. A. Trifonov, *Dalton Trans.* **2021**, *50*, 8487–8496.
[20] L. Zhu, Y. Dong, B. Yin, P. Ma, D. Li, *Dalton Trans.* **2021**, *50*, 12607–12618.
[21] T. A. Bazhenova, V. A. Kopotkov, D. V. Korchagin, E. A. Yureva, M. V. Zhidkov, A. I. Dmitriev, I. A. Yakushev, N. N. Efimov, K. A. Babeshkin, V. S. Mironov, E. B. Yagubskii, *Inorg. Chem. Front.* **2025**, *12*, 231–252.
[22] C. A. P. Goodwin, F. Ortu, D. Reta, N. F. Chilton, D. P. Mills, *Nature* **2017**, *548*, 439–442.

© 2025 The Author(s). Chemistry – A European Journal published by Wiley-VCH GmbH

Chemistry–A European Journal | Research Article doi.org/10.1002/chem.202500369 | Chemistry Europe European Chemical Societies Publishing

15213765, 2025, 33, Downloaded from https://chemistry-europe.onlinelibrary.wiley.com/doi/10.1002/chem.202500369, Wiley Online Library on [22/06/2025]. See the Terms and Conditions (https://onlinelibrary.wiley.com/terms-and-conditions) on Wiley Online Library for rules of use; OA articles are governed by the applicable Creative Commons License

[23] S. K. Gupta, T. Rajeshkumar, G. Rajaraman, R. Murugavel, *Chem. Sci.* **2016**, *7*, 5181–5191.
[24] M. S. Norre, C. Gao, S. Dey, S. K. Gupta, A. Borah, R. Murugavel, G. Rajaraman, J. Overgaard, *Inorg. Chem.* **2020**, *59*, 717–729.
[25] J. Corredoira-Vázquez, M. Fondo, J. Sanmartín-Matalobos, A. M. García-Deibe, Proceedings **2020**, *62*, 2. https://doi.org/10.3390/proceedings2020062002.
[26] P. Kalita, N. Ahmed, A. K. Bar, S. Dey, A. Jana, G. Rajaraman, J. P. Sutter, V. Chandrasekhar, *Inorg. Chem.* **2020**, *59*, 6603–6612.
[27] F. Wang, H. W. Gong, Y. Zhang, A. Q. Xue, W. H. Zhu, Y. Q. Zhang, Z. N. Huang, H. L. Sun, B. Liu, Y. Y. Fang, S. Gao, *Dalton Trans.* **2021**, *50*, 8736–8745.
[28] A. J. Brown, D. Pinkowicz, M. R. Saber, K. R. Dunbar, *Angew. Chem. Int. Ed. Engl.* **2015**, *54*, 5864–5868.
[29] E. Castellanos, F. Benner, S. Demir, *Inorg. Chem.* **2024**, *63*, 9888–9898.
[30] S. De, A. Mondal, Y. C. Chen, M. L. Tong, R. A. Layfield, *Chemistry* **2025**, *31*, e202500011.
[31] T. A. Bazhenova, V. A. Kopotkov, D. V. Korchagin, Y. V. Manakin, L. V. Zorina, S. V. Simonov, I. A. Yakushev, V. S. Mironov, A. N. Vasiliev, O. V. Maximova, E. B. Yagubskii, *Molecules* **2021**, *26*, 6908.
[32] L. Spillecke, C. Koo, O. Maximova, V. S. Mironov, V. A. Kopotkov, D. V. Korchagin, A. N. Vasiliev, E. B. Yagubskii, R. Klingeler, *Dalton Trans.* **2021**, *50*, 18143–18154.
[33] P. Comba, L. J. Daumann, R. Klingeler, C. Koo, M. J. Riley, A. E. Roberts, H. Wadepohl, J. Werner, *Chemistry* **2018**, *24*, 5319–5330.
[34] P. Comba, M. Enders, M. Grosshauser, M. Hiller, R. Klingeler, C. Koo, D. Muller, G. Rajaraman, A. Swain, M. Tavhelidse, H. Wadepohl, *Chemistry* **2021**, *27*, 9372–9382.
[35] P. Comba, M. Grosshauser, R. Klingeler, C. Koo, Y. Lan, D. Muller, J. Park, A. Powell, M. J. Riley, H. Wadepohl, *Inorg. Chem.* **2015**, *54*, 11247–11258.
[36] K. Momma, F. Izumi, *J. Appl. Crystallogr.* **2011**, *44*, 1272–1276.
[37] W. R. Hagen, *Dalton Trans.* **2006**, *45*, 4415–4434.
[38] D. Gatteschi, R. Sessoli, *Angew. Chem. Int. Ed. Engl.* **2003**, *42*, 268–297.
[39] M. Linzer, *J. App. Phys.* **1969**, *40*, 372–376.
[40] N. Ahmed, T. Sharma, L. Spillecke, C. Koo, K. U. Ansari, S. Tripathi, A. Caneschi, R. Klingeler, G. Rajaraman, M. Shanmugam, *Inorg. Chem.* **2022**, *61*, 5572–5587.
[41] S. M. J. Aubin, Z. Sun, L. Pardi, J. Krzystek, K. Folting, L.-C. Brunel, A. L. Rheingold, G. Christou, D. N. Hendrickson, *Inorg. Chem.* **1999**, *38*, 5329–5340.
[42] A. L. Barra, A. Caneschi, D. Gatteschi, R. Sessoli, *J. Am. Chem. Soc.* **2002**, *117*, 8855–8856.
[43] A. Das, K. Gieb, Y. Krupskaya, S. Demeshko, S. Dechert, R. Klingeler, V. Kataev, B. Buchner, P. Muller, F. Meyer, *J. Am. Chem. Soc.* **2011**, *133*, 3433–3443.
[44] D. P. Goldberg, J. Telser, J. Krzystek, A. G. Montalban, L.-C. Brunel, A. G. M. Barrett, B. M. Hoffman, E. P. R. Spectra from, *J. Am. Chem. Soc.* **1997**, *119*, 8722–8723.
[45] L. Spillecke, S. Tripathi, C. Koo, M. Ansari, S. Vaidya, A. Rasamsetty, T. Mallah, G. Rajaraman, M. Shanmugam, R. Klingeler, *Polyhedron* **2021**, *208*, 115389.
[46] S. Stoll, A. Schweiger, *J. Magn. Reson.* **2006**, *178*, 42–55.

Manuscript received: January 28, 2025
Revised manuscript received: April 15, 2025
Version of record online: May 15, 2025

© 2025 The Author(s). Chemistry – A European Journal published by Wiley-VCH GmbH

Supporting Information: The Relevance of Non-axiality and Low-lying Excited States for Slow Magnetic Relaxation in Pentagonal-bipyramidal Erbium(III) Complexes Probed by High-frequency EPR

Jan Arneth,*[a] Lena Spillecke,[a] Changyun Koo,[a],[c] Tamara A. Bazhenova,[b] Eduard B. Yagubskii,[b] and Rüdiger Klingeler*[a]

Corresponding authors: jan.arneth@kip.uni-heidelberg.de, ruediger.klingeler@kip.uni-heidelberg.de

Table of Contents

1. Additional HF-EPR Data on Complex **(1)** 2
2. Additional HF-EPR Data on Complex **(2)** 3

1. Additional HF-EPR Data on Complex (1)

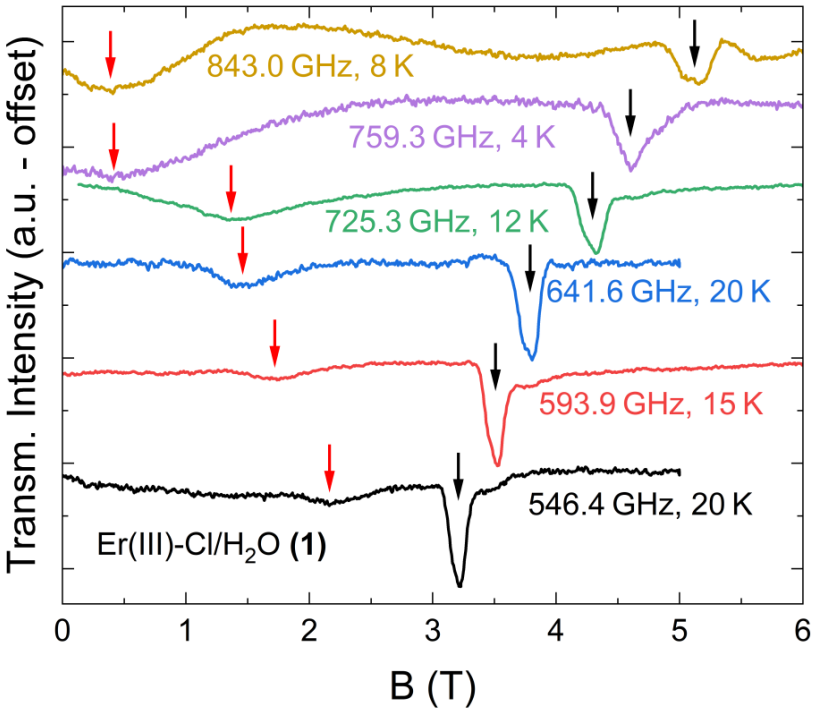


Figure S1. Loose powder HF-EPR spectra of complex **(1)** at selected fixed frequencies for $T > 2$ K. Arrows mark the read off resonance positions for the transitions arising from the ground state (black) and from excited states (red) as described in the main text.

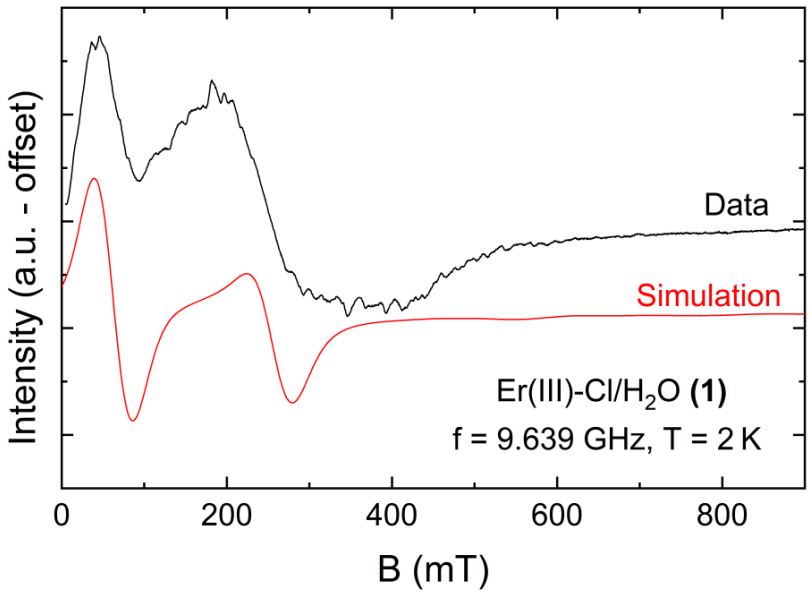


Figure S2. Fixed powder X-band spectrum of complex **(1)** at $f = 9.639$ GHz and $T = 2$ K and the corresponding simulation using a $S = 1/2$ pseudospin approximation with the parameters as described in the main text.

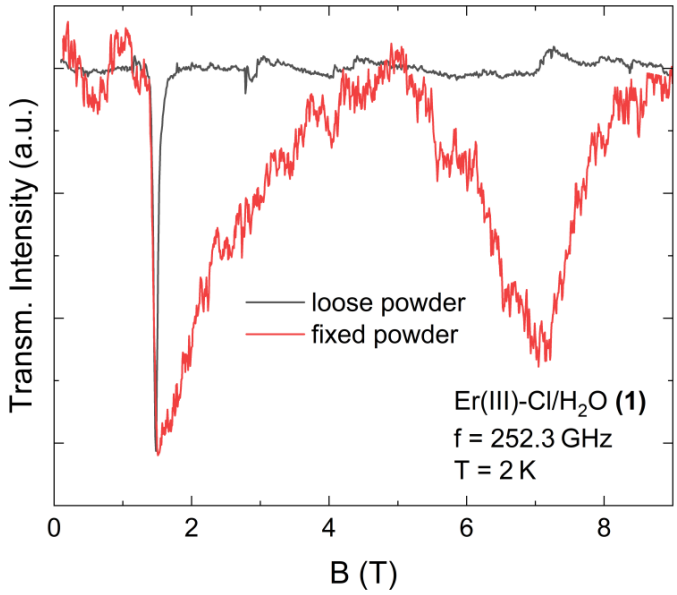


Figure S3. Comparison of loose and fixed powder HF-EPR spectra obtained at f = 252.3 GHz and T = 2 K for complex **(1)**. The fixed powder data has been scaled to match the maximum absorption with that of the loose powder data.

2. Additional HF-EPR Data on Complex (2)

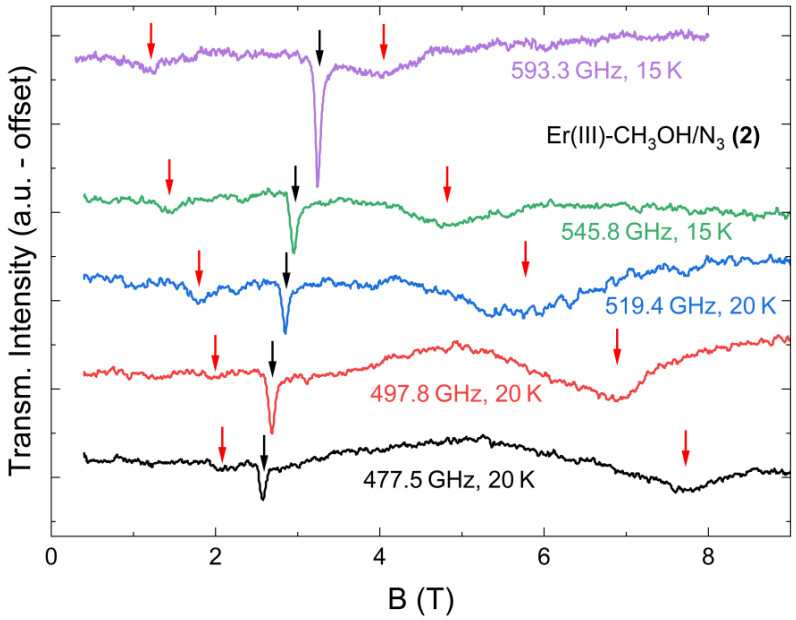


Figure S4. Loose powder HF-EPR spectra of complex **(2)** at selected fixed frequencies for T > 2 K. Arrows mark the read off resonance positions for the transitions arising from the ground state (black) and from excited states (red) as described in the main text.

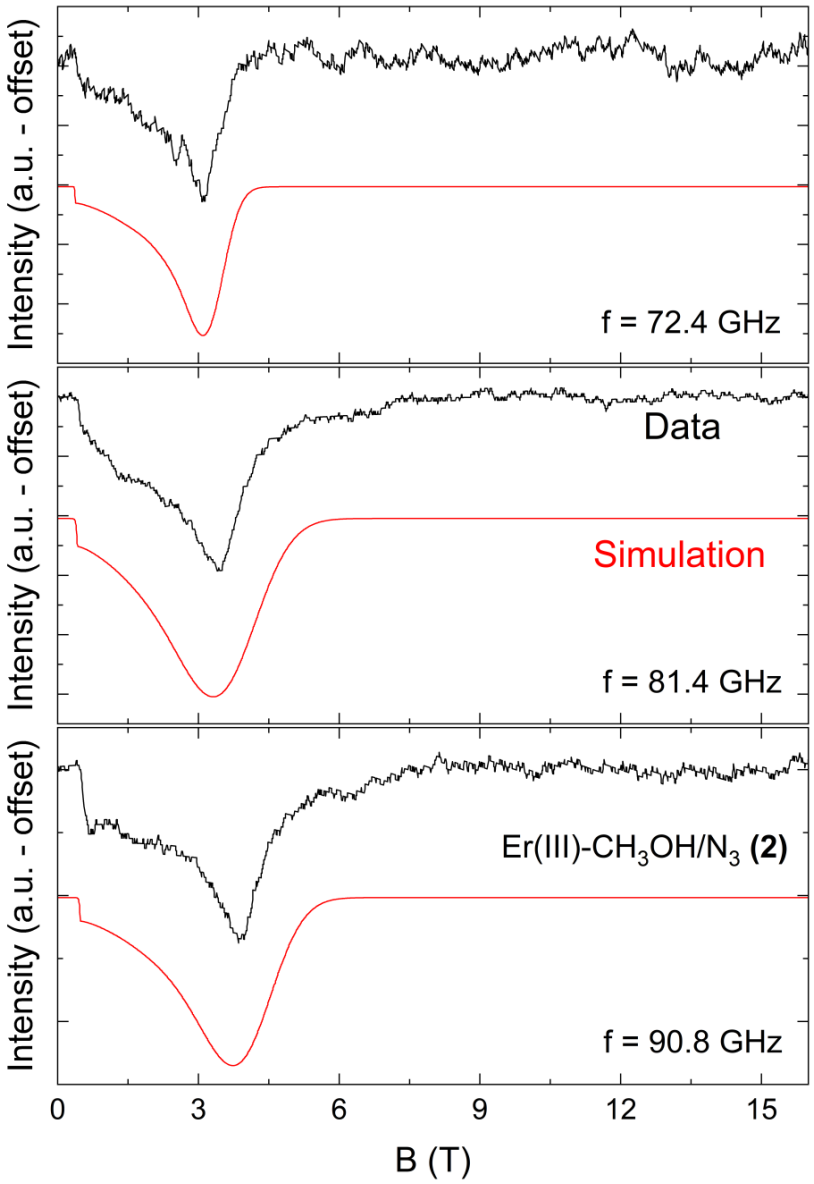


Figure S5. Fixed powder HF-EPR spectra of complex **(2)** at selected frequencies and T = 2K and simulations using a S = 1/2 pseudospin approximation with the parameters as described in the main text.

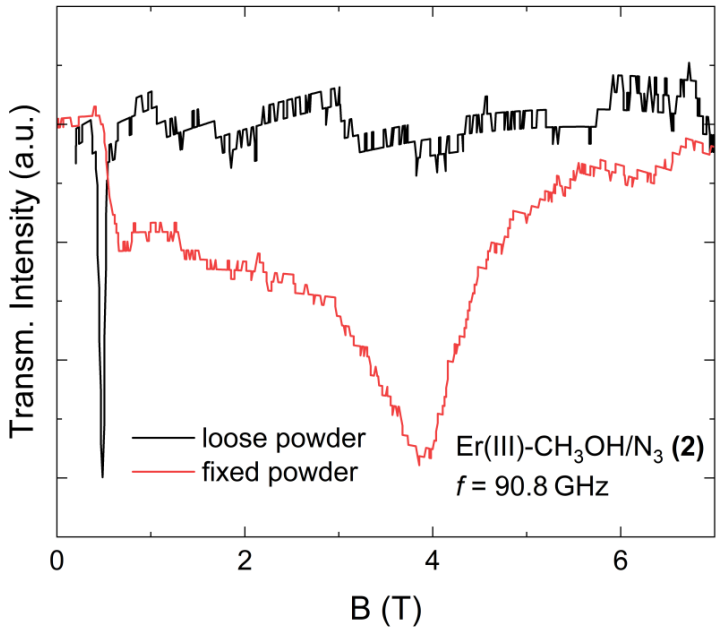


Figure S6. Comparison of loose and fixed powder HF-EPR spectra obtained at f = 90.8 GHz and T = 2 K for complex **(2)**. The fixed powder data has been scaled to match the maximum absorption with that of the loose powder data.

Chapter 6

The Interplay of Single Ion Anisotropy and Magnetic 3d-4f Interactions in $V_2^{III}Ln_2^{III}$ Butterfly Complexes

The results of this chapter were published as a research article in *Chemistry Europe* Volume 3, Issue 3 in April 2025 [112]. The corresponding manuscript is also available under the DOI: https://doi.org/10.1002/ceur.202500011. Specific contributions of each co-author, especially the contribution of J. Arneth, who serves as the corresponding and first author, are given in the following list:

- J. Arneth performed the magnetic susceptibility and HF-EPR experiments, analysed the corresponding data and the microSQUID data, constructed the plotted figures except Fig. 1 and Fig. S1, and wrote the manuscript draft except for the "Structural Analysis" section.
- X. Li, J. Braun, C. E. Anson and A. K. Powell synthesised the samples, conducted the structural analysis and wrote the "Structural Analysis" section in the manuscript.
- S. Paul and W. Wernsdorfer performed the microSQUID measurements, supported the corresponding data analysis and helped with writing the microSQUID section of the presented manuscript.
- R. Klingeler led the project and supported the data analysis and manuscript writing.
- All authors proofread the manuscript.

Check for updates

ChemistryEurope
Excellence in Chemistry Research Worldwide

Research Article
doi.org/10.1002/ceur.202500011

www.journal.chemistry-europe.org



The Interplay of Single Ion Anisotropy and Magnetic 3*d*-4*f* Interactions in $V^{III}_2Ln^{III}_2$ Butterfly Complexes

Jan Arneth[+],*[a] Xian-Feng Li[+],[b] Jonas Braun,*[b, c, d] Sagar Paul,[e] Michael Schulze,[e] Christopher E. Anson,[b] Wolfgang Wernsdorfer,[d, e] Annie K. Powell,*[b, c, d] and Rüdiger Klingeler*[a]

Within the framework of 3*d*–4*f* molecular magnets, the most thoroughly investigated architecture is that of butterfly-shaped coordination clusters as it provides an ideal testbed to study fundamental magnetic interactions. Here, we report the synthesis and characterisation of a series of isostructural $V^{III}_2Ln^{III}_2$ butterfly complexes, where Ln = Y ($\mathbf{1}_Y$), Tb ($\mathbf{2}_{Tb}$), Dy ($\mathbf{3}_{Dy}$), Ho ($\mathbf{4}_{Ho}$), Er ($\mathbf{5}_{Er}$), Tm ($\mathbf{6}_{Tm}$), Yb ($\mathbf{7}_{Yb}$), which extends the previous study on isostructural butterflies with Cr^{III}, Mn^{III} and Fe^{III}. In zero external field, compounds $\mathbf{2}_{Tb}$, $\mathbf{3}_{Dy}$ and $\mathbf{4}_{Ho}$ show clear maxima in the out-of-phase component of the ac susceptibility whereas small magnetic fields are needed to suppress quantum tunnelling in $\mathbf{6}_{Tm}$. Combined high-field electron paramagnetic resonance spectroscopy and magnetisation measurements unambiguously reveal an easy-plane anisotropy of the V^{III} ion and antiferromagnetic Ising-like 3*d*–4*f* exchange couplings. The strength of $J_{3d\text{-}4f}$ is shown to decrease upon variation of the 4*f* ion from Tb to Ho, while increasing antiferromagnetic interaction can be observed from Ho to Tm. The exact inverse chemical trend is found for the relative angle between the 3*d* and 4*f* main anisotropy axes, which highlights the important role of the lanthanide 4*f* electron distribution anisotropy for 3*d*–4*f* exchange.

Introduction

One approach to enhance the performance of Single Molecule Magnets (SMMs) such as coordination clusters which exhibit magnetic hysteresis solely due to magnetisation blocking on the molecular level,[1] is the idea of designing heterometallic 3*d*–4*f* complexes. This emerged as a promising pathway to higher blocking temperatures (T_B).[2–4] In these compounds the magnetic relaxation of the strongly anisotropic lanthanide moments, which is typically affected by quantum tunnelling and spin-phonon based relaxation pathways, can be slowed down *via* favourable magnetic interactions with the transition metal ions.[5–7] Although the combination of high effective energy barriers (U_{eff}) in 4*f*-based systems and slow magnetic relaxation of exchange coupled 3*d* ion systems appears to be a logical strategy, only a few examples in which the presence of paramagnetic 3*d* moments significantly improves the SMM properties have been reported.[8–10] Clearly the magnetic exchange coupling $J_{3d\text{-}4f}$ is one of the most important parameters influencing the performance of 3*d*–4*f*-based magnets. Hence knowledge on the underlying microscopic mechanisms is crucial for further advancements. The electronic structure of 4*f* ions is a further complication in the determination of the size and sign of $J_{3d\text{-}4f}$ and predictions are mostly based on quantum chemical calculations.[8,10–12] On the experimental side, high-frequency/high-field electron paramagnetic resonance (HF-EPR) spectroscopy has established itself as the main technique to investigate the magnetic 3*d*–4*f* coupling in heterometallic complexes as it allows to quantify the coupling parameter $J_{3d\text{-}4f}$ precisely.[13–16] Other spectroscopic methods, such as inelastic neutron scattering,[17] magnetic circular dichroism[18] and far-infrared transmission spectroscopy,[19] give further insights into the microscopic parameters governing the magnetic behaviour

[a] *J. Arneth,[+] Prof. Dr. R. Klingeler*
Kirchhoff-Institute for Physics
Heidelberg University
INF 227, D-69120 Heidelberg, Germany
E-mail: jan.arneth@kip.uni-heidelberg.de
ruediger.klingeler@kip.uni-heidelberg.de

[b] *Dr. X.-F. Li,[+] Dr. J. Braun, Dr. C. E. Anson, Prof. Dr. A. K. Powell*
Institute of Inorganic Chemistry
Karlsruhe Institute of Technology (KIT)
Kaiserstr. 12, D-76131 Karlsruhe, Germany
E-mail: jonas.braun2@kit.edu
annie.powell@kit.edu

[c] *Dr. J. Braun, Prof. Dr. A. K. Powell*
Institute of Nanotechnology
Karlsruhe Institute of Technology (KIT)
Kaiserstr. 12, D-76131 Karlsruhe, Germany
E-mail: jonas.braun2@kit.edu
annie.powell@kit.edu

[d] *Dr. J. Braun, Prof. Dr. W. Wernsdorfer, Prof. Dr. A. K. Powell*
Institute for Quantum Materials and Technology
Karlsruhe Institute of Technology (KIT)
Kaiserstr. 12, D-76131 Karlsruhe, Germany
E-mail: jonas.braun2@kit.edu
annie.powell@kit.edu

[e] *Dr. S. Paul, Dr. M. Schulze, Prof. Dr. W. Wernsdorfer*
Physikalisches Institut
Karlsruhe Institute of Technology (KIT)
Engesserstr. 15, D-76131 Karlsruhe, Germany

[+] *These authors have contributed equally.*

Supporting information for this article is available on the WWW under https://doi.org/10.1002/ceur.202500011

© 2023 Wiley-VCH GmbH. This is an open access article under the terms of the Creative Commons Attribution License, which permits use, distribution and reproduction in any medium, provided the original work is properly cited.

© 2023 Wiley-VCH GmbH

ChemistryEurope
Excellence in Chemistry Research Worldwide

Research Article
doi.org/10.1002/ceur.202500011

27514765, 2025, 3, Downloaded from https://chemistry-europe.onlinelibrary.wiley.com/doi/10.1002/ceur.202500011, Wiley Online Library on [22/06/2025]. See the Terms and Conditions (https://onlinelibrary.wiley.com/terms-and-conditions) on Wiley Online Library for rules of use; OA articles are governed by the applicable Creative Commons License

of 3*d*–4*f* magnets. Among the vast variety of available 3*d*–4*f* architectures, the butterfly-motif provides a useful test-bed system and many systematic studies have been performed regarding both their static and dynamic magnetic properties.[20–24] This motif can either have the 3*d* metal ions in the central "body" position with the 4*f* ions at the "wingtips" (Type I) or the inverse situation for Type II. The investigation of V^{III}-based butterfly systems has not been reported so far because of difficulties in obtaining stable V–Ln clusters with this desired oxidation state.

Here, we report the successful synthesis using Schlenk line techniques of a series of isostructural $V^{III}_2Ln^{III}_2$ Type II butterfly complexes, where Ln = Y (**1**$_{Y}$), Tb (**2**$_{Tb}$), Dy (**3**$_{Dy}$), Ho (**4**$_{Ho}$), Er (**5**$_{Er}$), Tm (**6**$_{Tm}$), Yb (**7**$_{Yb}$). Using combined high-field EPR and magnetisation studies we quantitatively determined the microscopic spin Hamiltonian parameters, such as 3*d*–4*f* coupling and relative angles between the main anisotropy axes. The dependence of $J_{3d\text{-}4f}$ on the 4*f* ion is discussed and compared to the experimental findings on other 3*d*–4*f* complexes. We show that two distinct chemical trends can be observed for lanthanide ions with predominantly oblate and prolate anisotropy shape and conclude that the 4*f* electron distribution plays a crucial role in the dominant 3*d*–4*f* charge transfer process. The importance of 4*f* charge density anisotropy becomes further evident from the magnetic relaxation behaviour as studied by ac susceptibility and low temperature μSQUID measurements.

Experimental Detail and Methods

Single crystal crystallographic data were measured on Stoe StadiVari diffractometers equipped with Mo- or Cu-microfocus sources or a MetalJet2 liquid Ga source. Structures were solved using SHELXT[25] and refined using SHELX-2019[26] within the Olex2 platform.[27] The lattice methanols and the methyls of some ligand *t*-butyl groups were disordered and refined with sets of partial occupancy atoms. These were assigned anisotropic thermal parameters except for minor components, and refined with similarity restraints applied to bond lengths and rigid-bond restraints applied to the temperature factors. Crystallographic data are given in Table S1. Full crystallographic data and details of the structural determinations for the structures in this paper have been deposited with the Cambridge Crystallographic Data Centre as supplementary publication nos. CCDC 2406392–2406398. Copies of the data can be obtained, free of charge, from https://www.ccdc.cam.ac.uk/structures/.

The direct current (dc) and alternating current (ac) magnetisation was studied in the temperature range $T = 1.8$–300 K by means of a Magnetic Properties Measurement System (MPMS3, Quantum Design) and a Physical Properties Measurement System (PPMS, Quantum Design). For all measurements powder samples were pelletised in polycarbonate capsules to avoid reorientation in external magnetic fields. The experimental data were corrected for the diamagnetic contribution of the sample holder and of the ligands calculated by means of Pascal's constants.[28] Simulations of the magnetic data were performed using the PHI software package.[29]

M(*B*) measurements over a temperature range of 0.03–5.0 K, on single crystals of compound **3**$_{Dy}$, were conducted using μSQUIDs. A single crystal of about 100 μm (long arm) length was placed near an array of μSQUIDs on a chip, within few μm gap between the crystal edge and the μSQUID loop to ensure optimal coupling. The crystal was thermalized with Apiezon™ grease and cooled to a base temperature of 30 mK in a dilution refrigerator. A 3D vector magnet allows for the application of the magnetic field in different directions within the SQUID plane with an angular accuracy better than 0.1°. Low-temperature *M*(*B*) measurements were carried out at varying field sweep rates (0.001 to 0.128 T s^{-1}) with a time resolution of ~1 ms. The easy axis of the crystal was identified using the 'transverse field method'.[30–31]

High-frequency/high-field electron paramagnetic (HF-EPR) resonance studies were performed using a phase sensitive millimetre vector network analyser (MVNA) by *ABmm* as a simultaneous microwave source and detector.[32] Temperature control from 2 K to 300 K was ensured by placing the sample space in the Variable Temperature Insert (VTI) of an Oxford magnet system equipped with a 16 T superconducting coil.[33] Polycrystalline powder samples were prepared in a brass ring sealed with kapton tape either as loose powder or fixed by mixing with eicosane. The former setup allows alignment of the crystallites with the external magnetic field, hence providing simplified pseudo-single-crystal spectra.[16,34–37] Alignment is ensured by sweeping up the magnetic field to 16 T prior to each measurement and confirmed by observation of corresponding orientation jumps in the transmitted microwave intensity signal. Spectral simulations of the HF-EPR data were performed using the EasySpin software package.[38]

Experimental Results

Structural Analysis

Compounds **1**$_{Y}$ to **7**$_{Yb}$ with the formula $[V_2Ln_2(\mu_2\text{-}OMe)_2(^t\text{Budea})_2(piv)_6]\cdot 2CH_3OH$ (Ln^{III} = Y^{III}, Tb^{III}, Dy^{III}, Ho^{III}, Er^{III}, Tm^{III} and Yb^{III}) all crystallise isomorphously and thus isostructurally in the triclinic space group $P\bar{1}$ with $Z = 1$ (Table S1); the molecular structure of **3**$_{Dy}$ is shown in Figure 1. The centrosymmetric V_2Dy_2 core corresponds to a Type II butterfly structure[24] with Dy(1) and Dy(1′) occupying the body position and V(1) and V(1′) are located at the wingtips. The two VDy_2 triangles are each bridged by a triply-bridging methoxide ligand, one above and the other below the V_2Dy_2 plane. The vanadiums are both chelated by a doubly-deprotonated $(^t\text{Budea})^{2-}$ ligand with the two oxygens each bridging to one of the Dy^{III} ions. The coordination is completed by four *syn*,*syn*-pivalates bridging the V–Dy edges of the core with two further pivalates each chelating a Dy^{III} ion.

The clusters are isostructural to Cr_2Dy_2 butterflies reported by Murray *et al.*.[8] Selected bond lengths and angles are compared in Table S2, where the expected trends in the Ln–O

© 2023 Wiley-VCH GmbH

ChemistryEurope
Excellence in Chemistry Research Worldwide

Research Article
doi.org/10.1002/ceur.202500011

27514765, 2025, 3, Downloaded from https://chemistry-europe.onlinelibrary.wiley.com/doi/10.1002/ceur.202500011, Wiley Online Library on [22/06/2025]. See the Terms and Conditions (https://onlinelibrary.wiley.com/terms-and-conditions) on Wiley Online Library for rules of use; OA articles are governed by the applicable Creative Commons License

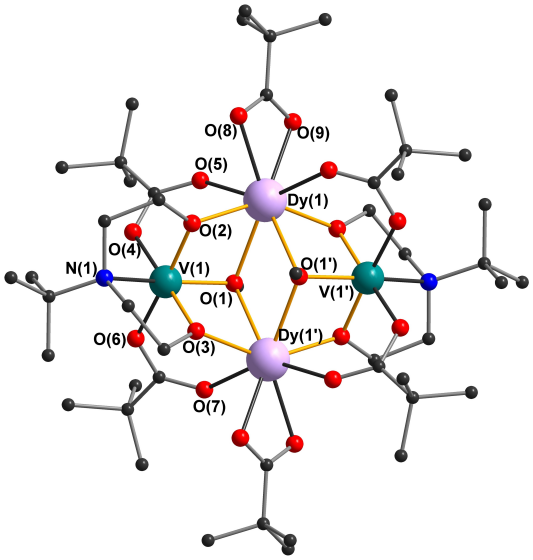


Figure 1. Molecular structure of the V_2Dy_2 cluster in $\mathbf{3}_{Dy}$. Hydrogen atoms and minor disorder are omitted for clarity. Primed atoms at 1-*x*, 1-*y*, 1-*z*.

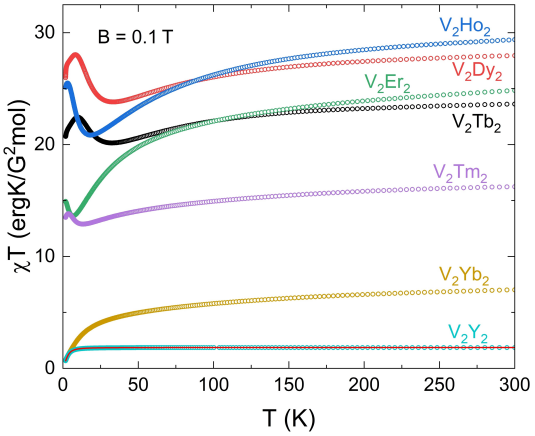


Figure 2. Temperature dependence of the χT-product of $\mathbf{1}_Y$-$\mathbf{7}_{Yb}$ in an external magnetic field of $B = 0.1$ T. The red solid line depicts a simulation of $\mathbf{1}_Y$ using the parameters obtained from HF-EPR (see text).

Table 1. Experimentally determined and theoretical free ion χT-values (in ergK/G²mol) of $\mathbf{1}_Y$ - $\mathbf{7}_{Yb}$.

	g_{Ln}	J_{Ln}	χT_{exp} (1.8 K)	χT_{exp} (300 K)	$\chi T_{free\ ion}$
$\mathbf{1}_Y$			0.68	1.86	2.0
$\mathbf{2}_{Tb}$	3/2	6	20.7	23.6	25.6
$\mathbf{3}_{Dy}$	4/3	15/2	26.0	28.0	30.3
$\mathbf{4}_{Ho}$	5/4	8	25.1	29.4	30.1
$\mathbf{5}_{Er}$	6/5	15/2	14.9	24.8	25.0
$\mathbf{6}_{Tm}$	7/6	6	13.5	16.2	16.3
$\mathbf{7}_{Yb}$	8/7	7/2	0.76	7.0	7.14

distances given the change in size of the Ln^{III} ions is clear. The V^{III} oxidation states in the complexes were confirmed by Bond Valence Sum Analysis,[39] with the calculated valences for V(1) being in the range 2.94–2.97 (see Table S3).

Direct Current (dc) Magnetisation

Variable-temperature static magnetic susceptibility measurements performed at $B = 0.1$ T on polycrystalline powders of $\mathbf{1}_Y$-$\mathbf{7}_{Yb}$ result in the χT-curves shown in Figure 2. For all the measured compounds the room temperature (300 K) χT-values which are summarized in Table 1 are slightly smaller than the expected free ion values for an uncoupled system of two V^{III} ions with $g = 2$ and two Ln^{III} ions. Such an observation is not surprising, since the LS-coupling in V^{III} typically leads to *g*-factors smaller than 2.[40–45] In the case of $\mathbf{1}_Y$, the magnetic data imply an average $g_{ave} = 1.93$, which is in excellent agreement with the results of our HF-EPR measurements, as discussed later. However, the influence of spin-orbit coupling in V^{III} can only partly explain the lower experimentally determined room temperature χT of $\mathbf{2}_{Tb}$ and $\mathbf{3}_{Dy}$. In these compounds, the too low value of χT might be the result of solvent molecules remaining in the crystal matrix or from the strongly anisotropic nature of the Ln moments such that even at 300 K not all m_J sub-levels are equally populated.[46]

The χT-product of $\mathbf{1}_Y$ is almost constant at temperatures above 10 K and rapidly decreases upon cooling below this value. As will be revealed by the HF-EPR studies, this drop is mainly attributed to the depopulation of the m_J sub-levels, in addition to a weak antiferromagnetic interaction between the V^{III} ions. A similar temperature dependence of χT is found in $\mathbf{7}_{Yb}$, albeit a weak decrease already begins close to room temperature and the steep drop occurs already at around 25 K. Both signatures presumably arise from the depopulation of the strongly split m_J sub-levels in the anisotropic Yb^{III} ions. A priori, antiferromagnetic intramolecular Yb–Yb coupling or intermolecular interaction might also yield such behaviour. However, for both we estimate an upper limit of dipolar interaction energy of less than 0.3 K which is way too small to account for the observed temperature dependence.

In contrast, the $\chi T(T)$-profiles for $\mathbf{2}_{Tb}$-$\mathbf{6}_{Tm}$ all exhibit a maximum at temperatures in the range 2–10 K, superposed upon the general decrease on cooling. Such behaviour could be attributed to intramolecular ferromagnetic interactions between the V^{III} and the Ln^{III} moments. However, the HF-EPR measurements reveal that it can actually be attributed to a parallel arrangement of the Ln^{III} spins on opposite sides of the butterfly body mediated by the antiferromagnetic V^{III}-Ln^{III} interactions. The position of the maximum in χT gives information about the J_{V-Ln} coupling strength, as discussed below.

© 2023 Wiley-VCH GmbH

ChemistryEurope
Excellence in Chemistry Research Worldwide

Research Article
doi.org/10.1002/ceur.202500011

27514765, 2025, 3, Downloaded from https://chemistry-europe.onlinelibrary.wiley.com/doi/10.1002/ceur.202500011, Wiley Online Library on [22/06/2025]. See the Terms and Conditions (https://onlinelibrary.wiley.com/terms-and-conditions) on Wiley Online Library for rules of use; OA articles are governed by the applicable Creative Commons License

High-Field EPR Studies

HF-EPR measurements on freshly ground powder samples from the same batch were carried out to determine the microscopic magnetic parameters. Figure 3 shows representative HF-EPR spectra of $\mathbf{1}_{Y}$ at variable temperature and fixed microwave frequency of $f = 395.4$ GHz (a) as well as at variable frequency and fixed temperature of $T = 2$ K (b). The spectra exhibit clear resonances in the accessible field and frequency range. In total two asymmetric resonance features can be identified as indicated by the vertical dashed lines in Figure 3(a). Upon increasing temperature both features become less pronounced, indicating that the initial state of the corresponding transition is (at least close to) the magnetic ground state. Moreover, the corresponding frequency dependence suggests that the low-field feature is associated with a symmetry-forbidden transition yielding $\triangle m = 2$, while the high-field feature is related to an allowed transition with $\triangle m = 1$. The allowed high-field feature exhibits its main spectral weight on its high-field side, thereby directly implying an easy-axis-type *g*-factor anisotropy.[47–48]

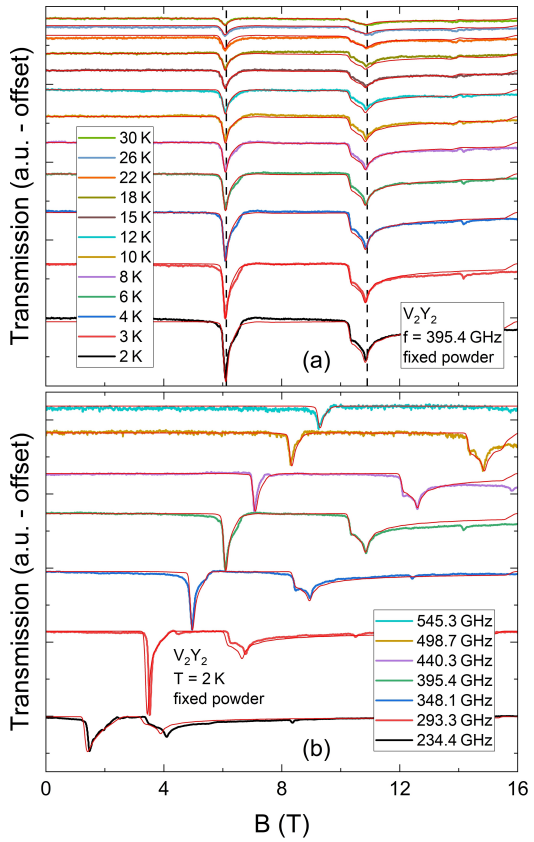


Figure 3. HF-EPR spectra of a fixed powder sample of $\mathbf{1}_{Y}$ at different temperatures and fixed frequency $f = 395.4$ GHz (a) and at different frequencies and constant temperature $T = 2$ K (b). Vertical dashed lines indicate the distinct resonance features. Red solid lines depict simulations using equation 1 with the parameters described in the main text.

In order to quantify the qualitatively discussed parameters we performed spectral simulations using an interacting dimer Hamiltonian in the form of

$$\hat{\mathcal{H}}_{1_Y} = \sum_{i=1}^{2}\left(\mu_B \mathbf{B}\bar{\bar{g}}\hat{\mathbf{S}}_i + D\hat{S}_{i,z}^2 + E\left(\hat{S}_{i,x}^2 - \hat{S}_{i,y}^2\right)\right) - J\hat{\mathbf{S}}_1\hat{\mathbf{S}}_2 \quad (1)$$

where $S_1 = S_2 = 1$, $\bar{\bar{g}} = (g_\perp, g_\perp, g_\parallel)$ denotes an axial *g*-tensor, *D* and *E* are the axial and rhombic anisotropy constants and *J* represents an isotropic Heisenberg interaction between the V^{III} moments. Note here that both the *g*-tensor and the crystal field parameters are fixed to be equal for both V^{III} sites, since their local ligand coordination, and hence the surrounding electrostatic potentials, are equivalent under point inversion. The best simulations of the experimental data were achieved by the parameters $g_\perp = 1.91(2)$, $g_\parallel = 1.98(2)$, $D = +9.3(4)$ K (6.45 cm^{-1}), $|E| = 0.25(5)$ K (0.17 cm^{-1}), $J = -0.18(6)$ K (0.12 cm^{-1}) and are shown as red solid lines in Figure 3. The spectral simulations confirm the easy-axis-character of the *g*-tensor, while simultaneously revealing an easy-plane single-ion anisotropy with a small rhombic distortion. The magnitude of the *D* and *E* parameters is not uncommon for V^{III} compounds reported in the literature.[40–45] In addition, this HF-EPR analysis reveals a weak antiferromagnetic coupling between the V^{III} moments which likely arises from a superexchange interaction *via* the diffuse empty orbitals of the diamagnetic Y^{III} ion.[49] Although *D* is the dominant term it is necessary to include the contribution of the parameters *E* and *J* in order to simulate the experimental data well. The parameter set extracted from HF-EPR also fully reproduces the observed magnetic data of $\mathbf{1}_{Y}$, as can be seen by the simulation depicted in Figure 2.

We additionally performed HF-EPR spectroscopy on loose powder samples of $\mathbf{2}_{Tb}$-$\mathbf{7}_{Yb}$, for which $\mathbf{2}_{Tb}$, $\mathbf{5}_{Er}$ and $\mathbf{6}_{Tm}$ show well-resolved resonance features in the accessible frequency- and field-range. The obtained resonance positions for $T = 2$ K are summarised in the magnetic field vs. resonance frequency diagrams in Figure 4, where distinct resonance features are marked by different symbols. Compared to the spectra of $\mathbf{1}_{Y}$, the resonance features in all three compounds are significantly less pronounced and exhibit strongly frequency-dependent line shapes. Upon following the main spectral weight clear resonance branches can be identified.

In $\mathbf{2}_{Tb}$ a single EPR-transition can be observed at frequencies ranging from 280 to 500 GHz. Up to at least 8 T its resonance frequency decreases linearly with magnetic field, corresponding to an effective *g*-factor of $g_{eff} \simeq 2$, close to the *g*-value found for the V^{III} ions in $\mathbf{1}_{Y}$. This suggests that the transition detected here is likely to be associated with an excitation involving the V^{III} ions in $\mathbf{2}_{Tb}$. However, the data also indicate a significant magnetic coupling to the Tb^{III} moments, since the extrapolated zero-field excitation gap $\triangle \simeq 515$ GHz of the resonance branch cannot be explained by the single-ion anisotropy of the V^{III} ions alone. The low temperature HF-EPR spectra of $\mathbf{5}_{Er}$ and $\mathbf{6}_{Tm}$ exhibit up to two ($\mathbf{5}_{Er}$) and four ($\mathbf{6}_{Tm}$) resonance features yielding

© 2023 Wiley-VCH GmbH

ChemistryEurope
Excellence in Chemistry Research Worldwide

Research Article
doi.org/10.1002/ceur.202500011

27514765, 2025, 3, Downloaded from https://chemistry-europe.onlinelibrary.wiley.com/doi/10.1002/ceur.202500011, Wiley Online Library on [22/06/2025]. See the Terms and Conditions (https://onlinelibrary.wiley.com/terms-and-conditions) on Wiley Online Library for rules of use; OA articles are governed by the applicable Creative Commons License

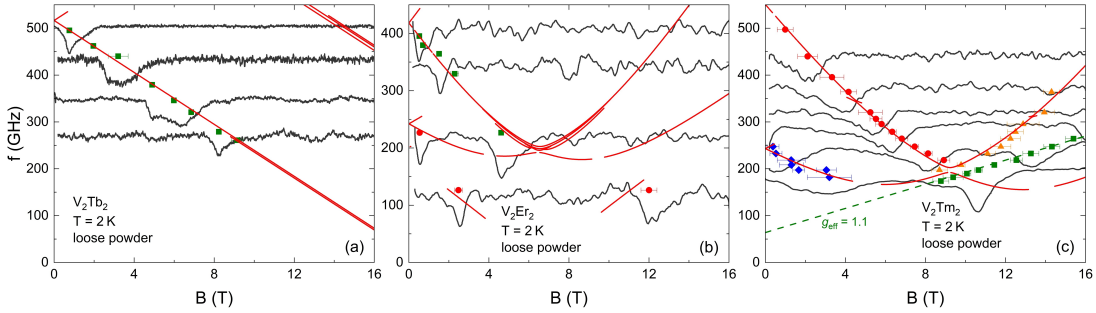


Figure 4. Magnetic field vs. resonance frequency plot of $\mathbf{2}_{Tb}$ (a), $\mathbf{5}_{Er}$ (b) and $\mathbf{6}_{Tm}$ (c) obtained from HF-EPR measurements at $T = 2$ K. Red solid lines depict simulations using equation 2 with the parameters shown in Table 2. Selected HF-EPR spectra are visible in the background and are shifted along the ordinate to align with the corresponding measurement frequency. The green dashed line in (c) marks the resonance branch which is associated with a transition between different m_J levels of the Tm^{III} ions as described in the text.

strongly curved branches with initial slopes corresponding to $g_{eff} \neq 2$. Interestingly, both complexes share a common low-energy zero-field excitation gap at $\triangle \simeq 240$ GHz, whereas the high-energy gaps differ significantly from each other. The temperature dependence of the HF-EPR spectra indicates that all observed transitions arise from either the ground or low-lying excited states (see Supplementary Material).

As a result of their large total angular momentum and complex anisotropy shape of Ln^{III} ions, simulations using full spin Hamiltonians for these ions in low-symmetry ligand fields generally exceed the manageable Hilbert and parameter space. However, in suitable coordination environments an axial charge distribution can lead to well-isolated ground state doublets, which allow for a treatment of Ln^{III} moments as Ising-spins at sufficiently low temperatures.[15–16,50–51] In the frame of this model the Hamiltonian of $\mathbf{2}_{Tb}$-$\mathbf{7}_{Yb}$ reads

$$\hat{\mathcal{H}}_{V_2Ln_2} = \vec{R}_x^{T}(\theta)\hat{\mathcal{H}}_{1_Y}\vec{R}_x(\theta) + \sum_{i=3}^{4}\left(\mu_B 2\alpha \mathbf{B}\vec{\tilde{g}}\hat{\mathbf{S}}_i - 2\alpha J_{V-Ln}\left(\hat{S}_{1,z}\hat{S}_{i,z} + \hat{S}_{2,z}\hat{S}_{i,z}\right)\right) \quad (2)$$

where $S_3 = S_4 = 1/2$, $\vec{\tilde{g}} = (0, 0, g_{Ln})$, α is a scaling factor to account for renormalization in the pseudospin transformation, and $\vec{R}_x(\theta)$ denotes a rotation of the local $\mathbf{1}_Y$-subsystem parameters ($\vec{\tilde{g}}$ and $\vec{D}$) by θ around the global x-axis.

Since the local environment around the V^{III} ions is essentially identical in all compounds, it is justifiable to fix the parameters obtained from the HF-EPR studies on $\mathbf{1}_Y$ in the simulations of $\mathbf{2}_{Tb}$-$\mathbf{7}_{Yb}$. In addition, it is assumed that the strongly Ising-like character of the Ln^{III} moments means that in a loose powder sample the crystallites can be oriented by the applied field such that the easy-anisotropy axes coincide with that of the lanthanide moments (here chosen parallel to the z-axis) and, hence, leads to an alignment of the molecules along the z-axis. The best simulations of the resonance branches are achieved by using $2\alpha J_{V\text{-}Tb} = -34.1$ K and $\theta = 0°$ for $\mathbf{2}_{Tb}$, $2\alpha J_{V\text{-}Er} = -8.6$ K and $\theta = 60°$ for $\mathbf{5}_{Er}$, and $2\alpha J_{V\text{-}Tm} = -12.2$ K and $\theta = 45°$ for $\mathbf{6}_{Tm}$, respectively. A more elaborate overview of the obtained spin Hamiltonian parameters is given in Table 2. It should be noted that neither the inclusion of magnetic dipolar coupling between the Ln^{III} moments nor an additional rotation of the V^{III} ion subsystem around its local y-axis significantly improved the simulations.

As can be seen in Figure 4, the experimentally observed resonance branches are well described by the spin Hamiltonian in equation 2. Only the low-energy branch at high magnetic fields in $\mathbf{6}_{Tm}$ (green squares) cannot be reproduced by our model. The slope of this branch corresponds to an effective g-factor of $g_{eff} \simeq 1.1$, which is close to the Landé-factor of Tm^{III}. Therefore, it seems reasonable that this resonance feature is associated with a transition between different m_J levels of the Tm^{III} ions that are effectively neglected in the Ising-approximation used here. Since α and $J_{V\text{-}Ln}$ are linearly correlated (see equation 2), this analysis of the HF-EPR data does not allow for a determination of the coupling constant $J_{V\text{-}Ln}$ but only of the magnetic coupling energy $2\alpha J_{V\text{-}Ln}$. In order to decouple the two parameters, we simulated the low-temperature magnetic data using the parameters obtained from the HF-EPR studies.

Figure 5 shows the isothermal magnetisation of $\mathbf{2}_{Tb}$ at $T = 1.8$ K and the corresponding simulations with $\alpha = 6$ and, hence, $J_{V\text{-}Tb} = -2.84$ K. The chosen model is in line with the experimental data up to at least 6 T and reproduces the key characteristics of the $M(B)$-profile *i.e.* a steep increase at small magnetic fields and an inflection point, indicating a change in the magnetic ground state, at $B \simeq 5$ T. The discrepancy at higher magnetic

Table 2. Spin Hamiltonian parameters obtained from combined analysis of HF-EPR and magnetisation data using equation 2.

	α	J_{V-Ln} (K)	$\tilde{g}_\perp$	θ (°)
$\mathbf{2}_{Tb}$	6	−2.84(4)	0.32	0(4)
$\mathbf{4}_{Ho}$	7	−0.55(11)	0.1	85(16)
$\mathbf{5}_{Er}$	6	−0.72(7)	0.32	60(8)
$\mathbf{6}_{Tm}$	6	−1.02(6)	0.15	45(5)

© 2023 Wiley-VCH GmbH

ChemistryEurope
Excellence in Chemistry Research Worldwide

Research Article
doi.org/10.1002/ceur.202500011

27514765, 2025, 3, Downloaded from https://chemistry-europe.onlinelibrary.wiley.com/doi/10.1002/ceur.202500011, Wiley Online Library on [22/06/2025]. See the Terms and Conditions (https://onlinelibrary.wiley.com/terms-and-conditions) on Wiley Online Library for rules of use; OA articles are governed by the applicable Creative Commons License

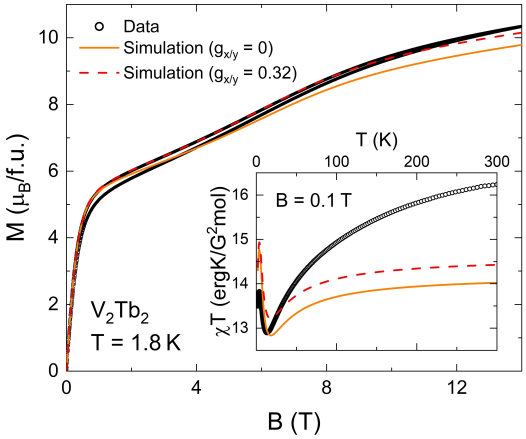


Figure 5. Isothermal magnetisation loop (0 T →7 T →0 T) of $\mathbf{2}_{Tb}$ at T = 1.8 K and simulations of the down-sweep using the strict Ising model (orange solid line) in equation 2 and an XXZ model (red dashed line) with the parameters shown in Table 2 (see the text). The inset depicts the measured and simulated $\chi T(T)$ at B = 0.1 T.

fields is likely associated with finite contributions from the transverse components of the Ln^{III} moments, *i.e.* their deviation from perfect Ising-spins in the fixed powder measurements. This can be modelled by introducing transversal components of the effective lanthanide g-tensor, such that $\tilde{g} = (\tilde{g}_{\perp}, \tilde{g}_{\perp}, g_{Ln})$. As seen in Figure 5, the experimental data are well simulated using this extended model with $\tilde{g}_{\perp} = 0.32$ over the entire magnetic field range.

Whereas the low-temperature χT-product of $\mathbf{2}_{Tb}$ (inset of Figure 5) can be fitted by the simulations using the same parameters as used for the $M(B)$ simulation, the Hamiltonian in equation 2 is not able to describe the χT-product at elevated temperatures. This is not unsurprising since the population of higher-lying m_J sub-levels means that the Ln^{III} moments no longer equate to Ising-spins. However, the qualitative behaviour of $\chi T(T)$, especially the position of the characteristic maximum at low and minimum at intermediate temperatures, is in line with this model.

An analogous analysis of combined HF-EPR and magnetisation data on $\mathbf{5}_{Er}$ and $\mathbf{6}_{Tm}$ (see Figure S2) results in the spin Hamiltonian parameters given in Table 2. In addition, despite showing no detectable HF-EPR signal, simulations of the magnetisation data also allow the determination of the microscopic parameters in $\mathbf{4}_{Ho}$, albeit with reduced accuracy.

Alternating Current (ac) Susceptibility

In order to probe their magnetic relaxation dynamics, ac susceptibility measurements with an oscillating field of $H_{ac} = 3$ Oe were performed on all investigated complexes. Compounds $\mathbf{2}_{Tb}$, $\mathbf{3}_{Dy}$ and $\mathbf{4}_{Ho}$ exhibit detectable out-of-phase (χ'') signals without applied dc field. Field-induced slow relaxation of the magnetisation with an applied dc field of 0.1 T could be observed for $\mathbf{6}_{Tm}$, suggesting that quantum tunnelling is the dominant relaxation mechanism when no external field is present. For all other compounds no χ'' signals could be observed in the accessible field and frequency range. The measured frequency dependence of the out-of-phase susceptibilities are shown in Figure 6. Apart from the measurement of $\mathbf{3}_{Dy}$ two distinct relaxation processes can clearly be discerned for all other compounds.

To corroborate this assignment, the data were fitted using a generalized Double-Debye-model, *i.e.* the sum of two Debye-relaxation functions

$$\chi_{ac}(f) = \sum_{n=1}^{2}\left(\chi_{S,n} + \frac{\chi_{T,n} - \chi_{S,n}}{1 + (if\tau_n)^{1-\alpha_n}}\right) \quad (3)$$

where χ_S and χ_T are the adiabatic and isothermal susceptibilities, τ denotes the relaxation time, and $0 < \alpha < 1$ qualitatively represents the distribution of relaxation times in the molecule. As can be seen from Figure 6 the chosen model describes the experimental results well. We note that one Debye function is not sufficient to reproduce the ac susceptibility of $\mathbf{3}_{Dy}$. This implies the presence of at least two relaxation processes with similar relaxation times. The nature of the underlying microscopic mechanisms leading to slow magnetic relaxation can be elucidated by the temperature dependence of τ. Qualitatively, the fast relaxation processes in $\mathbf{2}_{Tb}$, $\mathbf{4}_{Ho}$ and $\mathbf{6}_{Tm}$ shift to higher frequencies with increasing temperature, while the broad maximum in $\chi''(f)$ of $\mathbf{3}_{Dy}$ is almost temperature independent, indicative of dominant quantum tunnelling.

The relevance of under-barrier relaxation in $\mathbf{3}_{Dy}$ can also be seen from the μSQUID measurements depicted in Figure 7. At sub-Kelvin temperatures the single crystal $M(B)$ loops show a butterfly-shaped hysteresis which indicates fast zero field QTM and a slow thermal relaxation process in finite external

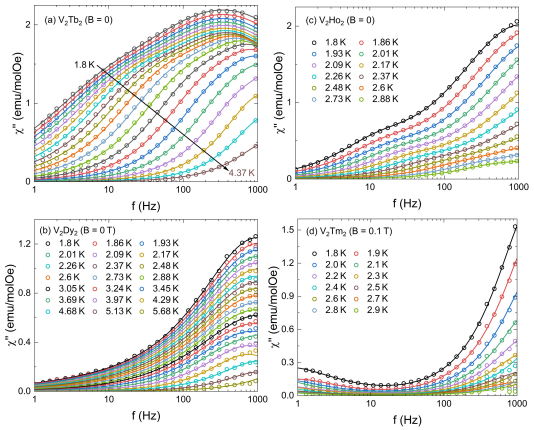


Figure 6. Out-of-phase ac susceptibility of $\mathbf{2}_{Tb}$ (a), $\mathbf{3}_{Dy}$ (b), $\mathbf{4}_{Ho}$ (c) and $\mathbf{6}_{Tm}$ (d) at selected temperatures. Solid lines depict fits of equation 3 to the data as described in the text. Corresponding in-phase ac susceptibility data and Cole-Cole plots are shown in the Supplementary Material.

© 2023 Wiley-VCH GmbH

ChemistryEurope
Excellence in Chemistry Research Worldwide

Research Article
doi.org/10.1002/ceur.202500011

27514765, 2025, 3, Downloaded from https://chemistry-europe.onlinelibrary.wiley.com/doi/10.1002/ceur.202500011, Wiley Online Library on [22/06/2025]. See the Terms and Conditions (https://onlinelibrary.wiley.com/terms-and-conditions) on Wiley Online Library for rules of use; OA articles are governed by the applicable Creative Commons License

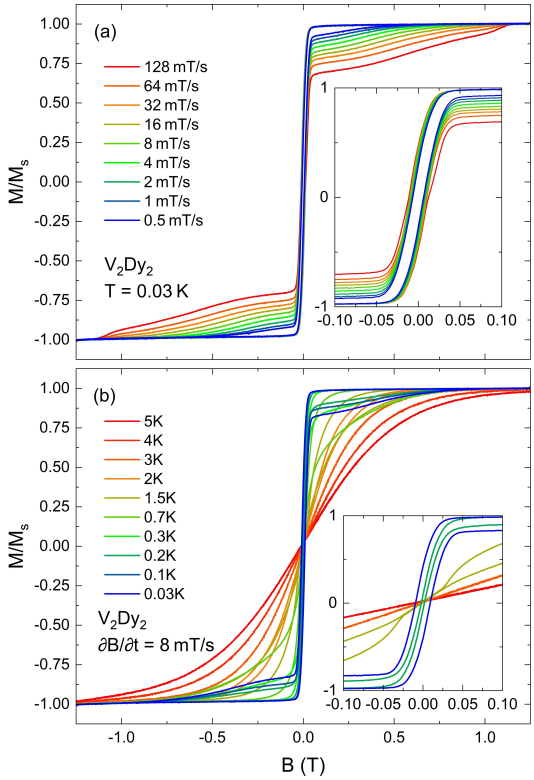


Figure 7. *M*(*B*) measurements on a single crystal of $\mathbf{3}_{Dy}$, at fixed bath temperature $T = 0.03$ K and different sweep rates of magnetic field (a), and fixed sweep rate $\partial B/\partial t = 8$ mT/s and different bath temperatures (b). The insets show the enlarged version of corresponding figures considering only a few curves for clarity.

magnetic fields. In agreement with our ac susceptibility data, even the fastest field scan rate of $\partial B/\partial t = 128$ mT/s yields only a small remanent magnetisation (Figure 7(a)). However, the magnetisation loops remain open (Figure 7(a) inset) with a small coercive field for all sweep rates. SMM behaviour in $\mathbf{3}_{Dy}$ at such low temperatures probably arises as a result of small effective internal fields originating from intramolecular magnetic interactions. Upon heating from the lowest temperatures (Figure 7(b)), the hysteresis region initially shrinks as it is expected when the contribution of temperature dependent relaxation processes increases. Interestingly, the inverse effect, i.e., widening of the hysteresis on increasing the temperature, can be observed in the temperature range $0.2\ \text{K} < T < 0.9\ \text{K}$. This is not a rare observation in low temperature *M*(*B*) measurements when QTM and thermal relaxation times compete at an avoided level crossing region.[52–53] While the overall shape of the *M(B)* loops at 30 mK is consistent with a predominantly ferromagnetic character, a magnetisation plateau appears near zero field as the bath temperature is increased (cf. *M(B,T = 1.5 K)* in the inset of Figure 7(b)). Using the exchange field approach,[53] an antiferromagnetic Dy–Dy coupling of $J_{Dy\text{-}Dy} = -6(1)$ mK can be read off the data (for a more detailed analysis and discussion see the SI).

A more quantitative investigation of the magnetic relaxation can be provided for both relaxation processes in $\mathbf{2}_{Tb}$ and for the slow process in $\mathbf{4}_{Ho}$ from a plot of τ vs T (cf. Figure 8) using the relaxation times extracted from the Debye fits. The linearity of $\ln(\tau)$ vs $1/T$ at high temperatures implies the presence of Orbach and/or slow Raman relaxation. In contrast, faster relaxation mechanisms, such as quantum tunnelling or fast Raman relaxation, dominate at low temperatures. We fit our data over the whole temperature range using

$$\tau^{-1} = \tau_{QTM}^{-1} + \tau_R^{-1}\frac{e^{-W/k_BT}}{(1+e^{-W/k_BT})^2} + \tau_O^{-1}e^{-U_O/k_BT} \quad (4)$$

Here, the first term denotes the temperature independent quantum tunnelling of magnetisation, the second term describes Raman relaxation involving only energetically low-lying optical phonons as suggested independently by Gu and Wu and by Lunghi *et al.*[54–56] and the third term represents Orbach relaxation. The resulting fit parameters, summarised in Table 3, indicate that at low temperatures quantum tunnelling is the main contribution to the fast relaxation process in $\mathbf{2}_{Tb}$, whereas the slower process is dominated by slow Raman relaxation. This finding is further corroborated by ac susceptibility measurements under a 0.1 T dc field showing that only one relaxation process is visible, which is mainly governed by Orbach and Raman relaxation (see Supplementary Material). At

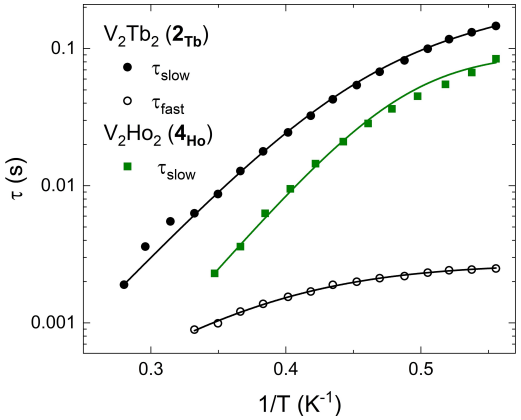


Figure 8. Temperature dependence of the relaxation times in $\mathbf{2}_{Tb}$ and $\mathbf{4}_{Ho}$ in the absence of an external static magnetic field. Solid lines depict fits to the data using equation 4 as described in the text.

Table 3. Parameters obtained by the fit of the temperature dependence of the relaxation times in $\mathbf{2}_{Tb}$ and $\mathbf{4}_{Ho}$ using equation 4.

	τ_{QTM} (s)	τ_R (s)	W (K)	τ_O (s)	U_O (K)
$\mathbf{2}_{Tb}$ - τ_{fast}	2.7×10^{-3}			1.0×10^{-5}	14.6
$\mathbf{2}_{Tb}$ - τ_{slow}		1.06	0.7	2.6×10^{-6}	23.6
$\mathbf{4}_{Ho}$ - τ_{slow}	0.1			3.1×10^{-7}	25.8

© 2023 Wiley-VCH GmbH

ChemistryEurope
Excellence in Chemistry Research Worldwide

Research Article
doi.org/10.1002/ceur.202500011

27514765, 2025, 3, Downloaded from https://chemistry-europe.onlinelibrary.wiley.com/doi/10.1002/ceur.202500011, Wiley Online Library on [22/06/2025]. See the Terms and Conditions (https://onlinelibrary.wiley.com/terms-and-conditions) on Wiley Online Library for rules of use; OA articles are governed by the applicable Creative Commons License

elevated temperatures magnetic relaxation happens predominantly *via* Orbach relaxation with effective barriers of U_{eff} = 14.6 K, 23.6 K (fast and slow process $\mathbf{2}_{Tb}$), and 25.8 K ($\mathbf{4}_{Ho}$), for the three sets of relaxation processes shown in Figure 8. These values are comparable to the barrier heights observed in other butterfly-shaped heterometallic 3d–4f complexes.[21]

The absence of a χ'' signal in $\mathbf{1}_Y$ directly indicates that slow magnetic relaxation in the V_2Ln_2 compounds can only be observed when paramagnetic Ln^{III} ions are present. Hence, a number of conclusions can be drawn from the presented ac susceptibility data: (i) Slow magnetic relaxation in zero field occurs only in $\mathbf{2}_{Tb}$, $\mathbf{3}_{Dy}$ and $\mathbf{4}_{Ho}$, implying that the ligand field around the Ln^{III} ions is more suitable for oblate charge distributions. (ii) Despite being predominantly prolate, the 4f-orbitals of Tm^{III} in $\mathbf{6}_{Tm}$ experience a considerable axial crystal field anisotropy, such that only small external magnetic fields are needed to suppress quantum tunnelling. (iii) Sizable magnetic coupling to the V^{III} moments is not sufficient to slow down the magnetic relaxation to the Hz or even sub-Hz scale.

Discussion

The discussion of 3*d*–4*f* coupling beyond dipole-dipole-interaction in the literature was initially based on a model proposed for a Gd_2Cu_4 complex by Kahn *et al.*[49] with similar ideas being reported by Gatteschi *et al.*.[57–58] In summary, the 3*d*–4*f* superexchange interaction arises from two distinct exchange mechanisms. The first of these is electron transfer from the occupied 3*d* orbitals of the transition metal ion into the empty 5*d* orbitals of the lanthanide favouring a ferromagnetic spin alignment due to enhanced Hund's coupling in the charge transfer state, as long as the 4*f* shell is at least half-filled.[49] The second is excitation of the transition metal 3*d* electrons into the partially filled lanthanide 4*f* orbitals leading to either a ferromagnetic or an antiferromagnetic contribution to $J_{3d\text{-}4f}$ depending on whether the corresponding orbitals are orthogonal to each other or overlap. Taking into account the influence of single ion anisotropy on the 3*d* orbitals, this model was further developed to include also other transition metal ions with $S > 1/2$.[6,14–15] Considering the magnitude of $J_{V\text{-}Ln}$ obtained from HF-EPR (Table 2), it becomes evident that dipolar interactions are negligible. Hence, the observation of antiferromagnetic interaction implies that electron exchange between 3*d* and 4*f* orbitals is the dominant coupling mechanism. This finding can be rationalised by the predominant π-character of the occupied V^{III} t_{2g} orbitals, which renders the ferromagnetic σ-type 3*d*–5*f* charge transfer rather inefficient[59] and favours direct orbital overlap with the Ln^{III} 4*f* orbitals.[60]

Figure 9(a) summarises the results of our HF-EPR studies by showing the dependence of $J_{V\text{-}Ln}$ and θ on the lanthanide ion. Of the studied complexes $\mathbf{2}_{Tb}$ exhibits the largest magnetic interaction between V^{III} and Ln^{III} moments. This coupling becomes significantly weaker when Tb^{III} is replaced by Ho^{III} and subsequently increases for the heavier lanthanides Er^{III} and Tm^{III}. Interestingly, the relative angle between the vanadium and lanthanide main anisotropy axes θ exhibits the inverse trend.

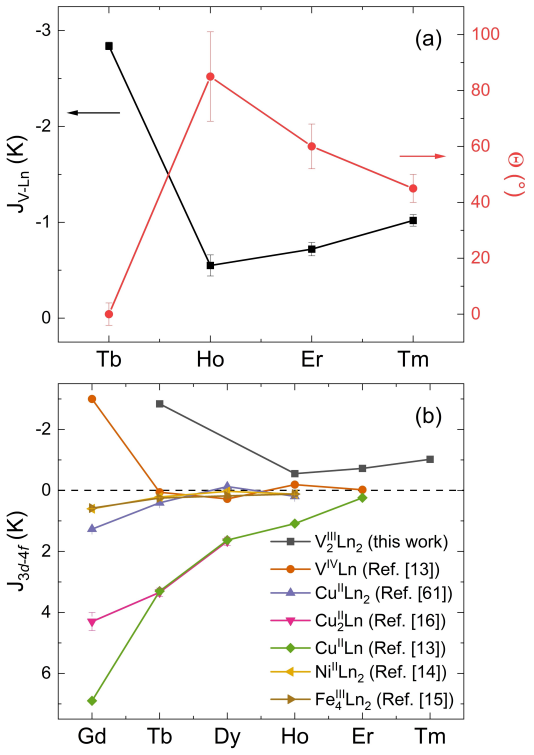


Figure 9. (a) Chemical trend of the V^{III}-Ln^{III} coupling constant and of the relative angle between the main anisotropy axes (see equation 2) as determined by HF-EPR. (b) Experimentally determined $J_{3d\text{-}4f}$ in different heterometallic complexes as reported in recent HF-EPR studies.

According to Kahn's model[49] the ferromagnetic contribution to $J_{V\text{-}Ln}$ is expected to decrease with increasing atomic number from Gd^{III} onwards as the amount of unpaired 4*f* electrons, and hence Hund's coupling in the charge transfer state $4f^n5d^1$, decreases along the series. While this mechanism qualitatively rationalises the increase of overall antiferromagnetic coupling from Ho^{III} to Tm^{III}, the finding of $\mathbf{2}_{Tb}$ exhibiting the largest $J_{V\text{-}Ln}$ represents an outlier. The reason for this is (likely) to be the decreasing orbital overlap between the partially filled 3*d* and 4*f* orbitals due to a rotation of the Ln^{III} easy anisotropy axis (see Figure 9). A similar mechanism has been found to explain the dependence of $J_{Cr\text{-}Gd}$ on the Cr-F–Gd bond angle in $Cr^{III}Gd^{III}$ complexes, where the 3*d*–4*f* orbital overlap is mainly varied by a rotation of the Cr^{III} anisotropy tensor via changes in the ligand field.[59]

In the literature, HF-EPR has established itself as the main method of choice for quantitative experimental determination of 3*d*–4*f* coupling.[14–16,50–51,61–62] An overview of the $J_{M\text{-}Ln}$ (M = transition metal) in different heterometallic complexes as obtained in recent HF-EPR studies is given in Table 4 and visualised in Figure 9(b). In most of the investigated compounds, namely those with Cu^{II}, Ni^{II} and Fe^{III} as the 3*d* ion, ferromagnetic 3*d*–4*f* interaction is found and rationalised by a

© 2023 Wiley-VCH GmbH

ChemistryEurope
Excellence in Chemistry Research Worldwide

Research Article
doi.org/10.1002/ceur.202500011

27514765, 2025, 3, Downloaded from https://chemistry-europe.onlinelibrary.wiley.com/doi/10.1002/ceur.202500011, Wiley Online Library on [22/06/2025]. See the Terms and Conditions (https://onlinelibrary.wiley.com/terms-and-conditions) on Wiley Online Library for rules of use; OA articles are governed by the applicable Creative Commons License

Table 4. Magnetic 3*d*–4*f* coupling in selected heterometallic molecular complexes as reported here and in the literature.

	J_{M-Ln} (K)						
Ln =	Gd	Tb	Dy	Ho	Er	Tm	Ref.
$V^{III}_2Ln_2$		−2.84(4)		−0.55(11)	−0.72(7)	−1.02(6)	this work
$V^{IV}Ln$	−3.0	0.06(1)	0.28(1)	−0.19	−0.02(1)		13
$Cu^{II}Ln_2$	1.271(7)	0.405(3)	−0.126(3)	0.196(13)			61
Cu^{II}_2Ln	4.3(3)	3.34(14)	1.67(14)				16
$Cu^{II}Ln$	6.9	> 3.3	1.63(1)	1.09(2)	0.24(1)		13
$Ni^{II}Ln_2$	0.602(8)	0.216(12)	0.031	0.122(3)			14
$Fe^{III}_4Ln_2$	0.58	0.25(5)	0.18(8)	0.12(8)			15

dominance of the 3*d* to 5*d* charge transfer process.[13–16,61] In contrast, the results on V^{III}-based butterfly complexes presented here evidence antiferromagnetic coupling between the 3*d* and 4*f* moments, which has also been observed in dinuclear V^{IV}-Ln molecules.[13] As mentioned above, the qualitative differences probably arise from different spatial distributions of the contributing 3*d* orbitals, *e.g.*, $3d_{x^2-y^2}$ for Cu^{II} and $3d_{xy}$ for $V^{IV/III}$, that determine the absence or presence of overlap with the Ln^{III} orbitals.[59–60] Similarly, the size of $J_{M\text{-}Ln}$ depends on the coordination geometry and on the influence of other magnetic orbitals in the corresponding electronic configuration. Whereas the expected chemical trend of decreasing $J_{M\text{-}Ln}$ for heavier lanthanide ions is generally confirmed by the experimental data, the studies are usually restricted to the series $Ln^{III} = Ce^{III}$-Ho^{III}. Here, we expand this range to include the Ln^{III} ions beyond Gd^{III} with prolate electron density distribution, *i.e.* Er^{III} and Tm^{III}. In fact, the two regimes observed in Figure 9 can be related to the 4*f* anisotropy shape for the later Ln^{III} ions: For the oblate Ln ions $J_{V\text{-}Ln}$ weakens with the Ln atomic number, but increases upon the series when the 4*f* electron distribution exhibits a prolate shape. The correlation of 4*f* anisotropy shape and magnetic 3*d*–4*f* coupling in the $V^{III}_2Ln_2$ butterfly series can be rationalised by considering changes in the Ln^{III} anisotropy axis. This leads to variation in orbital overlap as a result of ligand field effects, as described earlier.

Conclusions

We report the successful synthesis of a series of butterfly-motif $V^{III}_2Ln^{III}_2$ ($Ln^{III} = Tb^{III}$-Yb^{III}, Y^{III}) complexes and their magnetic characterisation *via* combined magnetic SQUID, μSQUID and HF-EPR studies. In particular, our analysis allows us to quantify 3*d*–4*f* coupling by treating the Ln^{III} moments as essentially Ising spins. Unlike for other 3*d*–4*f* complexes, $J_{V\text{-}Ln}$ does not monotonically decrease upon increasing Ln atomic number but is shown to exhibit opposite effects for oblate and prolate Ln 4*f* orbital distributions. This trend is rationalised through the variation in orbital overlap due to a rotation of the Ln^{III} anisotropy axis. The important role of 4*f* anisotropy shape is also confirmed by the ac susceptibility data which show the absence of slow magnetic relaxation in zero field for prolate Ln^{III} ions.

Supporting Information

The authors have referred to reference[53] and reference[39] and cited an additional reference within the Supporting Information.[63]

Details of the syntheses and crystallography together with Bond Valence Sum analyses and additional magnetic and HF-EPR data are provided in the Supplementary Information. Full crystallographic data and details of the structural determinations for the structures in this paper have been deposited with the Cambridge Crystallographic Data Centre as supplementary publication nos. CCDC 2406392–2406398. Copies of the data can be obtained, free of charge, from https://www.ccdc.cam.ac.uk/structures/

Acknowledgements

Measurements were supported by Deutsche Forschungsgemeinschaft (DFG) under Germany's Excellence Strategy EXC2181/1-390900948 (the Heidelberg STRUCTURES Excellence Cluster). J. A. acknowledges support by the International Max-Planck Research School for Quantum Dynamics (IMPRS-QD) Heidelberg. X.L., J.B., C.E.A and A.K.P acknowledge funding from the DFG CRC 1573 "4f for Future" and the Helmholtz Foundation POF MSE. X.-F.L. thanks the China Scholarship Council (CSC) for a scholarship. W.W. thanks the German Research Foundation (DFG) for the Gottfried Wilhelm Leibniz-Award, ZVN-2020_WE 4458-5.

Conflict of Interests

The authors declare no conflict of interest.

Data Availability Statement

Full crystallographic data and details of the structural determinations for the structures in this paper have been deposited with the Cambridge Crystallographic Data Centre as supplementary publication nos. CCDC 2406392-2406398. Copies of the data can be obtained, free of charge, from https://www.ccdc.ca-

© 2023 Wiley-VCH GmbH

ChemistryEurope
Excellence in Chemistry Research Worldwide

Research Article
doi.org/10.1002/ceur.202500011

27514765, 2025, 3, Downloaded from https://chemistry-europe.onlinelibrary.wiley.com/doi/10.1002/ceur.202500011, Wiley Online Library on [22/06/2025]. See the Terms and Conditions (https://onlinelibrary.wiley.com/terms-and-conditions) on Wiley Online Library for rules of use; OA articles are governed by the applicable Creative Commons License

m.ac.uk/structures/. Magnetic data is available on request from the corresponding author.

Keywords: 3d–4f Compounds · Exchange Interactions · HF-EPR · Magnetic Properties · Relaxation Mechanisms

[1] R. Sessoli, D. Gatteschi, A. Caneschi, M. A. Novak, *Nature* **1993**, *365*, 141–143.
[2] T. Kido, Y. Ikuta, Y. Sunatsuki, Y. Ogawa, N. Matsumoto, N. Re, *Inorg. Chem.* **2002**, *42*, 398–408.
[3] S. Osa, T. Kido, N. Matsumoto, N. Re, A. Pochaba, J. Mrozinski, *J. Am. Chem. Soc.* **2004**, *126*, 420–421.
[4] L. R. Piquer, E. C. Sanudo, *Dalton Trans.* **2015**, *44*, 8771–8780.
[5] X. L. Li, F. Y. Min, C. Wang, S. Y. Lin, Z. Liu, J. Tang, *Inorg. Chem.* **2015**, *54*, 4337–4344.
[6] T. Gupta, M. F. Beg, G. Rajaraman, *Inorg. Chem.* **2016**, *55*, 11201–11215.
[7] S. K. Singh, M. F. Beg, G. Rajaraman, *Chem. Eur. J.* **2016**, *22*, 672–680.
[8] S. K. Langley, D. P. Wielechowski, V. Vieru, N. F. Chilton, B. Moubaraki, B. F. Abrahams, L. F. Chibotaru, K. S. Murray, *Angew. Chem. Int. Ed.* **2013**, *52*, 12014–12019.
[9] S. K. Langley, D. P. Wielechowski, V. Vieru, N. F. Chilton, B. Moubaraki, L. F. Chibotaru, K. S. Murray, *Chem. Sci.* **2014**, *5*, 3246–3256.
[10] Y. Peng, M. K. Singh, V. Mereacre, C. E. Anson, G. Rajaraman, A. K. Powell, *Chem. Sci.* **2019**, *10*, 5528–5538.
[11] J. Rinck, G. Novitchi, W. Van den Heuvel, L. Ungur, Y. Lan, W. Wernsdorfer, C. E. Anson, L. F. Chibotaru, A. K. Powell, *Angew. Chem. Int. Ed.* **2010**, *49*, 7583–7587.
[12] J. L. Liu, J. Y. Wu, Y. C. Chen, V. Mereacre, A. K. Powell, L. Ungur, L. F. Chibotaru, X. M. Chen, M. L. Tong, *Angew. Chem. Int. Ed.* **2014**, *53*, 12966–12970.
[13] R. Watanabe, K. Fujiwara, A. Okazawa, G. Tanaka, S. Yoshii, H. Nojiri, T. Ishida, *Chem. Commun.* **2011**, *47*, 2110–2112.
[14] A. Okazawa, T. Shimada, N. Kojima, S. Yoshii, H. Nojiri, T. Ishida, *Inorg. Chem.* **2013**, *52*, 13351–13355.
[15] S. F. M. Schmidt, C. Koo, V. Mereacre, J. Park, D. W. Heermann, V. Kataev, C. E. Anson, D. Prodius, G. Novitchi, R. Klingeler, A. K. Powell, *Inorg. Chem.* **2017**, *56*, 4796–4806.
[16] N. Ahmed, T. Sharma, L. Spillecke, C. Koo, K. U. Ansari, S. Tripathi, A. Caneschi, R. Klingeler, G. Rajaraman, M. Shanmugam, *Inorg. Chem.* **2022**, *61*, 5572–5587.
[17] F. J. Kettles, V. A. Milway, F. Tuna, R. Valiente, L. H. Thomas, W. Wernsdorfer, S. T. Ochsenbein, M. Murrie, *Inorg. Chem.* **2014**, *53*, 8970–8978.
[18] X. Wang, S. Q. Wang, J. N. Chen, J. H. Jia, C. Wang, K. Paillot, I. Breslavetz, L. S. Long, L. Zheng, G. Rikken, C. Train, X. J. Kong, M. Atzori, *J. Am. Chem. Soc.* **2022**, *144*, 8837–8847.
[19] T. D. Kang, E. C. Standard, P. D. Rogers, K. H. Ahn, A. A. Sirenko, A. Dubroka, C. Bernhard, S. Park, Y. J. Choi, S. W. Cheong, *Phys. Rev. B* **2012**, *86*, 144112.
[20] S. K. Langley, L. Ungur, N. F. Chilton, B. Moubaraki, L. F. Chibotaru, K. S. Murray, *Inorg. Chem.* **2014**, *53*, 4303–4315.
[21] S. K. Langley, D. P. Wielechowski, N. F. Chilton, B. Moubaraki, K. S. Murray, *Inorg. Chem.* **2015**, *54*, 10497–10503.
[22] E. Moreno Pineda, N. F. Chilton, F. Tuna, R. E. Winpenny, E. J. McInnes, *Inorg. Chem.* **2015**, *54*, 5930–4591.
[23] Y. Peng, H. Kaemmerer, A. K. Powell, *Chem. Eur. J.* **2021**, *27*, 15043–15065.
[24] Y. Peng, A. K. Powell, *Coord. Chem. Rev.* **2021**, *426*, 213490.
[25] G. M. Sheldrick, *Acta Crystallogr. Sect. A* **2015**, *71*, 3–8.
[26] G. M. Sheldrick, *Acta Crystallogr. Sect. C* **2015**, *71*, 3–8.
[27] O. V. Dolomanov, L. J. Bourhis, R. J. Gildea, J. A. K. Howard, H. Puschmann, *J. Appl. Crystallogr.* **2009**, *42*, 339–341.
[28] G. A. Bain, J. F. Berry, *J. Chem. Educ.* **2008**, *85*, 532–536.
[29] N. F. Chilton, R. P. Anderson, L. D. Turner, A. Soncini, K. S. Murray, *J. Comput. Chem.* **2013**, *34*, 1164–1175.
[30] W. Wernsdorfer, N. E. Chakov, G. Christou, *Phys. Rev. B* **2004**, *70*, 132413.
[31] W. Wernsdorfer, *Supercond. Sci. Technol.* **2009**, *22*, 064013.
[32] P. Comba, M. Grosshauser, R. Klingeler, C. Koo, Y. Lan, D. Muller, J. Park, A. Powell, M. J. Riley, H. Wadepohl, *Inorg. Chem.* **2015**, *54*, 11247–11258.
[33] J. Werner, W. Hergett, M. Gertig, J. Park, C. Koo, R. Klingeler, *Phys. Rev. B* **2017**, *95*, 214414.
[34] A. L. Barra, P. Debrunner, D. Gatteschi, C. E. Schulz, R. Sessoli, *Europhys. Lett.* **1996**, *35*, 133–138.
[35] D. P. Goldberg, J. Telser, J. Kryzstek, A. G. Montalban, L.-C. Brunel, A. G. M. Barett, B. M. Hoffman, *J. Am. Chem. Soc.* **1997**, *119*, 8722–8723.
[36] L. Spillecke, C. Koo, O. Maximova, V. S. Mironov, V. A. Kopotkov, D. V. Korchagin, A. N. Vasiliev, E. B. Yagubskii, R. Klingeler, *Dalton Trans.* **2021**, *50*, 18143–18154.
[37] L. Spillecke, S. Tripathi, C. Koo, M. Ansari, S. Vaidya, A. Rasamsetty, T. Mallah, G. Rajaraman, M. Shanmugam, R. Klingeler, *Polyhedron* **2021**, *208*, 115389.
[38] S. Stoll, A. Schweiger, *J. Magn. Reson.* **2006**, *178*, 42–55.
[39] W. Liu, H. H. Thorp, *Inorg. Chem.* **1993**, *32*, 4102–4105.
[40] J. Krzystek, A. T. Fiedler, J. J. Sokol, A. Ozarowski, S. A. Zvyagin, T. C. Brunold, J. R. Long, L.-C. Brunel, J. Telser, *Inorg. Chem.* **2004**, *43*, 5654–5658.
[41] R. Beaulac, P. L. W. Tregenna-Piggott, A.-L. Barra, H. Weihe, D. Luneau, C. Reber, *Inorg. Chem.* **2006**, *45*, 3399–3407.
[42] J. Krzystek, A. Ozarowski, J. Telser, D. C. Crans, *Coord. Chem. Rev.* **2015**, *301–302*, 123–133.
[43] T. A. Bazhenova, L. V. Zorina, S. V. Simonov, V. S. Mironov, O. V. Maximova, L. Spillecke, C. Koo, R. Klingeler, Y. V. Manakin, A. N. Vasiliev, E. B. Yagubskii, *Dalton Trans.* **2020**, *49*, 15287–15298.
[44] M. R. Saber, K. Thirunavukkuarasu, S. M. Greer, S. Hill, K. R. Dunbar, *Inorg. Chem.* **2020**, *59*, 13262–13269.
[45] Z. Janas, J. Jezierska, A. Ozarowski, A. Bienko, T. Lis, A. Jezierski, M. Krawczyk, *Dalton Trans.* **2021**, *50*, 5184–5196.
[46] J. Tang, P. Zhang, *Lanthanide Single Molecule Magnets*, Springer Verlag, Berlin Heidelberg, **2015**.
[47] A. Abragam, B. Bleaney, *Electron Paramagnetic Resonance of Transition Ions*, Oxford University Press, Oxford, **2012**.
[48] P. Bertrand, *Electron Paramagnetic Resonance Spectroscopy - Fundamentals*, Springer Nature, Cham, **2020**.
[49] M. Andruh, I. Ramade, E. Codjovi, O. Guillou, O. Kahn, J. C. Trombe, *J. Am. Chem. Soc.* **1993**, *115*, 1822–1829.
[50] R. T. Galeev, L. V. Mingalieva, A. A. Sukhanov, V. K. Voronkova, Y. Peng, A. K. Powell, *Appl. Magn. Reson.* **2019**, *50*, 1429–1441.
[51] P. Comba, M. Enders, M. Grosshauser, M. Hiller, R. Klingeler, C. Koo, D. Muller, G. Rajaraman, A. Swain, M. Tavhelidse, H. Wadepohl, *Chem. Eur. J.* **2021**, *27*, 9372–9382.
[52] E. Moreno-Pineda, G. Taran, W. Wernsdorfer, M. Ruben, *Chem. Sci.* **2019**, *10*, 5138–5145.
[53] Z. Zhu, S. Paul, C. Zhao, J. Wu, X. Ying, L. Ungur, W. Wernsdorfer, F. Meyer, J. Tang, *J. Am. Chem. Soc.* **2024**, *146*, 18899–18904.
[54] L. Gu, R. Wu, *Phys. Rev. Lett.* **2020**, *125*, 117203.
[55] M. Briganti, F. Santanni, L. Tesi, F. Totti, R. Sessoli, A. Lunghi, *J. Am. Chem. Soc.* **2021**, *143*, 13633–13645.
[56] L. Gu, R. Wu, *Phys. Rev. B* **2021**, *103*, 014401.
[57] A. Bencini, C. Benelli, A. Caneschi, R. L. Carlin, A. Dei, D. Gatteschi, *J. Am. Chem. Soc.* **1985**, *107*, 8128–8136.
[58] G. Rajaraman, F. Totti, A. Bencini, A. Caneschi, R. Sessoli, D. Gatteschi, *Dalton Trans.* **2009**, 3153–3161.
[59] S. K. Singh, K. S. Pedersen, M. Sigrist, C. A. Thuesen, M. Schau-Magnussen, H. Mutka, S. Piligkos, H. Weihe, G. Rajaraman, J. Bendix, *Chem. Commun.* **2013**, *49*, 5583–5585.
[60] S. K. Singh, G. Rajaraman, *Dalton Trans.* **2013**, *42*, 3623–3630.
[61] A. Okazawa, R. Watanabe, M. Nezu, T. Shimada, S. Yoshii, H. Nojiri, T. Ishida, *Chem. Lett.* **2010**, *39*, 1331–1332.
[62] T. Ishida, R. Watanabe, K. Fujiwara, A. Okazawa, N. Kojima, G. Tanaka, S. Yoshii, H. Nojiri, *Dalton Trans.* **2012**, *41*, 13609–13619.
[63] C. F. Macrae, I. Sovago, S. J. Cottrell, P. T. A. Galek, P. McCabe, E. Pidcock, M. Platings, G. P. Shields, J. S. Stevens, M. Towler, P. A. Wood, *J. Appl. Crystallogr.* **2020**, *53*, 226–235.

Version of record online: April 11, 2025

© 2023 Wiley-VCH GmbH

ChemistryEurope

Supporting Information

The Interplay of Single Ion Anisotropy and Magnetic 3*d*-4*f* Interactions in $V^{III}_2Ln^{III}_2$ Butterfly Complexes

Jan Arneth,* Xian-Feng Li, Jonas Braun,* Sagar Paul, Michael Schulze, Christopher E. Anson, Wolfgang Wernsdorfer, Annie K. Powell,* and Rüdiger Klingeler*

The Interplay of Single Ion Anisotropy and Magnetic 3d-4f Interactions in $V^{III}_2Ln^{III}_2$ Butterfly Complexes

Jan Arneth,*[a]# Xian-Feng Li,[b]# Jonas Braun,*[b,c,d] Sagar Paul,[e] Michael Schulze,[e] Christopher E. Anson,[b] Wolfgang Wernsdorfer,[d,e] Annie K. Powell,*[b,c,d] Rüdiger Klingeler*[a]

These authors have contributed equally

Corresponding authors: jan.arneth@kip.uni-heidelberg.de, jonas.braun2@kit.edu, annie.powell@kit.edu and ruediger.klingeler@kip.uni-heidelberg.de

Table of Contents

1. Experimental 2
2. Bond Valence Sum (BVS) Analysis 7
3. Additional Magnetic Data 8
4. Additional HF-EPR Data 11

1. Experimental

1.1 Methods

Powder X-ray diffraction measurements were performed on a STOE STADI-P equipped with a Cu-Kα source with a characteristic wavelength of 1.5405 Å. Elemental analysis was performed on an Elementar Vario MicroCube. IR spectroscopy was performed on a Nicolet iS 50 with ATR attachment.

1.2 Synthesis

$LnCl_3 \cdot 6H_2O$ salts were produced using hydrochloric acid and the respective Ln oxide. All other reagents were obtained from commercial sources and used without further purification. All reactions were performed under the exclusion of oxygen using standard Schlenk techniques. Although the reaction solution is sensitive to oxidation, crystalline products were air stable.

$[V_2Ln_2(\mu_3\text{-}OMe)_2(^t Budea)_2(piv)_6]$

A solution of *N-tert*-butyl-diethanolamine (^{t}Bu-H_2dea) (1 mmol, 161.3 mg) in 5 ml MeCN was added to a solution of VCl_3 (0.5 mmol, 78.7 mg), $LnCl_3 \cdot 6H_2O$ (0.5 mmol) and pivalic acid (Hpiv) (4 mmol, 296.5 mg) in 16 ml of a 1:1 mixture of MeOH and MeCN under Schlenk conditions. After 10 minutes of stirring, 1 ml of Et_3N was added and the resulting mixture stirred for 24 hours at RT. Subsequently, the solution was filtered and left undisturbed for crystallisation. The products were obtained as purple crystals suitable for single crystal X-ray diffraction.

1_Y was obtained in a yield of 96.5 mg (0.073 mmol = 29% based on Y^{III}).
Anal. Calc (found) % for $V_2Y_2C_{48}H_{94}N_2O_{18} \cdot 2CH_3OH$: C, 45.11 (44.87); H, 7.72 (7.55); N, 2.10 (2.01).
Selected IR data (cm^{-1}): 2960 (m), 2926 (w), 2871 (w), 1560 (m), 1528 (w), 1481 (m), 1411 (m), 1375 (m), 1359 (m), 1226 (m), 1089 (w), 1089 (w), 1026 (w), 896 (w), 600 (w), 495 (w), 459 (w), 427 (w).

2_{Tb} was obtained in a yield of 198.6 mg (0.135 mmol = 54% based on Tb^{III}).
Anal. Calc (found) % for $V_2Tb_2C_{48}H_{94}N_2O_{18} \cdot 2CH_3OH$: C, 40.82 (40.73); H, 6.99 (7.03); N, 1.90 (1.87).
Selected IR data (cm^{-1}): 2960 (m), 2925 (w), 1563 (m), 1524 (w), 1481 (m), 1458 (w), 1409 (m), 1375 (m), 1359 (m), 1260 (w), 1225 (m), 1086 (m), 1049 (w), 1018 (w), 894 (w), 793 (m), 598 (w), 494 (w), 457 (w), 422 (w).

3_{Dy} was obtained in a yield of 229.1 mg (0.155 mmol = 62% based on Dy^{III}).
Anal. Calc (found) % for $V_2Dy_2C_{48}H_{94}N_2O_{18} \cdot 2CH_3OH$: C, 40.63 (40.59); H, 6.95 (6.70); N, 1.90 (1.83).
Selected IR data (cm^{-1}): 2960 (w), 2925 (w), 2870 (w), 1561 (m), 1527 (w), 1482 (m), 1409 (m), 1375 (w), 1359 (w), 1226 (w), 1088 (w), 1019 (w), 895 (w), 895 (w), 753 (w), 598 (w).

4_{Ho} was obtained in a yield of 167.6 mg (0.113 mmol = 45% based on Ho^{III}).
Anal. Calc (found) % for $V_2Ho_2C_{48}H_{94}N_2O_{18} \cdot 2CH_3OH$: C, 40.49 (40.38); H, 6.93 (6.87); N, 1.89 (1.82).
Selected IR data (cm^{-1}): 2956 (m), 2926 (w), 2867 (w), 1591 (m), 1569 (s), 1533 (w), 1481 (m), 1428 (m), 1407 (s), 1374 (m), 1358 (m), 1225 (m), 1097 (m), 1082 (w), 1021 (m), 909 (w), 896 (w), 794 (w), 601 (w), 580 (w), 497 (w), 462 (w), 427 (w).

5_{Er} was obtained in a yield of 160.7 mg (0.108 mmol = 43% based on Er^{III}).
Anal. Calc (found) % for $V_2Er_2C_{48}H_{94}N_2O_{18} \cdot 2CH_3OH$: C, 40.37 (40.31); H, 6.91 (6.84); N, 1.88 (1.84).
Selected IR data (cm^{-1}): 2962 (m), 2928 (w), 2871 (w), 1591 (m), 1571 (s), 1531 (w), 1481 (m), 1429 (m), 1409 (s), 1374 (m), 1359 (m), 1229 (m), 1099 (m), 1084 (w), 1027 (m), 909 (w), 899 (w), 798 (w), 601 (w), 585 (w), 497 (w), 466 (w), 427 (w).

6_{Tm} was obtained in a yield of 183.4 mg (0.123 mmol = 49% based on Tm^{III}).
Anal. Calc (found) % for $V_2Tm_2C_{48}H_{94}N_2O_{18}{\cdot}2CH_3OH$: C, 40.24 (40.15); H, 6.89 (6.74); N, 1.88 (1.74).
Selected IR data (cm^{-1}): 2959 (w), 2926 (w), 1562 (m), 1530 (w), 1481 (m), 1410 (m), 1375 (w), 1359 (w), 1226 (w), 1090 (w), 896 (w), 601 (w).

7_{Yb} was obtained in a yield of 119.9 mg (0.08 mg = 32% based on Yb^{III}).
Anal. Calc (found) % for $V_2Yb_2C_{48}H_{94}N_2O_{18}{\cdot}2CH_3OH$: C, 40.05 (39.41); H, 6.85 (6.75); N, 1.87 (1.76).
Selected IR data (cm^{-1}): 2961 (w), 2927 (w), 1563 (m), 1532 (w), 1482 (m), 1410 (m), 1375 (w), 1359 (w), 1225 (w), 1091 (w), 1020 (w), 603 (w).

Despite considerable efforts, it was unfortunately not possible to obtain the corresponding Gd^{III}-analogue in a pure form.

1.3 Crystallography

Table S1. Crystallographic data for compounds **1_Y** to **7_{Yb}**.

Compound	**1_Y**	**2_{Tb}**	**3_{Dy}**	**4_{Ho}**
Formula	$C_{50}H_{102}N_2O_{20}V_2Y_2$	$C_{50}H_{102}N_2O_{20}Tb_2V_2$	$C_{50}H_{102}Dy_2N_2O_{20}V_2$	$C_{50}H_{102}Ho_2N_2O_{20}V_2$
FW / g mol^{-1}	1331.03	1471.05	1478.21	1483.07
Crystal System	Triclinic	Triclinic	Triclinic	Triclinic
Space Group	$P\bar{1}$	$P\bar{1}$	$P\bar{1}$	$P\bar{1}$
a / Å	9.7025(3)	9.7942(5)	9.7345(3)	9.8522(4)
b / Å	13.5515(4)	13.5453(7)	13.6421(4)	13.4007(6)
c / Å	14.4081(5)	14.4123(8)	14.4772(4)	14.3546(6)
α / °	115.388(3)	115.277(4)	115.179(2)	115.041(3)
β / °	97.040(3)	96.802(4)	97.400(2)	96.839(3)
γ / °	104.724(3)	105.723(4)	104.700(2)	106.296(3)
U / $Å^3$	1596.10(10)	1602.91(16)	1620.21(9)	1585.22(12)
Z	1	1	1	1
T / K	180(2)	150(2)	180(2)	150(2)
F(000)	700	752	754	756
D_c / Mg m^{-3}	1.385	1.524	1.515	1.554
λ / Å	1.54178	1.34143	0.71073	1.34143
μ / mm^{-1}	5.300	13.293	2.625	13.056
Data Measured	13782	18150	21279	17314
Unique Data	5950	7556	10816	7483
R_{int}	0.0221	0.0358	0.0838	0.0407
Data with I ≥ 2□(I)	5816	7079	9654	7080
wR_2 (all data)	0.1104	0.1348	0.1459	0.1416
S (all data)	1.058	1.032	1.033	1.060
R_1 [I ≥ 2σ(I)]	0.0393	0.0497	0.0528	0.0508
Param./Restr.	425 / 85	397 / 35	403 / 42	395 / 43
Biggest diff. peak and hole / e$Å^{-3}$	+1.01 / -1.20	+2.04 / -2.83	+3.49 / -3.02	+2.67 / -2.13
CCDC number	2406392	2406393	2406394	2406395

Table S1 (continued). Crystallographic data for compounds $\mathbf{1_Y}$ to $\mathbf{7_{Yb}}$.

Compound	$\mathbf{5_{Er}}$	$\mathbf{6_{Tm}}$	$\mathbf{7_{Yb}}$
Formula	$C_{50}H_{102}Er_2N_2O_{20}V_2$	$C_{50}H_{102}N_2O_{20}Tm_2V_2$	$C_{50}H_{102}N_2O_{20}V_2Yb_2$
FW / g mol^{-1}	1487.73	1491.07	1499.29
Crystal System	Triclinic	Triclinic	Triclinic
Space Group	$P\bar{1}$	$P\bar{1}$	$P\bar{1}$
a / Å	9.7136(2)	9.6975(3)	9.7042(4)
b / Å	13.5673(3)	13.5481(4)	13.5421(7)
c / Å	14.3884(4)	14.3920(4)	14.3843(8)
α / °	115.124(2)	115.060(2)	115.042(4)
β / °	97.487(2)	97.580(2)	97.730(4)
γ / °	104.676(2)	104.511(2)	104.460(4)
U / Å^3	1598.37(7)	1595.96(9)	1595.00(16)
Z	1	1	1
T / K	180(2)	180(2)	180(2)
F(000)	758	760	762
D_c / Mg m^{-3}	1.546	1.551	1.561
λ / Å	1.34143	1.34143	1.34143
μ / mm^{-1}	10.460	10.966	11.498
Data Measured	18607	18954	15961
Unique Data	7538	7489	6814
R_{int}	0.0203	0.0179	0.0429
Data with I ≥ 2□(I)	7043	6987	5872
wR_2 (all data)	0.0836	0.0645	0.1604
S (all data)	1.042	1.029	1.106
R_1 [I ≥ 2σ(I)]	0.0305	0.0246	0.0560
Param./Restr.	437 / 160	436 / 124	414 / 37
Biggest diff. peak and hole / eÅ^{-3}	+0.68 / -0.68	+0.66 / -0.93	+1.86 / -1.96
CCDC number	2406396	2406397	2406398

Table S2. Selected bond lengths (Å) and angles (°) for $\mathbf{1_Y}$ to $\mathbf{7_{Yb}}$.

	$\mathbf{1_Y}$	$\mathbf{2_{Tb}}$	$\mathbf{3_{Dy}}$	$\mathbf{4_{Ho}}$	$\mathbf{5_{Er}}$	$\mathbf{6_{Tm}}$	$\mathbf{7_{Yb}}$
Ln1-O1	2.4345(16)	2.461(3)	2.461(2)	2.449(3)	2.4345(17)	2.4250(15)	2.418(4)
Ln1'-O1	2.4571(16)	2.472(3)	2.465(2)	2.450(3)	2.4476(17)	2.4373(15)	2.432(4)
Ln1-O2	2.2784(16)	2.301(3)	2.287(2)	2.280(3)	2.2620(17)	2.2517(15)	2.240(4)
Ln1-O3'	2.2661(16)	2.289(3)	2.273(2)	2.271(3)	2.2556(17)	2.2427(15)	2.231(4)
Ln1-O5	2.3444(18)	2.367(3)	2.353(3)	2.349(3)	2.3318(19)	2.3209(17)	2.314(4)
Ln1-O7'	2.3704(18)	2.398(3)	2.391(3)	2.387(3)	2.364(2)	2.3535(18)	2.349(4)
Ln1-O8	2.3680(19)	2.412(4)	2.390(3)	2.384(4)	2.373(2)	2.3613(18)	2.353(4)
Ln1-O9	2.3687(18)	2.384(3)	2.386(3)	2.350(4)	2.363(2)	2.3566(17)	2.343(4)
V1-O1	2.0516(17)	2.057(3)	2.050(2)	2.052(3)	2.0515(17)	2.0480(15)	2.049(4)
V1-O2	1.9266(16)	1.931(3)	1.933(2)	1.931(3)	1.9328(18)	1.9298(16)	1.929(4)
V1-O3	1.9262(16)	1.931(3)	1.936(2)	1.923(3)	1.9284(18)	1.9268(16)	1.925(4)
V1-O4	2.0258(17)	2.018(3)	2.024(2)	2.016(3)	2.0243(19)	2.0235(17)	2.031(4)
V1-O6	2.0111(17)	2.018(3)	2.014(3)	2.022(3)	2.0156(19)	2.0153(17)	2.008(4)
V1-N1	2.226(2)	2.236(4)	2.228(3)	2.225(4)	2.225(2)	2.2231(19)	2.220(5)
Ln1···Ln1'	4.1285(4)	4.1551(5)	4.1496(3)	4.1289(5)	4.1187(3)	4.1022(3)	4.0916(6)
Ln1···V1	3.3326(5)	3.3567(7)	3.3427(5)	3.3292(7)	3.3164(4)	3.3086(4)	3.2963(9)
Ln1'···V1	3.3265(4)	3.3556(7)	3.3428(5)	3.3272(8)	3.3175(4)	3.3080(4)	3.2984(9)
Ln1-O1-Ln1'	115.13(6)	114.77(11)	114.78(8)	114.89(12)	115.05(7)	115.06(6)	115.02(14)
V1-O1-Ln1	95.58(6)	95.55(11)	95.19(8)	94.99(12)	94.96(6)	95.04(6)	94.74(14)
V1-O1-Ln1'	94.66(6)	95.18(11)	95.08(8)	94.89(12)	94.61(6)	94.64(5)	94.41(13)
V1-O2-Ln1	104.54(7)	104.63(13)	104.46(10)	104.19(13)	104.21(7)	104.34(6)	104.27(16)
V1-O3-Ln1'	104.73(7)	105.02(12)	104.89(10)	104.66(14)	104.65(7)	104.75(6)	104.80(16)

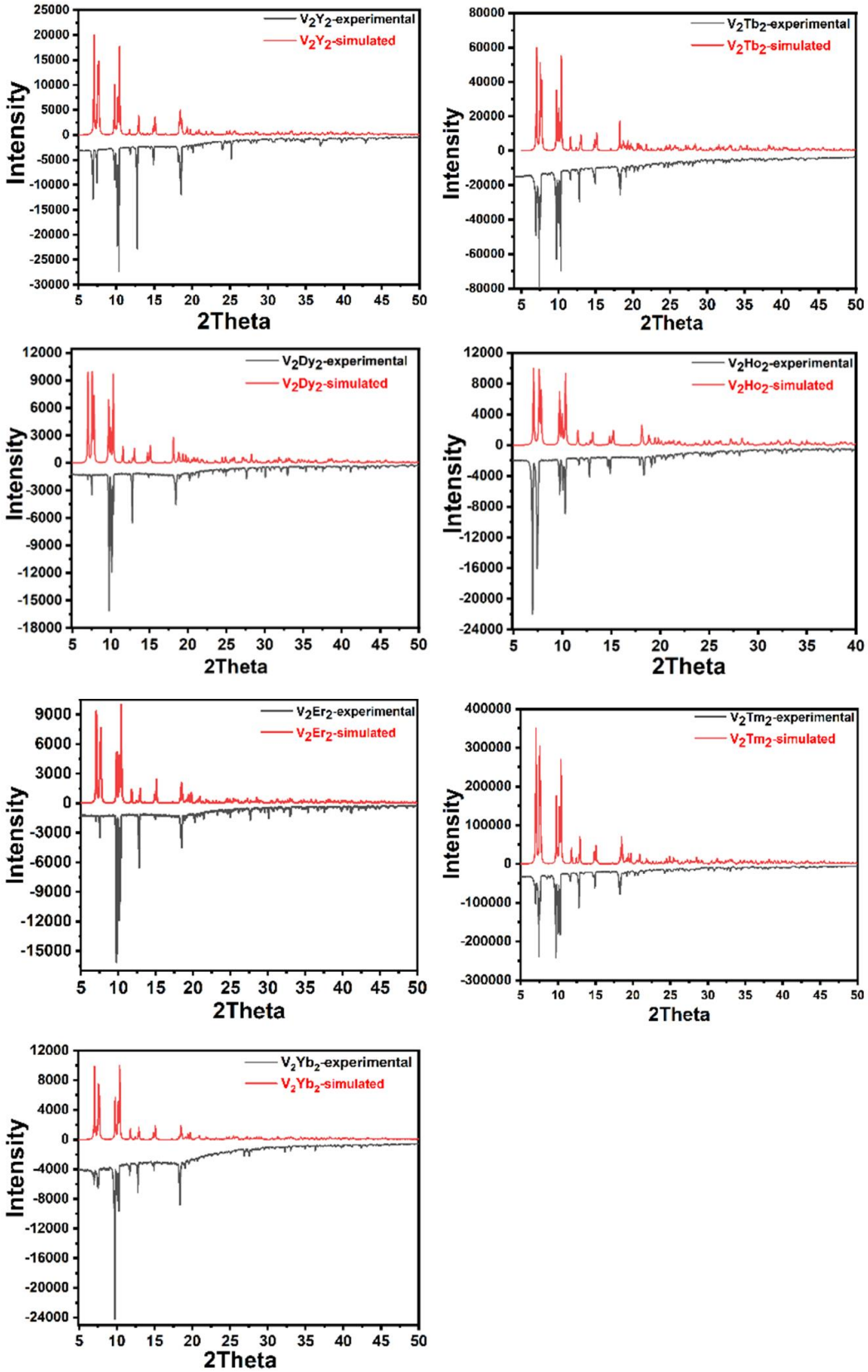


Figure S1. Experimental powder X-ray diffraction patterns and simulations using the single crystal structures and Mercury 2020.3.0.[63] for compounds $\mathbf{1}_{Y}$ – $\mathbf{7}_{Yb}$.

2. Bond Valence Sum (BVS) Analysis

Table S3. V^{III} valences calculated from Bond Valence Sum Analysis[39] for V(1) in compounds $\mathbf{1_Y}$-$\mathbf{7_{Yb}}$.

Compound	Calculated valence for V(1)
$\mathbf{1_Y}$	2.94
$\mathbf{2_{Tb}}$	2.97
$\mathbf{3_{Dy}}$	2.95
$\mathbf{4_{Ho}}$	2.97
$\mathbf{5_{Er}}$	2.96
$\mathbf{6_{Tm}}$	2.97
$\mathbf{7_{Yb}}$	2.97

3. Additional Magnetic Data

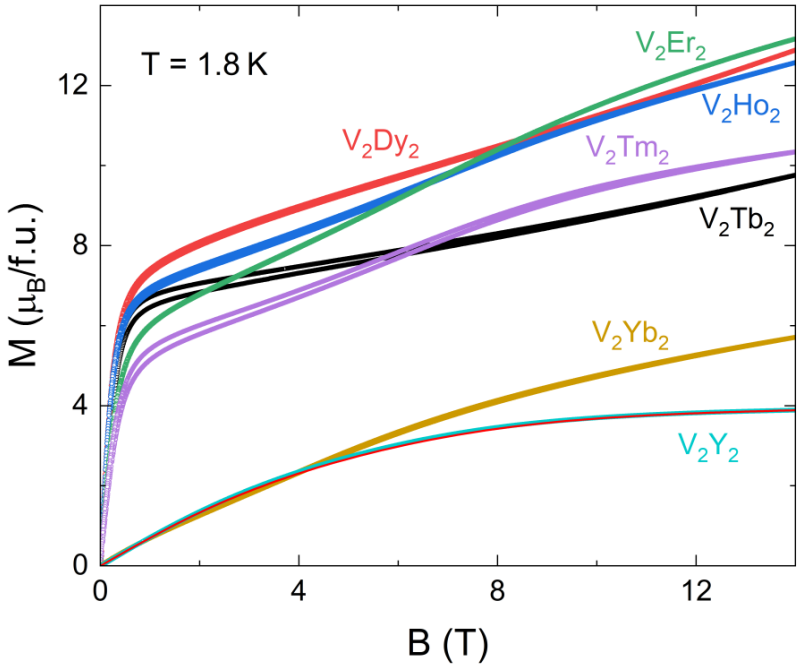


Figure S2. Isothermal magnetisation of **1**$_{Y}$ – **7**$_{Yb}$ at a constant temperature of T = 1.8 K. The red solid line depicts a simulation of **1**$_{Y}$ using the parameters obtained from HF-EPR (see the main text).

Analysis of the magnetisation plateau in the microSQUID data:

While the overall shape of the *M(B)* loops at 30 mK exhibits a predominantly ferromagnetic character, a magnetisation plateau appears near zero field as the bath temperature is increased (cf. inset of Fig. 7(b)). Such a temperature-induced transition indicates the presence of antiferromagnetic excited states several Kelvin above the ground state and can be rationalised with the help of the simulated Zeeman diagrams for **4**$_{Ho}$, **5**$_{Er}$ and **6**$_{Tm}$ presented in Figure S6. From the general trend it becomes evident that the antiferromagnetic state exhibits a small energy shift in zero field from an adjacent ferromagnetic state which leads to a level crossing at B < 0.5 T. As the spin temperature rises above 1 K, thermal population of the excited states via under-barrier temperature-dependent processes allows for the detection of the corresponding exchange field B_{ex} ≈ 0.05(1) T. Such a small exchange field can likely be attributed to the weak dipolar Dy-Dy coupling $J_{Dy\text{-}Dy}$. Assuming an Ising-like character of the Dy moments, $J_{Dy\text{-}Dy}$ can be estimated using the exchange field approach $J_{\mathrm{Dy-Dy}} = -\mu_B g_J \frac{B_{ex}}{m_J}$, with g_J = 4/3 and m_J = 15/2, yielding $J_{Dy\text{-}Dy}$ = -6(1) mK.[53]

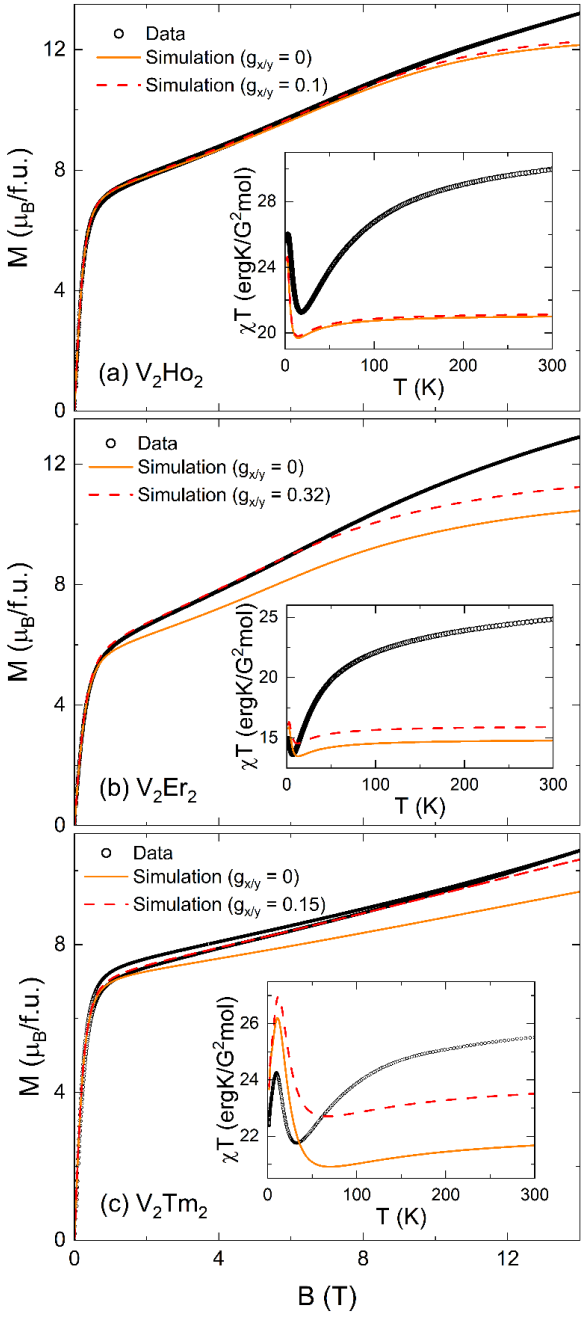


Figure S3. Isothermal magnetisation of **4**$_{Ho}$ (a), **5**$_{Er}$ (a) and **6**$_{Tm}$ (c) at T = 1.8 K and simulations using the strict Ising model (orange solid line) in equation 2 and an almost-Ising model (red dashed line) with the parameters shown in Table 2 (see the main text).

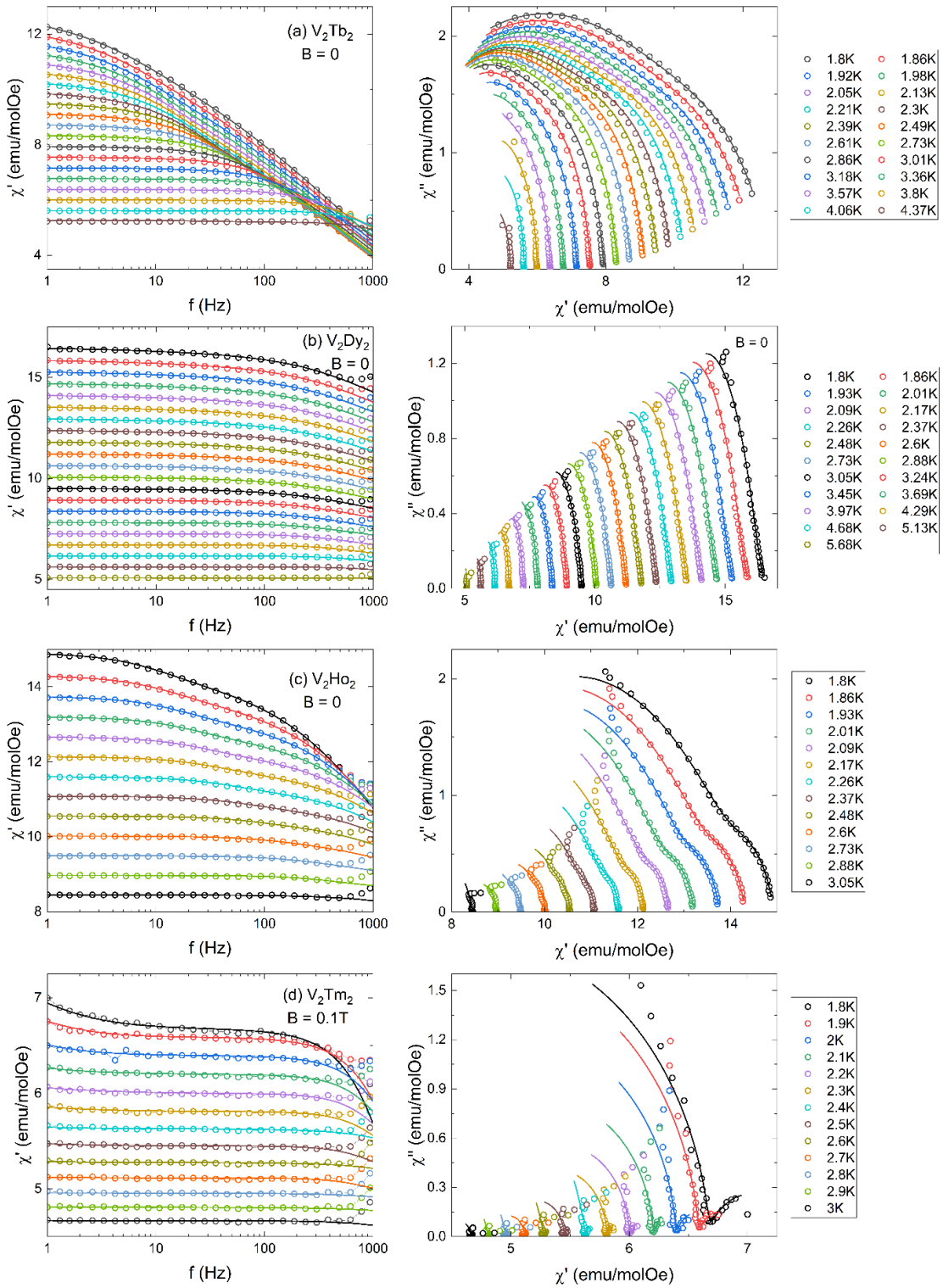


Figure S4. In-phase ac susceptibility (left) and Cole-Cole plots (right) of of **2**$_{Tb}$ (a) ,**3**$_{Dy}$ (b),**4**$_{Ho}$, (c) and **6**$_{Tm}$ (d) at selected temperatures. Solid lines depict fits of equation 3 to the data as described in the main text.

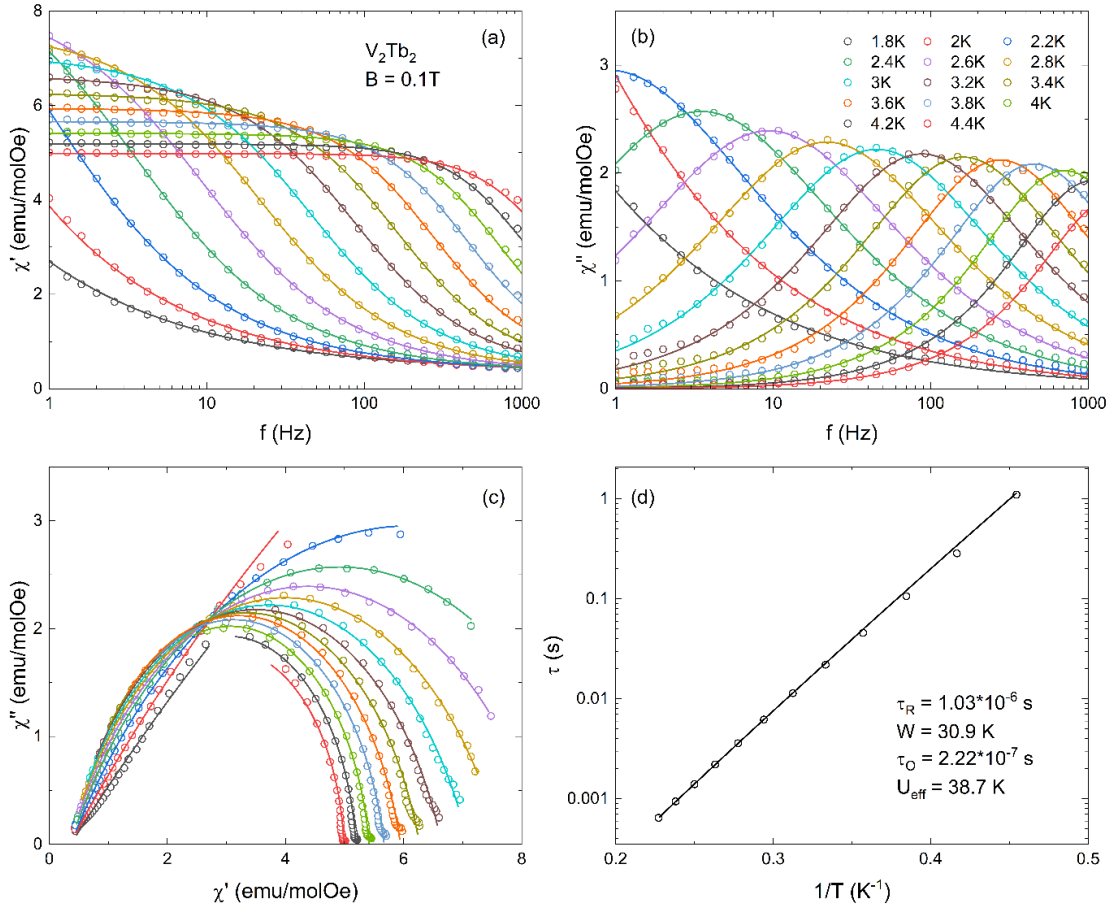


Figure S5. In-phase susceptibility (a), out-of-phase susceptibility (b), Cole-Cole plot (c) and Arrhenius plot of the obtained relaxation times at H_{ext} = 0.1 T of **2Tb**. Solid lines in (a), (b) and (c) depict fits of equation S1 to the data. The solid line in (d) depicts a fit of equation 4 (see the main text) with the parameters shown in the plot.

$$\chi_{ac}(f) = \left(\chi_{S,n} + \frac{\chi_T - \chi_S}{1+(if\tau)^{1-\alpha}}\right) \qquad \text{(S1)}$$

4. Additional HF-EPR Data

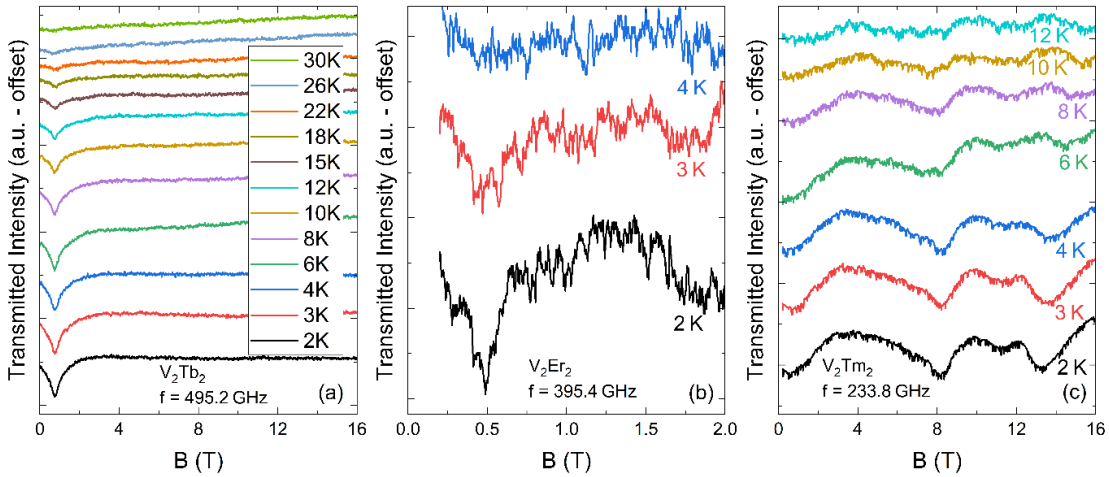


Figure S6. Loose powder HF-EPR spectra of **2**$_{Tb}$ (a), **5**$_{Er}$ (b) and **6**$_{Tm}$ (c) at fixed frequencies and variable temperatures.

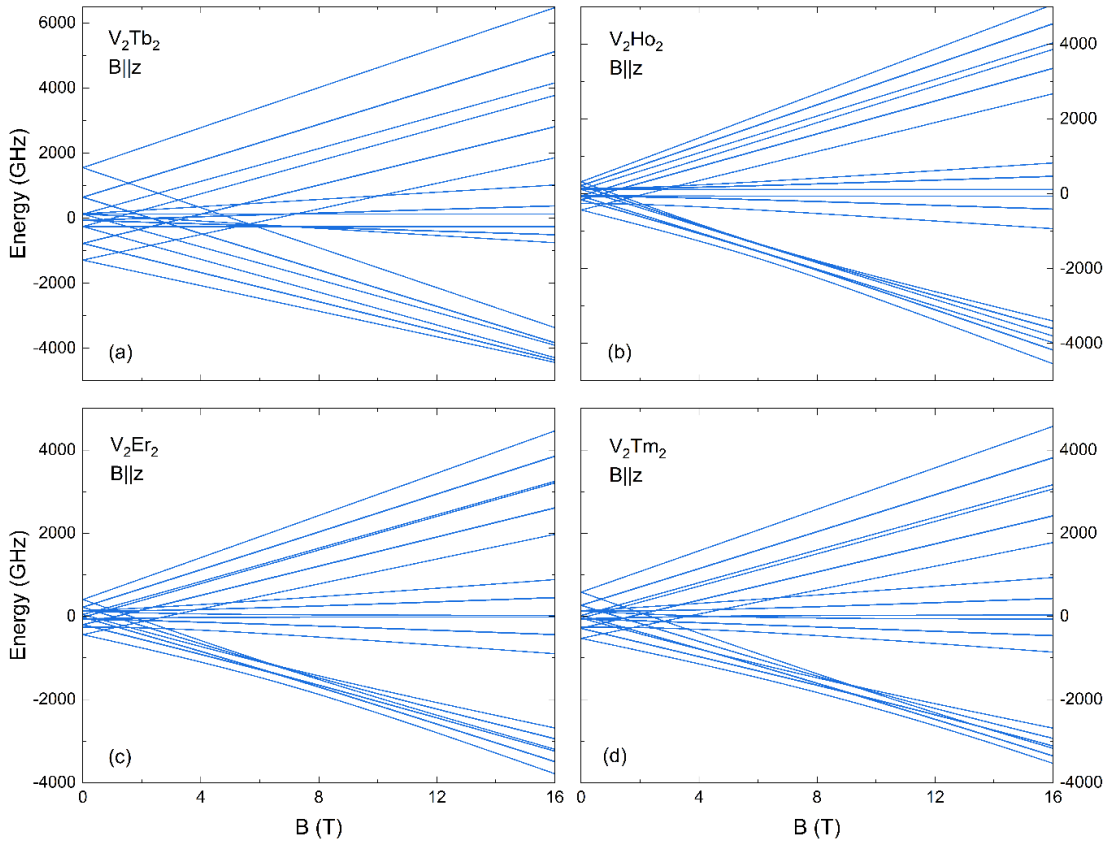


Figure S7. Simulated energy level diagram of **2**$_{Tb}$ (a), **4**$_{Ho}$ (b), **5**$_{Er}$ (c) and **6**$_{Tm}$ (d) for B||z using the spin Hamiltonian parameters listed in Tab. 2.

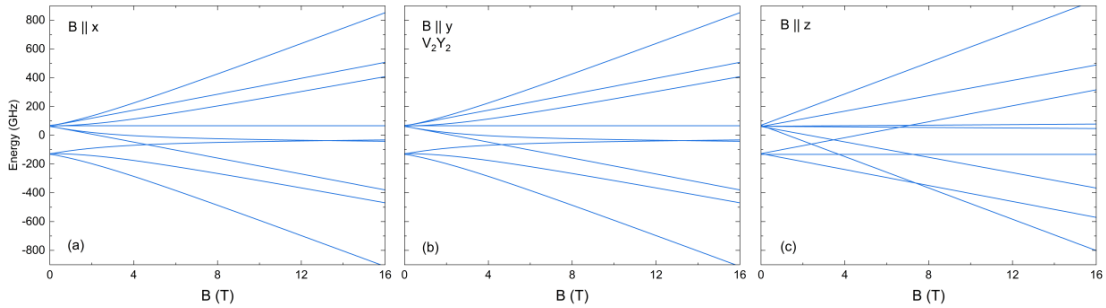


Figure S8. Simulated energy level diagram of **1**$_{Y}$ for B||x (a), B||y (b) and B||z (c) using the spin Hamiltonian parameters as described in the main text.

Chapter 7

Anisotropic Spin Chains in a Re^{IV}-based Metal-organic Compound

The preceding chapters presented the magnetic investigation of metal-organic molecular complexes based on $3d$ transition metal and $4f$ lanthanide ions, both of which have their own advantages and disadvantages over the other. Owing to intrinsically strong spin-orbit coupling in the $4f$ orbitals, lanthanide-based complexes typically exhibit large single-ion anisotropies, but their complex coordination chemistry often leads to ligand fields with low symmetry and, thus, to fast quantum tunnelling effects. Moreover, the localised nature of the $4f$ electrons limits the orbital overlap with neighbouring ions, such that magnetic exchange coupling involving lanthanide ions is generally weak. In contrast, the orbital contribution to the magnetic anisotropy in the $3d$ orbitals is suppressed by the surrounding ligand field, and the good relaxation properties of transition metal clusters usually arise from strong magnetic interactions between the metal centres.

A compromise between these effects is found in the $5d$ transition metal ions. In comparison to their lighter $3d$ and $4d$ counterparts, the $5d$ orbitals are more spatially extended and exhibit a larger spin-orbit coupling [38, 113]. This leads to strong anisotropic magnetic interactions, while still maintaining a sizeable single-ion anisotropy [114]. The chemical properties of $5d$ transition metal ions also allow for the construction of high-symmetry ligand fields [115, 116]. Yet, possible exchange paths to neighbouring ions are typically longer and involve more intermediate ions than in $3d$-based compounds. Among the $5d$ transition metal ions, Re^{IV} has attracted the most attention for possible SMM applications. In an octahedral coordination, the orbitally non-degenerate $^4A_{2g}$ electronic ground term with three unpaired electrons $S = 3/2$ yields large magnetic anisotropies [115–118] and eventually leads to single-ion magnet behaviour [36]. To explain the good relaxation properties, the nature of single-ion anisotropy in Re^{IV} was theoretically studied in great detail and the Re^{IV}-ligand covalency was found to drastically reduce the influence of quantum tunnelling processes [119, 120]. Similar to the idea of $3d$-$4f$ architectures, the combination of $3d$

and 5*d* transition metal ions into heterometallic clusters [121] introduced a new class of single-molecule [122] and single-chain magnets [35]. The key characteristic in this class of materials is given by the anisotropic magnetic 3*d*-5*d* coupling, which has been discussed recently in more detail [114, 123], but an elusive treatment remains missing. Unfortunately, the same holds for the magnetic interaction in supramolecular clusters based on 5*d* transition metal ions, as, for example, reported in Re^{IV} salts [124].

In this chapter, a Re^{IV}-based metal-organic compound is investigated using dc magnetisation measurements. Originally intended to serve as a reference sample for investigations on novel 4*f*-5*d* complexes, the studied sample exhibits intriguing magnetic properties that can not be explained by considering isolated molecules. The magnetic data clearly show the relevance of intermolecular Re-Re exchange interaction, which is studied by means of numerical calculations.

7.1 Molecular Structure

The studied sample was synthesised by Dr. Sukhen Bala and structurally characterised by Dr. Christopher E. Anson in the group of Prof. Dr. Annie K. Powell from the *Karlsruhe Institute of Technology* (KIT). Chemical reaction of $[Bu_4N][Re^{IV}Br_5(Hpyzc)]$ with $Y(OTf)_3$ and bipyridine in MeOH and MeCN at room temperature results in deep orange needle-shaped crystals suitable for single crystal X-ray diffraction. The compound was identified as the complex $[(Re^{IV}Br_5(\mu_2\text{-pyzc}))_2(Y^{III}(bpy)_2(OMe))_2]$ **(1)** crystallizing in the monoclinic space group $C2/c$. Fig. 7.1(a) depicts the molecular structure of **(1)**. The central, dimeric Y_2^{III} unit is bridged by the carboxylate groups of two $Re^{IV}Br_5(pyzc)^{2-}$ metalloligands and two methoxides. Two bpy ligands each complete the coordination spheres of the non-magnetic Y^{III} ions, such that the coordination geometry is best described as a square antiprism. As a part of the utilised metaloligand, the magnetic Re^{IV} ions are coordinated by five bromide ions forming an almost perfect square pyramid and one nitrogen ion, which is located on the middle axis below the base of this pyramid. Due to this coordination geometry, the local ligand field acting on the Re^{IV} ions is expected to exhibit a symmetry close to C_{4v}. The two distinct Re^{IV} positions within the molecular structure are related by an inversion symmetry.

Fig. 7.1(b) shows the crystal packing of complex **(1)** in the solid state. The crystallographic unit cell contains two molecular orientations, which are tilted by an angle of approximately 68° with respect to each other. As visualised in Fig. 7.1(c) by only considering the Re-Br-subsystem, the Re^{IV} ions form quasi-linear chains with alternating local Br_5 orientations along the *c*-axis of the crystal. These chains assume a non-regular hexagonal structure in the *ab*-plane (Fig. 7.1(d)), where the closest interchain distance occurs between neighbouring chains along the *a*-axis. In contrast to the Re-Br bonds within a $ReBr_5$ unit, the Br-Br bonds connecting two of those units are not of ionic origin, but arise from short contact (type 1) halogen-halogen interaction [127].

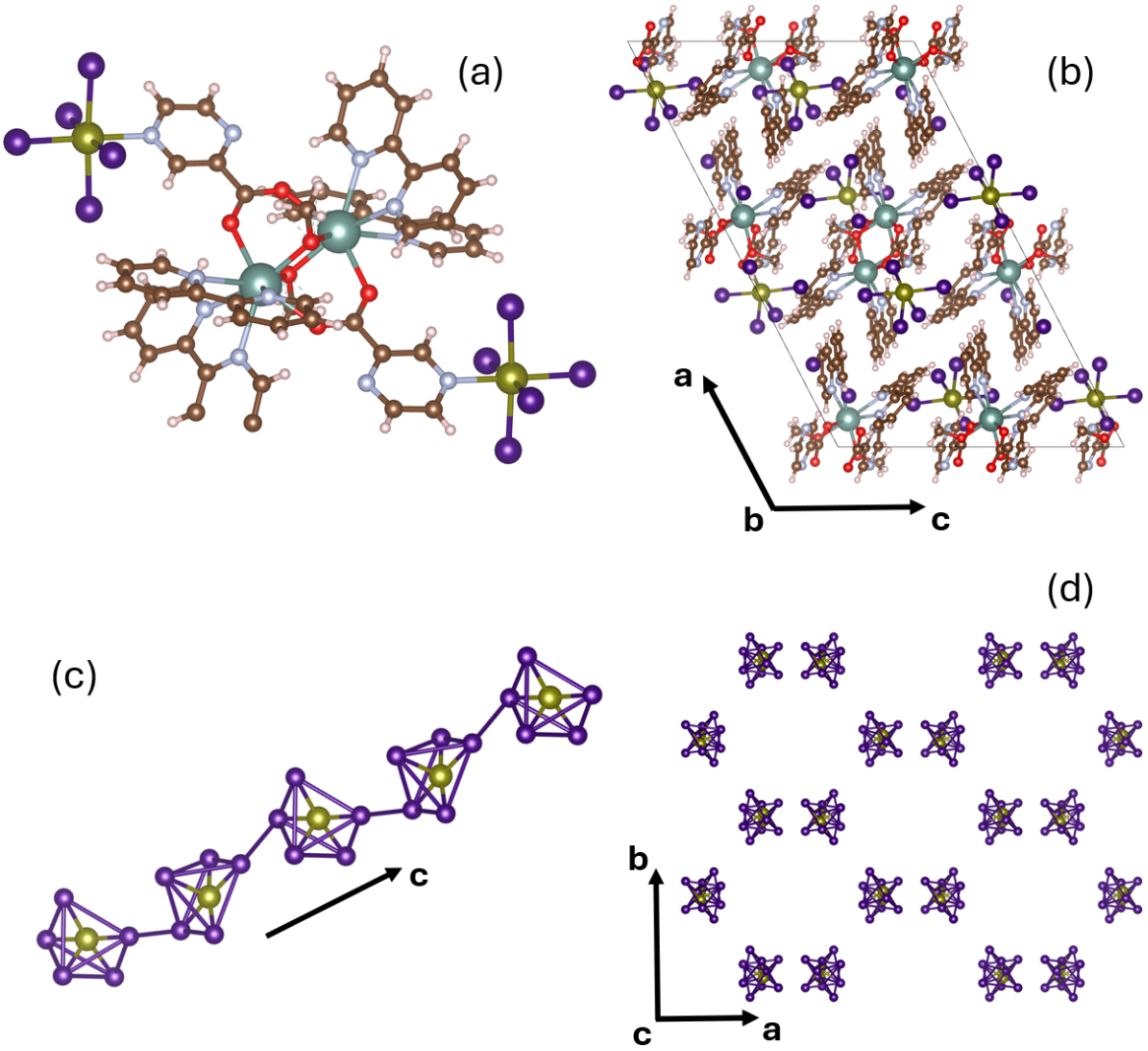


Figure 7.1. (a) Molecular structure and (b) crystal packing of complex **(1)** as obtained from single crystal X-ray diffraction [125]. Gold: Re(IV); Turquoise: Y(III); Purple: Br; Light blue: N; Brown: C; Red: O; White: H. (c) and (d) show the chain-like structure of the Re-Br-subsystem. Purple lines do not depict true ionic Br-Br bonds, but are only a guide to the eye. Figures were generated by VESTA [126].

7.2 Direct Current Magnetisation

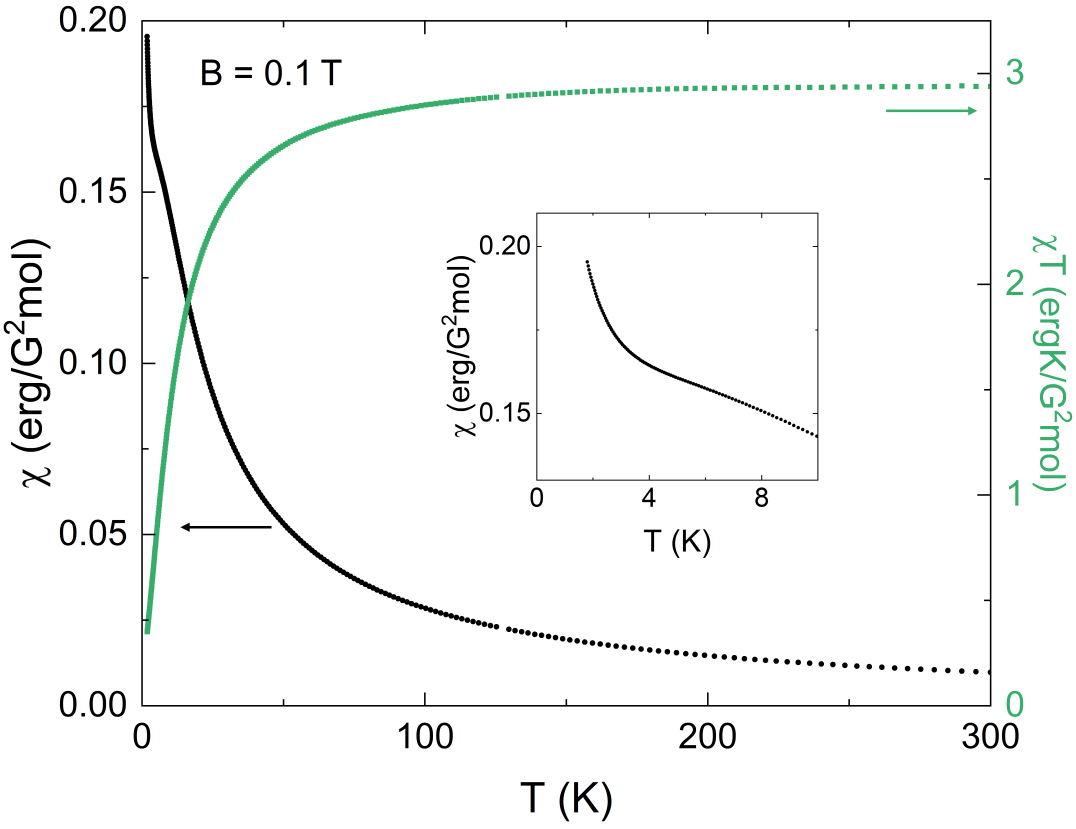


Figure 7.2. Temperature dependence of the static magnetic susceptibility (black circles) and corresponding χT-product (green squares) of complex **(1)** at $B = 0.1$ T. The inset shows a zoom into the low-temperature region of $\chi(T)$.

Direct current magnetisation measurements were conducted on a fixed polycrystalline powder sample using a magnetic properties measurement system (MPMS) as described in Chapter 3. The temperature dependence of the static magnetic susceptibility and the respective χT-profile of complex **(1)** at $B = 0.1$ T are depicted in Fig. 7.2. Upon cooling from room temperature, χ exhibits a Curie-like behaviour, which also manifests itself as an approximately constant χT-profile down to 150 K. For two Re^{IV} ions with $S = 3/2$, the value $\chi T(T = 300\,\mathrm{K}) = 2.94\,\mathrm{ergK/G^2mol}$ corresponds to $g = 1.8$. Such a small g-factor is not uncommon for Re^{IV} ions in a cubic ligand field symmetry and likely results from the intrinsically strong spin-orbit coupling in the $5d$ orbitals [36, 124, 128]. Below 150 K, χT starts to decrease first slowly and then more rapidly when cooling below 50 K. Such an observed decrease probably arises from the depopulation of the m_s-Stark levels and/or from antiferromagnetic interactions between the Re^{IV} moments. The presence of antiferromagnetic coupling is further supported by the observation of a small shoulder marking the onset of a maximum in χ at low temperatures. This maximum is, however, superimposed by a further Curie-like increase of the static magnetic susceptibility, which might arise from a small fraction of non-interacting Re^{IV} spins in the sample.

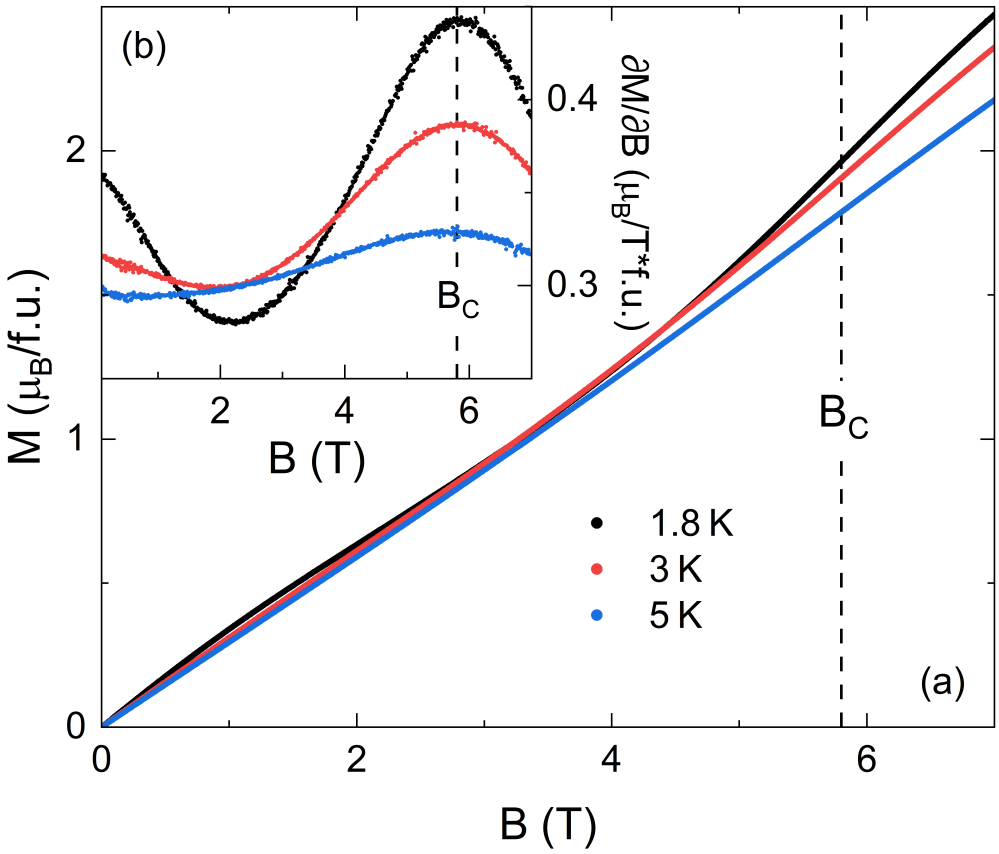


Figure 7.3. Isothermal magnetisation of complex **(1)** at various selected temperatures (a). The inset (b) shows the corresponding isothermal susceptibility $\partial M/\partial B$. Vertical dashed lines mark the level crossing at B_C.

Clear signatures of antiferromagnetic interactions can also be seen in the isothermal magnetisation of complex **(1)** as displayed in Fig. 7.3. At small magnetic fields, $M(B, T = 1.8\,\mathrm{K})$ increases almost linearly, but then begins to exhibit weak right-bending up to 2.1 T. From there on, clear left-bending occurs until another point of inflection at $B_C = 5.8$ T marks the appearance of a level-crossing. All of these features are better visible in the isothermal magnetic susceptibility $\partial M/\partial B$ (c.f. inset of Fig. 7.3) and unambiguously reveal antiferromagnetic coupling between the Re^{IV} ions. The highest measured magnetisation of $2.47\,\mu_B$/f.u. at 7 T is still less than half of the saturation magnetisation $M_{sat} = 5.4\,\mu_B$/f.u. expected for two Re^{IV} ions with $g = 1.8$. At higher temperatures up to 5 K, all observed features remain visible at the same B_C in the data, but become broader due to thermal fluctuations.

The unambiguous observation of antiferromagnetic coupling in complex **(1)** implies the presence of intermolecular magnetic interactions between the Re^{IV} ions. Most presumably, those interactions correspond to the magnetic coupling along the Re^{IV} chains as mediated by the short-contact halogen-halogen bonds (see Fig. 7.1). Similar exchange mechanisms were also reported in bisadeninium Re^{IV} salts [124]. Halogen-halogen-bond-mediated intermolecular coupling was, moreover, demonstrated to arise in radical- and 3*d* transition metal-based supramolecular clusters [129–133] and found

to govern the magnetic relaxation in polycrystalline samples of $4f$ lanthanide single-molecule magnets [134]. To determine the microscopic spin Hamiltonian parameters, the static magnetic susceptibility at $B = 0.1$ T and the isothermal magnetisation at $T = 1.8$ K were simulated using

$$\mathcal{H} = (1 - n_{\mathrm{imp}}) \left(\sum_{\mathrm{i}}^{N} g\boldsymbol{B}\hat{\boldsymbol{S}}_{\mathrm{i}} + \hat{\boldsymbol{S}}_{\mathrm{i}} \overleftrightarrow{D}_{\mathrm{i}} \hat{\boldsymbol{S}}_{\mathrm{i}} + \sum_{<\mathrm{i,j}>}^{N} J\hat{\boldsymbol{S}}_{\mathrm{i}}\hat{\boldsymbol{S}}_{\mathrm{j}} \right) + n_{\mathrm{imp}} \left(g\boldsymbol{B}\hat{\boldsymbol{S}} + D\hat{S}_{\mathrm{z}}^{2} \right). \quad (7.1)$$

The first part describes the contribution of a $S = 3/2$ Heisenberg chain with nearest-neighbour interactions between N sites exhibiting a local single-ion anisotropy. To account for the alternating tilting of the C_{4v}-symmetric, local NBr_5 ligand field, $\overleftrightarrow{D}_{\mathrm{i}} = \mathrm{diag}(0, 0, D)$ for even i and $\overleftrightarrow{D}_{\mathrm{i}} = \boldsymbol{R}_{\mathrm{x}}^{\mathrm{T}}(68°)\mathrm{diag}(0, 0, D)\boldsymbol{R}_{\mathrm{x}}(68°)$ for odd i is used. Here, $\boldsymbol{R}_{\mathrm{x}}(\theta)$ denotes a rotation around the global x-axis.[1] The second part describes the behaviour of non-interacting, but equally coordinated Re^{IV} impurity moments with $S = 3/2$. To ensure a correct scaling, the ratio of uncoupled Re^{IV} spins is defined by the factor n_{imp}.

Due to the exponentially-growing Hilbert space, simulations of the Hamiltonian (7.1) by means of exact diagonalisation are restricted to a finite chain length of $N = 6$ and employing periodic boundary conditions. However, chain lengths in real microcrystals are typically on the order of a few 100 lattice site [135, 136]. To investigate the putative influence of finite-size effects, simulations of the static magnetic susceptibility using the Hamiltonian (7.1) were performed for different chain lengths N. Fig. 7.4 displays the results of simulations of M/B employing the finite-temperature Lanczos method (FTLM) [137, 138], density-matrix renormalisation-group technique (DMRG) [139, 140], and exact diagonalisation (ED) up to $N = 12$. All FTLM and DMRG calculations were performed by Prof. Dr. Jürgen Schnack and Lukas Horstmann from *Bielefeld University*. Numerical simulations by means of exact diagonalisation of the spin Hamiltonian were carried out by the present author using the *EasySpin* MatLab software package [141]. As can be seen from the overlap of DMRG and ED simulations for $N = 3$ to $N = 12$ down to low temperatures, the used spin Hamiltonian (7.1) is very robust against finite-size effects. This probably arises due to the single-ion anisotropy term, which allows for a more classical treatment of the Re^{IV} moments. In contrast, the $N = 3$ FTLM calculation strongly deviates from the observed general behaviour at low temperatures, since the physical approximations employed in this method are no longer valid when thermal energy is comparable to the first excitation energy gap [142]. Nonetheless, the numerical findings demonstrate that reliable simulations of the magnetic properties can be performed by exact diagonalisation of the Hamiltonian (7.1) even for $N = 6$.

The best simulation of the magnetic properties of complex **(1)** using this approach is shown in Fig. 7.5 and yields the parameters $g = 1.8$, $D = +8.64$ K, $J = +2.40$ K and

[1] Since no transversal anisotropy is assumed in the Hamiltonian (7.1), the same results are obtained for rotations of the local single-ion anisotropy tensor around the global y-axis.

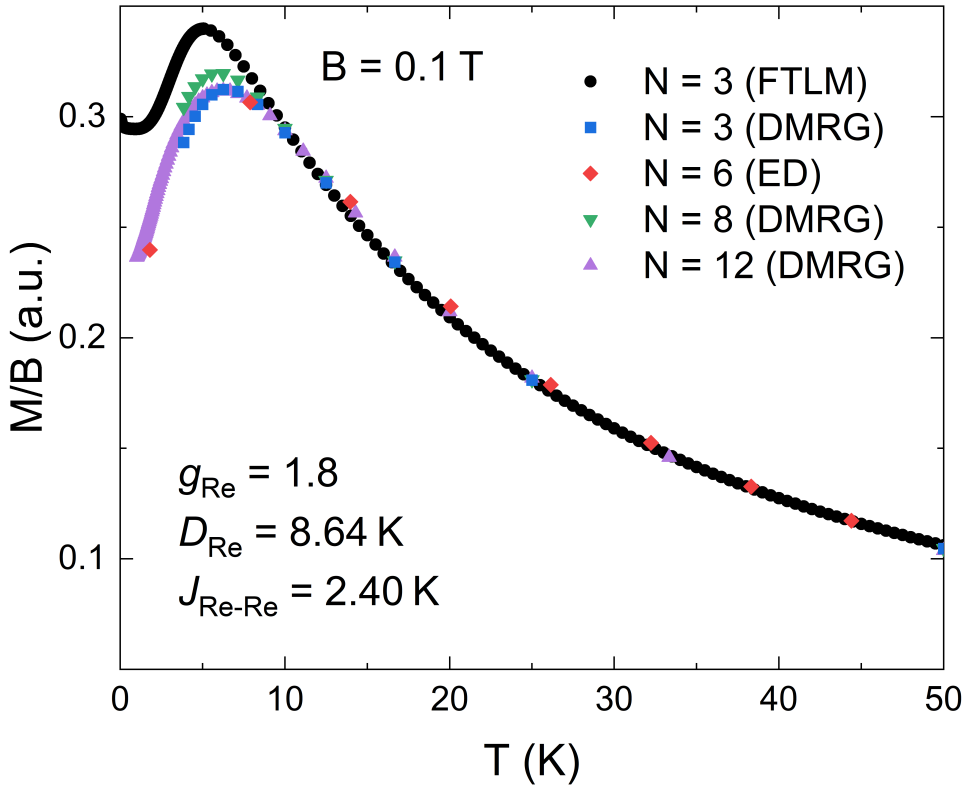


Figure 7.4. Simulated static magnetic susceptibility M/B at $B = 0.1$ T using the Hamiltonian (7.1) with different chain lengths N and the parameters shown in the plot. Simulations employing the finite-temperature Lanczos method (FTLM), density-matrix renormalisation-group technique (DMRG) and exact diagonalisation (ED) were performed by Prof. Dr. Jürgen Schnack, Lukas Horstmann and the present author, respectively.

$n_{\mathrm{imp}} = 0.05$. As can be seen, the simulated static magnetic susceptibility at $B = 0.1$ T agrees well with the experimentally obtained susceptibility down to 50 K, but begins to deviate towards lower temperatures. The isothermal magnetisation at 1.8 K also seems well reproduced by the performed simulations. However, the discrepancy to the experimentally obtained data becomes clearer when considering the isothermal susceptibility displayed in Fig. 7.5(d). Firstly, the numerical simulations predict an additional intermediate maximum of $\partial M/\partial B$ at $B = 3.9$ T, which is not present in the measured susceptibility. Secondly, the used model overestimates the transition field B_{C} of the observed level crossing by more than 1 T. In an attempt to directly simulate $\partial M/\partial B$, the transition field B_{C} was found to only weakly depend on the single-ion anisotropy D. Instead, B_{C} is mainly determined by the magnetic Re-Re-coupling J. The best match of the simulated transition field to the experimentally measured one is achieved by $J = 3.36$ K. However, no parameter set was found that adequately described the experimental magnetic data using this value (see Fig. 7.6).

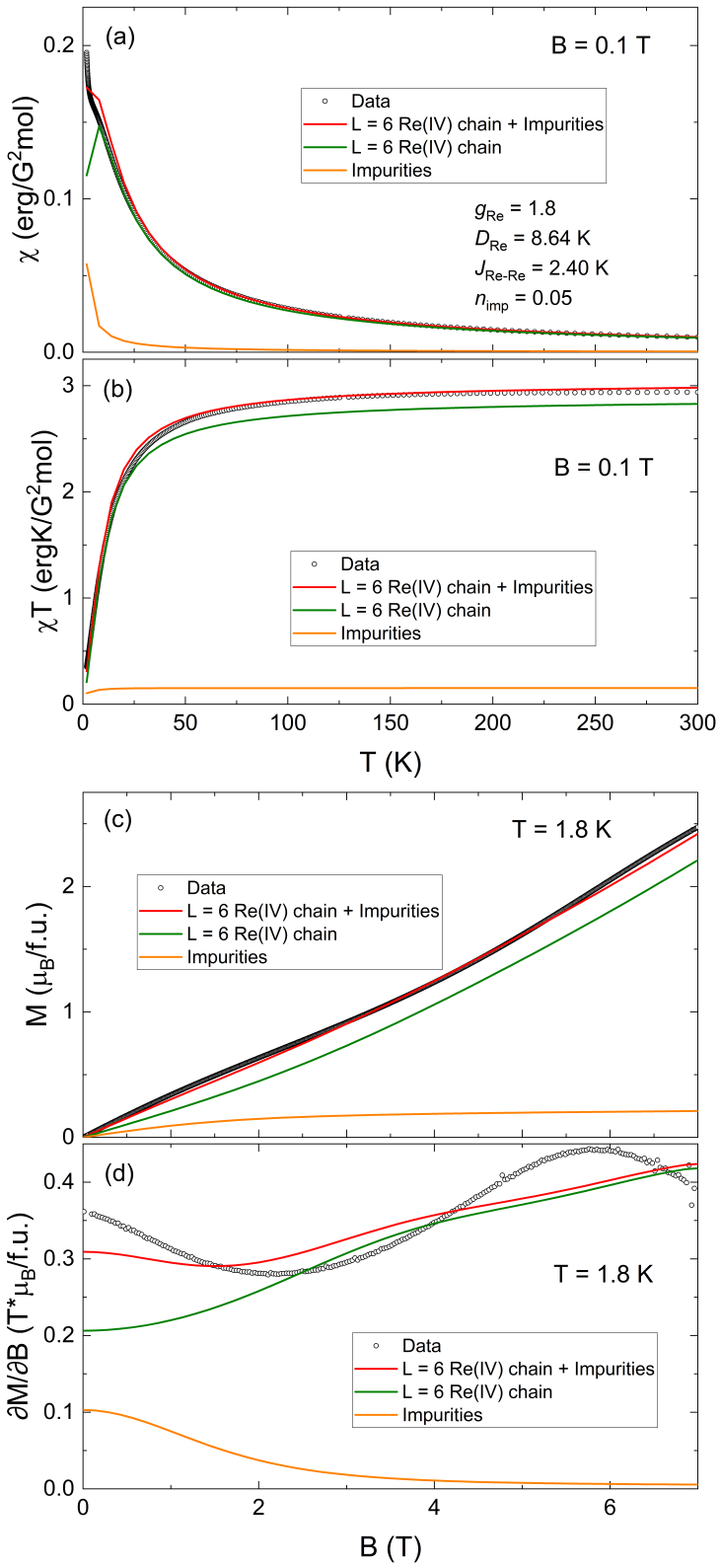


Figure 7.5. Best simulation of the static magnetic susceptibility at $B = 0.1$ T (a) and isothermal magnetisation at $T = 1.8$ K (c) of complex **(1)** using the Hamiltonian (7.1) and the parameters as described in the text. (b) and (d) depict the corresponding simulations of χT and $\partial M/\partial B$, respectively.

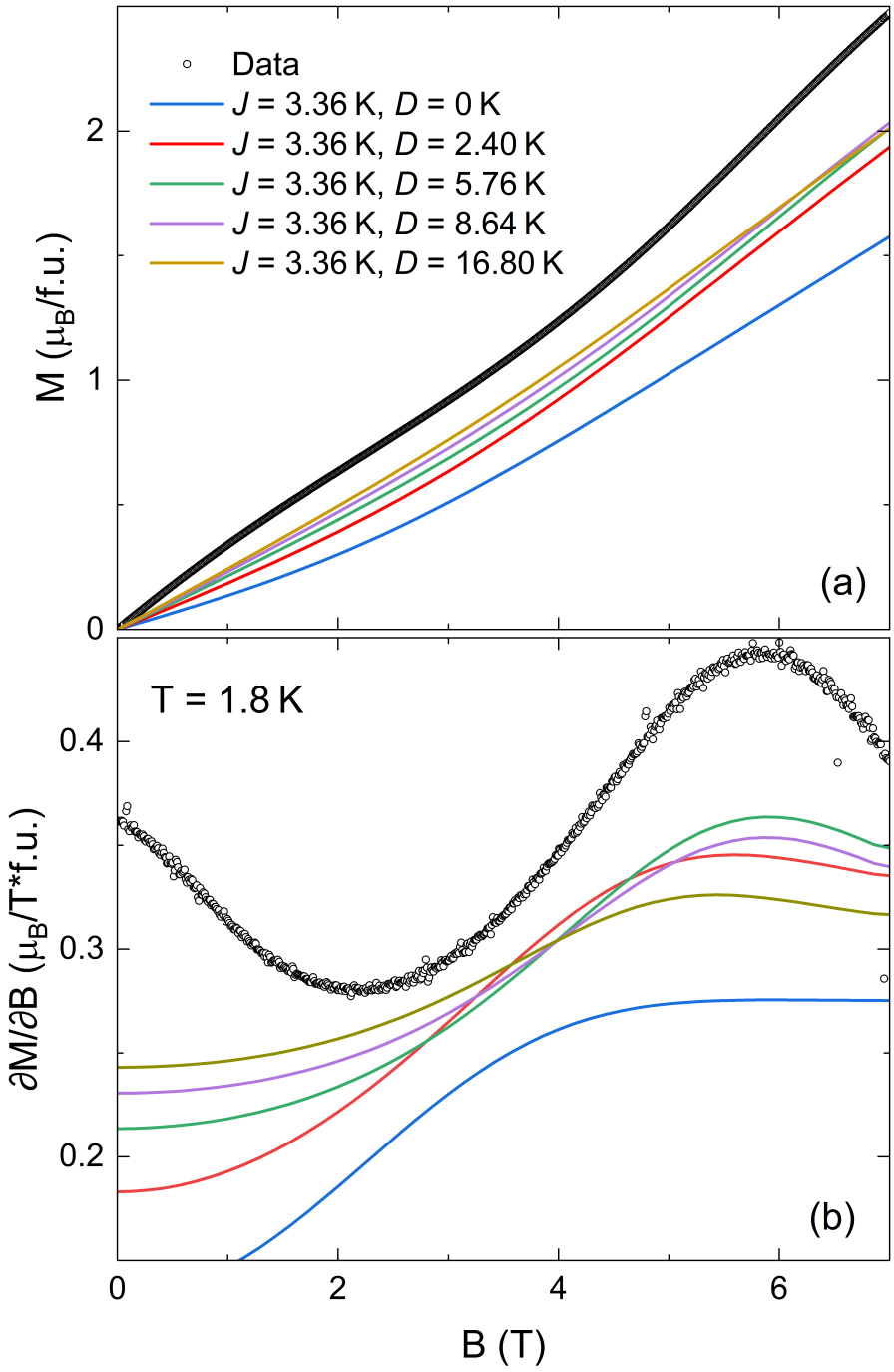


Figure 7.6. Simulations of the isothermal magnetisation (a) and corresponding magnetic susceptibility (b) of complex **(1)** at $T = 1.8$ K using the Hamiltonian (7.1) with fixed $J = 3.36$ K, $g = 1.8$ and various values of D.

The inability to simulate the experimental magnetic data using the Hamiltonian (7.1) directly indicates that the description of complex **(1)** as a $S = 3/2$ Heisenberg chain with local single-ion anisotropy conveys the basic aspects of the magnetic response, but lacks important details. Since the local ligand field surrounding the Re^{IV} ions exhibits almost perfect C_{4v} symmetry, transverse or higher-order anisotropy terms are expected to be small and, thus, unlikely to significantly alter the numerical results. More plausibly, the combination of strong spin-orbit coupling and the diffuse nature of the $5d$ orbitals allows for considerably anisotropic exchange interaction [38]. Such exchange mechanisms are not included in the used model. An alternative approach may also be given by including an interchain coupling term in the Hamiltonian (7.1). As the Re^{IV}-chains, pointing along the crystallographic c axis, each form close pairs along a, the additional coupling term extends eq. (7.1) to a spin-ladder model. However, both of the discussed specifications require enhanced computational power and more complex numerical techniques, such as finite temperature Lanczos [137, 138], density-matrix renormalisation-group [139, 140] or Monte-Carlo methods [143], are required to perform the corresponding simulations. Such calculations are beyond the scope of this thesis, and a collaboration with research groups which are specialised in the simulation of spin Hamiltonians has started to tackle the problem.

7.3 Conclusion

Within this chapter, the static magnetic properties of a Re^{IV}-based metal-organic complex with the general formula $[(Re^{IV}Br_5(\mu_2\text{-pyzc}))_2(Y^{III}(bpy)_2(OMe))_2]$ **(1)** are reported. The experimental data reveal the presence of intermolecular antiferromagnetic interactions mediated by short-contact halogen-halogen bonds. As such, the Re^{IV} ions form $S = 3/2$ spin chains with local single-ion anisotropy. Numerical simulations show that the magnetic coupling within the Re^{IV} network can not be described by an isotropic Heisenberg interaction along the chains. Instead, other effects, such as anisotropic exchange or interchain coupling, are needed to describe the magnetic data.

Chapter 8

Summary and Conclusion

This thesis presents the detailed magnetic investigation of novel metal-organic molecular complexes hosting $4f$ lanthanide as well as $3d$ and $5d$ transition metal ions. Magnetic characterisation relies primarily on tunable high-frequency/high-field electron paramagnetic resonance spectroscopy (HF-EPR), supported by static and dynamic magnetisation measurements. The employed HF-EPR setup enables the study of low-energy excitations over a wide range of experimental parameters: $T = 2 - 300$ K, $B = 0 - 16$ T and $f = 30 - 1000$ GHz. Analysis of the HF-EPR spectra and magnetisation data provides direct access to the microscopic spin Hamiltonian parameters that govern the magnetic properties of the investigated compounds.

In the muffin-shaped complex $[Er(PPTMP)_2(H_2O)][OTf]_3$, the triply-capped, slightly distorted trigonal-prismatic ligand field surrounding the central Er^{III} ion gives rise to fast quantum tunnelling of the magnetisation (QTM) in the magnetic ground state, which can be suppressed by a small external static magnetic field $B_{dc} = 0.1$ T. Using HF-EPR spectroscopy, the effective g-tensors and zero field splittings (Δ) of the two energetically lowest Kramers doublets (KD) are experimentally determined. The absence of SMM-behaviour due to a significant mixing of states is rationalised by the presence of pronounced transverse components in the ground state effective g-tensor. When ground state QTM is quenched, slow magnetic relaxation likely occurs through a thermally-activated process involving the first excited Kramers doublet at 780 GHz (37.4 K) above the ground state. The higher-lying excited KDs are strongly gapped ($\Delta \gg 1$ THz) and probably do not contribute to the relaxation dynamics. From loose powder measurements, it can be inferred that the symmetry of the electrostatic ligand field favours $m_J = \pm 9/2$ as the magnetic ground state and $m_J = 5/2$ as the first excited state of the $^4I_{15/2}$ multiplet. Comparison of the experimental data with the predictions of numerical *ab-initio* calculations shows that the explicit treatment of spin-orbit coupling in CASOCI calculations provides an excellent description of the magnetic properties of mononuclear Er^{III} complexes.

Analogous investigations on a series of three pentagonal-bipyramidal (PBP) complexes Er(DAPMBH/H_2DAPS)X with similar equatorial N_2O_3 Schiff base coordination but different apical ligands (X = (H_2O)Cl **(1)**, (CH_3OH)N_3 **(2)** and Cl_2 **(3)**) reveal a stabilisation of the $m_J = \pm 11/2$ Kramers doublet due to the local pseudo-D_{5h} lig-

and field symmetry around the central Er^{III} ion. All complexes exhibit pronounced transverse components in the effective g-tensor, which leads to fast ground state QTM in zero external magnetic field and thermally-assisted QTM (TA-QTM) *via* the low-energy excited KDs when a small static magnetic field is applied. The presence of two charged axial ligands in complex **(3)** results in significantly low-lying excited states ($\Delta^{(3)}_{1\rightarrow2}$ = 13.9 K and $\Delta^{(3)}_{1\rightarrow3}$ = 22.1 K) compared to **(1)** ($\Delta^{(1)}_{1\rightarrow2}$ = 39.6 K) and **(2)** ($\Delta^{(2)}_{1\rightarrow2}$ = 36.8 K), where one of the axial ligands is neutral. This finding accounts for the observed absence of slow magnetic relaxation at B_{dc} = 0.1 T in **(3)**. The experimental results emphasise that both the axiality of g_{eff} and the size of $\Delta_{1\rightarrow2}$ play a similarly crucial role for the relaxation rate of TA-QTM. While numerical crystal field analysis of the static magnetic susceptibility accurately reproduces the spectroscopically obtained spin Hamiltonian parameters for all complexes, *ab-initio* CASSCF calculations are found to strongly overestimate the energy splittings in the anionic complex **(3)**. This discrepancy likely arises due to the complexity of numerical structure optimisation for charged molecular complexes in the solid state.

The magnetic relaxation dynamics in the family of isostructural, butterfly-shaped $V^{III}_2Ln^{III}_2$ complexes with the general formula $[V_2Ln_2(\mu_2\text{-OMe})_2(^t\text{Budea})_2(\text{piv})_6]$ (Ln^{III} = Y^{III}, Tb^{III}, Dy^{III}, Ho^{III}, Er^{III}, Tm^{III} and Yb^{III}) are mainly governed by the incorporated lanthanide ion. As such, the local ligand field gives rise to weak SMM-behaviour in all compounds hosting rare earth ions with predominantly oblate electron distribution (Tb^{III}, Dy^{III} and Ho^{III}) and field-induced slow magnetic relaxation in V_2Tm_2. The complex V_2Y_2 can be described as a weak antiferromagnetically coupled ($J = -0.18$ K) dimer consisting of two V^{III} ions with dominant easy-plane-type single-ion anisotropy (D = 9.3 K). Modelling of the lanthanide moments as (quasi-)Ising spins at sufficiently low temperatures, magnetic fields, and excitation frequencies allows for a quantitative determination of the antiferromagnetic 3*d*-4*f* coupling J_{V-Ln} and the relative angle between the V^{III} and Ln^{III} principal anisotropy axes θ. The observed inverse correlation of J_{V-Ln} and θ along with their non-monotonous dependence on the Ln atomic number suggests that 3*d*→4*f* charge transfer is the dominant exchange process between V^{III} and Ln^{III} ions. This presents a stark contrast to other molecular 3*d*-4*f* complexes based on Cu^{II}, Ni^{II} and Fe^{III} ions studied in the literature, where a dominant 3*d*→5*d* charge transfer process results in ferromagnetic 3*d*-4*f* coupling. The findings are rationalised by the predominantly π-character of the partially filled t_{2g} orbitals in V^{III}, which highlights the important role of the spatial distributions of the contributing 3*d* and 4*f* orbitals for the design of heterometallic 3*d*-4*f* molecular magnets.

Antiferromagnetic intermolecular interactions that are mediated by short-contact halogen-halogen-bonds in the complex $[(Re^{IV}Br_5(\mu\text{-pyzc}))_2(Y(bpy)_2(OMe))_2]$ lead to the formation of $S = 3/2$ spin chains with local single-ion anisotropy. The numerical calculations demonstrate that the corresponding spin model is quite robust against finite-size effects, such that reliable simulations can be performed even when including only $N = 6$ spins with periodic boundary conditions. However, the $S = 3/2$ Heisenberg-chain model with local single-ion anisotropy can not adequately describe the experi-

mental magnetic data. Thus, the diffuse nature and strong spin-orbit coupling of the involved $5d$ orbitals yield more complex exchange effects, such as anisotropic coupling or interchain interactions.

In conclusion, the thesis at hand provides valuable insights into the magnetic properties of metal-organic molecular complexes through the quantitative determination of the microscopic spin Hamiltonian parameters. Taken together, the findings emphasise that for the rational design of molecular materials, ligand field engineering, orbital symmetry control and targeted tuning of exchange pathways have to be pursued in parallel. This requires further research to move beyond the search for optimised parameters in isolation, but instead calls for an understanding of how multiple microscopic parameters act in concert to produce the macroscopic magnetic response. Such an integrated design philosophy holds promise not only for improving the performance of known single-molecule magnets but also for accessing entirely new regimes of magnetic behaviour. By bridging synthetic chemistry, magnetisation studies, HF-EPR spectroscopy, and quantum-chemical calculations, the present work contributes to this holistic approach, which potentially guides novel magnetic materials toward both fundamental insight and functional application.

Appendix A

Measurements on Toroidal Cu_6Ln_3 Complexes

This appendix presents the experimental results of low temperature direct current magnetisation and HF-EPR studies on a series of toroidal $Cu^{II}Ln^{III}$ (Ln = Y, Gd, Dy) complexes. The polycrystalline powder samples were synthesised by Deepanshu Chauhan in the group of Prof. Dr. Gopalan Rajamaran at the *Indian Institute of Technology Bombay* (IIT Bombay).

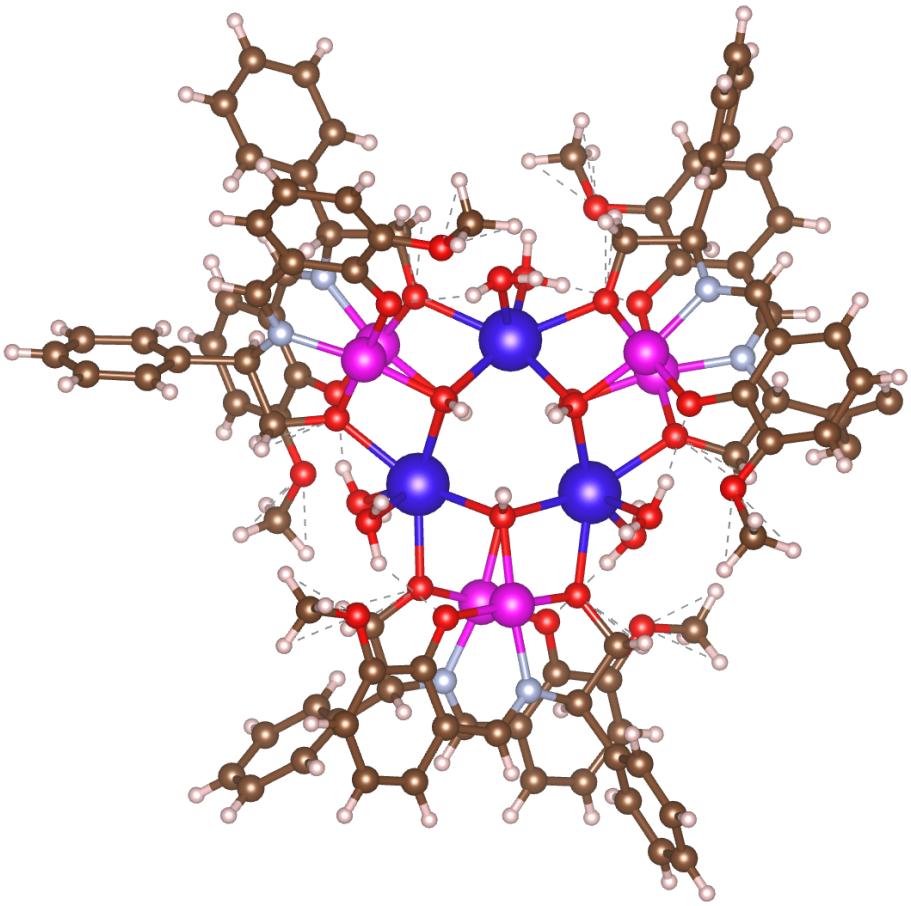


Figure A.1. Molecular structure of the Cu_6Ln_3 complexes as obtained from single crystal X-ray diffraction [144]. Pink: Cu(II); Dark blue: Ln(III); Light blue: N; Red: O; Brown: C; White: H. Figure was generated by VESTA [126].

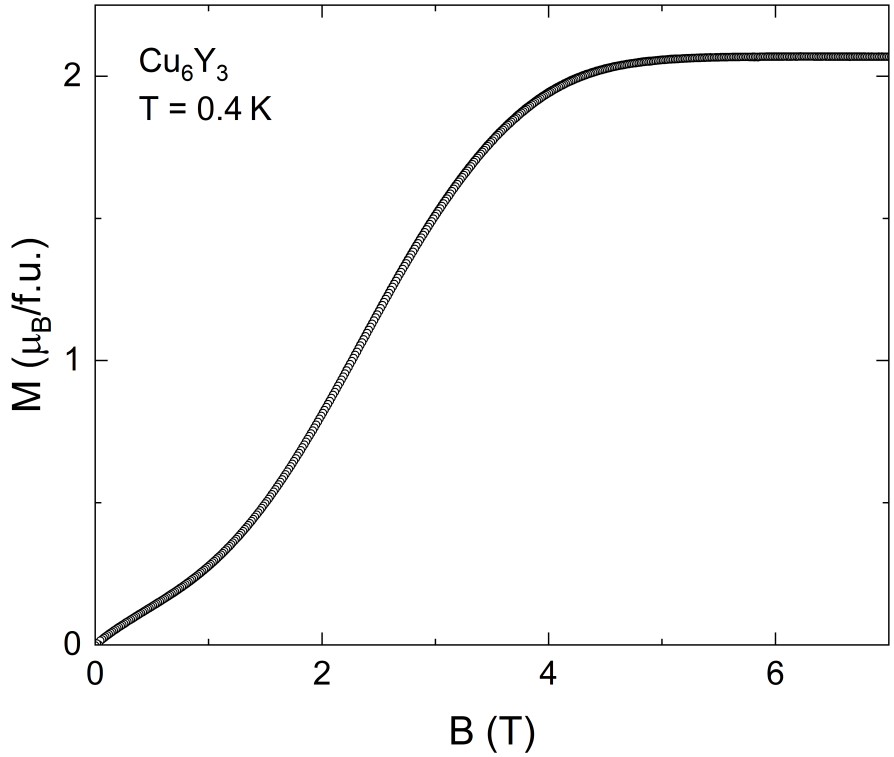


Figure A.2. Isothermal magnetisation of Cu_6Y_3 at $T = 0.4$ K.

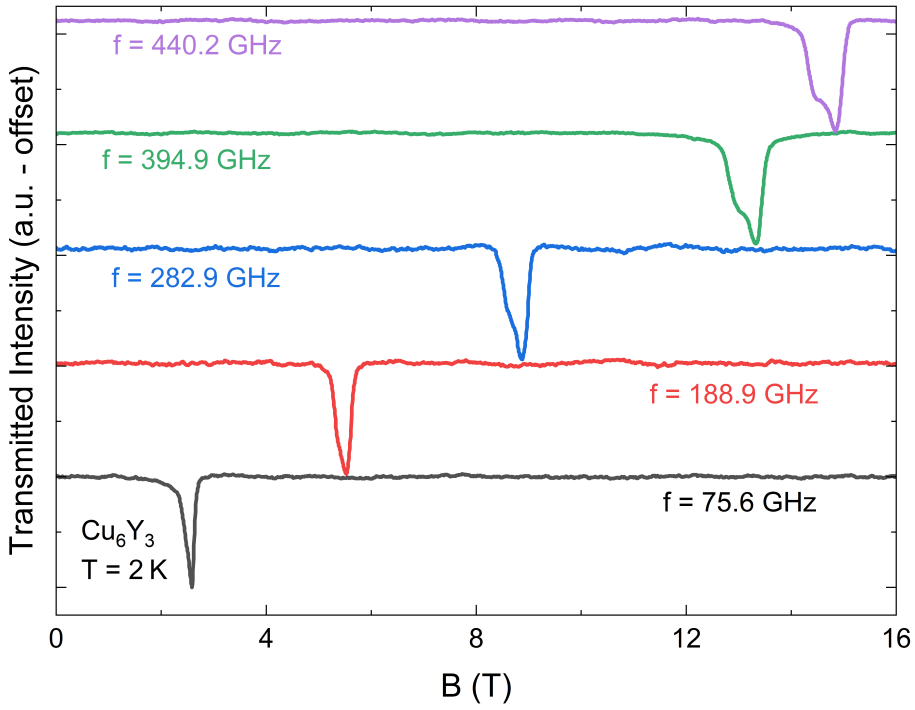


Figure A.3. HF-EPR spectra of Cu_6Y_3 obtained at various frequencies and $T = 2$ K.

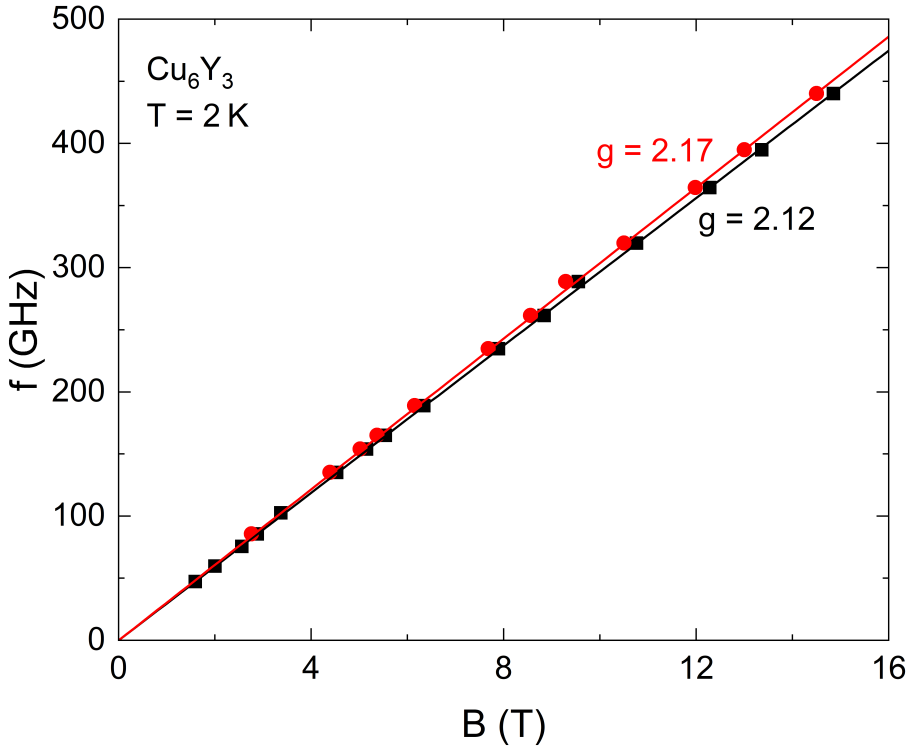


Figure A.4. Frequency versus resonance field diagram of Cu_6Y_3 at $T = 2$ K obtained by collecting the resonance positions at different frequencies. Solid lines depict linear fits of the type $f = g\mu_B B/h$ to the resonance branches.

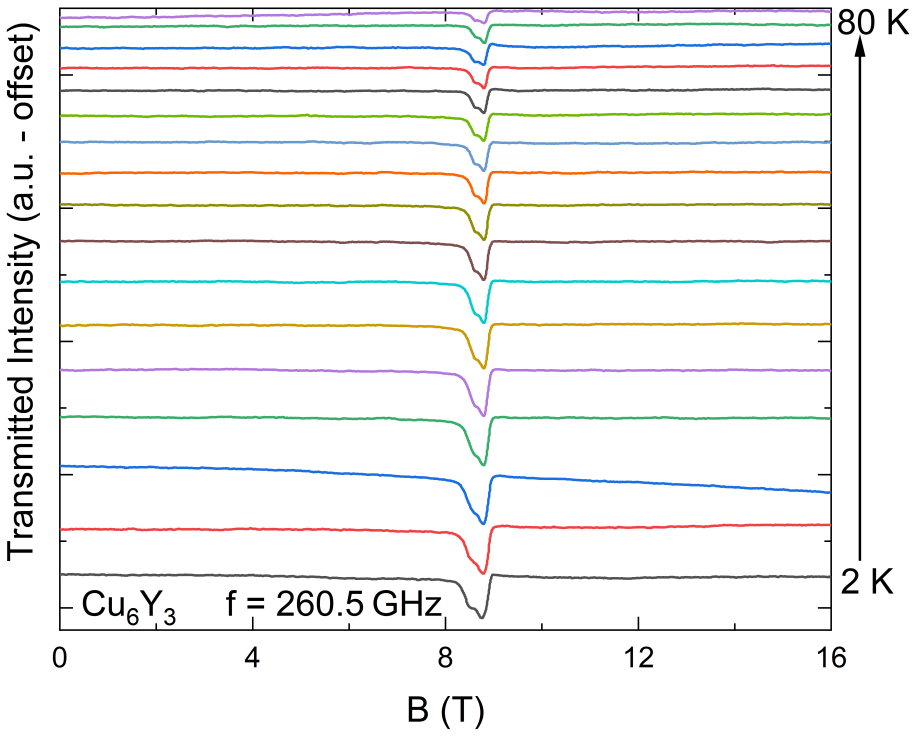


Figure A.5. HF-EPR spectra of Cu_6Y_3 obtained at $f = 260.5$ GHz and at various temperatures.

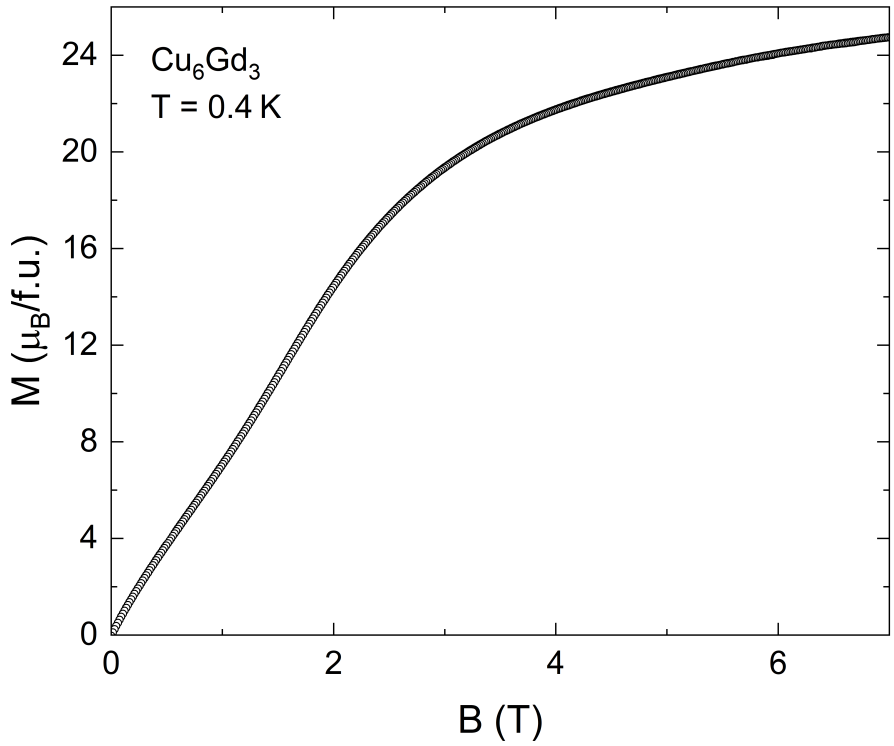


Figure A.6. Isothermal magnetisation of Cu_6Gd_3 at $T = 0.4$ K.

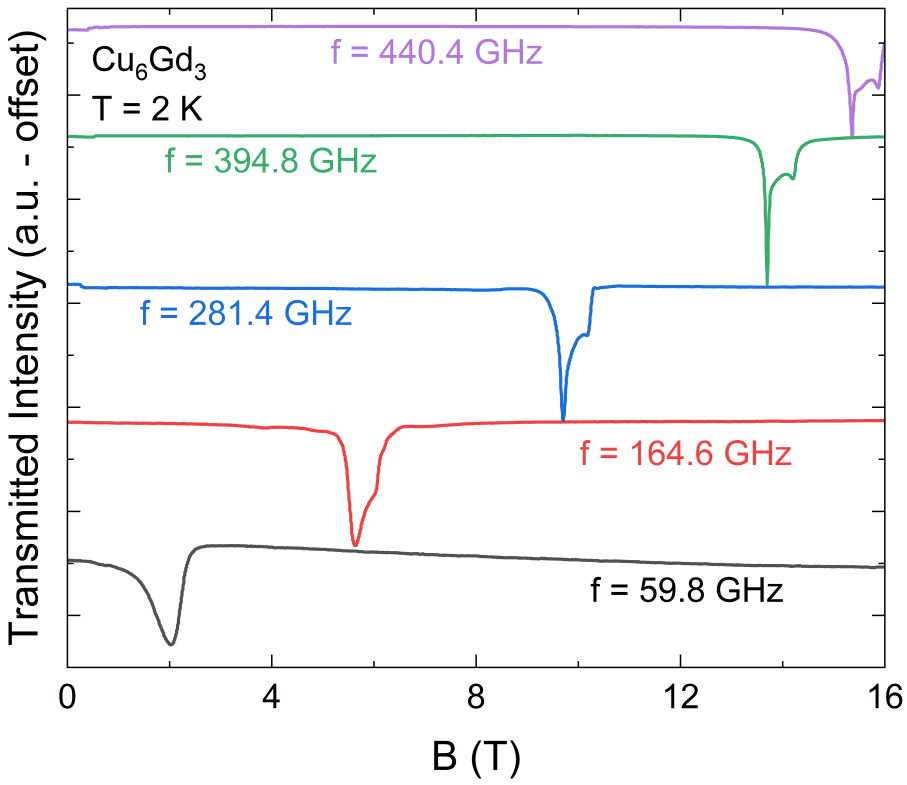


Figure A.7. HF-EPR spectra of Cu_6Gd_3 obtained at various frequencies at $T = 2$ K.

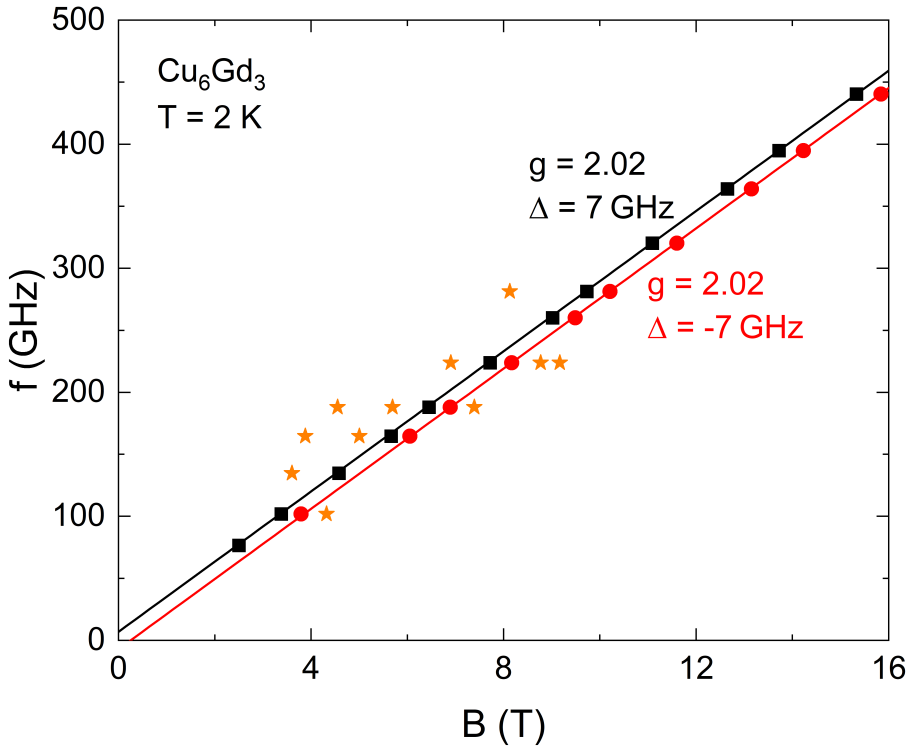


Figure A.8. Frequency versus resonance field diagram of Cu_6Gd_3 at $T = 2$ K obtained by collecting the resonance positions at different frequencies. Solid lines depict linear fits of the type $f = g\mu_B B/h + \Delta$ to the resonance branches.

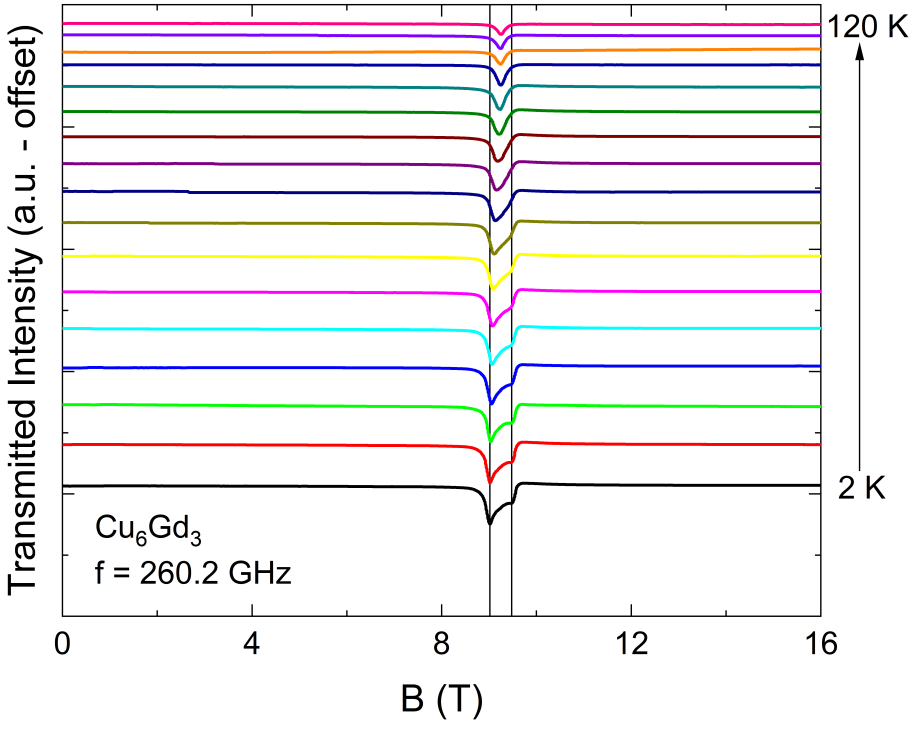


Figure A.9. HF-EPR spectra of Cu_6Gd_3 obtained at $f = 260.2$ GHz and at various temperatures.

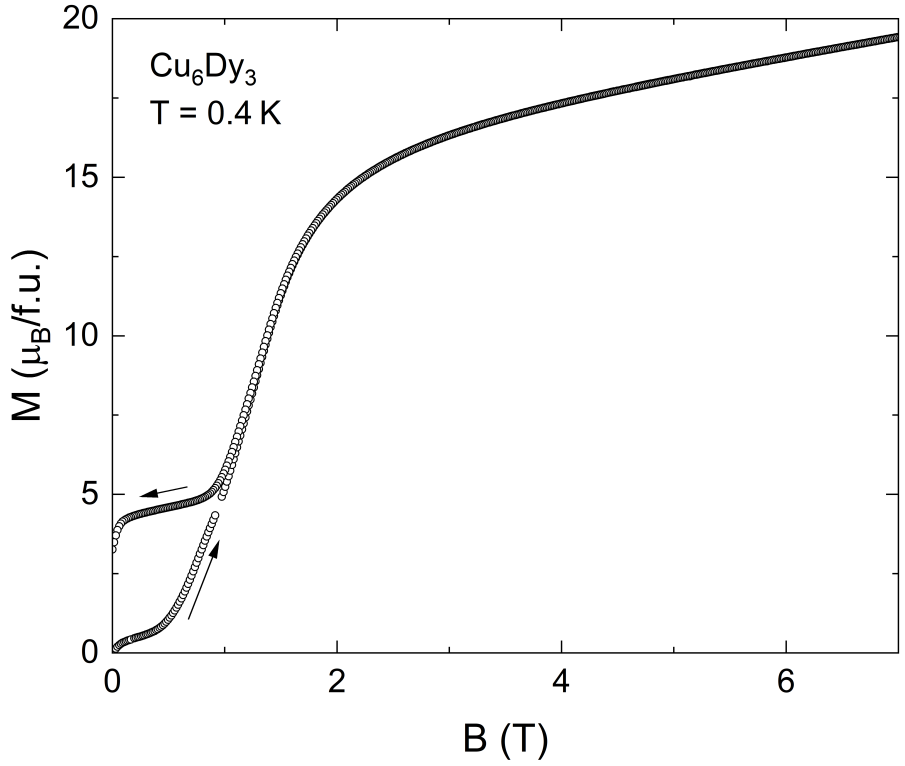


Figure A.10. Isothermal magnetisation of Cu_6Dy_3 at $T = 0.4$ K. Arrows depict the direction of the field-sweep.

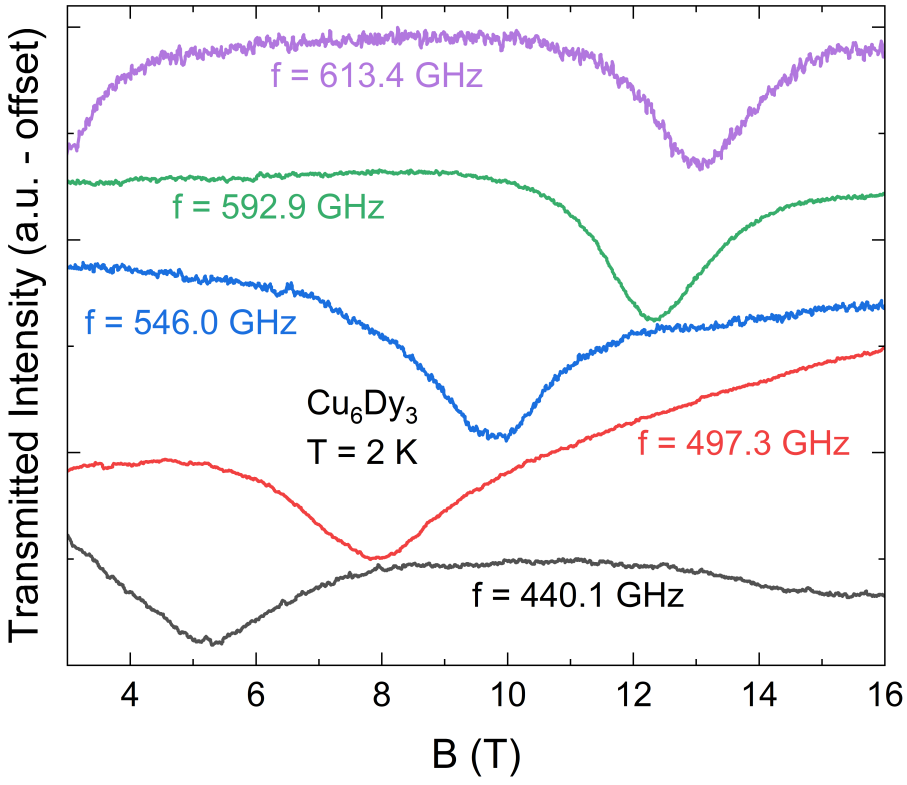


Figure A.11. HF-EPR spectra of Cu_6Dy_3 obtained at various frequencies at $T = 2$ K.

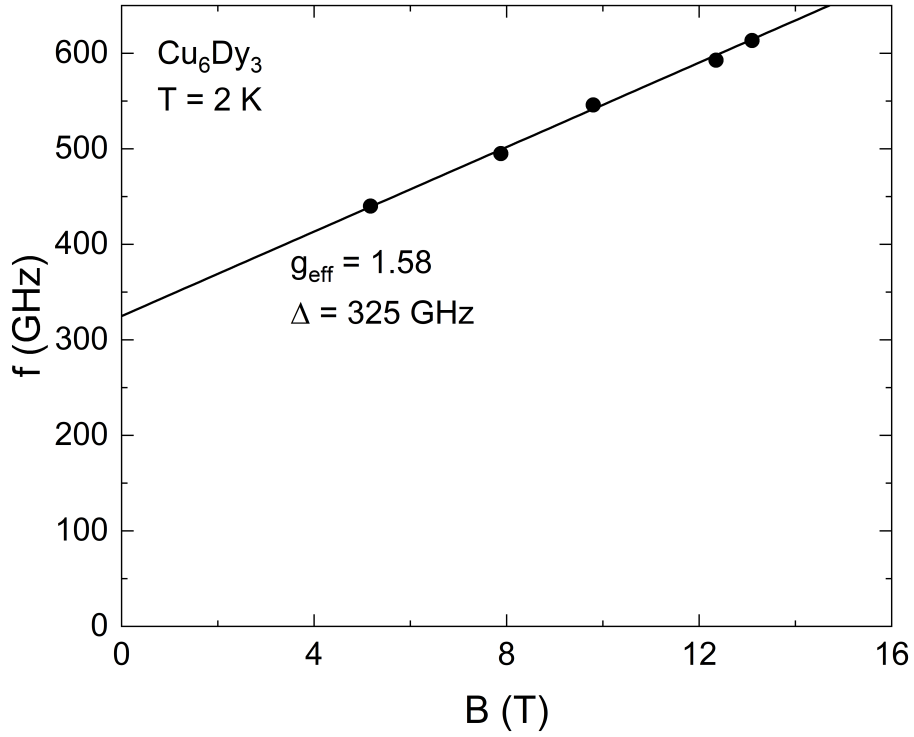


Figure A.12. Frequency versus resonance field diagram of Cu_6Dy_3 at $T = 2$ K obtained by collecting the resonance positions at different frequencies. Solid lines depict linear fits of the type $f = g_{\mathrm{eff}}\mu_{\mathrm{B}}B/h + \Delta$ to the resonance branches.

Appendix B

Magnetisation Studies on Dimeric Ln_2 Complexes

This appendix presents the experimental results of alternating and direct current magnetisation studies on a series of dimeric Ln_2^{III} (Ln = Nd, Gd, Dy, Ho, Er) complexes. The polycrystalline powder samples were synthesised by Yangxin Chen in the group of Prof. Dr. Annie K. Powell at the *Karlsruhe Institute for Technology* (KIT).

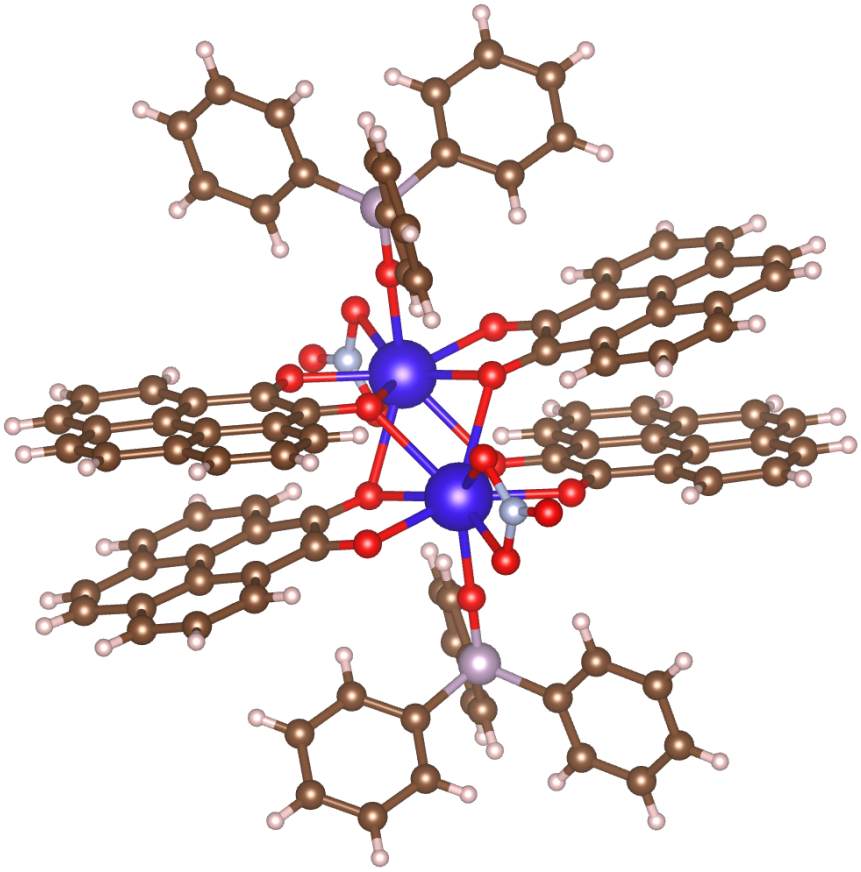


Figure B.1. Molecular structure of the dimeric Ln_2 complexes as obtained from single crystal X-ray diffraction [125]. Dark blue: Ln(III); Light blue: N; Grey: P; Red: O; Brown: C; White: H. Figure was generated by VESTA [126].

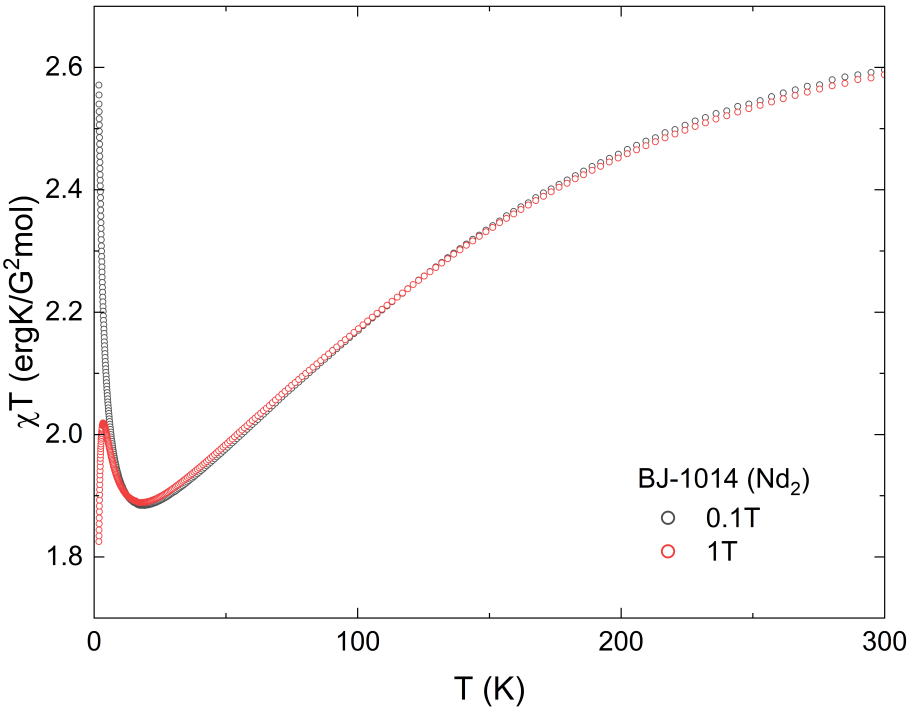


Figure B.2. Static magnetic susceptibility of Nd_2 at various magnetic fields.

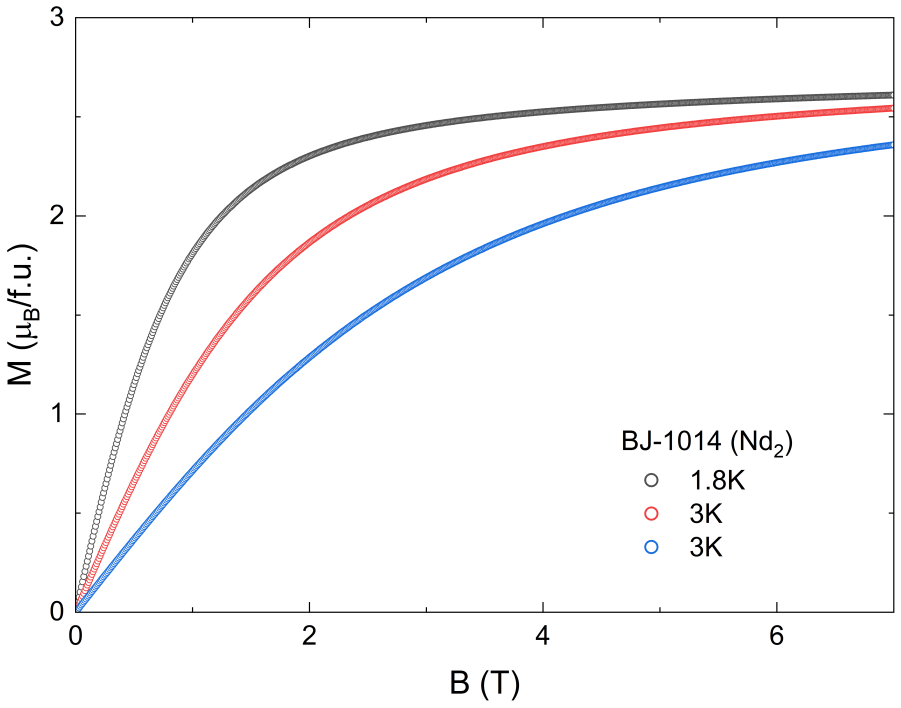


Figure B.3. Isothermal magnetisation of Nd_2 at various temperatures.

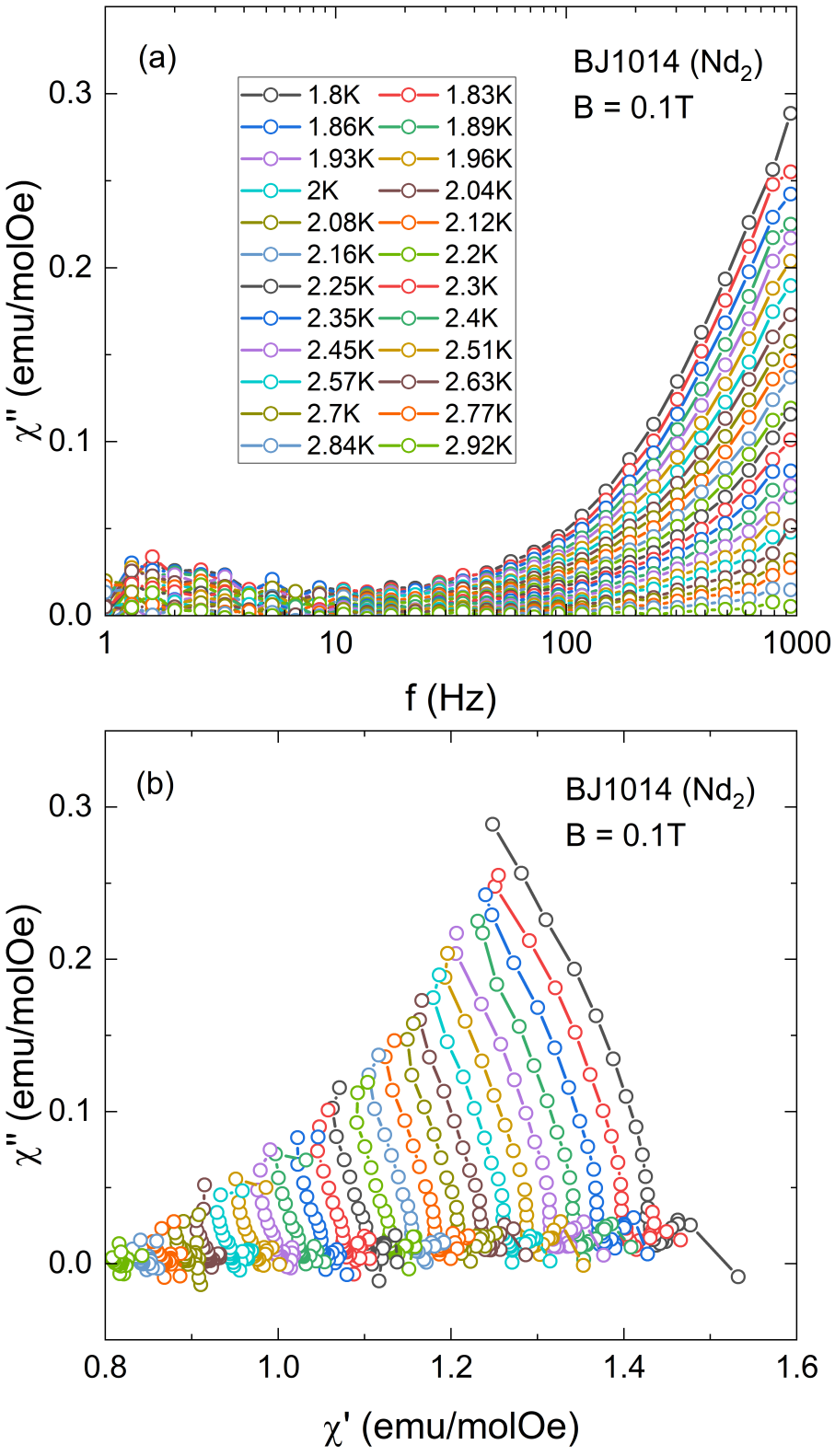


Figure B.4. Out-of-phase dynamic magnetic susceptibility (a) and Cole-Cole plot (b) of Nd_2 at $B = 0.1$ T and various temperatures.

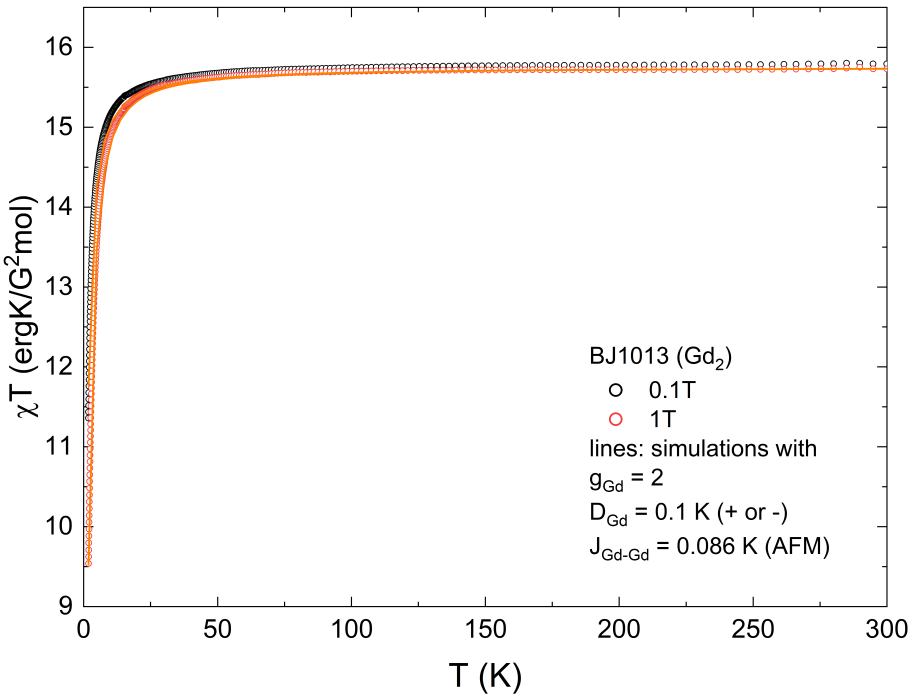


Figure B.5. Static magnetic susceptibility of Gd_2 at various magnetic fields. Solid orange lines depict fits of a coupled dimer model with local magnetic anisotropy to the data.

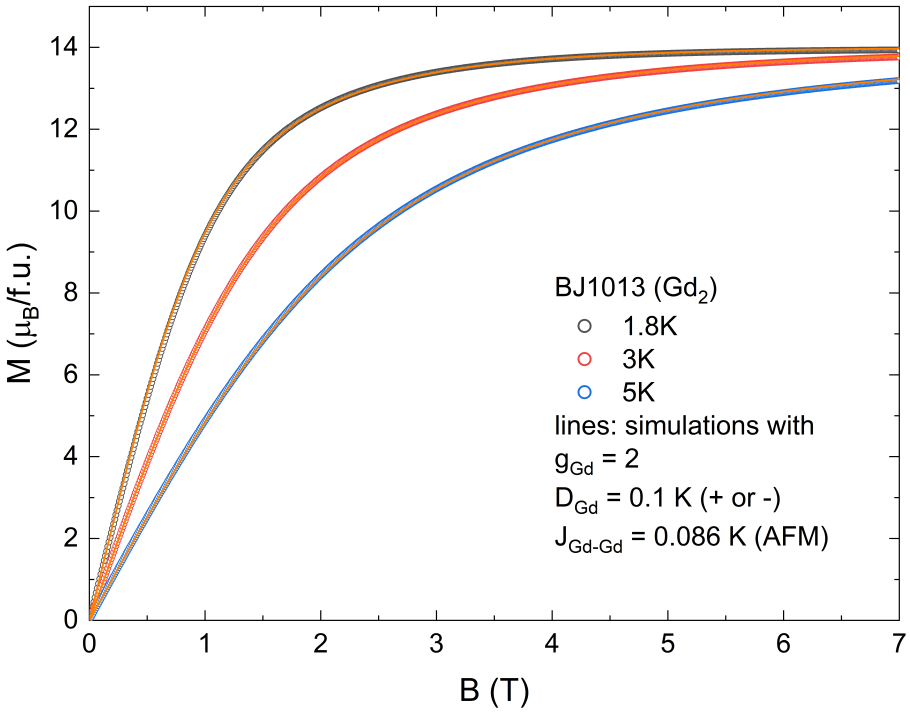


Figure B.6. Isothermal magnetisation of Gd_2 at various temperatures. Solid orange lines depict fits of a coupled dimer model with local magnetic anisotropy to the data.

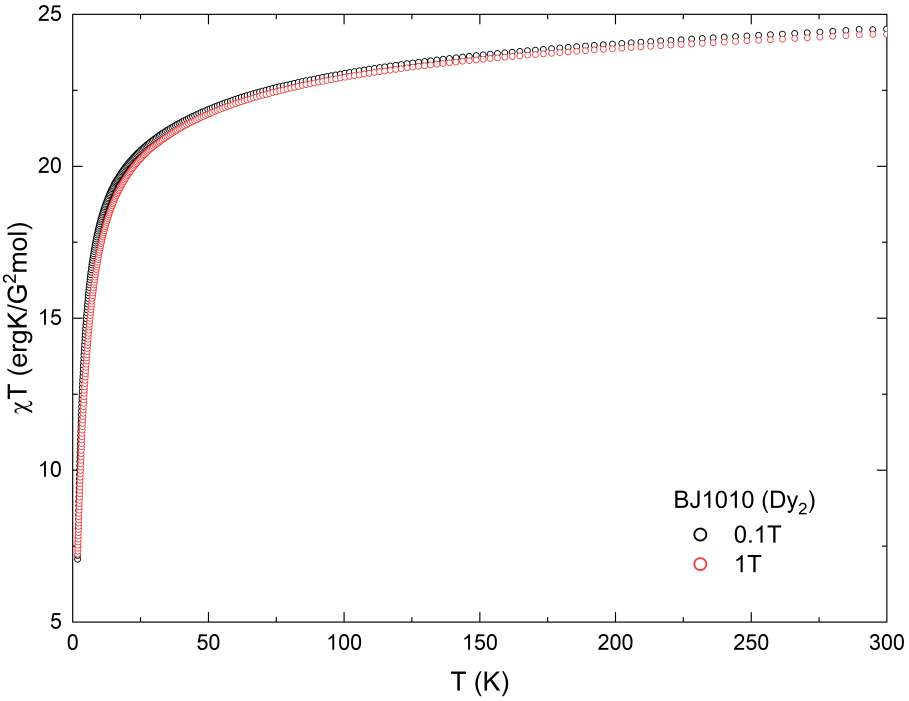


Figure B.7. Static magnetic susceptibility of Dy_2 at various magnetic fields.

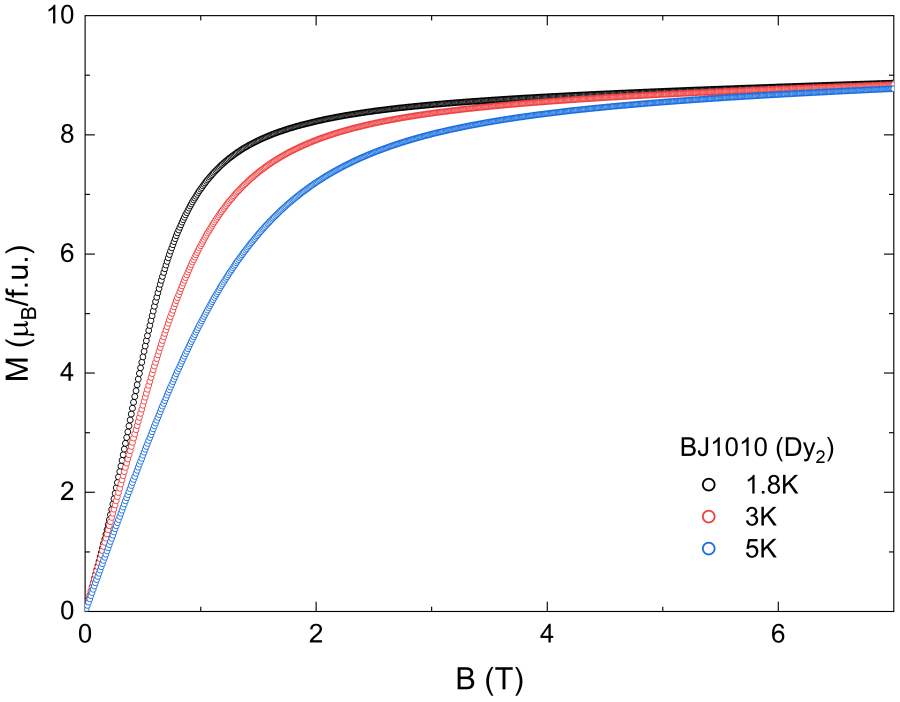


Figure B.8. Isothermal magnetisation of Dy_2 at various temperatures.

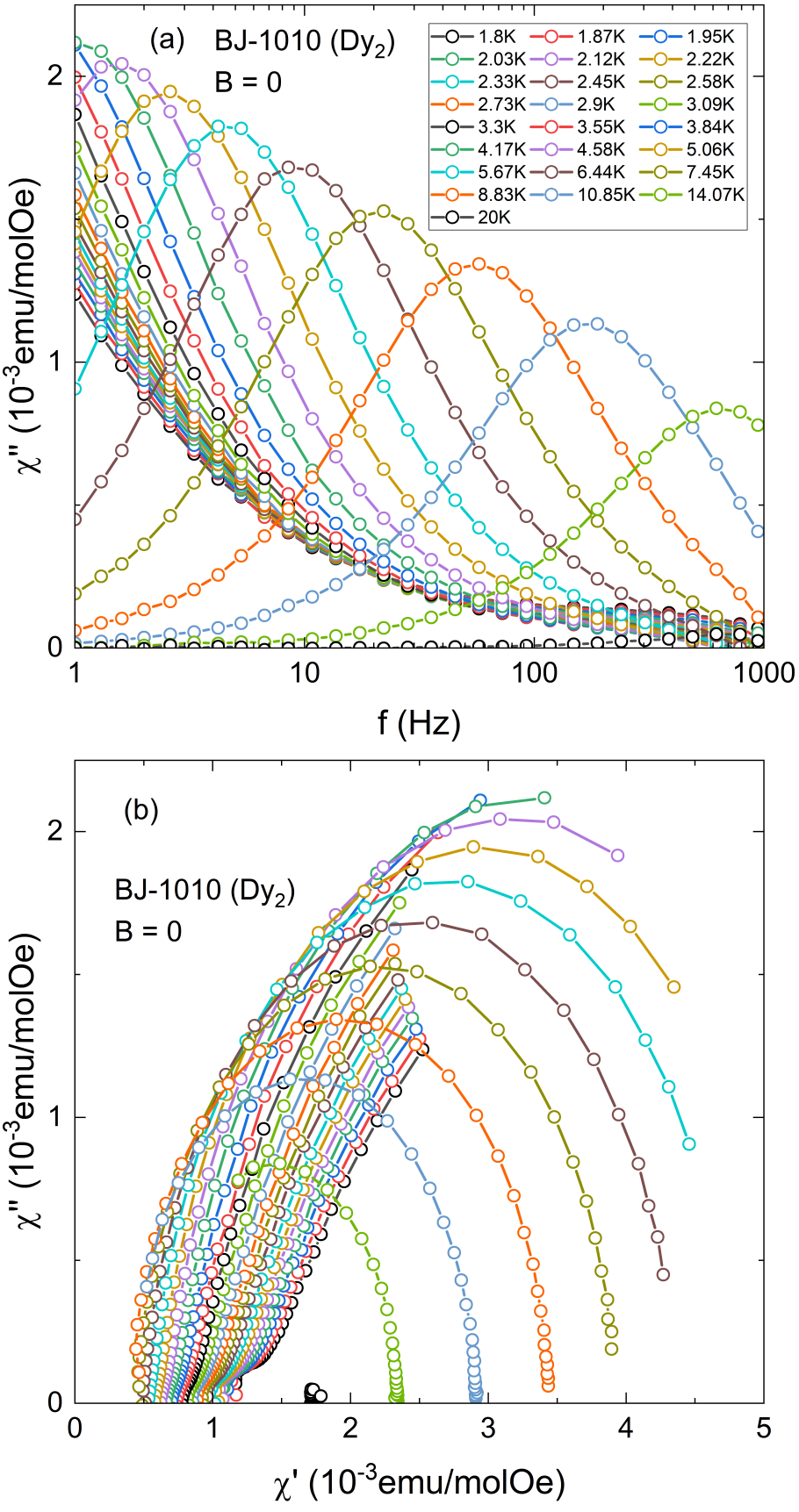


Figure B.9. Out-of-phase dynamic magnetic susceptibility (a) and Cole-Cole plot (b) of Dy_2 at $B = 0$ and various temperatures.

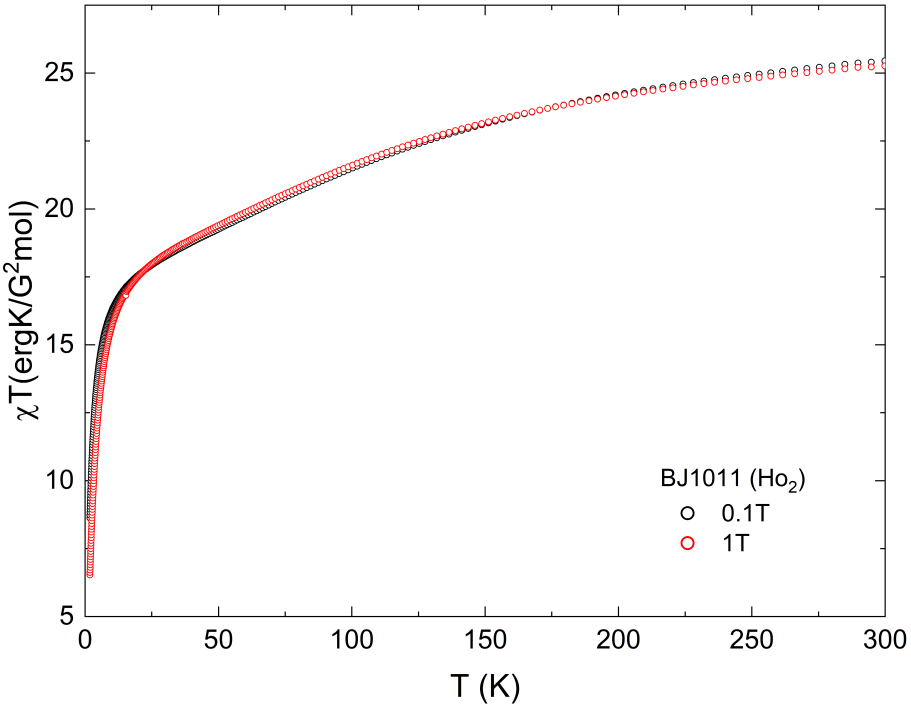


Figure B.10. Static magnetic susceptibility of Ho_2 at various magnetic fields.

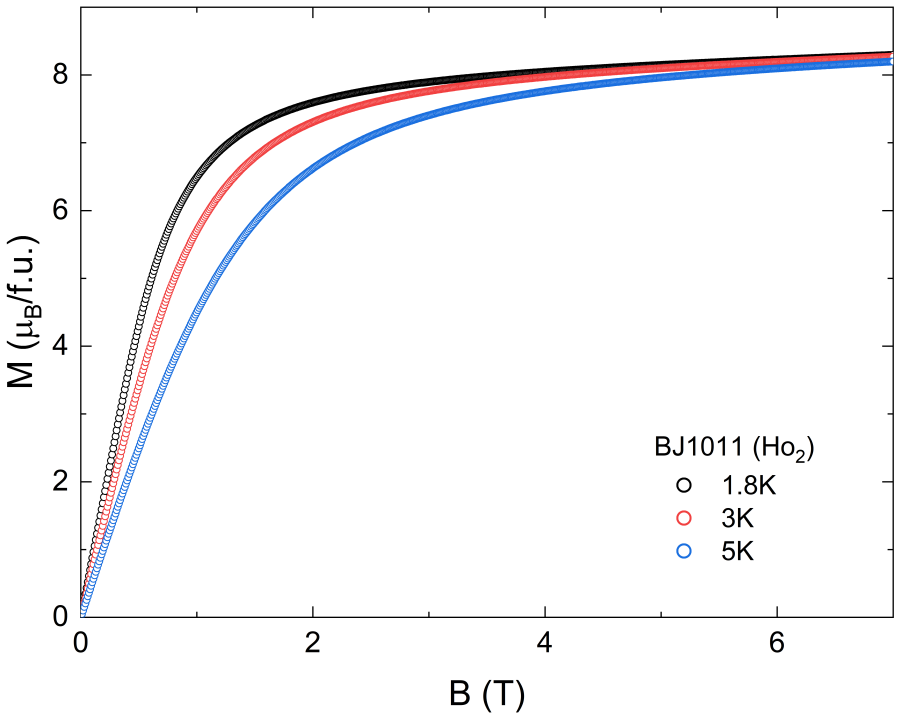


Figure B.11. Isothermal magnetisation of Ho_2 at various temperatures.

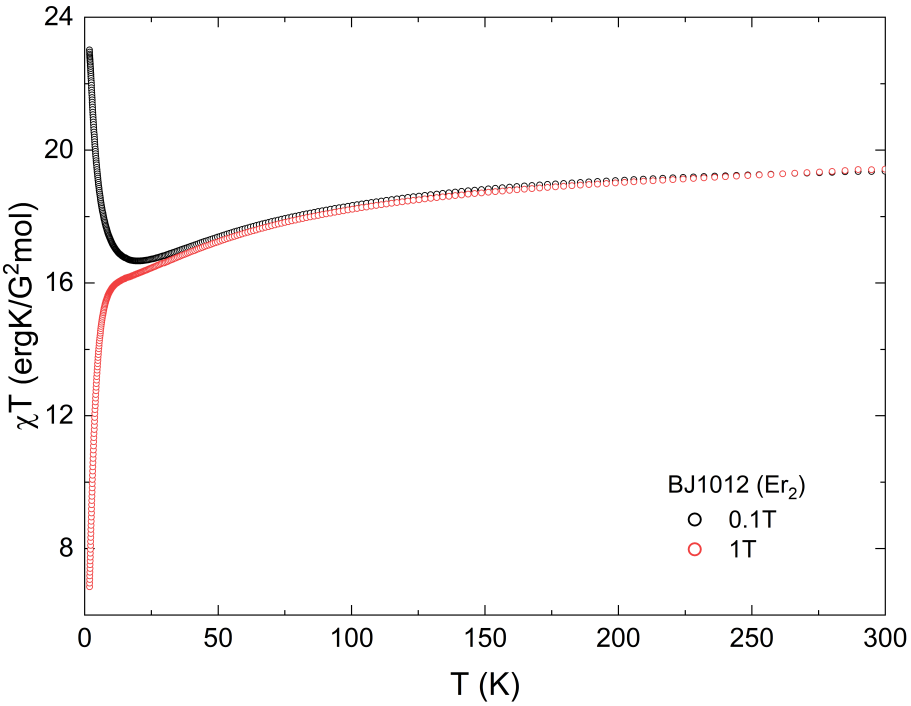


Figure B.12. Static magnetic susceptibility of Er_2 at various magnetic fields.

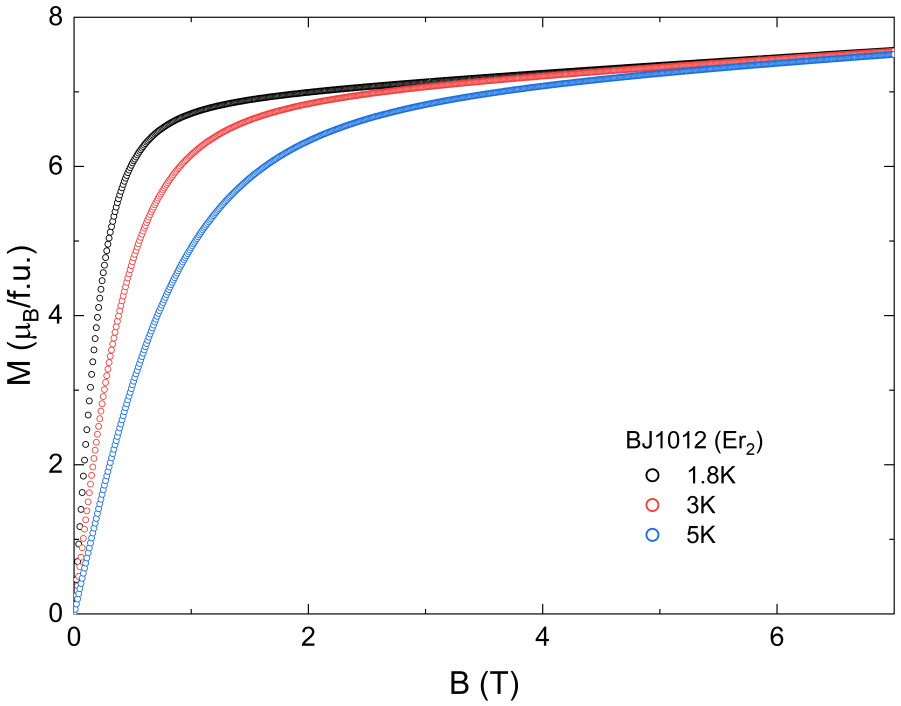


Figure B.13. Isothermal magnetisation of Er_2 at various temperatures.

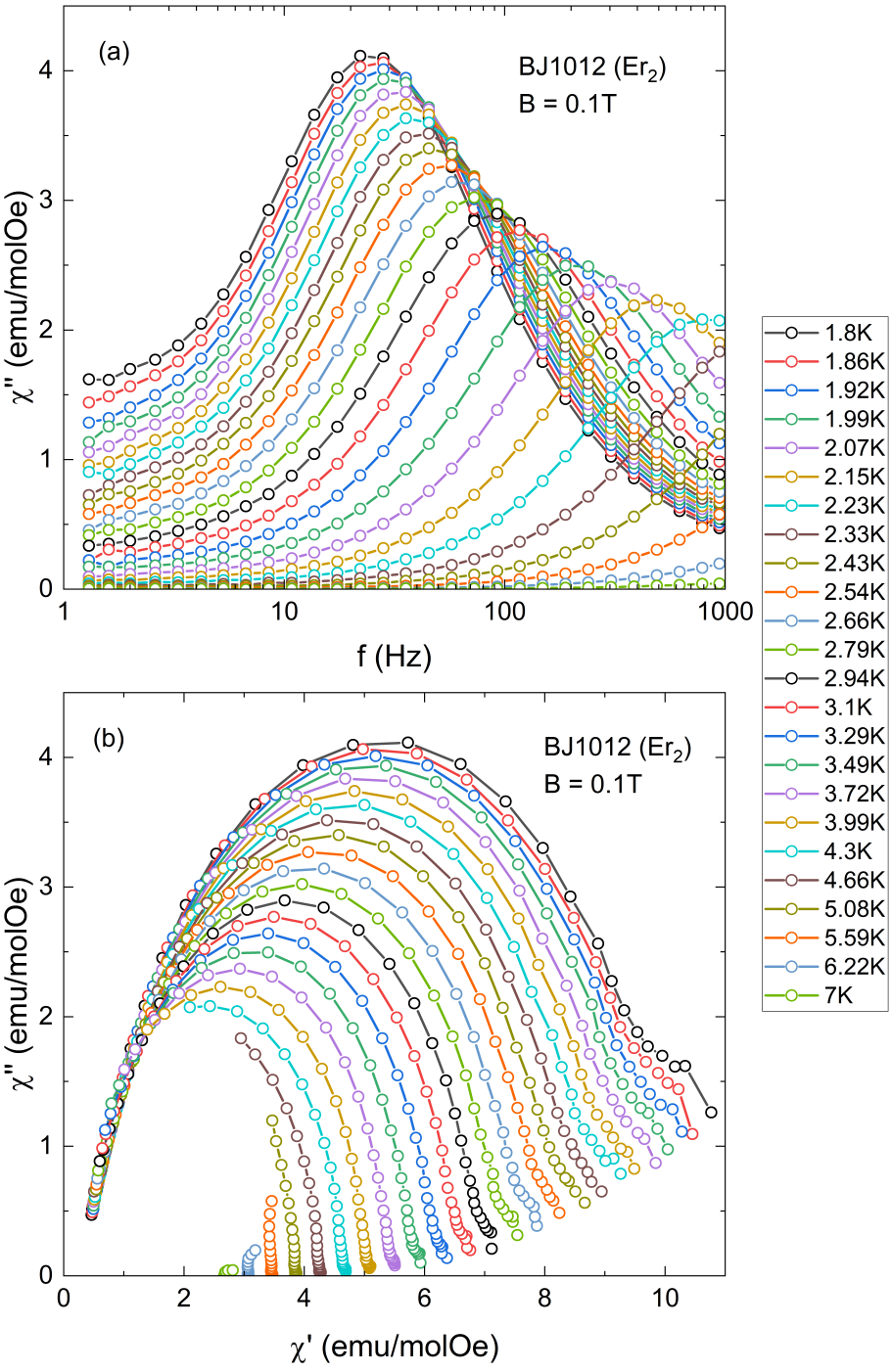
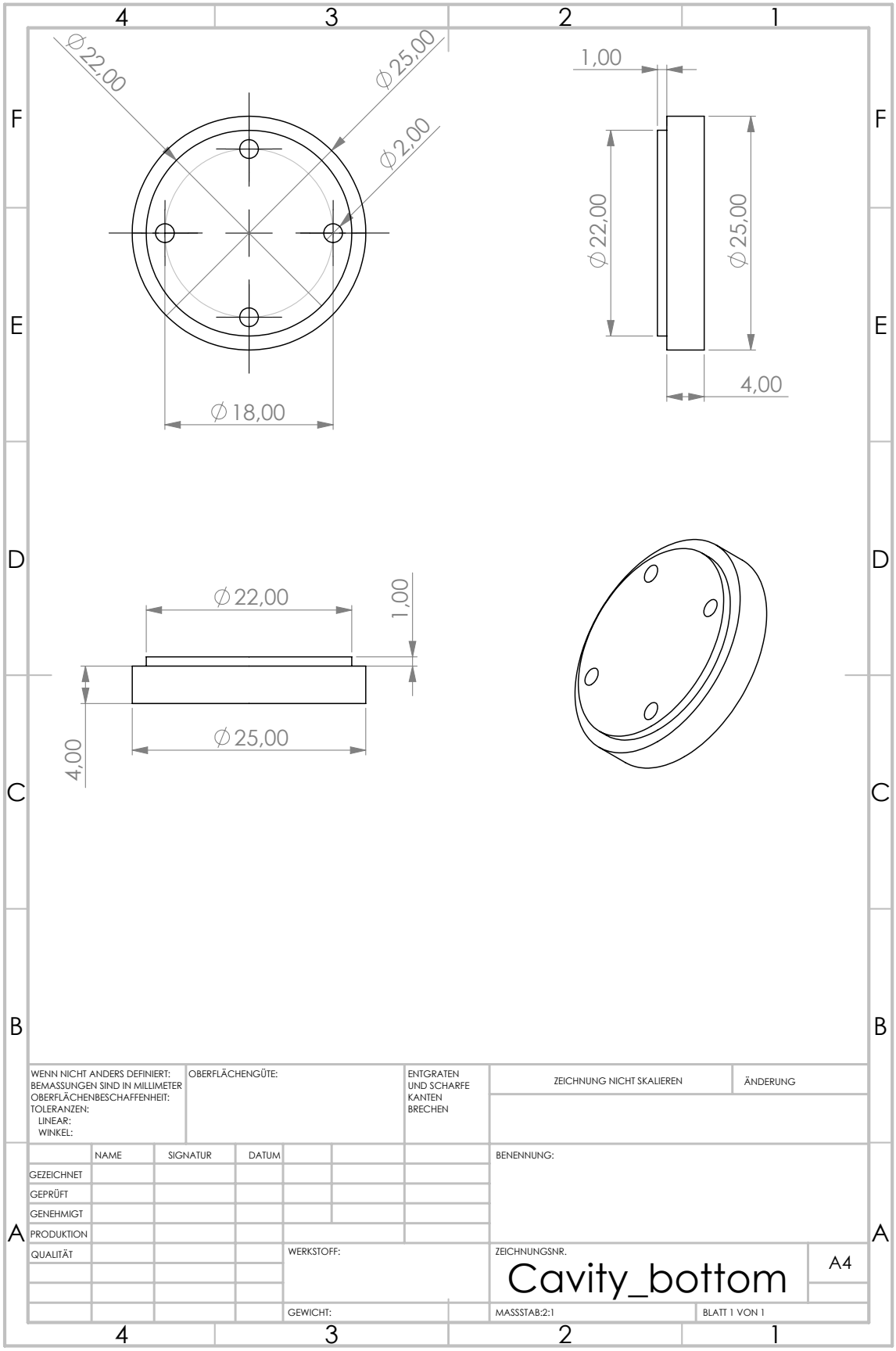
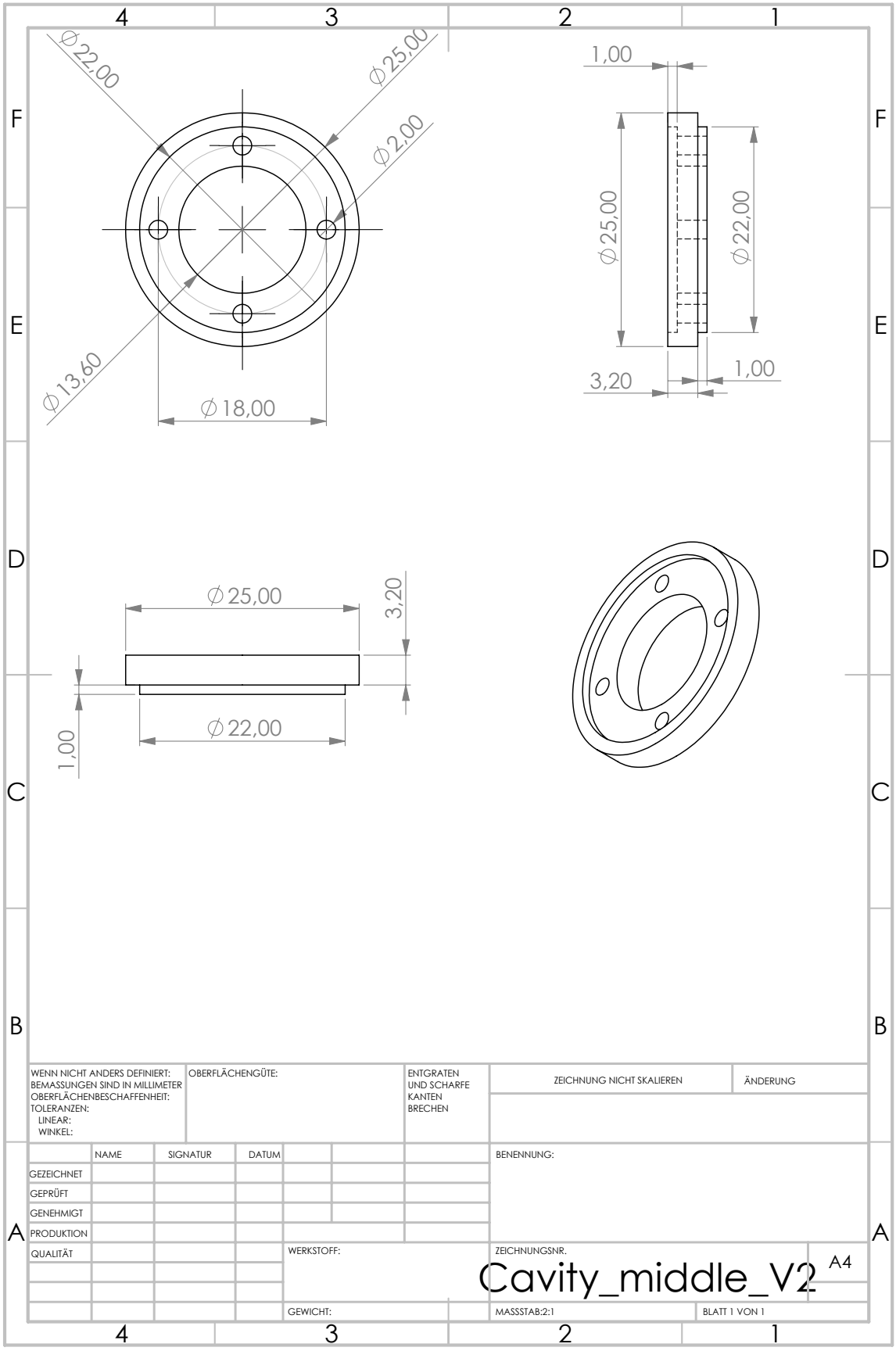


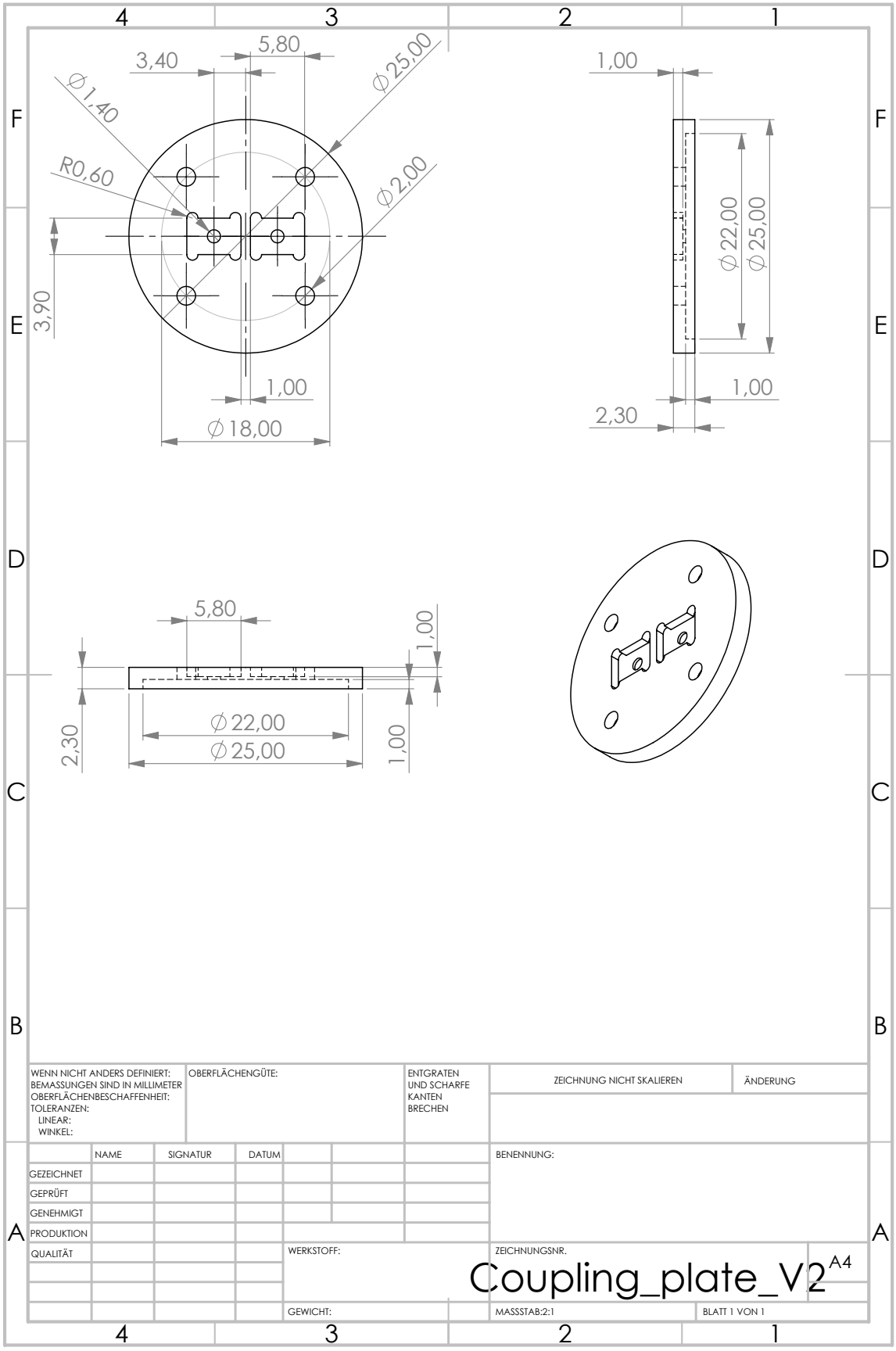
Figure B.14. Out-of-phase dynamic magnetic susceptibility (a) and Cole-Cole plot (b) of Er_2 at $B = 0.1$ T and various temperatures.

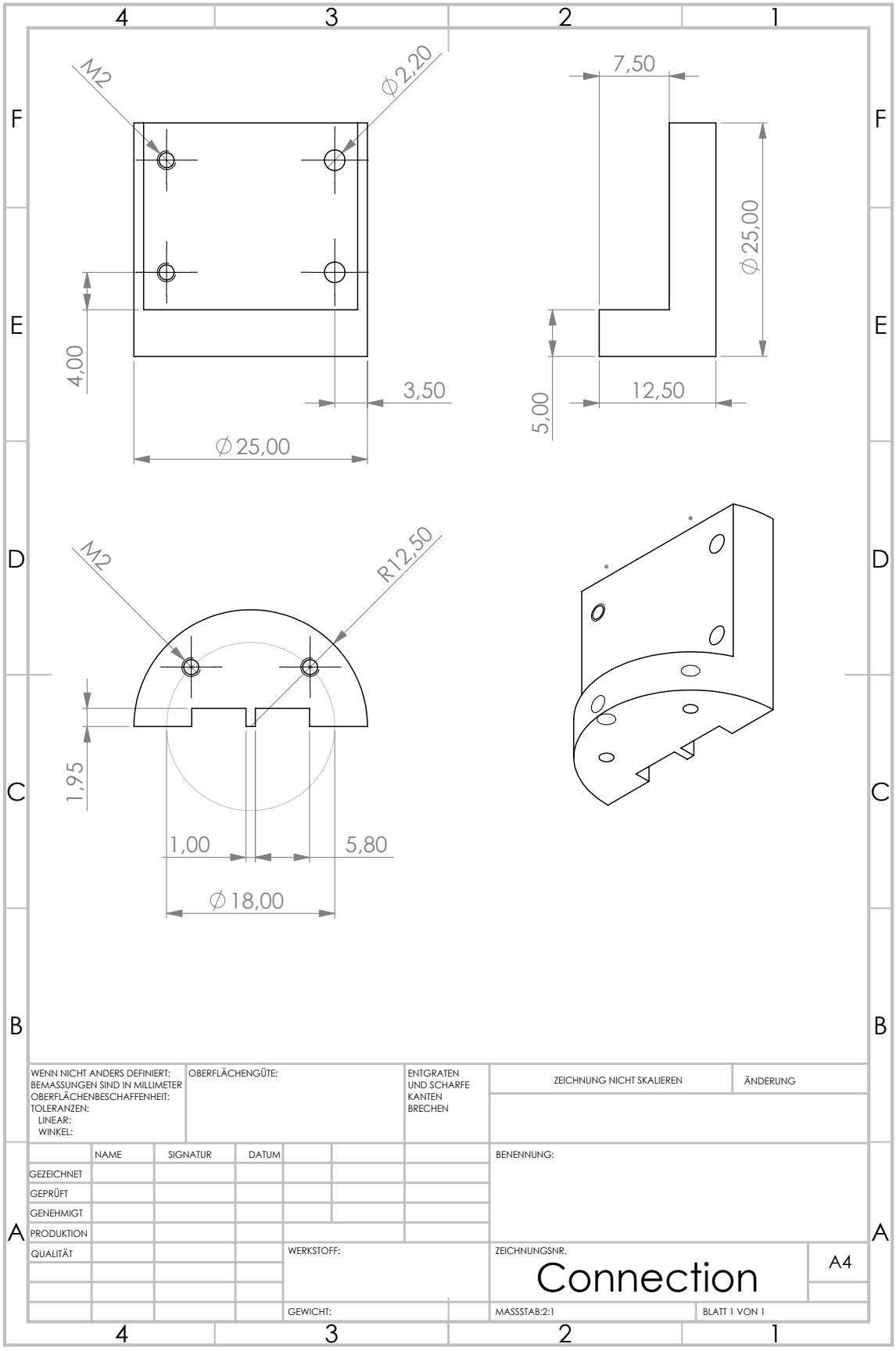
Appendix C

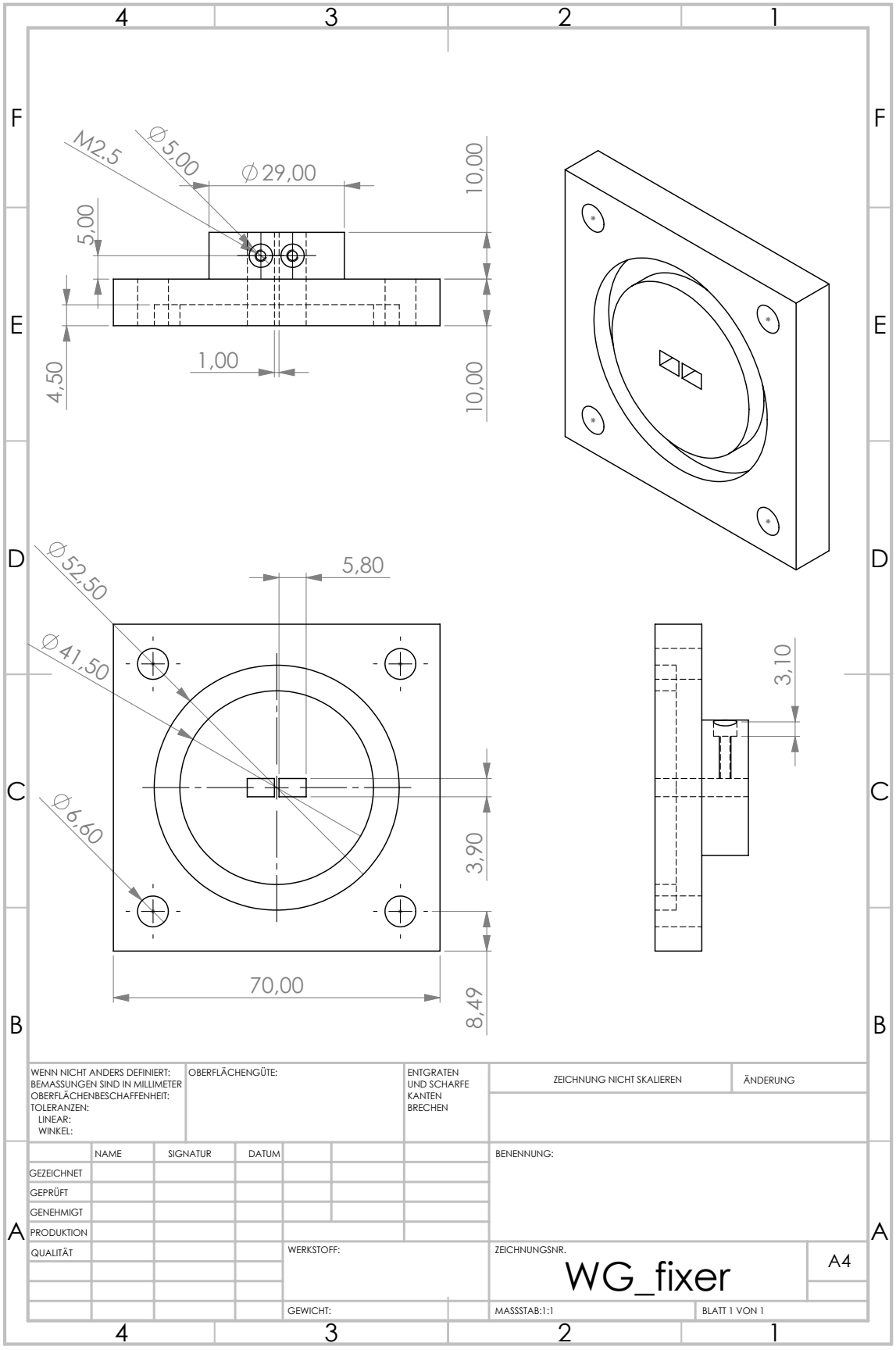
Construction of a V-band Cavity for the HF-EPR Setup

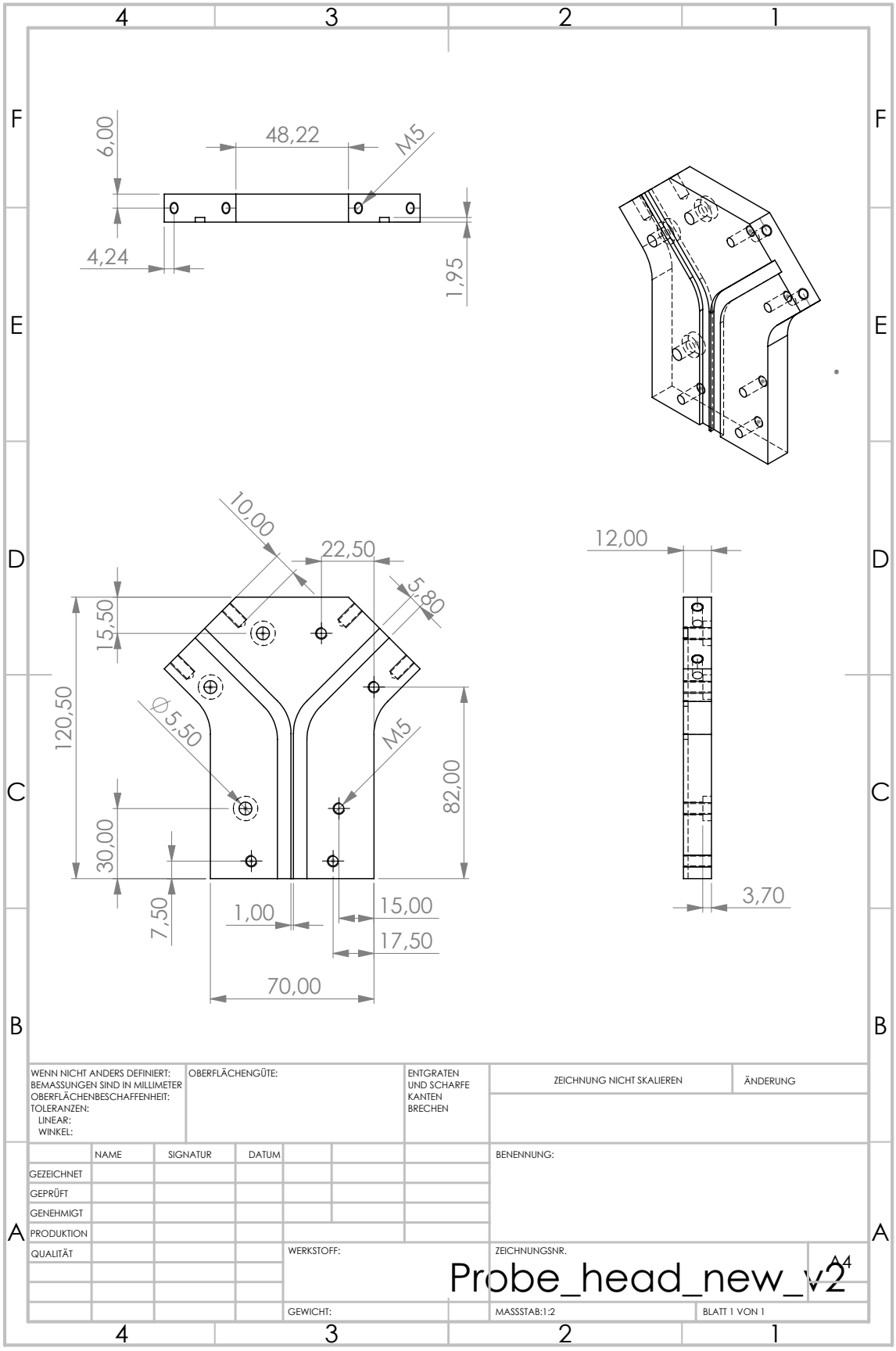

4
3
2
1
F
E
D
C
B
A
∅22,00
∅25,00
∅2,00
∅18,00
1,00
∅22,00
∅25,00
4,00
∅22,00
1,00
∅25,00
4,00
WENN NICHT ANDERS DEFINIERT:
BEMASSUNGEN SIND IN MILLIMETER
OBERFLÄCHENBESCHAFFENHEIT:
TOLERANZEN:
LINEAR:
WINKEL:
OBERFLÄCHENGÜTE:
ENTGRATEN UND SCHARFE KANTEN BRECHEN
ZEICHNUNG NICHT SKALIEREN
ÄNDERUNG
NAME
SIGNATUR
DATUM
GEZEICHNET
GEPRÜFT
GENEHMIGT
PRODUKTION
QUALITÄT
BENENNUNG:
WERKSTOFF:
GEWICHT:
ZEICHNUNGSNR.
Cavity_bottom
A4
MASSSTAB:2:1
BLATT 1 VON 1


4
3
2
1
F
E
D
C
B
A
⌀22,00
⌀25,00
⌀2,00
⌀13,60
⌀18,00
1,00
⌀25,00
⌀22,00
3,20
1,00
⌀25,00
3,20
⌀22,00
1,00
WENN NICHT ANDERS DEFINIERT:
BEMASSUNGEN SIND IN MILLIMETER
OBERFLÄCHENBESCHAFFENHEIT:
TOLERANZEN:
LINEAR:
WINKEL:
OBERFLÄCHENGÜTE:
ENTGRATEN UND SCHARFE KANTEN BRECHEN
ZEICHNUNG NICHT SKALIEREN
ÄNDERUNG
NAME
SIGNATUR
DATUM
GEZEICHNET
GEPRÜFT
GENEHMIGT
PRODUKTION
QUALITÄT
BENENNUNG:
WERKSTOFF:
ZEICHNUNGSNR.
A4
Cavity_middle_V2
GEWICHT:
MASSSTAB:2:1
BLATT 1 VON 1


4
3
2
1
F
E
D
C
B
A
5,80
3,40
⌀1,40
⌀25,00
R0,60
⌀2,00
3,90
1,00
⌀18,00
1,00
⌀22,00
⌀25,00
1,00
2,30
5,80
1,00
⌀22,00
⌀25,00
2,30
1,00
WENN NICHT ANDERS DEFINIERT:
BEMASSUNGEN SIND IN MILLIMETER
OBERFLÄCHENBESCHAFFENHEIT:
TOLERANZEN:
LINEAR:
WINKEL:
OBERFLÄCHENGÜTE:
ENTGRATEN UND SCHARFE KANTEN BRECHEN
ZEICHNUNG NICHT SKALIEREN
ÄNDERUNG
NAME
SIGNATUR
DATUM
GEZEICHNET
GEPRÜFT
GENEHMIGT
PRODUKTION
QUALITÄT
BENENNUNG:
WERKSTOFF:
ZEICHNUNGSNR.
Coupling_plate_V2
A4
GEWICHT:
MASSSTAB:2:1
BLATT 1 VON 1


M2
⌀2,20
4,00
3,50
⌀25,00
7,50
⌀25,00
5,00
12,50
M2
R12,50
1,95
1,00
5,80
⌀18,00
WENN NICHT ANDERS DEFINIERT:
BEMASSUNGEN SIND IN MILLIMETER
OBERFLÄCHENBESCHAFFENHEIT:
TOLERANZEN:
LINEAR:
WINKEL:
OBERFLÄCHENGÜTE:
ENTGRATEN UND SCHARFE KANTEN BRECHEN
ZEICHNUNG NICHT SKALIEREN
ÄNDERUNG
NAME
SIGNATUR
DATUM
BENENNUNG:
GEZEICHNET
GEPRÜFT
GENEHMIGT
PRODUKTION
QUALITÄT
WERKSTOFF:
ZEICHNUNGSNR.
Connection
A4
GEWICHT:
MASSSTAB:2:1
BLATT 1 VON 1


4
3
2
1
F
E
D
C
B
A
M2.5
∅5,00
∅29,00
10,00
5,00
1,00
4,50
10,00
∅52,50
∅41,50
∅6,60
5,80
3,90
70,00
8,49
3,10
WENN NICHT ANDERS DEFINIERT:
BEMASSUNGEN SIND IN MILLIMETER
OBERFLÄCHENBESCHAFFENHEIT:
TOLERANZEN:
LINEAR:
WINKEL:
OBERFLÄCHENGÜTE:
ENTGRATEN UND SCHARFE KANTEN BRECHEN
ZEICHNUNG NICHT SKALIEREN
ÄNDERUNG
NAME
SIGNATUR
DATUM
GEZEICHNET
GEPRÜFT
GENEHMIGT
PRODUKTION
QUALITÄT
BENENNUNG:
WERKSTOFF:
ZEICHNUNGSNR.
WG_fixer
A4
GEWICHT:
MASSSTAB:1:1
BLATT 1 VON 1


4
3
2
1
F
E
D
C
B
A
6,00
48,22
M5
4,24
1,95
10,00
22,50
5,80
15,50
120,50
Ø5,50
M5
82,00
30,00
7,50
1,00
15,00
17,50
70,00
12,00
3,70
WENN NICHT ANDERS DEFINIERT:
BEMASSUNGEN SIND IN MILLIMETER
OBERFLÄCHENBESCHAFFENHEIT:
TOLERANZEN:
LINEAR:
WINKEL:
OBERFLÄCHENGÜTE:
ENTGRATEN UND SCHARFE KANTEN BRECHEN
ZEICHNUNG NICHT SKALIEREN
ÄNDERUNG
NAME
SIGNATUR
DATUM
GEZEICHNET
GEPRÜFT
GENEHMIGT
PRODUKTION
QUALITÄT
BENENNUNG:
WERKSTOFF:
ZEICHNUNGSNR.
A4
Probe_head_new_v2
GEWICHT:
MASSSTAB:1:2
BLATT 1 VON 1

Appendix D

Studies Beyond the Scope of this Thesis

The following appendix sections present two dilatometric studies on the inorganic compound $Na_2Co_2TeO_6$. The corresponding data were measured in the frame of the author's Master thesis [145], but the data analysis and interpretation was conducted during his doctoral studies.

D.1 Signatures of a Quantum Critical Endpoint in the Kitaev Candidate $Na_2Co_2TeO_6$

The results of this section were published as a research Letter in *Physical Review B* Volume 110, Issue 14 in October 2024 [146]. The corresponding manuscript is also available under the DOI: https://doi.org/10.1103/PhysRevB.110.L140402. Specific contributions of each co-author, especially the contribution of J. Arneth, who serves as the corresponding and first author, are given in the following list:

- J. Arneth performed the dilatometry and magnetisation measurements, analysed the corresponding data, constructed the plotted figures, and wrote the presented manuscript draft.
- K.-Y. Choi, R. Kalaivanan and R. Sankar grew the single crystalline samples and conducted the structural analysis.
- R. Klingeler led the project and supported the data analysis and manuscript writing.
- All authors proofread the manuscript.

PHYSICAL REVIEW B **110**, L140402 (2024)

Letter Editors' Suggestion

Signatures of a quantum critical endpoint in the Kitaev candidate $Na_2Co_2TeO_6$

J. Arneth,[1,*] K.-Y. Choi,[2] R. Kalaivanan,[3] R. Sankar,[3] and R. Klingeler[1,†]

[1]*Kirchhoff Institute for Physics, Heidelberg University, INF 227, D-69120 Heidelberg, Germany*

[2]*Department of Physics, Sungkyunkwan University, Suwon 16419, Republic of Korea*

[3]*Institute of Physics, Academia Sinica, Taipei 11529, Taiwan*

(Received 26 April 2024; revised 24 July 2024; accepted 11 September 2024; published 2 October 2024)

The putative Kitaev material $Na_2Co_2TeO_6$ has recently been proposed to enter a quantum spin disordered state when magnetic fields are applied in parallel to the honeycomb layers. In this Letter we uncover signatures of a quantum critical endpoint (QCEP) associated with the assumed order-disorder transition by means of high-resolution capacitance dilatometry. At the critical field $B_C \simeq 6$ T, a sign change of the out-of-plane thermal expansion coefficient α_c indicates the accumulation of entropy upon crossing the phase boundary. The proportional relationship between isothermal magnetization and magnetostriction signals that the QCEP can be tuned by magnetic field and pressure simultaneously. The presented results expand the material classes that exhibit metamagnetic quantum criticality to honeycomb antiferromagnets with possible Kitaev interactions.

DOI: 10.1103/PhysRevB.110.L140402

Within the framework of the everlasting search for a quantum spin liquid (QSL), the exactly solvable Kitaev model offers a promising route to a long-range entangled yet magnetically disordered state with exotic elementary excitations, such as Majorana fermions [1]. At the heart of this model lie strongly anisotropic, bond-dependent Ising interactions in a $S = 1/2$ honeycomb network, leading to pronounced magnetic frustration. The first wave of Kitaev candidate materials consisted of d^5 transition metal ions with strong spin-orbit coupling (SOC) situated in edge-sharing anion octahedra [2,3]. Among many experimental results arising from such theoretical proposals especially the $5d$ iridate Na_2IrO_3 and the $4d$ ruthenate α-$RuCl_3$ have managed to stand out, since both exhibit promising characteristics hinting at proximity to the QSL phase [4–6].

However, over time the list of materials possibly realizing the Kitaev model has also expanded to include cobaltates with a high-spin d^7 electronic configuration [7–9]. In these systems the presence of spin-active e_g electrons is suggested to reduce the strength of Heisenberg interactions J, thereby enhancing the dominance of the Kitaev contributions. Out of these "second wave" materials, $Na_2Co_2TeO_6$ has quickly been regarded as the most promising compound due to its notable similarities to α-$RuCl_3$: Even though $Na_2Co_2TeO_6$ exhibits magnetic long-range order below $T_N = 27$ K, the first reported antiferromagnetic zigzag ground state [10]—recently revised as a triple-**q** order [11,12]—is a promising indication of a proximate QSL state, as these two phases are adjacent in the parameter space of the Kitaev-Heisenberg model [13]. Indeed, a discontinuous phase transition appears when a magnetic field of $B_C \sim 6$ T is applied along the direction of the nearest-neighbor Co-Co bonds [14,15]. Despite the lack of knowledge about the exact magnetic ground state in the high-field phase of $Na_2Co_2TeO_6$, the experimental and theoretical results suggest the emergence of magnetic disorder at the critical field [16–18].

Here, we further highlight the intriguing effects of in-plane magnetic fields on $Na_2Co_2TeO_6$ by showing that the first-order phase transition at B_C exhibits strong signatures of quantum critical behavior close to a quantum critical endpoint (QCEP). The role of magnetoelastic coupling is elucidated by thermal expansion and magnetostriction measurements between 2 and 300 K and up to 15 T on high-quality single crystals of $Na_2Co_2TeO_6$ grown as described in Ref. [19]. Note that the presence of a potential antiferromagnetic impurity phase [20] is ruled out by our magnetization data (cf. Supplemental Material [21]). Out-of-plane relative length changes dL_c/L_c, i.e., along the crystallographic c direction, were studied on a 0.145-mm-thin single crystal by means of a three-terminal high-resolution capacitance dilatometer (Kuechler Innovative Measurement Technology) in a home-built setup placed inside a variable temperature insert of an Oxford magnet system [22,23]. From the relative length changes the linear thermal expansion coefficient $\alpha_c = 1/L_c \times (\partial L_c/\partial T)$ was derived. Magnetic fields were applied along the direction of first-neighbor Co-Co bonds ($B||a^*$) within the hexagonal planes. Thermal expansion and magnetostriction measurements were performed at rates of 0.3 K/min and 0.3 T/min, respectively. The magnetization was studied by means of a physical properties measurement system (PPMS, Quantum Design) using the vibrating sample magnetometer (VSM) option.

The low-temperature out-of-plane thermal expansion of $Na_2Co_2TeO_6$ is shown in Fig. 1 for representative magnetic fields $B||a^*$.[1] In zero magnetic field, the c axis continuously shrinks upon cooling, but notably, it also shows a sharp kink at

*Contact author: jan.arneth@kip.uni-heidelberg.de

†Contact author: klingeler@kip.uni-heidelberg.de

[1]The measurements have been performed following a field-cooled (FC) protocol where the sample was cooled in the applied field.

 ©2024 American Physical Society

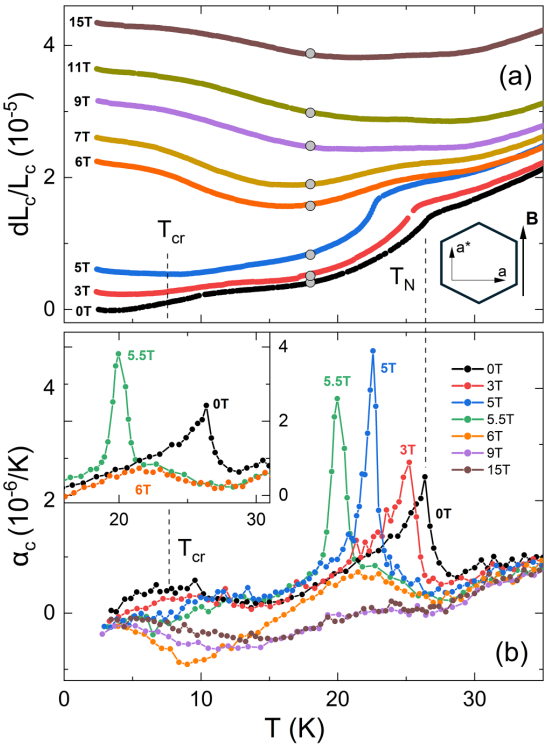


FIG. 1. (a) Out-of-plane thermal expansion dL_c/L_c and (b) linear thermal expansion coefficient α_c for both zero and finite magnetic fields applied $B||a^*$. As a reference point, $L(T = 2\ \mathrm{K}; B = 0\ \mathrm{T})$ is set to zero and data at different fields in (a) are scaled according to the magnetostriction measurements at 18 K (gray markers; see Fig. 3). T_N and T_{cr} mark the evolution of long-range magnetic order and the additional hump in zero field. Inset: Anomalies in α_c at T_N for $B = 0$, 5.5, and 6 T.

the antiferromagnetic ordering temperature $T_N = 26.8(3)$ K, which is reflected by a corresponding λ-shaped peak in the thermal expansion coefficient α_c [Fig. 1(b)]. The pronounced anomaly unambiguously indicates significant coupling between spin and lattice degrees of freedom in $Na_2Co_2TeO_6$. Interestingly, at around $T_{cr} = 7.5(9)$ K, another steplike feature can be found in the thermal expansion data as well as a corresponding broad hump in α_c. Note that the observation of a λ-shaped anomaly at T_N and a broad hump at T_{cr} resembles the overall behavior of the specific heat capacity c_p of $Na_2Co_2TeO_6$ as reported in Ref. [15]. In their study Yao *et al.* attribute the broad hump at T_{cr} to magnetic interplane correlations that remain short ranged due to Na disorder in separating layers.

While the thermal expansion coefficient at temperatures above T_N is not particularly sensitive to magnetic fields applied along the a^* axis, the anomaly at T_N shifts to lower temperatures and becomes more pronounced in magnetic fields up to 5 T. Concomitantly, the initially λ-shaped anomaly evolves into an even more pronounced symmetric peak and a small preceding steplike feature [see $\alpha_c(5.5\ \mathrm{T})$ in the inset in Fig. 1(b)]. The observed symmetric peak-shaped anomaly implies an associated jump in L_c, i.e., a first-order phase transition. At fields $B \geqslant 6$ T, a clear anomaly is no longer visible in the length changes and in α_c only the small steplike increase can be identified. Also for the humplike feature at T_{cr}, two field regimes can be identified: For $B \leqslant 5$ T, the steplike shrinking of the c axis continuously diminishes with increasing external magnetic field while it reappears for $B \geqslant 6$ T, albeit now signaling an anomalous *increase* in length [Fig. 1(a)]. Eventually, at $B > 10$ T, the c axis only weakly depends on temperature $T < 30$ K and α_c is independent on the applied field in this regime (see the Supplemental Material [21] for all thermal expansion data). For the further analysis of the data, we hence use $\alpha_c(15\ \mathrm{T})$ as an estimate of the nonmagnetic thermal expansion, since at such high fields the spins are completely polarized at sufficiently low temperatures. Similar methods have been used in the literature, e.g., in the closely related honeycomb magnet α-$RuCl_3$ [24].

We particularly emphasize the field dependence of the thermal expansion around T_{cr}: It is already evident from the c-axis dependence in Fig. 1(a) that α_c shows a sign change from positive at small fields to negative at fields $B \geqslant 6$ T. At intermediate fields around 5.5 T the thermal expansion coefficient almost vanishes below 10 K. The field effects are particularly visible when considering the thermal expansion coefficient as a function of B at fixed temperature of $T = 8$ K as shown in Fig. 2(a) (for other temperatures see the Supplemental Material [21]).[2] Here, we also plot the bare magnetic contribution $\alpha_c^{\mathrm{mag}} = \alpha_c - \alpha_c^{\mathrm{nonmag}}$ by using $\alpha_c^{\mathrm{nonmag}} \simeq \alpha_c(15\ \mathrm{T})$. Both data sets clearly imply a sign change in thermal expansion at $B_C(8\ \mathrm{K}) \simeq 5.5$ T which coincides well with the field-driven first-order phase transition occurring in the same field range [15,16,25,26].

In recent literature, the corresponding discontinuity in the magnetization at B_C has been attributed to an order-disorder transition into a QSL-like state [16]. Here, we uncover another intriguing property of the anomalous behavior at B_C, that is, its distinct signatures of quantum criticality. Since the linear thermal expansion coefficient is directly proportional to the pressure dependence of the entropy via the Maxwell relation $\alpha_c \sim \partial S/\partial p_c|_T$, a sign change of α_c upon the application of magnetic fields implies a maximum of the magnetic contribution to the entropy at B_C. Such an accumulation of S_{mag} is regularly expected to occur at a quantum critical point (QCP) [27–29]. It is important to note that the here reported quantum criticality, and hence also its critical properties, differs from the commonly discussed ones in the way that the underlying phase transition is not continuous but of a first-order type. In this scenario the so-called metamagnetic quantum critical endpoint (QCEP) is understood to be the endpoint of a line of a first-order phase transition when the temperature is reduced to zero [27,28,30]. Our interpretation is further supported by the data in Ref. [31], the detailed

[2] At $T = 8$ K, zero-field thermal expansion shows a hump associated to pronounced critical fluctuations so that the effects of magnetic fields can be expected to be particularly large. In addition, at lowest temperatures, thermal expansion vanishes so that the signal-to-noise ratio decreases at lowest temperatures under study.

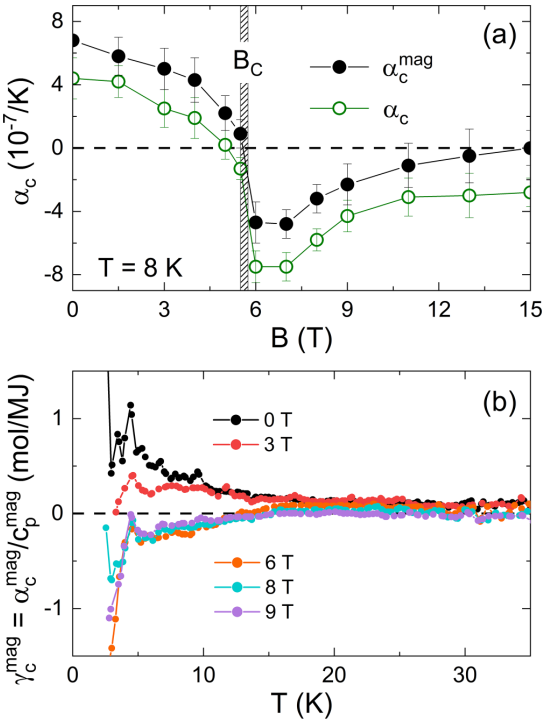


FIG. 2. (a) Out-of-plane linear thermal expansion coefficient and its magnetic contribution at 8 K as a function of magnetic field. The vertical dashed region marks the first-order phase transition at B_C. (b) Temperature dependence of the unidirectional magnetic Grüneisen parameter γ_c^{mag}, obtained by dividing the magnetic contributions to α_c and c_p from Ref. [15], at selected magnetic fields applied along the a^* axis.

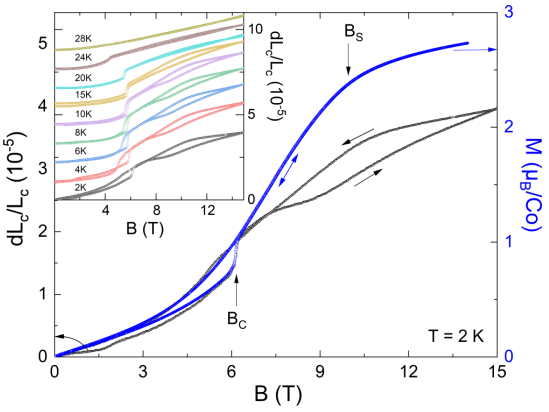


FIG. 3. Isothermal magnetostriction $L_c(B)$ (black) and magnetization $M(B)$ (blue) at $T = 2$ K for $B||a^*$. Arrows denote the direction of the field sweep. The inset depicts magnetostriction measurements at various temperatures, which are shifted along the ordinate. B_C and B_S mark the critical field and the saturation field, respectively.

inspection of which shows that the in-plane thermal expansion coefficient α_{a^*} changes its sign, too, at $B||a^* = 6$ T [31].

A key signature of metamagnetic quantum criticality is a sign change of the magnetic Grüneisen parameter, which is defined as the ratio of the magnetic contributions to the thermal expansion coefficient and the specific heat capacity $\gamma_{mag} = \alpha^{mag}/c_p^{mag}$ [27,28,32]. Figure 2(b) shows the uniaxial magnetic Grüneisen parameter of $Na_2Co_2TeO_6$ at representative magnetic fields as calculated from our thermal expansion data and the specific heat capacity measured in Ref. [15]. The resulting Grüneisen ratio is close to zero at $T > 20$ K but continuously increases upon cooling for $B \leqslant 5$ T. The opposite trend appears for $B \geqslant 6$ T. Extrapolating the temperature dependence for $T \to 0$ the data indicate a divergence at zero temperature, which can, however, not be seen directly in the data due to limited resolution and tiny length changes at low temperatures.

Signatures of metamagnetic quantum criticality as described in the present Letter have been first found and discussed in $Sr_3Ru_2O_7$ [32–34]. Later on, a sign change of the out-of-plane thermal expansion coefficient connected to a first-order phase transition was also observed in $CeRu_2Si_2$ [35,36] and in $Ca_{1.8}Sr_{0.2}RuO_4$ [37]. Additionally, indications of QCEPs were found in UGe_2 [38], UCoAl [39], and $ZrZn_2$ [40]. To our knowledge, metamagnetic quantum criticality has been reported exclusively in itinerant electron systems, which highlights the finding of $Na_2Co_2TeO_6$ exhibiting a quantum critical endpoint as an antiferromagnetic insulator. At this point it is noteworthy that thermal expansion in the closely related Kitaev candidate α-$RuCl_3$ also hints at the emergence of a quantum phase transition at B_C, which is debated to precede a QSL state [24]. In α-$RuCl_3$, however, the transition into the putative magnetically disordered phase exhibits a rather continuous character, which leads to differing quantum critical properties as compared to $Na_2Co_2TeO_6$.

The coupling of spin and lattice degrees of freedom can be also directly studied through magnetostriction experiments. Figure 3 shows the relative out-of-plane length changes (black) and the isothermal magnetization (blue) of $Na_2Co_2TeO_6$ at 1.8 K for $B||a^*$. As can be seen, the discontinuity in the magnetization is accompanied by a positive jump in the c-axis length, suggesting that both magnetic field and uniaxial pressure can be used as tuning parameters of the QCEP [27]. At $B_S(2\text{ K}) \simeq 10$ T, the magnetization implies the evolution of the polarized spin configuration. Similar to the field region around B_C, dL_c exhibits pronounced differences between the up- and down-sweep of the magnetic field starting from 8 T, while no corresponding hysteresis is observed in the magnetization data. As depicted in the inset of Fig. 3, the hysteresis region at $B_C(T)$ narrows as the temperature is increased and totally vanishes at $T \geqslant T_N$. Notably, hysteresis in magnetostriction above $B_C(T)$ ranges well beyond $B_S(T)$ and persists up to at least 24 K, i.e., in the whole reported quantum disordered regime [16]. The hysteresis diminishes but the hysteretic field range does not shrink upon heating. This indicates magnetostructural domain effects rather than a weak first-order character of the phase boundary $B_S(T)$. In addition, the magnetostriction exhibits a weak discontinuity of unknown origin at $B \simeq 1.5$ T when the field is increased from zero, but not when the field is subsequently decreased. At

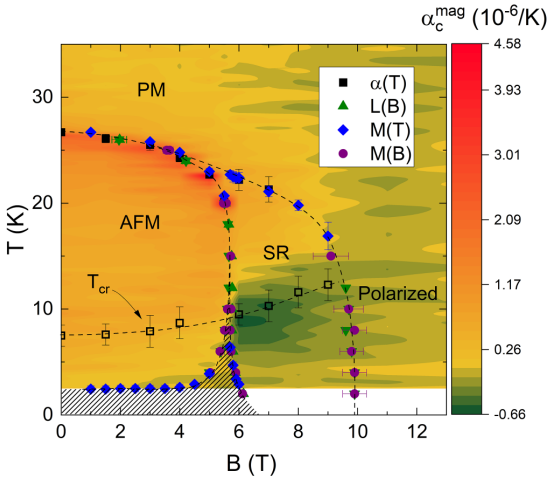


FIG. 4. Magnetic phase diagram of $Na_2Co_2TeO_6$ for magnetic fields applied $B||a^*$ as constructed from magnetic and dilatometric measurements. PM, AFM, and SR denote the paramagnetic, canted antiferromagnetic, and spin reoriented phase, respectively. The hatched area shows the hysteresis region observed in M and L_c (see the text). Additionally, $\alpha_c^{mag}(T, B)$ is depicted in color scale. The distinct data sets are shown in the Supplemental Material [21].

intermediate temperatures around 6 K this results in crossing of the up- and down-sweep magnetostriction at approximately 5.5 T.

Noteworthy, field-induced magnetization and length changes, at 2 K, closely track each other, i.e., the curves can be well overlapped by a single scaling factor, up to the critical field B_C. This observation parallels the findings of magnetostriction measurements on $Sr_3Ru_2O_7$ [34] and $CeRu_2Si_2$ [36]. Following the arguments discussed in that frame, such a good proportionality of $M(B)$ and $L_c(B)$ implies that variations in uniaxial pressure and magnetic field probe the same thermodynamic information as expected in a quantum critical regime [27]. Hence, the magnetostriction data strongly corroborate the results of our thermal expansion measurements.

Collecting the anomalies found in dilatometric and magnetic quantities allows for the construction of the magnetoelastic phase diagram shown in Fig. 4 (see the Supplemental Material [21] for the magnetic measurements). In agreement with most phase diagrams reported in the literature [15,16], our dilatometric studies imply three distinct thermodynamic phases: Coming from the high-temperature paramagnetic (PM) regime the spin system undergoes a continuous phase transition into a canted antiferromagnetic (AFM) state at T_N. Upon increasing the magnetic field along the Co-Co bonds, $Na_2Co_2TeO_6$ exhibits a first-order phase transition showing strong signs of quantum criticality. Above B_C, the spins reorient (SR) out of their low-field configuration into a yet unknown magnetic structure while above $B_S(2\,\mathrm{K}) = 10\,\mathrm{T}$, the magnetic moments are almost fully polarized. As indicated by the shaded area in Fig. 4, the AFM/SR phase boundary exhibits pronounced hysteresis at low temperatures. At low temperatures, our data suggest that the system does not return into the AFM phase even when the magnetic field is decreased back to zero.

In conclusion, our measurements of the thermal expansion and magnetostriction consequently give insights into the important role of magnetoelastic coupling in the Kitaev candidate material $Na_2Co_2TeO_6$. A sign change of the Grüneisen parameter at the critical field B_C indicates the accumulation of entropy in the (B, T) plane above the critical field and thereby implies the existence of a metamagnetic QCEP. In addition, the proportional relationship between isothermal magnetization and magnetostriction for $B \leqslant B_C$ signals that the QCEP can be tuned by a magnetic field and pressure simultaneously. The presented results expand the scope of sample classes that exhibit metamagnetic quantum criticality to honeycomb antiferromagnets with possibly Kitaev-like interactions and, hence, contribute to the understanding of quantum criticality in antiferromagnetic insulating systems.

We acknowledge support by Deutsche Forschungsgemeinschaft (DFG) under Germany's Excellence Strategy EXC2181/1-390900948 (the Heidelberg STRUCTURES Excellence Cluster). J.A. acknowledges support by the IMPRS-QD Heidelberg. K.Y.C. was supported by the National Research Foundation (NRF) of Korea (Grants No. 2020R1A5A1016518 and No. RS-2023-00209121). R.S. acknowledges the financial support provided by the Ministry of Science and Technology in Taiwan under Project No. NSTC (113-2124-M-001-045-MY3 and 113-2124-M-001-003), Financial support from the Center of Atomic Initiative for New Materials (AI-Mat), National Taiwan University, (Project No. 113L900801) and Academia Sinica for the budget of AS-iMATE-113-12.

[1] A. Kitaev, Anyons in an exactly solved model and beyond, Ann. Phys. **321**, 2 (2006).

[2] G. Jackeli and G. Khaliullin, Mott insulators in the strong spin-orbit coupling limit: From Heisenberg to a quantum compass and Kitaev models, Phys. Rev. Lett. **102**, 017205 (2009).

[3] H. Takagi, T. Takayama, G. Jackeli, G. Khaliullin, and S. E. Nagler, Concept and realization of Kitaev quantum spin liquids, Nat. Rev. Phys. **1**, 264 (2019).

[4] S. Hwan Chun, J.-W. Kim, J. Kim, H. Zheng, C. C. Stoumpos, C. D. Malliakas, J. F. Mitchell, K. Mehlawat, Y. Singh, Y. Choi, T. Gog, A. Al-Zein, M. M. Sala, M. Krisch, J. Chaloupka, G. Jackeli, G. Khaliullin, and B. J. Kim, Direct evidence for dominant bond-directional interactions in a honeycomb lattice iridate Na_2IrO_3, Nat. Phys. **11**, 462 (2015).

[5] S.-H. Do, S.-Y. Park, J. Yoshitake, J. Nasu, Y. Motome, Y. S. Kwon, D. T. Adroja, D. J. Voneshen, K. Kim, T.-H. Jang, J.-H. Park, K.-Y. Choi, and S. Ji, Majorana fermions in the Kitaev quantum spin system α-$RuCl_3$, Nat. Phys. **13**, 1079 (2017).

[6] Y. Kasahara, T. Ohnishi, Y. Mizukami, O. Tanaka, S. Ma, K. Sugii, N. Kurita, H. Tanaka, J. Nasu, Y. Motome, T. Shibauchi,

and Y. Matsuda, Majorana quantization and half-integer thermal quantum Hall effect in a Kitaev spin liquid, Nature (London) **559**, 227 (2018).

[7] H. Liu and G. Khaliullin, Pseudospin exchange interactions in d^7 cobalt compounds: Possible realization of the Kitaev model, Phys. Rev. B **97**, 014407 (2018).

[8] R. Sano, Y. Kato, and Y. Motome, Kitaev-Heisenberg Hamiltonian for high-spin d^7 Mott insulators, Phys. Rev. B **97**, 014408 (2018).

[9] H. Liu, J. Chaloupka, and G. Khaliullin, Kitaev spin liquid in d^7 transition metal compounds, Phys. Rev. Lett. **125**, 047201 (2020).

[10] A. K. Bera, S. M. Yusuf, A. Kumar, and C. Ritter, Zigzag antiferromagnetic ground state with anisotropic correlation lengths in the quasi-two-dimensional honeycomb lattice compound $Na_2Co_2TeO_6$, Phys. Rev. B **95**, 094424 (2017).

[11] W. Chen, X. Li, Z. Hu, Z. Hu, L. Yue, R. Sutarto, F. He, K. Iida, K. Kamazawa, W. Yu, X. Lin, and Y. Li, Spin-orbit phase behavior of $Na_2Co_2TeO_6$ at low temperatures, Phys. Rev. B **103**, L180404 (2021).

[12] W. G. F. Krüger, W. Chen, X. Jin, Y. Li, and L. Janssen, Triple-q Order in $Na_2Co_2TeO_6$ from Proximity to Hidden-SU(2)-Symmetric Point, Phys. Rev. Lett. **131**, 146702 (2023).

[13] J. Chaloupka, G. Jackeli, and G. Khaliullin, Zigzag magnetic order in the iridium oxide Na_2IrO_3, Phys. Rev. Lett. **110**, 097204 (2013).

[14] G. Xiao, Z. Xia, W. Zhang, X. Yue, S. Huang, X. Zhang, F. Yang, Y. Song, M. Wei, H. Deng, and D. Jiang, Crystal growth and the magnetic properties of $Na_2Co_2TeO_6$ with quasi-two-dimensional honeycomb lattice, Cryst. Growth Des. **19**, 2658 (2019).

[15] W. Yao and Y. Li, Ferrimagnetism and anisotropic phase tunability by magnetic fields in $Na_2Co_2TeO_6$, Phys. Rev. B **101**, 085120 (2020).

[16] G. Lin, J. Jeong, C. Kim, Y. Wang, Q. Huang, T. Masuda, S. Asai, S. Itoh, G. Günther, M. Russina, Z. Lu, J. Sheng, L. Wang, J. Wang, G. Wang, Q. Ren, C. Xi, W. Tong, L. Ling, Z. Liu *et al.*, Field-induced quantum spin disordered state in spin-1/2 honeycomb magnet $Na_2Co_2TeO_6$, Nat. Commun. **12**, 5559 (2021).

[17] L. Xiang, R. Dhakal, M. Ozerov, Y. Jiang, B. S. Mou, A. Ozarowski, Q. Huang, H. Zhou, J. Fang, S. M. Winter, Z. Jiang, and D. Smirnov, Disorder-enriched magnetic excitations in a Heisenberg-Kitaev quantum magnet $Na_2Co_2TeO_6$, Phys. Rev. Lett. **131**, 076701 (2023).

[18] X. Hong, M. Gillig, W. Yao, L. Janssen, V. Kocsis, S. Gass, Y. Li, A. U. B. Wolter, B. Büchner, and C. Hess, Phonon thermal transport shaped by strong spin-phonon scattering in a Kitaev material $Na_2Co_2TeO_6$, npj Quantum Mater. **9**, 18 (2024).

[19] C. H. Lee, S. Lee, Y. S. Choi, Z. H. Jang, R. Kalaivanan, R. Sankar, and K.-Y. Choi, Multistage development of anisotropic magnetic correlations in the Co-based honeycomb lattice $Na_2Co_2TeO_6$, Phys. Rev. B **103**, 214447 (2021).

[20] E. Dufault, F. Bahrami, A. Streeter, X. Yao, E. Gonzalez, Q. Zhang, and F. Tafti, Introducing the monoclinic polymorph of the honeycomb magnet $Na_2Co_2TeO_6$, Phys. Rev. B **108**, 064405 (2023).

[21] See Supplemental Material at http://link.aps.org/supplemental/10.1103/PhysRevB.110.L140402 for additional information on the measurements and complementary dilatometric and magnetic data.

[22] R. Küchler, T. Bauer, M. Brando, and F. Steglich, A compact and miniaturized high resolution capacitance dilatometer for measuring thermal expansion and magnetostriction, Rev. Sci. Instrum. **83**, 095102 (2012).

[23] J. Werner, W. Hergett, M. Gertig, J. Park, C. Koo, and R. Klingeler, Anisotropy-governed competition of magnetic phases in the honeycomb quantum magnet $Na_3Ni_2SbO_6$ studied by dilatometry and high-frequency ESR, Phys. Rev. B **95**, 214414 (2017).

[24] S. Gass, P. M. Cônsoli, V. Kocsis, L. T. Corredor, P. Lampen-Kelley, D. G. Mandrus, S. E. Nagler, L. Janssen, M. Vojta, B. Büchner, and A. U. B. Wolter, Field-induced transitions in the Kitaev material α-$RuCl_3$ probed by thermal expansion and magnetostriction, Phys. Rev. B **101**, 245158 (2020).

[25] L. Viciu, Q. Huang, E. Morosan, H. Zandbergen, N. Greenbaum, T. McQueen, and R. Cava, Structure and basic magnetic properties of the honeycomb lattice compounds $Na_2Co_2TeO_6$ and $Na_3Co_2SbO_6$, J. Solid State Chem. **180**, 1060 (2007).

[26] E. Lefrançois, M. Songvilay, J. Robert, G. Nataf, E. Jordan, L. Chaix, C. V. Colin, P. Lejay, A. Hadj-Azzem, R. Ballou, and V. Simonet, Magnetic properties of the honeycomb oxide $Na_2Co_2TeO_6$, Phys. Rev. B **94**, 214416 (2016).

[27] M. Garst and A. Rosch, Sign change of the Grüneisen parameter and magnetocaloric effect near quantum critical points, Phys. Rev. B **72**, 205129 (2005).

[28] A. J. Millis, A. J. Schofield, G. G. Lonzarich, and S. A. Grigera, Metamagnetic quantum criticality in metals, Phys. Rev. Lett. **88**, 217204 (2002).

[29] P. Gegenwart, Grüneisen parameter studies on heavy fermion quantum criticality, Rep. Prog. Phys. **79**, 114502 (2016).

[30] C. Beneke and M. Vojta, Divergence of the Grüneisen ratio at symmetry-enhanced first-order quantum phase transitions, Phys. Rev. B **103**, 174420 (2021).

[31] S. Zhang, S. Lee, A. J. Woods, W. K. Peria, S. M. Thomas, R. Movshovich, E. Brosha, Q. Huang, H. Zhou, V. S. Zapf, and M. Lee, Electronic and magnetic phase diagrams of the Kitaev quantum spin liquid candidate $Na_2Co_2TeO_6$, Phys. Rev. B **108**, 064421 (2023).

[32] P. Gegenwart, F. Weickert, M. Garst, R. S. Perry, and Y. Maeno, Metamagnetic quantum criticality in $Sr_3Ru_2O_7$ studied by thermal expansion, Phys. Rev. Lett. **96**, 136402 (2006).

[33] S. A. Grigera, R. S. Perry, A. J. Schofield, M. Chiao, S. R. Julian, G. G. Lonzarich, S. I. Ikeda, Y. Maeno, A. J. Millis, and A. P. Mackenzie, Magnetic field-tuned quantum criticality in the metallic ruthenate $Sr_3Ru_2O_7$, Science **294**, 329 (2001).

[34] S. A. Grigera, P. Gegenwart, R. A. Borzi, F. Weickert, A. J. Schofield, R. S. Perry, T. Tayama, T. Sakakibara, Y. Maeno, A. G. Green, and A. P. Mackenzie, Disorder-sensitive phase formation linked to metamagnetic quantum criticality, Science **306**, 1154 (2004).

[35] C. Paulsen, A. Lacerda, J. Tholence, and J. Flouquet, Low temperature properties of heavy-fermion $CeRu_2Si_2$ studied by magnetization experiments, Phys. B: Condens. Matter **165–166**, 433 (1990).

[36] F. Weickert, M. Brando, F. Steglich, P. Gegenwart, and M. Garst, Universal signatures of the metamagnetic quantum critical endpoint: Application to $CeRu_2Si_2$, Phys. Rev. B **81**, 134438 (2010).

[37] J. Baier, P. Steffens, O. Schumann, M. Kriener, S. Stark, H. Hartmann, O. Friedt, A. Revcolevschi, P. G. Radaelli, S. Nakatsuji, Y. Maeno, J. A. Mydosh, T. Lorenz, and M. Braden, Magnetoelastic coupling across the metamagnetic transition in $Ca_{2-x}Sr_xRuO_4 (0.2 \leqslant x \leqslant 0.5)$, J. Low Temp. Phys. **147**, 405 (2007).

[38] V. Taufour, D. Aoki, G. Knebel, and J. Flouquet, Tricritical point and wing structure in the itinerant ferromagnet UGe_2, Phys. Rev. Lett. **105**, 217201 (2010).

[39] D. Aoki, T. Combier, V. Taufour, T. D. Matsuda, G. Knebel, H. Kotegawa, and J. Flouquet, Ferromagnetic quantum critical endpoint in UCoAl, J. Phys. Soc. Jpn. **80**, 094711 (2011).

[40] M. Uhlarz, C. Pfleiderer, and S. M. Hayden, Quantum phase transitions in the itinerant ferromagnet $ZrZn_2$, Phys. Rev. Lett. **93**, 256404 (2004).

Supplemental Material: Signatures of a Quantum Critical Endpoint in the Kitaev candidate $Na_2Co_2TeO_6$

J. Arneth,[1,*] K.-Y. Choi,[2] R. Kalaivanan,[3] R. Sankar,[3] and R. Klingeler[1,†]

[1] *Kirchhoff Institute for Physics, Heidelberg University, INF 227, D-69120 Heidelberg, Germany*
[2] *Department of Physics, Sungkyunkwan University, Suwon 16419, Republic of Korea*
[3] *Institute of Physics, Academia Sinica, Taipei 11529, Taiwan*

(Dated: September 12, 2024)

PACS numbers:

I. THERMAL EXPANSION COEFFICIENT

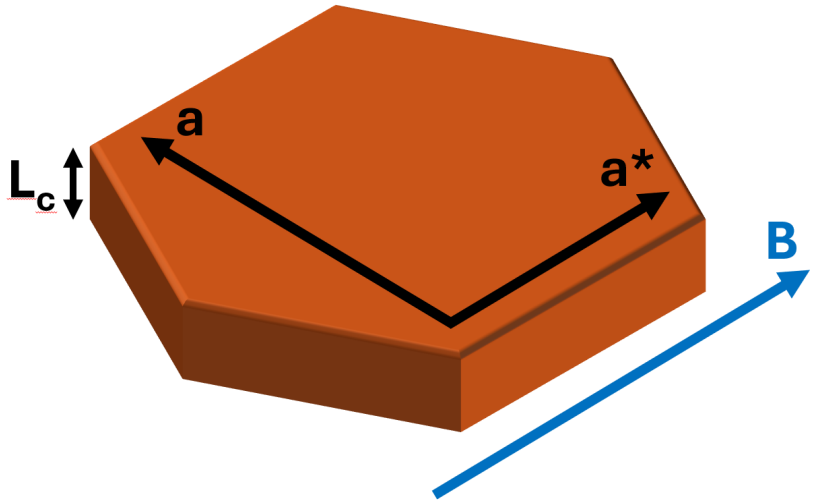


FIG. 1: Schematic depiction of the used measurement geometry. The hexagonal shape reflects a stacking of honeycomb layers. All measurements have been performed by measuring the out-of-plane length L_c while the external magnetic field is applied along the Co-Co-bonds within the lattice planes.

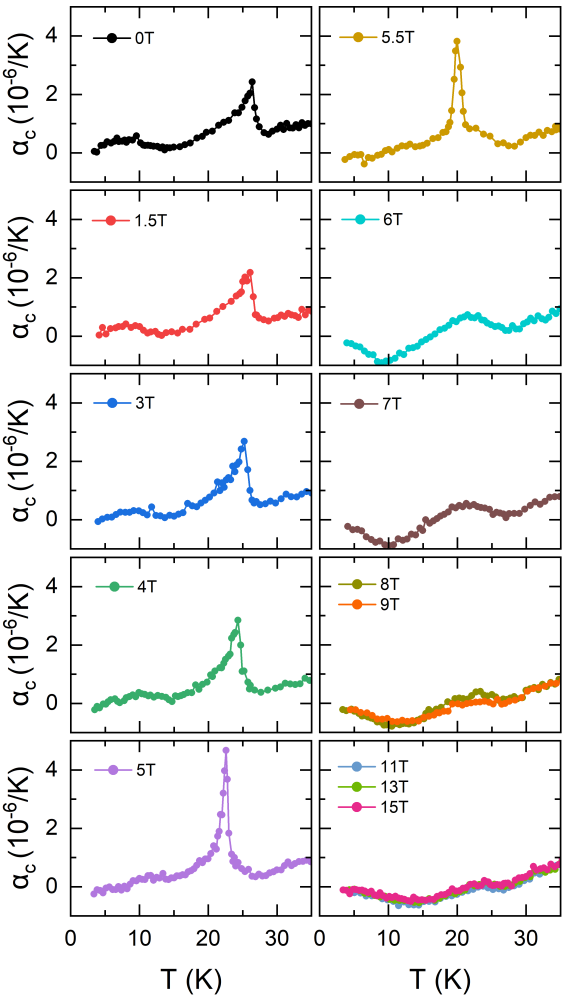


FIG. 2: Linear thermal expansion coefficient α_c for various magnetic fields applied $B||a^*$.

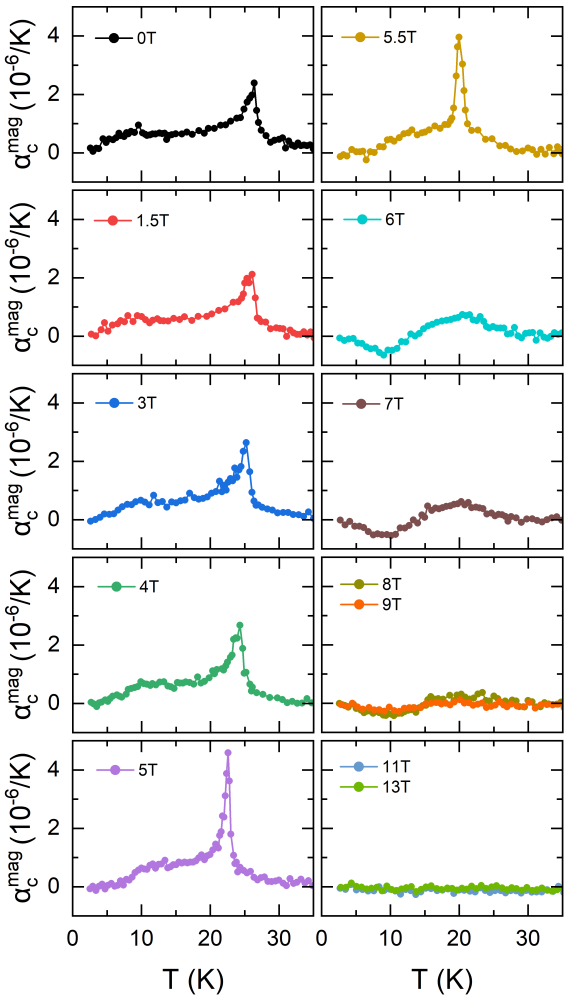


FIG. 3: Magnetic contribution $\alpha_c^{\rm mag} = \alpha_c(B||a^*) - \alpha_c(B||a^* = 15)$ T at selected magnetic fields applied along the a^* axis.

4

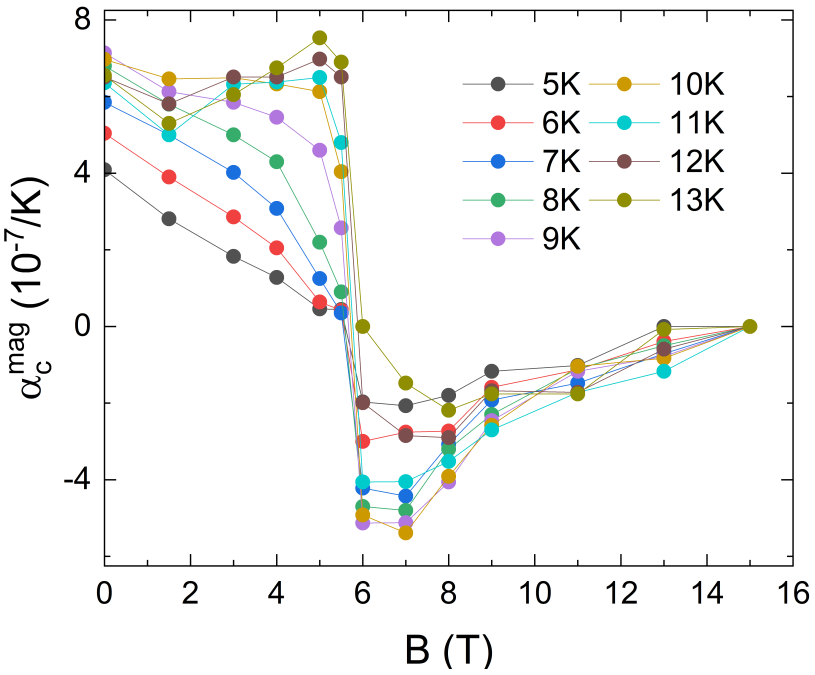


FIG. 4: Magnetic contribution to the linear thermal expansion coefficient $\alpha_c^{\rm mag} = \alpha_c(B||a^*) - \alpha_c(B||a^* = 15)$ T as a function of magnetic field applied along the a^* axis at selected temperatures.

II. ISOTHERMAL MAGNETOSTRICTION AND MAGNETISATION

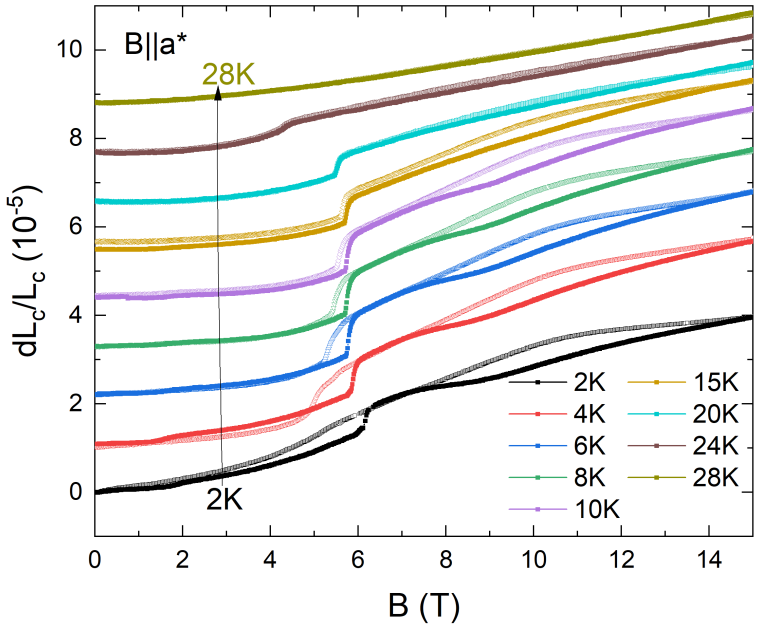


FIG. 5: Out-of-plane magnetostriction for $B||a^*$ at selected temperatures. The data are shifted by 1.1×10^{-5} along the ordinate.

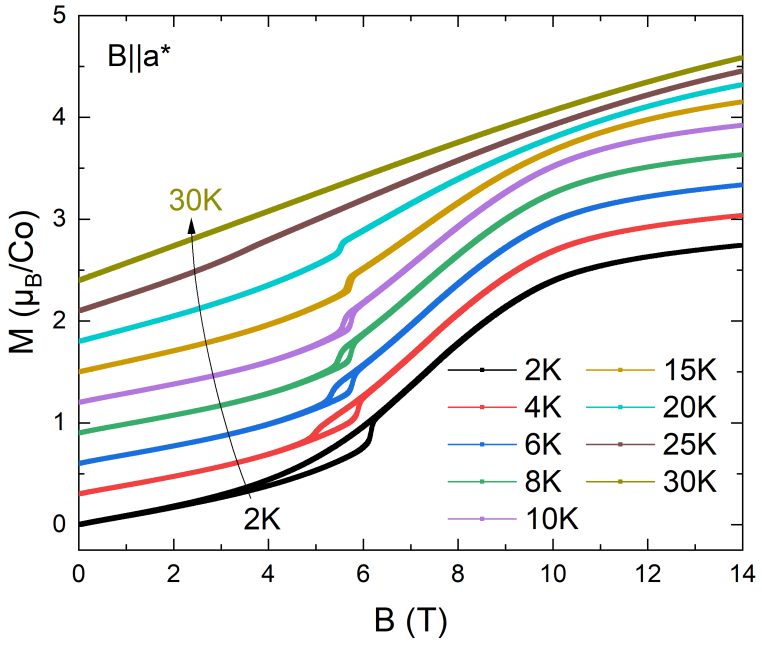


FIG. 6: Isothermal magnetization for $B||a^*$ at selected temperatures. The data are shifted by $0.3\,\mu_B$/Co along the ordinate.

III. THERMAL EXPANSION IN APPLIED MAGNETIC FIELDS

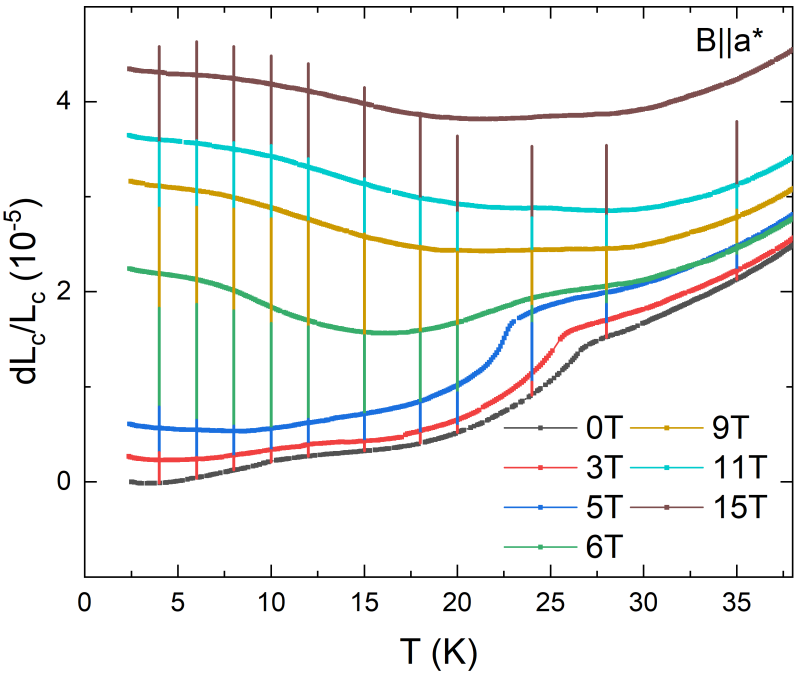


FIG. 7: Out-of-plane relative length changes as a function of temperature at selected magnetic fields applied along the a^* axis. The curves are shifted with respect to the magnetostriction data (vertical lines) at 18 K.

IV. STATIC MAGNETIC SUSCEPTIBILITY

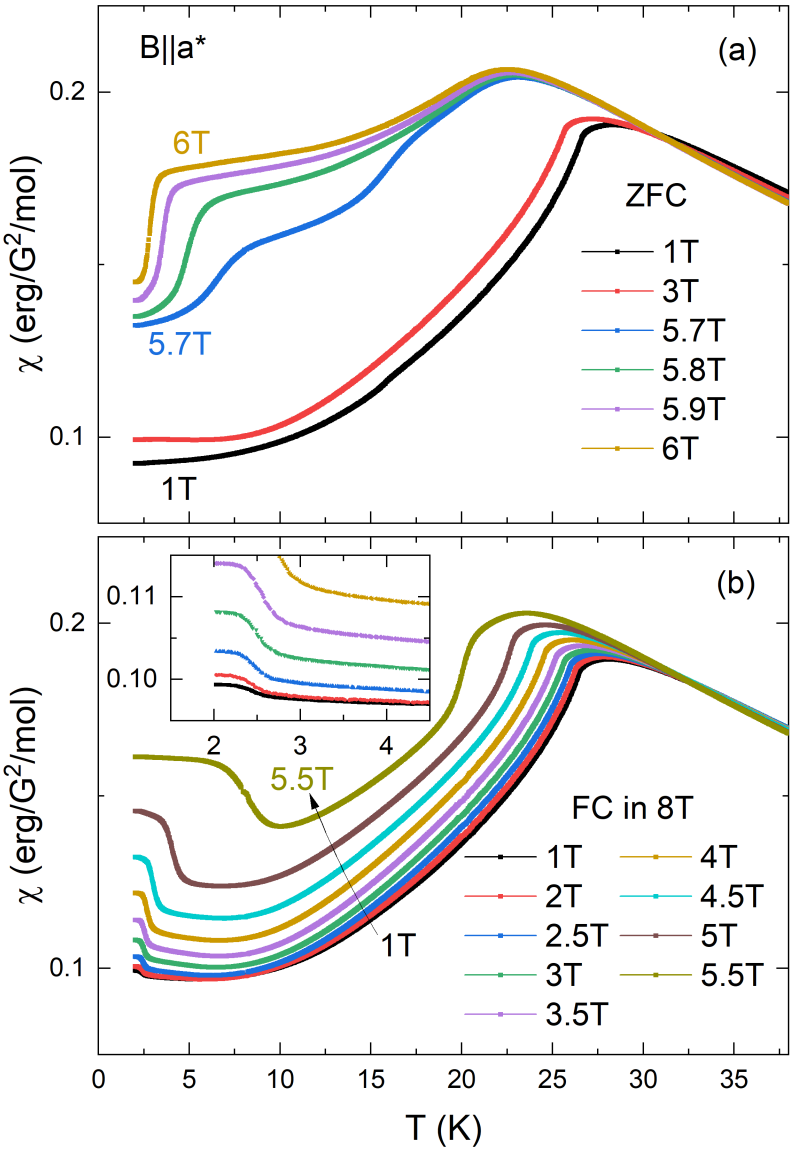


FIG. 8: Temperature dependence of the static magnetic susceptibility at selected magnetic fields applied along the a^* axis. In (a) the data is acquired upon heating under zero-field-cooled (ZFC) conditions, i.e., subsequent to cooling to 1.8 K without external magnetic field and, thus, initially preparing the system in the AFM state. In (b) the data is acquired upon heating subsequent to cooling to 1.8 K in an external magnetic field of $B||a^* = 8$ T. Hence, the system is initially prepared in the SR state. The inset depicts a zoom into the low-temperature region of the data.

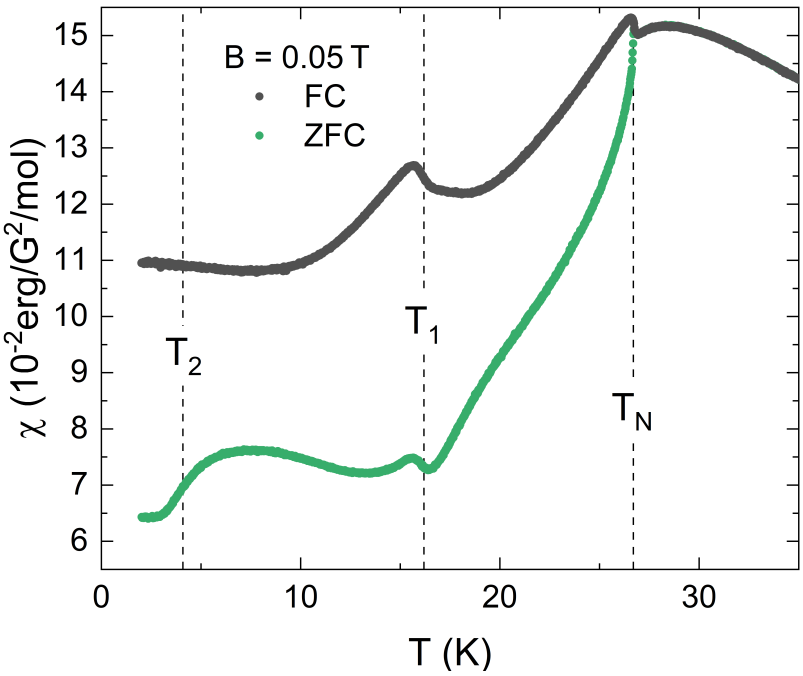


FIG. 9: Static magnetic susceptibility at $B = 0.05$ T applied along the a^* axis measured under field-cooled (black) and zero-field-cooled (green) conditions. Dashed vertical lines mark anomalies in the data at T_N, T_1 and T_2.

D.2 Competing Interactions and the Effects of Uniaxial Out-of-plane Perturbations in the Honeycomb Antiferromagnet $Na_2Co_2TeO_6$

The results of this section were submitted as a research article to *Physical Review Materials*. A preprint of the manuscript has been uploaded to *arXiv* under the arXiv number: 2506.06189 with the DOI: https://doi.org/10.48550/arXiv.2506.06189 [147]. Specific contributions of each co-author, especially the contribution of J. Arneth, who serves as the corresponding and first author, are given in the following list:

- J. Arneth performed the dilatometry and magnetisation measurements, analysed the corresponding data, constructed the plotted figures, and wrote the presented manuscript draft.
- K.-Y. Choi, R. Kalaivanan and R. Sankar grew the single crystalline samples and conducted the structural analysis.
- R. Klingeler led the project and supported the data analysis and manuscript writing.
- All authors proofread the manuscript.

arXiv:2506.06189v1 [cond-mat.str-el] 6 Jun 2025

Competing Interactions and the Effects of Uniaxial Out-of-plane Perturbations in the Honeycomb Antiferromagnet $Na_2Co_2TeO_6$

J. Arneth,[1,*] R. Kalaivanan,[2] R. Sankar,[2] K.-Y. Choi,[3] and R. Klingeler[1,†]

[1] *Kirchhoff Institute for Physics, Heidelberg University, INF 227, D-69120 Heidelberg, Germany*

[2] *Institute of Physics, Academia Sinica, Taipei 11529, Taiwan*

[3] *Department of Physics, Sungkyunkwan University, Suwon 16419, Republic of Korea*

(Dated: June 12, 2025)

Despite exhibiting magnetic long-range order below $T_N = 26.7$ K, the honeycomb cobaltate $Na_2Co_2TeO_6$ is predicted to enter a Kitaev spin liquid state when subjected to small external perturbations. While most of the reported literature investigates the effects of magnetic fields applied parallel to the honeycomb layers, we present high-resolution capacitance dilatometry studies for fields perpendicular to the Co-planes up to 15 T. Grüneisen analysis reveals the effect of uniaxial out-of-plane strain and shows that antiferromagnetic order in $Na_2Co_2TeO_6$ is stabilized at a rate of $\partial T_N/\partial p_c = 0.28(5)$ K/GPa. Further, failure of the Grüneisen scaling at low temperatures around $T_{cr} \simeq 7.5$ K demonstrates the presence of competing energy scales. In contrast to an only weak field dependence of the anomaly at T_N, a broad hump at $T_{cr}(B = 0\ \mathrm{T})$ evolves into a sharp peak at high fields applied $B \parallel c$. Our magnetostriction data show that a kink in the magnetisation at $B_C \simeq 4.6$ T is accompanied by an inflection point in the field-induced length changes, which is likely related to weak unequal spin canting. All observed phenomena leave their signatures in the magnetoelastic phase diagram as constructed by our experimental results.

I. INTRODUCTION

Unlike in the prime example of frustrated magnetism, the triangular antiferromagnet, the exactly solvable Kitaev model introduces magnetic frustration not by the geometry of the underlying lattice but via strongly anisotropic bond-dependent magnetic interactions that can not be simultaneously satisfied for a honeycomb network of $S = 1/2$ [1]. At low temperatures, the resulting magnetic ground state of this model system is given by a quantum spin liquid (QSL) phase, which features fractionalized elementary excitations. Hence, it did not take long until the first suggestions of extremely fault-tolerant quantum computers based on materials realizing the Kitaev model were put forward [2–4]. However, so far, the search for actual compounds hosting a Kitaev quantum spin liquid ground state continues. After thorough investigation of the initial 'first wave' candidates, which were mainly based on $4d$ and $5d$ late transition metal ions with strong spin-orbit coupling [5–9], two independent theoretical studies predicted that sufficiently strong Kitaev interactions might emerge also in high-spin Co^{2+} honeycomb lattice systems [10–12].

Among these 'second wave' compounds, $Na_2Co_2TeO_6$ has attracted the most attention by far [13–17]. Although antiferromagnetic long-range order emerges at $T_N \simeq 26.7$ K, thermodynamic and spectroscopic studies suggest that $Na_2Co_2TeO_6$ can be described by an extended Heisenberg-Kitaev model with coupling parameters reasonably close to hosting a QSL ground state [18–22]. Such an assignment, thus, prompts the idea of using external perturbations, including magnetic and electric fields or pressure, to tune the balance of the magnetic interactions in favour of the Kitaev exchange. The bulk of the recent literature focuses dominantly on the influence of magnetic fields applied perpendicular to the Co-Co bonds within the honeycomb planes since the system undergoes a first-order phase transition into a putative spin disordered state at $B \parallel a^* \simeq 6$ T [16, 17, 23]. We have recently shown that this transition exhibits signatures of a quantum critical endpoint [24]. Yet, the exact magnetic state in the high-field phase of $Na_2Co_2TeO_6$ remains unclear.

In this work, we explore the effects of two, only scarcely investigated perturbations, namely *uniaxial* pressure and magnetic fields applied perpendicular to the Co-layers [25–27]. We employ high-resolution capacitance dilatometry which has been proven as a valuable method to elucidate and quantify spin-lattice coupling in layered correlated electron systems [28–32]. Using Grüneisen analysis, we find competing energy scales at low temperatures and determine the uniaxial pressure coefficient of T_N from the experimental data at zero magnetic field. Magnetostriction and thermal expansion measurements for fields $B \parallel c$ up to 15 T enable us to elucidate the role of magnetoelastic

* jan.arneth@kip.uni-heidelberg.de
† klingeler@kip.uni-heidelberg.de

coupling in the thermodynamic properties of $Na_2Co_2TeO_6$. We also present the magnetoelastic phase diagram, which corroborates the findings of our analysis.

II. EXPERIMENTAL METHODS

All experiments have been performed on a high-quality 0.145 mm thin ($L_c(300\,\mathrm{K}, 0\,\mathrm{T}) = 0.145$ mm) single crystal of $Na_2Co_2TeO_6$ grown as described in Ref. [33]. The possible formation of an antiferromagnetic polymorph impurity phase [34] is excluded by our magnetisation data (see Fig. A1 in the Appendix). Out-of-plane relative length changes dL_c/L_c, i.e., along the crystallographic c-direction, were studied by means of a three-terminal high-resolution capacitance dilatometer (Kuechler Innovative Measurement Technology) in a home-built set-up placed inside a Variable Temperature Insert of an Oxford magnet system [35, 36]. Magnetic fields were applied in the direction of the measured length changes, i.e. $B \parallel c$. From the relative length changes the linear thermal expansion coefficient $\alpha_c = 1/L_c \times (\partial L_c/\partial T)$ and the longitudinal magnetostriction coefficient $\lambda_c = 1/L_c \times (\partial L_c/\partial B)$ were derived. Thermal expansion and magnetostriction measurements were performed at sweep rates of 0.3 K/min and 0.3 T/min, respectively. The magnetisation was studied using the vibrating sample magnetometer (VSM) option of a Physical Properties Measurement System (PPMS-14, Quantum Design).

III. EXPERIMENTAL RESULTS

The out-of-plane thermal expansion dL_c/L_c of $Na_2Co_2TeO_6$ at $B = 0$ T, shown in Fig. 1a, demonstrates a distinct kink at the long-range magnetic ordering temperature T_N as well as a broad step-like feature at lower temperature around T_{cr}. [24] Consequently, the evolution of antiferromagnetic long-range order is signalled by a sharp λ-shaped anomaly in α_c (see the inset), thereby evidencing the presence of pronounced magnetoelastic coupling. According to the Ehrenfest relation $\partial T_N/\partial p_c = T_N V_m \Delta\alpha_c/\Delta C_p$, [37, 38], where V_m denotes the molecular volume, the sign of the anomalous length changes, i.e., shrinking of the c axis upon entering the antiferromagnetic state, directly implies a positive uniaxial pressure dependence of T_N for compression along the c axis. Quantifying the size of the actual jumps in α_c and c_p from Ref. [39] by means of area conserving constructions [40–42], as depicted in the inset of Fig. 1(a) yields $\partial T_N/\partial p_c = 0.26(5)$ K/GPa.

A more detailed investigation of the uniaxial pressure effects in $Na_2Co_2TeO_6$ is achieved by performing a Grüneisen analysis [43–45], for which we extract the magnetic contribution to the thermal expansion coefficient using $\alpha_c^{mag} = \alpha_c(B) - \alpha_c(B \parallel a^* = 15\,\mathrm{T})$ as described in Ref. [24]. This approach utilizes that magnetic contributions to the thermal expansion are strongly suppressed by $B||a^*$, such that $\alpha_c(B \parallel a^* = 15\,\mathrm{T}) \simeq \alpha_c^{non-mag}$, with $\alpha_c^{non-mag}$ being the non-magnetic (phononic) contributions to the thermal expansion coefficient. As visible in Fig. 1b, α_c^{mag} and c_p^{mag} exhibit a similar temperature dependence in the vicinity of the anomaly at T_N, and can, hence, be scaled onto each other by a temperature-independent magnetic Grüneisen parameter $\gamma_c^{mag} = \alpha_c^{mag}/c_p^{mag} = 0.12(2)$ mol/MJ around T_N. This experimental observation implies that the emergence of antiferromagnetic long-range order in $Na_2Co_2TeO_6$ is driven by a single dominant energy scale ϵ^*. The uniaxial pressure dependence of ϵ^* is given by the Grüneisen relation $V_m\gamma_c^{mag} = \partial \ln \epsilon^*/\partial p_c \simeq 1\,\%/\mathrm{GPa}$. Since only one energy scale significantly contributes to the entropy changes at T_N, it is straightforward to identify ϵ^* with the magnetic ordering temperature, i.e., $\epsilon^* \propto T_N$. Doing so yields the uniaxial pressure dependence of $\partial T_N/\partial p_c = 0.28(5)$ K/GPa, which is in excellent agreement with the value obtained from the Ehrenfest analysis.

In contrast to the observation of a temperature-independent magnetic Grüneisen parameter around T_N, α_c^{mag} and c_p^{mag} follow a significantly different temperature dependence below $T \simeq 18$ K, such that the Grüneisen scaling using only a single parameter γ_c^{mag} is not possible at low temperatures. Hence, our data imply that the anomalous entropy changes around T_{cr} can not exclusively be attributed to the magnetic interplane interaction as discussed in Ref. [39] but must arise from at least two competing energy scales.

The small positive pressure dependence of T_N signals that antiferromagnetic long-range order in $Na_2Co_2TeO_6$ is weakly stabilised upon compression of the lattice along the c axis. As discussed for other 2D quantum magnets [31, 32, 46], this likely results from increasing intralayer coupling, which presumably resembles the dominant energy scale ϵ^*, due to changes in the Co-O-Co bond angle. An enhancement of the magnetic interplane interaction as a result of rising orbital overlap also seems plausible, but is rather unlikely to significantly contribute to T_N. [13, 47] In contrast to the small positive value of $\partial T_N/\partial p_c$ determined for $Na_2Co_2TeO_6$ here, compressive uniaxial strain perpendicular to the honeycomb planes of the closely related Kitaev candidate $\alpha-RuCl_3$ was found to shift the balance of magnetic couplings in favour of the Kitaev exchange, and thereby suppresses antiferromagnetic order at a rate of $\partial T_N/\partial p_c \simeq -12\,\mathrm{K/GPa}$ [28, 29, 48], which is almost two orders of magnitude larger than reported here for $Na_2Co_2TeO_6$. This

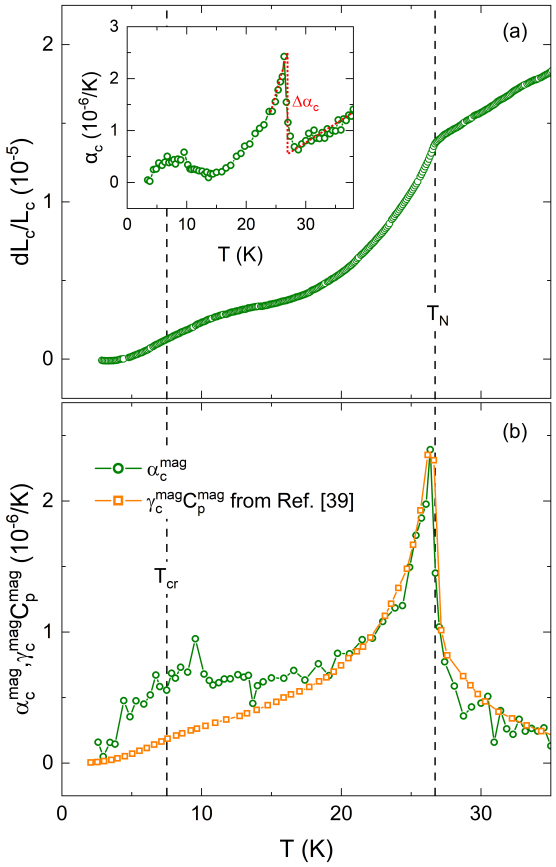


FIG. 1. (a) Out-of-plane thermal expansion dL_c/L_c and corresponding thermal expansion coefficient α_c (inset) at $B = 0$ T. Dotted red lines in the inset illustrate the determination of the jump $\Delta\alpha_c$, at T_N, employing an area-conserving construction. (b) Magnetic contribution to the thermal expansion coefficient and to the specific heat capacity from Ref. [39] scaled by the magnetic Grüneisen parameter γ_c^{mag} as described in the text. Dashed black lines mark the anomalies observed at T_N and T_{cr}.

discrepancy likely results from the important role of interlayer interactions in the exchange frustration mechanism found for $\alpha-RuCl_3$ [49], whereas magnetic coupling in $Na_2Co_2TeO_6$ is effectively two-dimensional. Hence, our results emphasize that, despite showing similar physical properties as $\alpha-RuCl_3$, uniaxial out-of-plane pressure is *not* a suitable external perturbation to tune $Na_2Co_2TeO_6$ into a QSL state.

The effects of magnetic fields applied perpendicular to the Co-layers on the thermal expansion coefficient are displayed in Fig. 2. While both anomalies at T_N and T_{cr} are visible for all measured fields up to 15 T and no new features occur in α_c, the data illustrate quite different field effects on the two anomalies. In agreement with reported magnetic susceptibility measurements [26, 39], the thermal expansion data in Fig. 2 demonstrate only a small suppression of T_N in an applied field $B \parallel c = 15$ T. This contradicts the effect of magnetic fields applied parallel to the honeycomb planes which yield the complete suppression of long-range magnetic order already for $B \perp c \simeq 10$ T. Our data hence confirm a strongly anisotropic magnetic field effect on the ground state of $Na_2Co_2TeO_6$. At the same time, the data in Fig. 2 show that the pronounced λ-shaped anomaly associated with the evolution of long-range antiferromagnetic order evolves into a broader step-like feature indicating the suppression of critical fluctuations. In contrast to the only small changes at T_N, the broad hump centred around T_{cr} is strongly affected by magnetic fields along the c axis. Specifically, up to $B = 9$ T, the feature becomes significantly more pronounced and turns into a sharp, almost symmetric peak which again starts to decrease for even higher fields. Simultaneously, T_{cr} follows a non-monotonous magnetic field dependence, that is, the associated hump shifts to lower temperatures in both small and high magnetic

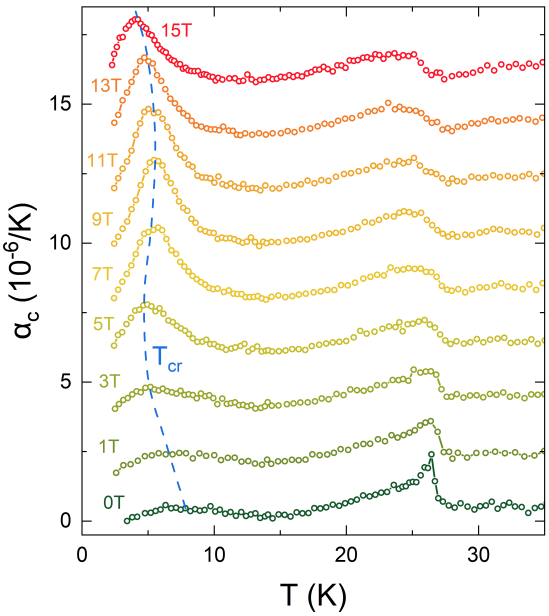


FIG. 2. Out-of-plane thermal expansion coefficient at selected magnetic fields applied $B \parallel$ c. The data are shifted along the ordinate for better visibility. The dashed line qualitatively marks the field dependence of $T_{\rm cr}$.

fields, whereas a positive $\partial T_{\rm cr}/\partial B$ is observed in the field range $3\,{\rm T} \lesssim B \lesssim 9\,{\rm T}$ (see the dashed line in Fig. 2 and Fig. 4).

The quantitatively and qualitatively contrasting field dependencies of both the size and the positions of the anomalies at $T_{\rm N}$ and $T_{\rm cr}$ clearly imply their different microscopic origin and, hence, the presence of multiple competing energy scales. In particular, our data evidence that the competing energy scales are differently affected by magnetic fields $B||c$. While the ratio of the jumps $\Delta\alpha_{\rm c}$ and $\Delta c_{\rm p}$ from Ref. [39] at $T_{\rm N}$ is roughly constant in the different magnetic fields and, thereby, indicates a rather field-independent pressure dependence $\partial T_{\rm N}/\partial p_{\rm c}$, the findings for $T_{\rm cr}$ are very different: Exploiting the Grüneisen relation implies the increase of $\partial \ln T_{\rm cr}/\partial p_{\rm c}$ with the external magnetic field by a factor of 3 in $B = 5$ T and of nearly 5 in $B = 9$ T (see Tab. I). The strong variation of the uniaxial pressure coefficient of $T_{\rm cr}$ upon application of magnetic fields $B||c$ can be directly read-off the data in Fig. 2 where the associated peak in $\alpha_{\rm c}$ is roughly six times larger at 9 T than in zero field while the corresponding feature in $c_{\rm p}$ only doubles in size [39]. The increasing pressure coefficient implies that the competing energy scale evolving around $T_{\rm cr}$ becomes more susceptible to out-of-plane lattice strain when magnetic fields $B \parallel c$ are applied which qualitatively corroborates its assignment with short-ranged out-of-plane correlations.

$B \parallel c$	$\partial T_{\rm N}/\partial p_{\rm c}$ (K/GPa)	$\partial \ln T_{\rm cr}/\partial p_{\rm c}$ (%/GPa)
0	0.28(5)	6.1(17)
5	0.27(5)	17(5)
9	0.28(6)	27(6)

TABLE I. Pressure dependecies of $T_{\rm N}$ and $T_{\rm cr}$ at different magnetic fields applied $B \parallel c$ (see the text).

Magnetoelastic coupling in $Na_2Co_2TeO_6$ is further investigated by our magnetostriction studies. The field-induced length changes up to 14 T measured at $T = 2$ K are shown in Fig. 3a. For comparison, the isothermal magnetisation obtained at the same temperature is shown in the diagram as well. We observe the following main features: Starting from zero field, $dL_{\rm c}/L_{\rm c}(B)$ is concave and continuously decreases with magnetic field. At $B_{\rm C} \simeq 4.6$ T, magnetostriction changes its curvature from concave to convex but continues to decrease further until a minimum appears around $B_{\rm min} \simeq 8$ T. Above 8 T, the c axis continuously expands up to the highest measured field. The inflection point in $dL_{\rm c}/L_{\rm c}(B)$ coincides with a kink in the isothermal magnetisation at $B_{\rm C}$, which has been observed but is only scarcely discussed in the literature [26, 27]. The correspondence of lattice and magnetization changes is better

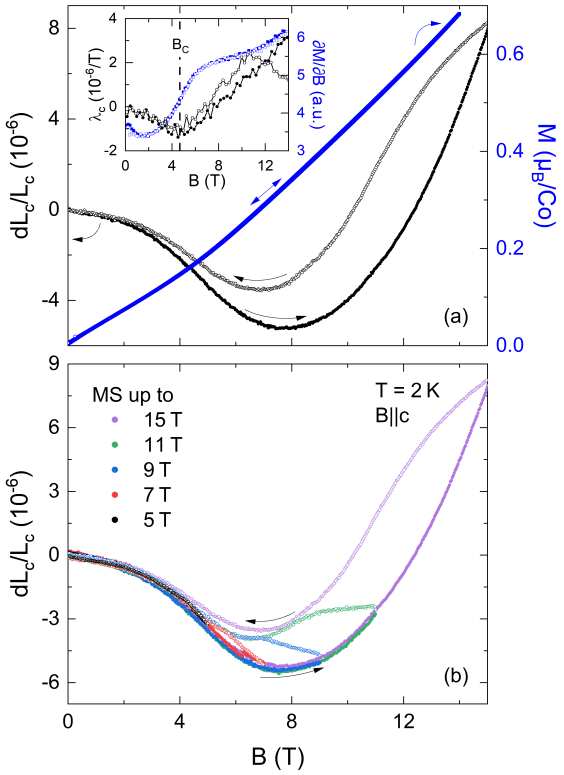


FIG. 3. (a) Out-of-plane magnetostriction and isothermal magnetisation for $B \parallel$ c at $T = 2$ K. The inset displays the corresponding magnetostriction coefficient λ_c and susceptibility $\partial M/\partial B$. (b) Out-of-plane magnetostriction at $T = 2$ K up to different maximum magnetic fields $B \parallel c$. Closed (open) symbols depict up-(down-)sweeps of the magnetic field.

visible in the respective first derivatives, i.e., in the magnetostriction coefficient λ_c and in the differential magnetic susceptibility $\partial M/\partial B$ shown in the inset of Fig. 3, where the minimum in λ_c coincides with a distinct jump in $\partial M/\partial B$. Simultaneously, a low-temperature upturn of the static magnetic susceptibility $\chi_c(T) = M_c(T)/B$ is found only for $B \gtrsim 5$ T (see Fig. A2), which has been heuristically related to a change of the ferrimagnetic spin canting along c [39]. In agreement with recent electron spin resonance spectroscopy studies revealing the softening of a magnon excitation mode and, hence, symmetry-breaking in a similar field region [50, 51], the here presented magnetic data exhibit characteristics of a continuous (second-order) phase transition at B_C. On the other hand, the associated magnetostrictive response implies a weak discontinuous character at most, which renders the assignment of the observed anomalies to a second-order thermodynamic phase boundary unclear. The position of B_C is virtually temperature-independent up to 6 K, i.e., around $T_{cr}(B \simeq 5$ T), above which no associated feature can be discerned (see Fig. A3). Following the interpretation of B_C marking a phase transition, the absence of corresponding features at temperatures above T_{cr} indicates that the latter signals a phase boundary as well (cf. the magnetoelastic phase diagram in Fig. 4).

In contrast to the results of pulsed magnetisation measurements in Ref. [26], we neither observe a peak centred around 9 T in our quasi-static $\partial M/\partial B$ data nor identify any corresponding features in the lattice parameters. We conclude that the reported characteristics may be associated with dynamic effects at higher sweep rates. Notably, our c axis magnetostriction data in Fig. 3 display pronounced hysteresis from $B \simeq 2$ T up to the highest field of 14 T while the up- and down-sweep of the isothermal magnetisation perfectly coincide within the resolution of our experiment. A similar finding, i.e., hysteretic behaviour in the field-induced length changes, but not in the magnetic properties, was discussed to arise from the formation of structural domains also for fields along the a^* axis [24]. Our data, hence, imply that structural domains are present for $B \parallel c$ as well. Interestingly, hysteresis in $dL_c/L_c(B)$ only occurs when the magnetic field is increased beyond B_C (see Fig. 3b). Following the putative assignment of B_C to a phase boundary,

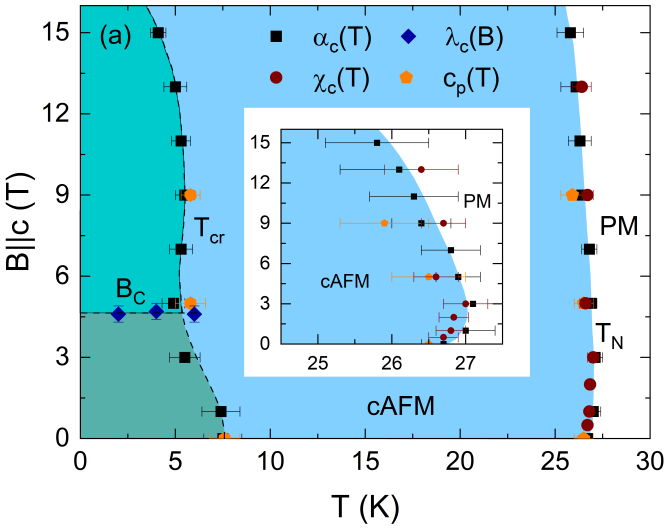


FIG. 4. Magnetoelastic phase diagram of $Na_2Co_2TeO_6$ for $B \parallel c$ as constructed from dilatometry and magnetisation data. For comparison, anomaly position in specific heat data from Ref. [39] are shown, too. PM and cAFM denote the paramagnetic and canted antiferromagnetic phase, respectively. All lines and coloured areas are guide to the eye.

this observation would imply that structural domains appear in the presumed high-field phase. Such domain effects could, therefore, explain the observed unusual shape of the anomaly marking B_C in the magnetostriction. Note here that, while the minimum in dL_c/L_c shifts by roughly 1 T between up- and down-sweep, the position of B_C is independent of the direction of the magnetic field sweep.

The anomaly positions extracted from our magnetic and dilatometric data are summarised in the magnetoelastic phase diagram shown in Fig. 4. For reference, we also include the results of the specific heat capacity measurements from Ref. [39]. As discussed earlier, the phase boundary marked by T_N separating the paramagnetic (PM) from the canted antiferromagnetic (cAFM) state is rather robust against magnetic fields applied along the c axis. In numbers, an external field of 15 T reduces the Néel temperature by only about 1 K. A more detailed investigation, moreover, reveals that T_N does not decrease continuously but two different regimes can be identified (see the inset of Fig. 4). At high magnetic fields $B \gtrsim 5$ T, the magnetic order is suppressed by magnetic fields as expected for long-range antiferromagnetic order. In contrast, $\partial T_N/\partial B$ is positive for small fields up to at least 3 T which likely arises due to ferrimagnetic spin canting along c in the magnetic ground state. Note that the observed positive field dependence of T_N is thermodynamically linked to the sign of the corresponding anomalies in the magnetic susceptibility by means of the Ehrenfest relation $\partial T/\partial B = -TV\Delta(\partial M/\partial T)/\Delta c_p$ [37]. The superposition of these two regimes leads to a maximum in T_N at $B \simeq 4$ T. At this point, it is noteworthy that the sign change of $\partial T_N/\partial B$ occurs at fields only slightly smaller than B_C. Thus, one might speculate that the low-temperature features at B_C and the changes in the slope $T_{cr}(B)$ in this field range result from the same microscopic mechanism (possibly a change of spin canting along c) as the sign change in $\partial T_N/\partial B$.

The magnetic field dependence of T_{cr} is also not monotonous but can be separated into three regions. For $B \lesssim 3-5$ T, the observed peaks in α_c and c_p shifts to smaller temperatures with increasing external field. Subsequently, T_{cr} increases (this behaviour is better visible directly in the α_c data in Fig. 2) at intermediate fields up to 9 T until being suppressed again by even higher magnetic fields. The first crossover region also falls into the field range of B_C hinting at an intertwining of the two phenomena. The second sign change of $\partial T_{cr}/\partial B$ is not accompanied by any distinct features in the here presented static thermodynamic properties but might be related to the peak occurring around 9 T in the pulsed magnetisation measurements, which would imply a spin dynamic origin [26]. The observation of clear anomalies in the thermodynamic response functions strongly implies that T_{cr} and B_C are associated with phase transitions, the exact nature of which remains an open question.

IV. CONCLUSIONS

In conclusion, we report a detailed dilatometric study on the Kitaev spin liquid candidate $Na_2Co_2TeO_6$ up to high magnetic fields applied $B \parallel c$. In contrast to the findings for the closely related α-$RuCl_3$, uniaxial compression perpendicular to the honeycomb planes is demonstrated to stabilise the antiferromagnetic ground state in $Na_2Co_2TeO_6$. Moreover, the calculated pressure coefficient $\partial T_N/\partial p_c = 0.28(5)$ K/GPa is almost two orders of magnitude smaller than in α-$RuCl_3$ which renders tensile out-of-plane strain a rather ineffective perturbation to drive $Na_2Co_2TeO_6$ into a spin disordered phase. While the entropy changes around T_N are dominated by a single energy scale ϵ^*, the failure of Grüneisen scaling around T_{cr} implies competing interactions at lower temperatures. Magnetic fields applied parallel to the honeycomb layers do not significantly suppress the magnetic order, but the low-temperature energy scale is found to become increasingly sensitive to lattice changes at high fields. The conclusion of strong coupling between spin and lattice degrees of freedom is further corroborated by our magnetostriction measurements showing that both the isothermal magnetization and the field-induced length changes exhibit a clear feature at B_C which putatively arises from a change in the spin canting along the c axis. The magnetoelastic phase diagram reveals sign changes in the field dependencies of both T_N and T_{cr} connected to B_C. Summarising, our investigations provide a deeper understanding of the role of magnetoelastic coupling in the ground state properties of $Na_2Co_2TeO_6$.

ACKNOWLEDGMENTS

We acknowledge support by Deutsche Forschungsgemeinschaft (DFG) under Germany's Excellence Strategy EXC2181/1-390900948 (the Heidelberg STRUCTURES Excellence Cluster). JA acknowledges support by the IMPRS-QD Heidelberg. KYC was supported by the National Research Foundation (NRF) of Korea (Grant Nos. 2020R1A5A1016518 and RS-2023-00209121). R.S. acknowledges the financial support provided by the Ministry of Science and Technology in Taiwan under project numbers NSTC 111-2124-M-001-007, Financial support from the Center of Atomic Initiative for New Materials (AI-Mat), (Project No. 108L9008) and Academia Sinica for the budget of AS-iMATE-113-12.

APPENDIX

Appendix A: Static magnetic susceptibility

The out-of-plane static magnetic susceptibility of $Na_2Co_2TeO_6$ at $B = 0.05$ T, shown in Fig. A1, is characterised by a pronounced kink at $T_N = 26.8$ K marking the evolution of canted antiferromagnetic long-range order. Due to unequal spin canting on the two different Co-sites, χ_c exhibits a rather ferrimagnetic behaviour, i.e., strong hysteresis below T_N and initially negative net magnetisation after field cooling. In addition to the prominent anomaly at T_N, a small jump can be identified at low temperatures in the ZFC data. The absence of this feature in the FC data implies that it is associated with dynamic effects, such as domain wall movement. Importantly, we do not observe any additional anomalies in the susceptibility that might correspond to putative impurity phases, such as the antiferromagnetic polymorph reported in Ref. [34].

The effects of higher magnetic fields $B \parallel c$ on χ_c are depicted in Fig. A2. In agreement with the thermal expansion data, T_N is only hardly affected by the external fields. However, the corresponding anomaly is found to exhibit a different shape in small and high fields: While T_N is marked by a pronounced upwards kink, i.e., $\Delta\partial M/\partial B > 0$ upon heating, for $B \lesssim 3$ T, the anomaly exhibits the opposite sign for $B \gtrsim 5$ t. Utilizing the Ehrenfest relation, this straightforwardly corroborates the findings of the magnetoelastic phase diagram as described in the main text. Simultaneously, χ_c exhibits a small upturn at low temperatures for $B \geq 5$ T, but not for $B \leq 3$ T, which might be related to the critical field B_C and is discussed in more detail in the main text.

Appendix B: Magnetostriction at higher temperatures

Fig. A3 shows the out-of-plane magnetostriction of $Na_2Co_2TeO_6$ at selected temperatures measured for increasing magnetic fields $B \parallel c$. On increasing the temperature, shrinking of the c axis at small fields becomes less pronounced and both the minimum and the inflection point in dL_c/L_c gradually broaden until they are no longer discernable for

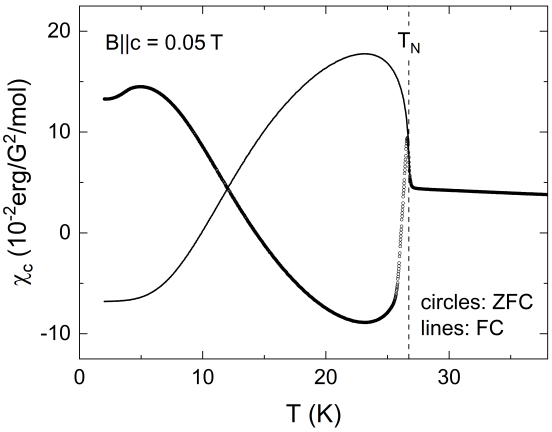


FIG. A1. Zero field cooled (ZFC) and field cooled (FC) out-of-plane magnetic susceptibility at $B = 0.05$ T. The dashed vertical line marks the emergence of magnetic order at T_N.

$T \gtrsim 8$ K. At temperatures higher than 6 K, magnetostriction is positive in the entire measured field range. While the position of $B_{\min}$ shifts with varying temperature, B_C is essentially temperature independent.

[1] A. Kitaev, Anyons in an exactly solved model and beyond, Ann. Phys. **321**, 2 (2006).
[2] A. Kitaev, Fault-tolerant quantum computation by anyons, Ann. Phys. **303**, 2–30 (2003).
[3] L.-M. Duan, E. Demler, and M. D. Lukin, Controlling spin exchange interactions of ultracold atoms in optical lattices, Phys. Rev. Lett. **91**, 090402 (2003).
[4] A. Micheli, G. K. Brennen, and P. Zoller, A toolbox for lattice-spin models with polar molecules, Nature Phys. **2**, 341–347 (2006).
[5] G. Jackeli and G. Khaliullin, Mott Insulators in the Strong Spin-Orbit Coupling Limit: From Heisenberg to a Quantum Compass and Kitaev Models, Phys. Rev. Lett. **102**, 017205 (2009).
[6] Y. Singh and P. Gegenwart, Antiferromagnetic Mott insulating state in single crystals of the honeycomb lattice material Na_2IrO_3, Phys. Rev. B **82**, 064412 (2010).
[7] Y. Singh, S. Manni, J. Reuther, T. Berlijn, R. Thomale, W. Ku, S. Trebst, and P. Gegenwart, Relevance of the Heisenberg-Kitaev Model for the Honeycomb Lattice Iridates A_2IrO_3, Phys. Rev. Lett. **108**, 127203 (2012).
[8] J. Nasu, J. Knolle, D. Kovrizhin, Y. Motome, and R. Moessner, Fermionic response from fractionalization in an insulating two-dimensional magnet, Nature Phys. **12**, 912–915 (2016).
[9] H. Takagi, T. Takayama, G. Jackeli, G. Khaliullin, and S. E. Nagler, Concept and realization of Kitaev quantum spin liquids, Nat. Rev. Phys. **1**, 264 (2019).
[10] H. Liu and G. Khaliullin, Pseudospin exchange interactions in d^7 cobalt compounds: Possible realization of the Kitaev model, Phys. Rev. B **97**, 014407 (2018).
[11] R. Sano, Y. Kato, and Y. Motome, Kitaev-Heisenberg Hamiltonian for high-spin d^7 Mott insulators, Phys. Rev. B **97**, 014408 (2018).
[12] H. Liu, J. Chaloupka, and G. Khaliullin, Kitaev Spin Liquid in d^7 Transition Metal Compounds, Phys. Rev. Lett. **125**, 047201 (2020).
[13] L. Viciu, Q. Huang, E. Morosan, H. Zandbergen, N. Greenbaum, T. McQueen, and R. Cava, Structure and basic magnetic properties of the honeycomb lattice compounds $Na_2Co_2TeO_6$ and $Na_3Co_2SbO_6$, J. Solid State Chem. **180**, 1060 (2007).
[14] E. Lefrançois, M. Songvilay, J. Robert, G. Nataf, E. Jordan, L. Chaix, C. V. Colin, P. Lejay, A. Hadj-Azzem, R. Ballou, and V. Simonet, Magnetic properties of the honeycomb oxide $Na_2Co_2TeO_6$, Phys. Rev. B **94**, 214416 (2016).
[15] G. Xiao, Z. Xia, W. Zhang, X. Yue, S. Huang, X. Zhang, F. Yang, Y. Song, M. Wei, H. Deng, and D. Jiang, Crystal Growth and the Magnetic Properties of $Na_2Co_2TeO_6$ with Quasi-Two-Dimensional Honeycomb Lattice, Cryst. Growth Des. **19**, 2658 (2019).
[16] G. Lin, J. Jeong, C. Kim, Y. Wang, Q. Huang, T. Masuda, S. Asai, S. Itoh, G. Günther, M. Russina, Z. Lu, J. Sheng, L. Wang, J. Wang, G. Wang, Q. Ren, C. Xi, W. Tong, L. Ling, Z. Liu, L. Wu, J. Mei, Z. Qu, H. Zhou, X. Wang, J.-G. Park, Y. Wan, and J. Ma, Field-induced quantum spin disordered state in spin-1/2 honeycomb magnet $Na_2Co_2TeO_6$, Nat. Comm. **12**, 5559 (2021).

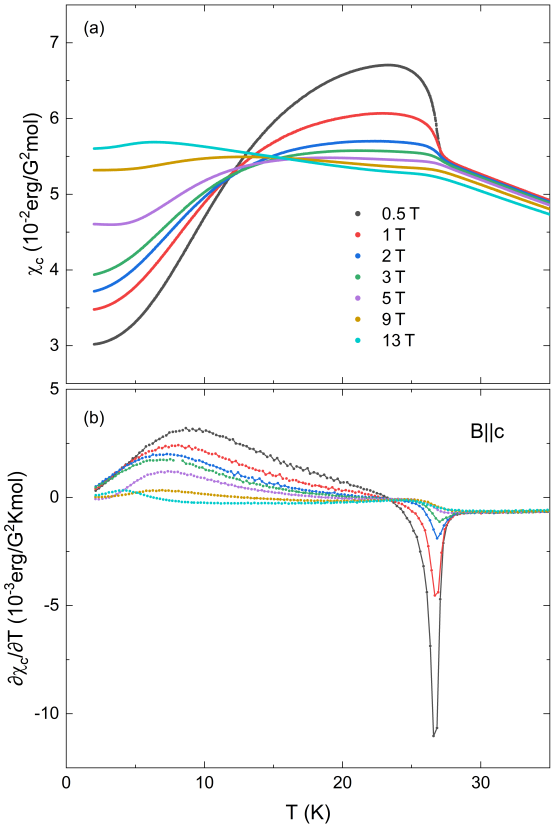


FIG. A2. Out-of-plane magnetic susceptibility (a) and its temperature derivative (b) at various selected external magnetic fields. All measurements were performed following a field-cooled protocol.

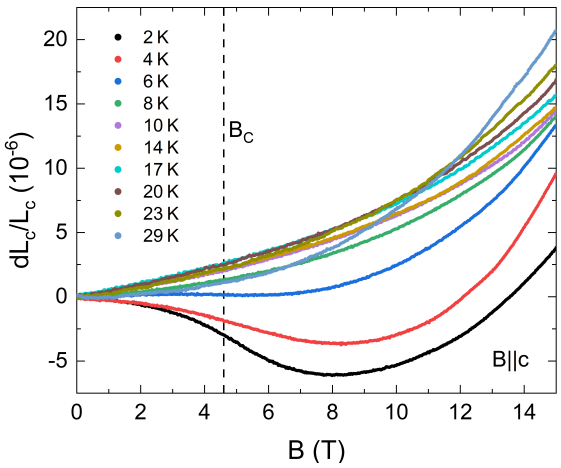


FIG. A3. Out-of-plane magnetostriction for $B \parallel c$ measured at selected temperatures. For better visibility only the up-sweeps are shown. The black dashed line marks the critical field B_C.

[17] X. Hong, M. Gillig, W. Yao, L. Janssen, V. Kocsis, S. Gass, Y. Li, A. U. B. Wolter, B. Büchner, and C. Hess, Phonon thermal transport shaped by strong spin-phonon scattering in a Kitaev material $Na_2Co_2TeO_6$, npj quantum mat. **9**, 18 (2024).
[18] M. Songvilay, J. Robert, S. Petit, J. A. Rodriguez-Rivera, W. D. Ratcliff, F. Damay, V. Balédent, M. Jiménez-Ruiz, P. Lejay, E. Pachoud, A. Hadj-Azzem, V. Simonet, and C. Stock, Kitaev interactions in the Co honeycomb antiferromagnets $Na_3Co_2SbO_6$ and $Na_2Co_2TeO_6$, Phys. Rev. B **102**, 224429 (2020).
[19] C. Kim, J. Jeong, G. Lin, P. Park, T. Masuda, S. Asai, S. Itoh, H.-S. Kim, H. Zhou, J. Ma, and J.-G. Park, Antiferromagnetic Kitaev interaction in $J_{\text{eff}} = 1/2$ cobalt honeycomb materials $Na_3Co_2SbO_6$ and $Na_2Co_2TeO_6$, J. Phys.: Condens. Matter **34**, 045802 (2021).
[20] A. M. Samarakoon, Q. Chen, H. Zhou, and V. O. Garlea, Static and dynamic magnetic properties of honeycomb lattice antiferromagnets $Na_2M_2TeO_6$, M = Co and Ni, Phys. Rev. B **104**, 184415 (2021).
[21] A. L. Sanders, R. A. Mole, J. Liu, A. J. Brown, D. Yu, C. D. Ling, and S. Rachel, Dominant Kitaev interactions in the honeycomb materials $Na_3Co_2SbO_6$ and $Na_2Co_2TeO_6$, Phys. Rev. B **106**, 014413 (2022).
[22] W. G. F. Krüger, W. Chen, X. Jin, Y. Li, and L. Janssen, Triple-q Order in $Na_2Co_2TeO_6$ from Proximity to Hidden-SU(2)-Symmetric Point, Phys. Rev. Lett. **131**, 146702 (2023).
[23] L. Xiang, R. Dhakal, M. Ozerov, Y. Jiang, B. S. Mou, A. Ozarowski, Q. Huang, H. Zhou, J. Fang, S. M. Winter, Z. Jiang, and D. Smirnov, Disorder-Enriched Magnetic Excitations in a Heisenberg-Kitaev Quantum Magnet $Na_2Co_2TeO_6$, Phys. Rev. Lett. **131**, 076701 (2023).
[24] J. Arneth, K.-Y. Choi, R. Kalaivanan, R. Sankar, and R. Klingeler, Signatures of a quantum critical endpoint in the Kitaev candidate $Na_2Co_2TeO_6$, Phys. Rev. B **110**, L140402 (2024).
[25] G. Xiao, Z. Xia, Y. Song, and L. Xiao, Magnetic properties and phase diagram of quasi-two-dimensional $Na_2Co_2TeO_6$ single crystal under high magnetic field, J. Phys.: Condens. Matter **34**, 075801 (2021).
[26] S. Zhang, S. Lee, E. Brosha, Q. Huang, H. Zhou, V. S. Zapf, and M. Lee, Out-of-plane magnetic phase diagram of the Kitaev quantum magnet $Na_2Co_2TeO_6$, Phys. Rev. B **110**, 144431 (2024).
[27] X.-G. Zhou, H. Li, C. Kim, K. Matsuo, Z. Yang, A. Miyata, G. Su, K. Kindo, J.-G. Park, Y. Kohama, W. Li, and Y. H. Matsuda, Emergent quantum disordered phase in $Na_2Co_2TeO_6$ under intermediate magnetic fields along c axis (2024), arXiv:2408.01957.
[28] M. He, X. Wang, L. Wang, F. Hardy, T. Wolf, P. Adelmann, T. Brückel, Y. Su, and C. Meingast, Uniaxial and hydrostatic pressure effects in α-RuCl3 single crystals via thermal-expansion measurements, J. Phys. Condens. Matter **30**, 385702 (2018).
[29] S. Gass, P. M. Cônsoli, V. Kocsis, L. T. Corredor, P. Lampen-Kelley, D. G. Mandrus, S. E. Nagler, L. Janssen, M. Vojta, B. Büchner, and A. U. B. Wolter, Field-induced transitions in the Kitaev material $\alpha-RuCl_3$ probed by thermal expansion and magnetostriction, Phys. Rev. B **101**, 245158 (2020).
[30] S. Spachmann, P. Berdonosov, M. Markina, A. Vasiliev, and R. Klingeler, Linear magnetoelastic coupling and magnetic phase diagrams of the buckled-kagomé antiferromagnet $Cu_3Bi(SeO_3)_2O_2Cl$, Scientific Reports **12**, 7383 (2022).
[31] J. Arneth, M. Jonak, S. Spachmann, M. Abdel-Hafiez, Y. O. Kvashnin, and R. Klingeler, Uniaxial pressure effects in the two-dimensional van der Waals ferromagnet CrI_3, Phys. Rev. B **105**, L060404 (2022).
[32] S. Spachmann, S. Selter, B. Büchner, S. Aswartham, and R. Klingeler, Strong uniaxial pressure dependencies evidencing spin-lattice coupling and spin fluctuations in $Cr_2Ge_2Te_6$, Phys. Rev. B **107**, 184421 (2023).
[33] C. H. Lee, S. Lee, Y. S. Choi, Z. H. Jang, R. Kalaivanan, R. Sankar, and K.-Y. Choi, Multistage development of anisotropic magnetic correlations in the Co-based honeycomb lattice $Na_2Co_2TeO_6$, Phys. Rev. B **103**, 214447 (2021).
[34] E. Dufault, F. Bahrami, A. Streeter, X. Yao, E. Gonzalez, Q. Zhang, and F. Tafti, Introducing the monoclinic polymorph of the honeycomb magnet $Na_2Co_2TeO_6$, Phys. Rev. B **108**, 064405 (2023).
[35] R. Küchler, T. Bauer, M. Brando, and F. Steglich, A compact and miniaturized high resolution capacitance dilatometer for measuring thermal expansion and magnetostriction, Rev. Sci. Instrum. **83**, 095102 (2012).
[36] J. Werner, W. Hergett, M. Gertig, J. Park, C. Koo, and R. Klingeler, Anisotropy-governed competition of magnetic phases in the honeycomb quantum magnet $Na_3Ni_2SbO_6$ studied by dilatometry and high-frequency ESR, Phys. Rev. B **95**, 214414 (2017).
[37] T. M. Nieuwenhuizen, Ehrenfest relations at the glass transition: Solution to an old paradox, Phys. Rev. Lett. **79**, 1317 (1997).
[38] P. Moin, Ehrenfest equations for second-order phase transition under hydrostatic and uniaxial stresses, Phase Transitions **89**, 1074–1077 (2016).
[39] W. Yao and Y. Li, Ferrimagnetism and anisotropic phase tunability by magnetic fields in $Na_2Co_2TeO_6$, Phys. Rev. B **101**, 085120 (2020).
[40] C. Meingast, B. Blank, H. Bürkle, B. Obst, T. Wolf, H. Wühl, V. Selvamanickam, and K. Salama, Anisotropic pressure dependence of T_c in single-crystal $YBa_2Cu_3O_7$ via thermal expansion, Phys. Rev. B **41**, 11299 (1990).
[41] M. Majumder, R. S. Manna, G. Simutis, J. C. Orain, T. Dey, F. Freund, A. Jesche, R. Khasanov, P. K. Biswas, E. Bykova, N. Dubrovinskaia, L. S. Dubrovinsky, R. Yadav, L. Hozoi, S. Nishimoto, A. A. Tsirlin, and P. Gegenwart, Breakdown of Magnetic Order in the Pressurized Kitaev Iridate $\beta-Li_2IrO_3$, Phys. Rev. Lett. **120**, 237202 (2018).
[42] L. Gries, M. Jonak, A. Elghandour, K. Dey, and R. Klingeler, Role of magnetoelastic coupling and magnetic anisotropy in $MnTiO_3$, Phys. Rev. B **106**, 174425 (2022).
[43] T. Barron and G. White, *Heat Capacity and Thermal Expansion at Low Temperatures* (Springer New York, NY, 1999).
[44] J. Franse, M. van Sprang, A. De Visser, and P. Brommer, Grüneisen analysis of specific heat and thermal expansion of heavy-fermion UPt_3, Physica B: Condensed Matter **154**, 379–389 (1989).

[45] R. Klingeler, J. Geck, S. Arumugam, N. Tristan, P. Reutler, B. Büchner, L. Pinsard-Gaudart, and A. Revcolevschi, Pressure-induced melting of the orbital polaron lattice in $La_{1-x}Sr_xMnO_3$, Phys. Rev. B **73**, 214432 (2006).
[46] Y. Huang, A. K. Pathak, J.-Y. Tsai, C. Rumsey, M. Ivill, N. Kramer, Y. Hu, M. Trebbin, Q. Yan, and S. Ren, Pressure-controlled magnetism in 2d molecular layers, Nat. Commun. **14**, 3186 (2023).
[47] A. K. Bera, S. M. Yusuf, A. Kumar, and C. Ritter, Zigzag antiferromagnetic ground state with anisotropic correlation lengths in the quasi-two-dimensional honeycomb lattice compound $Na_2Co_2TeO_6$, Phys. Rev. B **95**, 094424 (2017).
[48] D. A. S. Kaib, S. Biswas, K. Riedl, S. M. Winter, and R. Valentí, Magnetoelastic coupling and effects of uniaxial strain in $\alpha - RuCl_3$ from first principles, Phys. Rev. B **103**, L140402 (2021).
[49] C. Balz, L. Janssen, P. Lampen-Kelley, A. Banerjee, Y. H. Liu, J.-Q. Yan, D. G. Mandrus, M. Vojta, and S. E. Nagler, Field-induced intermediate ordered phase and anisotropic interlayer interactions in $\alpha-RuCl_3$, Phys. Rev. B **103**, 174417 (2021).
[50] A. K. Bera, S. M. Yusuf, F. Orlandi, P. Manuel, L. Bhaskaran, and S. A. Zvyagin, Field-induced phase transitions and anisotropic magnetic properties of the Kitaev-Heisenberg compound $Na_2Co_2TeO_6$, Phys. Rev. B **108**, 214419 (2023).
[51] L. Bischoff, J. Arneth, R. Kalaivanan, R. Sankar, K.-Y. Choi, and R. Klingeler, Spin waves in $Na_2Co_2TeO_6$ studied by high-frequency/high-field ESR: Successes and failures of the triple-q model, unpublished.

Bibliography

[1] Press release: The nobel prize in physics 1943. `https://www.nobelprize.org/prizes/physics/1943/summary/`. Accessed: 2025-07-18.

[2] W. Gerlach and O. Stern. Der experimentelle Nachweis der Richtungsquantelung im Magnetfeld. *Zeitschrift für Physik*, 9(1):349–352, 1922.

[3] S. Blundell. *Magnetism in Condensed Matter*. Oxford Master Series in Condensed Matter Physics. Oxford University Press, London, England, 2001.

[4] J. Crangle. *Solid State Magnetism*. Springer US, 1991.

[5] J. M. D. Coey and Stuart S. P. Parking, editors. *Handbook of Magnetism and Magnetic Materials*. Springer International Publishing, 2021.

[6] R. Sessoli, D. Gatteschi, A. Caneschi, and M. A. Novak. Magnetic bistability in a metal-ion cluster. *Nature*, 365(6442):141–143, 1993.

[7] G. Christou, D. Gatteschi, D. N. Hendrickson, and R. Sessoli. Single-Molecule Magnets. *MRS Bulletin*, 25(11):66–71, 2000.

[8] L. Gunther and B. Barbara, editors. *Quantum Tunneling of Magnetization — QTM '94*. Springer Netherlands, 1995.

[9] J. R. Friedman, M. P. Sarachik, J. Tejada, and R. Ziolo. Macroscopic Measurement of Resonant Magnetization Tunneling in High-Spin Molecules. *Physical Review Letters*, 76:3830–3833, 1996.

[10] L. Thomas, F. Lionti, R. Ballou, D. Gatteschi, R. Sessoli, and B. Barbara. Macroscopic quantum tunnelling of magnetization in a single crystal of nanomagnets. *Nature*, 383(6596):145–147, 1996.

[11] C. Sangregorio, T. Ohm, C. Paulsen, R. Sessoli, and D. Gatteschi. Quantum tunneling of the magnetization in an iron cluster nanomagnet. *Physical Review Letters*, 78:4645–4648, 1997.

[12] W. Wernsdorfer and R. Sessoli. Quantum Phase Interference and Parity Effects in Magnetic Molecular Clusters. *Science*, 284(5411):133–135, 1999.

[13] A.-L. Barra, P. Debrunner, D. Gatteschi, C. E. Schulz, and R. Sessoli. Superparamagnetic-like behavior in an octanuclear iron cluster. *Europhysics Letters (EPL)*, 35(2):133–138, 1996.

[14] S. M. J. Aubin, M. W. Wemple, D. M. Adams, H.-L. Tsai, G. Christou, and D. N. Hendrickson. Distorted $Mn^{IV}Mn^{III}_3$ Cubane Complexes as Single-Molecule Magnets. *Journal of the American Chemical Society*, 118(33):7746–7754, 1996.

[15] S. M. J. Aubin, N. R. Dilley, M. W. Wemple, M. B. Maple, G. Christou, and D. N. Hendrickson. Half-Integer-Spin Small Molecule Magnet Exhibiting Resonant Magnetization Tunneling. *Journal of the American Chemical Society*, 120(4):839–840, 1998.

[16] S. L. Castro, Z. Sun, C. M. Grant, J. C. Bollinger, D. N. Hendrickson, and G. Christou. Single-Molecule Magnets: Tetranuclear Vanadium(III) Complexes with a Butterfly Structure and an S = 3 Ground State. *Journal of the American Chemical Society*, 120(10):2365–2375, 1998.

[17] G. Aromí, S. M. J. Aubin, M. A. Bolcar, G. Christou, H. J. Eppley, K. Folting, D. N. Hendrickson, J. C. Huffman, R. C. Squire, H.-L. Tsai, S. Wang, and M. W. Wemple. Manganese carboxylate clusters: from structuralaesthetics to single-molecule magnets. *Polyhedron*, 17(17):3005–3020, 1998.

[18] D. Gatteschi and R. Sessoli. Quantum Tunneling of Magnetization and Related Phenomena in Molecular Materials. *Angewandte Chemie International Edition*, 42(3):268–297, 2003.

[19] A. J. Tasiopoulos, A. Vinslava, W. Wernsdorfer, K. A. Abboud, and G. Christou. Giant Single-Molecule Magnets: A Mn_{84} Torus and Its Supramolecular Nanotubes. *Angewandte Chemie*, 116(16):2169–2173, 2004.

[20] M. Murugesu, M. Habrych, W. Wernsdorfer, K. A. Abboud, and G. Christou. Single-Molecule Magnets: A Mn_{25} Complex with a Record $S = 51/2$ Spin for a Molecular Species. *Journal of the American Chemical Society*, 126(15):4766–4767, 2004.

[21] T. C. Stamatatos, K. A. Abboud, W. Wernsdorfer, and G. Christou. "Spin Tweaking" of a High-Spin Molecule: An Mn_{25} Single-Molecule Magnet with an $S = 61/2$ Ground State. *Angewandte Chemie International Edition*, 46(6):884–888, 2007.

[22] G. Aromí, J.-P. Claude, M. J. Knapp, J. C. Huffman, D. N. Hendrickson, and G. Christou. High-Spin Molecules: Hexanuclear $[Mn_6O_4Cl_4(Me_2dbm)_6]$ (Me_2dbmH = 4,4'-Dimethyldibenzoylmethane) with a Near Tetrahedral $[Mn_6O_4Cl_4]^{6+}$ Core and a $S = 12$ Ground State. *Journal of the American Chemical Society*, 120(12):2977–2978, 1998.

[23] G. L. Abbati, A. Cornia, A. C. Fabretti, A. Caneschi, and D. Gatteschi. A Ferromagnetic Ring of Six Manganese(III) Ions with a S = 12 Ground State. *Inorganic Chemistry*, 37(7):1430–1431, 1998.

[24] N. Ishikawa, M. Sugita, T. Ishikawa, S. Koshihara, and Y. Kaizu. Lanthanide Double-Decker Complexes Functioning as Magnets at the Single-Molecular Level. *Journal of the American Chemical Society*, 125(29):8694–8695, 2003.

[25] J. Tang and P. Zhang. *Lanthanide Single Molecule Magnets*. Springer Berlin Heidelberg, 2015.

[26] S. T. Liddle and J. van Slageren. Improving f-element single molecule magnets. *Chemical Society Reviews*, 44(19):6655–6669, 2015.

[27] S. Osa, T. Kido, N. Matsumoto, N. Re, A. Pochaba, and J. Mrozinski. A Tetranuclear 3d-4f Single Molecule Magnet: $[Cu^{II}LTb^{III}(hfac)_2]_2$. *Journal of the American Chemical Society*, 126(2):420–421, 2003.

[28] C. M. Zaleski, E. C. Depperman, J. W. Kampf, M. L. Kirk, and V. L. Pecoraro. Synthesis, Structure, and Magnetic Properties of a Large Lanthanide-Transition-Metal Single-Molecule Magnet. *Angewandte Chemie International Edition*, 43(30):3912–3914, 2004.

[29] J.-P. Costes, M. Auchel, F. Dahan, V. Peyrou, S. Shova, and W. Wernsdorfer. Synthesis, Structures, and Magnetic Properties of Tetranuclear Cu^{II}-Ln^{III} Complexes. *Inorganic Chemistry*, 45(5):1924–1934, 2006.

[30] Y. Peng and A. K. Powell. What do 3d-4f butterflies tell us? *Coordination Chemistry Reviews*, 426:213490, 2021.

[31] S. K. Langley, N. F. Chilton, L. Ungur, B. Moubaraki, L. F. Chibotaru, and K. S. Murray. Heterometallic Tetranuclear $[Ln_2^{III}Co_2^{III}]$ Complexes Including Suppression of Quantum Tunneling of Magnetization in the $[Dy_2^{III}Co_2^{III}]$ Single Molecule Magnet. *Inorganic Chemistry*, 51(21):11873–11881, 2012.

[32] S. K. Langley, D. P. Wielechowski, V. Vieru, N. F. Chilton, B. Moubaraki, B. F. Abrahams, L. F. Chibotaru, and K. S. Murray. A $Cr_2^{III}Dy_2^{III}$ Single-Molecule Magnet: Enhancing the Blocking Temperature through 3d Magnetic Exchange. *Angewandte Chemie International Edition*, 52(46):12014–12019, 2013.

[33] S. K. Langley, D. P. Wielechowski, V. Vieru, N. F. Chilton, B. Moubaraki, L. F. Chibotaru, and K. S. Murray. Modulation of slow magnetic relaxation by tuning magnetic exchange in Cr_2Dy_2 single molecule magnets. *Chemical Science*, 5(8):3246–3256, 2014.

[34] J. Martínez-Lillo, D. Armentano, G. De Munno, W. Wernsdorfer, J. M. Clemente-Juan, J. Krzystek, F. Lloret, M. Julve, and J. Faus. Heterotetranuclear Oxalato-Bridged $Re_3^{IV}M^{II}$ (M = Mn, Fe, Co, Ni, Cu) Complexes: A

New Example of a Single-Molecule Magnet (M = Ni). *Inorganic Chemistry*, 48(7):3027–3038, 2009.

[35] T. D. Harris, M. V. Bennett, R. Clérac, and J. R. Long. $[ReCl_4(CN)_2]^{2-}$: A High Magnetic Anisotropy Building Unit Giving Rise to the Single-Chain Magnets $(DMF)_4MReCl_4(CN)_2$ (M = Mn, Fe, Co, Ni). *Journal of the American Chemical Society*, 132(11):3980–3988, 2010.

[36] J. Martínez-Lillo, T. F. Mastropietro, E. Lhotel, C. Paulsen, J. Cano, G. De Munno, J. Faus, F. Lloret, M. Julve, S. Nellutla, and J. Krzystek. Highly Anisotropic Rhenium(IV) Complexes: New Examples of Mononuclear Single-Molecule Magnets. *Journal of the American Chemical Society*, 135(37):13737–13748, 2013.

[37] X.-Y. Wang, C. Avendaño, and K. R. Dunbar. Molecular magnetic materials based on 4d and 5d transition metals. *Chemical Society Reviews*, 40(6):3213, 2011.

[38] E. Ruiz, A. Rodríguez-Fortea, S. Alvarez, and M. Verdaguer. Is It Possible To Get High T_C Magnets with Prussian Blue Analogues? A Theoretical Prospect. *Chemistry – A European Journal*, 11(7):2135–2144, 2005.

[39] M. N. Leuenberger and Daniel Loss. Quantum computing in molecular magnets. *Nature*, 410(6830):789–793, 2001.

[40] D. Stepanenko, M. Trif, and D. Loss. Quantum computing with molecular magnets. *Inorganica Chimica Acta*, 361(14–15):3740–3745, 2008.

[41] Y. I. Spichkin, A. K. Zvezdin, S. P. Gubin, A. S. Mischenko, and A. M. Tishin. Magnetic molecular clusters as promising materials for refrigeration in low-temperature regions. *Journal of Physics D: Applied Physics*, 34(8):1162–1166, 2001.

[42] A. R. Rocha, V. M. García-suárez, S. W. Bailey, C. J. Lambert, J. Ferrer, and S. Sanvito. Towards molecular spintronics. *Nature Materials*, 4(4):335–339, 2005.

[43] L. Bogani and W. Wernsdorfer. Molecular spintronics using single-molecule magnets. *Nature Materials*, 7(3):179–186, 2008.

[44] S. Sanvito. Molecular spintronics. *Chemical Society Reviews*, 40(6):3336, 2011.

[45] K. S. Pedersen, J. Bendix, and R. Clérac. Single-molecule magnet engineering: building-block approaches. *Chemical Communications*, 50(34):4396–4415, 2014.

[46] E. Coronado. Molecular magnetism: from chemical design to spin control in molecules, materials and devices. *Nature Reviews Materials*, 5(2):87–104, 2019.

[47] A.-L. Barra, A. Caneschi, D. Gatteschi, and R. Sessoli. High-Frequency EPR Spectra for the Analysis of Magnetic Anisotropy in Large Magnetic Clusters. *Journal of the American Chemical Society*, 117(34):8855–8856, 1995.

[48] S. Hill, R. S. Edwards, S. I. Jones, S. Maccagnano, J. M. North, N. Aliaga, E.-C. Yang, N. S. Dalal, G. Christou, and D. N. Hendrickson. Single Crystal High Frequency Cavity-based EPR Spectroscopy of Single Molecule Magnets. *MRS Proceedings*, 746, 2002.

[49] J. Krzystek, A. Ozarowski, and J. Telser. Multi-frequency, high-field EPR as a powerful tool to accurately determine zero-field splitting in high-spin transition metal coordination complexes. *Coordination Chemistry Reviews*, 250(17–18):2308–2324, 2006.

[50] L. Spillecke. *High-frequency/high-field Electron Paramagnetic Resonance Investigations on Metal-Organic Molecular Compounds*. PhD thesis, Heidelberg University, 2021.

[51] A. Okazawa, T. Nogami, H. Nojiri, and T. Ishida. Ferromagnetic Dy-Ni and Antiferromagnetic Dy-Cu Couplings in Single-Molecule Magnets [Dy_2Ni] and [Dy_2Cu]. *Inorganic Chemistry*, 47(21):9763–9765, 2008.

[52] K. Fujiwara, A. Okazawa, N. Kojima, G. Tanaka, S. Yoshii, H. Nojiri, and T. Ishida. Oximato-bridged light-lanthanide Ln_4Cu complexes showing ferromagnetic Ln-Cu exchange coupling. *Chemical Physics Letters*, 530:49–54, 2012.

[53] A. Abragam and B. Bleaney. *Electron paramagnetic resonance of transition ions*. Oxford Classic Texts in the Physical Sciences. Oxford University Press, London, England, 2012.

[54] D. Khomskii. *Transition Metal Compounds*. Cambridge University Press, Cambridge, England, 2014.

[55] C. Benelli and D. Gatteschi. *Introduction to Molecular Magnetism: From Transition Metals to Lanthanides*. Wiley-VCH Verlag, Weinheim, Germany, 2015.

[56] D. Gatteschi, R. Sessoli, and J. Villain. *Molecular Nanomagnets*. Oxford University Press, 2006.

[57] S. Gao, editor. *Molecular Nanomagnets and Related Phenomena*. Springer Berlin Heidelberg, 2015.

[58] M. Born and R. Oppenheimer. Zur Quantentheorie der Molekeln. *Annalen der Physik*, 389(20):457–484, 1927.

[59] D. R. Hartree. The Wave Mechanics of an Atom with a Non-Coulomb Central Field. Part II. Some Results and Discussion. *Mathematical Proceedings of the Cambridge Philosophical Society*, 24(1):111–132, 1928.

[60] V. Fock. Näherungsmethode zur Lösung des quantenmechanischen Mehrkörperproblems. *Zeitschrift für Physik*, 61(1–2):126–148, 1930.

[61] J. C. Slater. Note on Hartree's Method. *Physical Review*, 35:210–211, 1930.

[62] D. R. Hartree and W. Hartee. Self-consistent field, with exchange, for beryllium. *Proceedings of the Royal Society of London. Series A - Mathematical and Physical Sciences*, 150(869):9–33, 1935.

[63] D. J. Griffiths and D. F. Schroeter. *Introduction to Quantum Mechanics*. Cambridge University Press, 3 edition, 2018.

[64] B. Bransden and C. Joachain. *Physics of Atoms and Molecules*. Pearson Education, 2014.

[65] W. Pauli. Über den Zusammenhang des Abschlusses der Elektronengruppen im Atom mit der Komplexstruktur der Spektren. *Zeitschrift für Physik*, 31(1):765–783, 1925.

[66] F. Hund. *Linienspektren: Und Periodisches System der Elemente*. Springer Berlin Heidelberg, 1927.

[67] P. Zeeman. Ueber einen Einfluss der Magnetisierung auf die Natur des von einer Substanz emittirten Lichtes. In *Verhandlungen der Physikalischen Gesellschaft zu Berlin. Jg. 15*. Leipzig Barth, 1896.

[68] L. H. Thomas. The Motion of the Spinning Electron. *Nature*, 117(2945):514–514, 1926.

[69] K. W. H. Stevens. Matrix Elements and Operator Equivalents Connected with the Magnetic Properties of Rare Earth Ions. *Proceedings of the Physical Society. Section A*, 65(3):209–215, 1952.

[70] C. Rudowicz and C. Y. Chung. The generalization of the extended Stevens operators to higher ranks and spins, and a systematic review of the tables of the tensor operators and their matrix elements. *Journal of Physics: Condensed Matter*, 16(32):5825–5847, 2004.

[71] K. A. Gschneidner Jr. and L. Eyring, editors. *Handbook on the Physics and Chemistry of Rare Earths. Vol. 23*. Elsevier Science, 1996.

[72] R. A. Layfield and M. Murugesu. *Lanthanides and Actinides in Molecular Magnetism*. Wiley-VCH Verlag, Weinheim, Germany, 2015.

[73] H. A. Kramers. Théorie générale de la rotation paramagnétique dans les cristaux. *Proceedings of the Royal Netherlands Academy of Arts and Sciences*, 33(6–10):959 –972, 1930.

[74] S. Zhang, W. Mo, B. Yin, G. Zhang, D. Yang, X. Lü, and S. Chen. The slow magnetic relaxation regulated by the coordination, configuration and intermolecular dipolar field in two mononuclear Dy^{III} single-molecule magnets (SMMs). *Dalton Transactions*, 47(35):12393–12405, 2018.

[75] M. Anand. Thermal and dipolar interaction effect on the relaxation in a linear chain of magnetic nanoparticles. *Journal of Magnetism and Magnetic Materials*, 522:167538, 2021.

[76] J.-Q. Huang, Q.-W. Chen, Y.-S. Ding, X.-F. Zhu, B.-W. Wang, F. Pan, and Z. Zheng. Enhancement of Single-Molecule Magnet Properties by Manipulating Intramolecular Dipolar Interactions. *Advanced Science*, 12(1), 2024.

[77] S. E. Palmer and J. T. Chalker. Order induced by dipolar interactions in a geometrically frustrated antiferromagnet. *Physical Review B*, 62:488–492, 2000.

[78] A. Morello, F. L. Mettes, F. Luis, J. F. Fernández, J. Krzystek, G. Aromí, G. Christou, and L. J. de Jongh. Long-Range Ferromagnetic Dipolar Ordering of High-Spin Molecular Clusters. *Physical Review Letters*, 90:017206, 2003.

[79] A. Morello, F. L. Mettes, O. N. Bakharev, H. B. Brom, L. J. de Jongh, F. Luis, J. F. Fernández, and G. Aromí. Magnetic dipolar ordering and relaxation in the high-spin molecular cluster compound Mn_6. *Physical Review B*, 73:134406, 2006.

[80] D. C. Johnston. Magnetic dipole interactions in crystals. *Physical Review B*, 93:014421, 2016.

[81] J. B. Goodenough. An interpretation of the magnetic properties of the perovskite-type mixed crystals $La_{1-x}Sr_xCoO_{3-\lambda}$. *Journal of Physics and Chemistry of Solids*, 6(2–3):287–297, 1958.

[82] J. B. Goodenough. Theory of the Role of Covalence in the Perovskite-Type Manganites $[La, M(II)]MnO_3$. *Physical Review*, 100:564–573, 1955.

[83] J. Kanamori. Superexchange interaction and symmetry properties of electron orbitals. *Journal of Physics and Chemistry of Solids*, 10(2–3):87–98, 1959.

[84] A. Bencini, C. Benelli, A. Caneschi, R. L. Carlin, A. Dei, and D. Gatteschi. Crystal and molecular structure of and magnetic coupling in two complexes containing gadolinium(III) and copper(II) ions. *Journal of the American Chemical Society*, 107(26):8128–8136, 1985.

[85] M. Andruh, I. Ramade, E. Codjovi, O. Guillou, O. Kahn, and J. C. Trombe. Crystal structure and magnetic properties of $[Ln_2Cu_4]$ hexanuclear clusters (where Ln = trivalent lanthanide). Mechanism of the gadolinium(III)-copper(II) magnetic interaction. *Journal of the American Chemical Society*, 115(5):1822–1829, 1993.

[86] H. B. G. Casimir and F. K. du Pré. Note on the thermodynamic interpretation of paramagnetic relaxation phenomena. *Physica*, 5(6):507–511, 1938.

[87] K. C. Kao. *Dielectric Phenomena in Solids*. Elsevier, 2004.

[88] K. S. Cole and R. H. Cole. Dispersion and Absorption in Dielectrics I. Alternating Current Characteristics. *The Journal of Chemical Physics*, 9(4):341–351, 1941.

[89] D. W. Davidson and R. H. Cole. Dielectric Relaxation in Glycerol, Propylene Glycol, and n-Propanol. *The Journal of Chemical Physics*, 19(12):1484–1490, 1951.

[90] S. Havriliak and S. Negami. A complex plane representation of dielectric and mechanical relaxation processes in some polymers. *Polymer*, 8:161–210, 1967.

[91] L. Gu and R. Wu. Origins of Slow Magnetic Relaxation in Single-Molecule Magnets. *Physical Review Letters*, 125:117203, 2020.

[92] L. Gu and R. Wu. Origin of the anomalously low Raman exponents in single molecule magnets. *Physical Review B*, 103:014401, 2021.

[93] M. Briganti, F. Santanni, L. Tesi, F. Totti, R. Sessoli, and A. Lunghi. A Complete *Ab Initio* View of Orbach and Raman Spin–Lattice Relaxation in a Dysprosium Coordination Compound. *Journal of the American Chemical Society*, 143(34):13633–13645, 2021.

[94] Quantum Design, Inc. *Magnetic Property Measurement System MPMS3 User's Manual*, 15th edition, June 2016.

[95] Quantum Design, Inc. *Physical Property Measurement System Vibrating Sample Magnetometer (VSM) Option User's Manual*, 4th edition, January 2008.

[96] Quantum Design, Inc. *User guide iHelium3 for the MPMS3*, 1st edition, January 2018.

[97] J. Clarke and A. I. Braginski. *The SQUID handbook: Fundamentals and technology of SQUIDs and SQUID systems v. 1.* The SQUID Handbook. Set. Wiley-VCH Verlag, Weinheim, Germany, 2004.

[98] M. Buchner, K. Höfler, B. Henne, V. Ney, and A. Ney. Tutorial: Basic principles, limits of detection, and pitfalls of highly sensitive SQUID magnetometry for nanomagnetism and spintronics. *Journal of Applied Physics*, 124(16), 2018.

[99] S. Foner. Versatile and Sensitive Vibrating-Sample Magnetometer. *Review of Scientific Instruments*, 30(7):548–557, 1959.

[100] Quantum Design, Inc. *Magnetic Property Measurement System AC Option User's Manual*, 2nd edition, November 1999.

[101] G. A. Bain and J. F. Berry. Diamagnetic Corrections and Pascal's Constants. *Journal of Chemical Education*, 85(4):532, 2008.

[102] J. Park. *High-field Electron Spin Resonance study on Correlated Transition Metal Compounds and Metal-Organic Compounds*. PhD thesis, Heidelberg University, 2015.

[103] C. Enss and S. Hunklinger. *Tieftemperaturphysik*. Springer, Berlin, Germany, 2000.

[104] C. P. Poole. *Electron Spin Resonance: A Comprehensive Treatise on Experimental Techniques*. Interscience Publishers, 1967.

[105] G. Feher and A. F. Kip. Electron Spin Resonance Absorption in Metals. I. Experimental. *Physical Review*, 98:337–348, 1955.

[106] M. Linzer. Line Parameters of Lorentzian Curves Containing Arbitrary Mixtures of Absorption and Dispersion. *Journal of Applied Physics*, 40(1):372–376, 1969.

[107] G. E. Pake and E. M. Purcell. Line Shapes in Nuclear Paramagnetism. *Physical Review*, 74:1184–1188, 1948.

[108] J. Arneth, C. Pachl, G. Greif, B. Beier, P. W. Roesky, K. Fink, and R. Klingeler. Towards Understanding Prolate $4f$ Monomers: Numerical Predictions and Experimental Validation of Electronic Properties and Slow Relaxation in a Muffin-shaped Er^{III} Complex. *arXiv:2507.15547*, 2025.

[109] J. Arneth, L. Spillecke, C. Koo, T. A. Bazhenova, E. B. Yagubskii, and R. Klingeler. The Relevance of Non-Axiality and Low-Lying Excited States for Slow Magnetic Relaxation in Pentagonal-Bipyramidal Erbium(III) Complexes Probed by High-frequency EPR. *Chemistry – A European Journal*, 31(33), 2025.

[110] L. Spillecke, C. Koo, O. Maximova, V. S. Mironov, V. A. Kopotkov, D. V. Korchagin, A. N. Vasiliev, E. B. Yagubskii, and R. Klingeler. Magnetic behavior of the novel pentagonal-bipyramidal erbium(iii) complex $(Et_3NH)[Er(H_2DAPS)Cl_2]$: high-frequency EPR study and crystal-field analysis. *Dalton Transactions*, 50(48):18143–18154, 2021.

[111] T. A. Bazhenova, V. A. Kopotkov, D. V. Korchagin, Y. V. Manakin, L. V. Zorina, S. V. Simonov, I. A. Yakushev, V. S. Mironov, A. N. Vasiliev, O. V. Maximova, and E. B. Yagubskii. A Series of Novel Pentagonal-Bipyramidal Erbium(III) Complexes with Acyclic Chelating N_3O_2 Schiff-Base Ligands: Synthesis, Structure, and Magnetism. *Molecules*, 26(22):6908, 2021.

[112] J. Arneth, X.-F. Li, J. Braun, S. Paul, M. Schulze, C. E. Anson, W. Wernsdorfer, A. K. Powell, and R. Klingeler. The Interplay of Single Ion Anisotropy and Magnetic $3d$-$4f$ Interactions in $V_2^{III}Ln_2^{III}$ Butterfly Complexes. *ChemistryEurope*, 3(3), 2025.

[113] D. Visinescu, C. Desplanches, I. Imaz, V. Bahers, R. Pradhan, F. A. Villamena, P. Guionneau, and J.-P. Sutter. Evidence for Increased Exchange Interactions with 5d Compared to 4d Metal Ions. Experimental and Theoretical Insights into the Ferromagnetic Interactions of a Series of Trinuclear $[(M(CN)_8)^{3-}/Ni^{II}]$ Compounds (M = Mo^V or W^V). *Journal of the American Chemical Society*, 128(31):10202–10212, 2006.

[114] J. Dreiser, K. S. Pedersen, A. Schnegg, K. Holldack, J. Nehrkorn, M. Sigrist, P. Tregenna-Piggott, H. Mutka, H. Weihe, V. S. Mironov, J. Bendix, and O. Waldmann. Three-Axis Anisotropic Exchange Coupling in the Single-Molecule Magnets $NEt_4[Mn_2^{III}(5\text{-Brsalen})_2(MeOH)_2M^{III}(CN)_6]$ (M = Ru, Os). *Chemistry – A European Journal*, 19(11):3693–3701, 2013.

[115] K. S. Pedersen, M. Sigrist, M. A. Sørensen, A.-L. Barra, T. Weyhermüller, S. Piligkos, C. A. Thuesen, M. G. Vinum, H. Mutka, H. Weihe, R. Clérac, and J. Bendix. $[ReF_6]^{2-}$: A Robust Module for the Design of Molecule-Based Magnetic Materials. *Angewandte Chemie International Edition*, 53(5):1351–1354, 2014.

[116] J.-L. Liu, K. S. Pedersen, S. M. Greer, I. Oyarzabal, A. Mondal, S. Hill, F. Wilhelm, A. Rogalev, A. Tressaud, E. Durand, J. R. Long, and R. Clérac. Access to Heteroleptic Fluorido-Cyanido Complexes with a Large Magnetic Anisotropy by Fluoride Abstraction. *Angewandte Chemie International Edition*, 59(26):10306–10310, 2020.

[117] A. Tomkiewicz, F. Villain, and J. Mrozinski. Magnetic properties and EXAFS study of methylammonium hexaiodorhenate(IV) salts. *Journal of Molecular Structure*, 555(1–3):383–390, 2000.

[118] A. Tomkiewicz, T.J. Bartczak, R. Kruszyński, and J. Mroziński. Magnetic properties, crystal and molecular stucture of $(NBu_4)_2$ $[ReCl_4(ox)]$. *Journal of Molecular Structure*, 595(1–3):225–231, 2001.

[119] Ł. Kucharski, G. Kamieniarz, M. Antkowiak, and A. Drzewiński. Single-Ion Anisotropy Estimates for the Rhenium(IV-Based) Molecular Magnets: Modeling and Simulations Studies. *Journal of the Physical Society of Japan*, 83(6):064702, 2014.

[120] S. K. Singh and G. Rajaraman. Deciphering the origin of giant magnetic anisotropy and fast quantum tunnelling in Rhenium(IV) single-molecule magnets. *Nature Communications*, 7(1), 2016.

[121] F. Karadas, C. Avendano, M. G. Hilfiger, A. V. Prosvirin, and K. R. Dunbar. Use of a rhenium cyanide nanomagnet as a building block for new clusters and extended networks. *Dalton Transactions*, 39(20):4968, 2010.

[122] J. Martínez-Lillo, D. Armentano, G. De Munno, W. Wernsdorfer, M. Julve, F. Lloret, and J. Faus. A Heterotetranuclear [$Ni^{II}Re_3^{IV}$] Single-Molecule Magnet. *Journal of the American Chemical Society*, 128(44):14218–14219, 2006.

[123] V. S. Mironov, T. A. Bazhenova, Y. V. Manakin, and E. B. Yagubskii. Pentagonal-bipyramidal 4d and 5d complexes with unquenched orbital angular momentum as a unique platform for advanced single-molecule magnets: current state and perspectives. *Dalton Transactions*, 52(3):509–539, 2023.

[124] D. Armentano, M. A. Barquero, C. Rojas-Dotti, N. Moliner, G. De Munno, E. K. Brechin, and J. Martínez-Lillo. Enhancement of Intermolecular Magnetic Exchange through Halogen···Halogen Interactions in Bisadeninium Rhenium(IV) Salts. *Crystal Growth and Design*, 17(10):5342–5348, 2017.

[125] Christoper E. Anson, private correspondence.

[126] K. Momma and F. Izumi. VESTA 3 for three-dimensional visualization of crystal, volumetric and morphology data. *Journal of Applied Crystallography*, 44(6):1272–1276, 2011.

[127] G. R. Desiraju and R. Parthasarathy. The nature of halogen · · · halogen interactions: are short halogen contacts due to specific attractive forces or due to close packing of nonspherical atoms? *Journal of the American Chemical Society*, 111(23):8725–8726, 1989.

[128] J. Martínez-Lillo, D. Armentano, G. De Munno, and J. Faus. Magnetostructural study on a series of rhenium(IV) complexes containing biimH_2, pyim and bipy ligands. *Polyhedron*, 27(5):1447–1454, 2008.

[129] D. Wang, Z. Wang, S. Wu, Arramel, X. Yin, C. S. Tang, Y. P. Feng, J. Wu, and A. T. S. Wee. Realizing Two-Dimensional Supramolecular Arrays of a Spin Molecule via Halogen Bonding. *ACS Nanoscience Au*, 2(4):333–340, 2022.

[130] A. V. Gurbanov, T. Hökelek, G. Z. Mammadova, K. I. Hasanov, T. A. Javadzade, and A. N. Belay. Crystal structure and Hirshfeld surface analysis of supramolecular aggregate of 2,2,6,6-tetramethylpiperidin-1-ium bromide with 1,2,3,4-tetrafluoro-5,6-diiodobenzene. *Acta Crystallographica Section E Crystallographic Communications*, 81(1):53–57, 2025.

[131] M. Atzori, F. Artizzu, E. Sessini, L. Marchiò, D. Loche, A. Serpe, P. Deplano, G. Concas, F. Pop, N. Avarvari, and M. L. Mercuri. Halogen-bonding in a new family of tris(haloanilato)metallate(III) magnetic molecular building blocks. *Dalton Transactions*, 43(19):7006–7019, 2014.

[132] J. L. Manson, Q.-z. Huang, C. M. Brown, J. W. Lynn, M. B. Stone, J. Singleton, and F. Xiao. Magnetic Structure and Exchange Interactions in Quasi-One-Dimensional $MnCl_2(urea)_2$. *Inorganic Chemistry*, 54(24):11897–11905, 2015.

[133] F. Ding, C. Yang, X. Gong, H. Zheng, X. Zhou, L. Li, L. Zhang, D. Wang, and B. Pan. Structure, phase transition and properties of the one-dimensional antiferromagnet Cu(2,6-dimethylpyrazine)Br_2. *RSC Advances*, 11(37):22565–22570, 2021.

[134] J. Braun. *The Influence of Intra- and Intermolecular Interactions on the Magnetic and Optical Properties of Lanthanide and Transition Metal Complexes*. PhD thesis, Karlsruhe Institute of Technology, 2023.

[135] M. Ferbinteanu, H. Miyasaka, W. Wernsdorfer, K. Nakata, K. Sugiura, M. Yamashita, C. Coulon, and R. Clérac. Single-Chain Magnet $(NEt_4)[Mn_2(5\text{-}MeOsalen)_2Fe(CN)_6]$ Made of Mn^{III}-Fe^{III}-Mn^{III} Trinuclear Single-Molecule Magnet with an $S_T = 9/2$ Spin Ground State. *Journal of the American Chemical Society*, 127(9):3090–3099, 2005.

[136] Y. Oshima, H. Nojiri, K. Asakura, T. Sakai, M. Yamashita, and H. Miyasaka. Collective magnetic excitation in a single-chain magnet by electron spin resonance measurements. *Physical Review B*, 73:214435, 2006.

[137] J. Schnack and O. Wendland. Properties of highly frustrated magnetic molecules studied by the finite-temperature Lanczos method. *The European Physical Journal B*, 78(4):535–541, 2010.

[138] O. Hanebaum and J. Schnack. Advanced finite-temperature Lanczos method for anisotropic spin systems. *The European Physical Journal B*, 87(9), 2014.

[139] M. Exler and J. Schnack. Evaluation of the low-lying energy spectrum of magnetic Keplerate molecules using the density-matrix renormalization group technique. *Physical Review B*, 67:094440, 2003.

[140] J. Ummethum, J. Nehrkorn, S. Mukherjee, N. B. Ivanov, S. Stuiber, T. Strässle, P. L. W. Tregenna-Piggott, H. Mutka, G. Christou, O. Waldmann, and J. Schnack. Discrete antiferromagnetic spin-wave excitations in the giant ferric wheel Fe_{18}. *Physical Review B*, 86:104403, 2012.

[141] S. Stoll and A. Schweiger. EasySpin, a comprehensive software package for spectral simulation and analysis in EPR. *Journal of Magnetic Resonance*, 178(1):42–55, 2006.

[142] J. Schnack, J. Richter, and R. Steinigeweg. Accuracy of the finite-temperature Lanczos method compared to simple typicality-based estimates. *Physical Review Research*, 2:013186, 2020.

[143] P. Henelius and R. S. Fishman. Hybrid quantum-classical monte carlo study of a molecule-based magnet. *Physical Review B*, 78:214405, 2008.

[144] Deepanshu Chauhan, private correspondence.

[145] J. Arneth. High-resolution Dilatometry Studies on the Honeycomb Quantum Magnets CrI_3 and $Na_2Co_2TeO_6$ and on $La_4Ni_3O_{10}$. Master's thesis, Heidelberg University, 2021.

[146] J. Arneth, K.-Y. Choi, R. Kalaivanan, R. Sankar, and R. Klingeler. Signatures of a quantum critical endpoint in the Kitaev candidate $Na_2Co_2TeO_6$. *Physical Review B*, 110:L140402, 2024.

[147] J. Arneth, R. Kalaivanan, R. Sankar, K. Y. Choi, and R. Klingeler. Competing Interactions and the Effects of Uniaxial Out-of-plane Perturbations in the Honeycomb Antiferromagnet $Na_2Co_2TeO_6$. *arXiv:2506.06189*, 2025.

[148] Source: Trust me bro!

Acknowledgements

The final part of this thesis should be used to thank (certainly not all) the people who significantly contributed to the success of my doctoral studies:

First and foremost, my profound gratitude goes to Prof. Dr. Rüdiger Klingeler for giving me the opportunity to perform this research under his supervision. Not only did his around-the-clock-support and on-eye-level mentoring create a very pleasant working environment, but the trust that he placed in me also greatly helped me on my path to become an independent researcher. Although we sometimes hold different values, we almost always had a good time together also outside of the laboratory. This ultimately manifests itself in the *Heidelberg University* sweatpants that he now wears sometimes at home.

A special thanks goes to Prof. Dr. Maurits Haverkort for acting as the second referee and for being part of my thesis advisory committee. I always enjoyed giving or listening to the scientific talks in his group seminar, discussing about electron correlations with the whole team and, of course, the barbecue with a view on the terrace afterwards.

I would love to thank Dr. Changyun Koo for introducing me to the powerful technique of HF-EPR and the wonderful field of molecular magnetism and for supervising me during the first year of my doctoral studies. I wish you all the best at your new position and that everything works out for you and your family in the future.

The conducted research would not have been possible without the help of all my collaborators. In particular, I want to acknowledge the *Schau-Ins-Land* team, highlighting Dr. Jonas Braun, Dr. Dennis Westerbeck, Dr. Julius Mutschler, Prof. Dr. Oliver Waldmann, Prof. Dr. Jürgen Schnack and Prof. Dr. Annie Powell, for all the days of valuable discussions with one or the other joint beer.

Similarly, none of the presented experiments could have been performed without the technical support from the KIP workshop team and from Rudi Eitel, who, on top of that, always ensured the availability of liquid helium.

I also want to acknowledge all the people from the KIP Verwaltung, especially Elke Schmetzer, Min Young Tenz and Beatrice Schwöbel, for always helping me out with bureaucracy and organisational issues.

A warm thanks coming directly from the heart is addressed to my office mate and good friend Lukas Gries, who has been on this journey with me, since we started our Master's projects. His presence and support made the long, hard days in the laboratory very enjoyable and the already great working trips, group events and summer

schools even better. I wish you all the best for finishing your doctoral studies and I am sure that, no matter where we both end up, we will continue to send each other plenty of (funny) memes [148].

Generally, I want to thank all present and former members of F25 for creating such a wonderful, pleasant space to work in. In particular, this work greatly benefited from long scientific discussions with Dr. Ahmed Elghandour, Dr. Martin Jonak, Tom Wickenh(ä)user, Luca Bischof and Rahel Ohlendorf.

On a personal level, a very special thanks goes out to my close friends Maurice Wesch, Andreas Stach and Malte Thomas for always being there for me and putting up with me, even when I am constantly complaining about all the stuff that went wrong in the lab. Really, I love you guys ♡

At this point, I do not come around thanking also the two most wonderful (not trained) dogs, Twinkie and Chewie Arneth, for cheering me up with their wagging tails and loud howling when I step through the door at my parent's home.

A very warm and special "Thank you" is directed at my girlfriend Nathalie Probst for her constant support and encouragement during my doctoral studies. Thank you for understanding my busy schedule and, most importantly, for always making me feel comfortable and home, whenever I return from work.

Finally, I want to express my deepest gratitude to my parents Andrea and Markus Arneth for their unconditional generosity, support and love over all these years; For always having an open ear for my (personal and work-related) problems; For their guidance and for always giving me strength during hard times. I would not be the person that I am right now, if it was not for you and I sure hope to make you proud. Words can not fully express what I want to say, but please know that I am eternally grateful for what you have done for me.

Erklärung

Ich versichere, dass ich diese Arbeit selbstständig verfasst und keine anderen als die angegebenen Quellen und Hilfsmittel benutzt habe.

Heidelberg, den 11.08.2025,